UNIVERSITAT DE BARCELONA

Electron Energy Loss Spectroscopy Solutions for Nanoscale Materials Science Problems

Sònia Estradé Albiol

Electron Energy Loss Spectroscopy Solutions for Nanoscale Materials Science Problems

Tesi que presenta **Sònia Estradé Albiol** per optar al títol de
Doctor per la Universitat de Barcelona en el marc del
Programa de Doctorat en Nanociències

Directors de la Tesi:
Dr. Francesca Peiró Martínez
Dr. Jordi Arbiol Cobos

MIND-IN^{2}UB, Departament d'Electrònica, Universitat de Barcelona

UNIVERSITAT DE BARCELONA

Al Joan,

a la Maite,
al Salvador,
a la Tere,

i al F. Miquel

My hovercraft is full of EELS

Monty Python

The Hungarian Phrasebook Sketch

Acknowledgements

This thesis has been a rather eventful journey. One filled with extremely significant episodes, most of them good, some of them bad. Well, *even grieves are a joy long after to the one that remembers all that was wrought and endured*, if we are to believe the classics. A journey definitively filled with sheer oddity. Take, for instance, the strange coincidence that had me working closely with someone named Sònia, someone name Estrader (mind the r) and yet again, with someone called Arbiol (mind the r once more) –how unlikely is that? and how unsettling?.. I did not spend all those years playing dungeons and dragons and not learn a thing or two about courage, but still.

Anyway, most importantly, it has been a journey I could not have undertaken on my own. And this seems to be the right place to acknowledge the people and institutions that have helped me along the way.

First of all, I want to acknowledge my alma mater for funding me through an APIF (formerly known as BRD) grant, and Prof. J.R. Morante for finding the means to fund me before that.

I also want to thank the staff at Serveis Cientificotècnics, especially Dr. Quim Portillo, Joan Mendoza and Dr. Aranzazu Villuendas, for their help and support. I want to thank Dr. Albert Romano, Dr. Francisco Hernández, Román Jiménez, Dr. María Jesús López (at UB) and Rosa Córdoba (at INA, in Zaragoza) for helping me with FIB sample preparation, and for always having a good piece of advice to give me. I also want to thank my colleague Dr. Daniel Prades, for his DFT simulations of EEL spectra, and for being such a nice, helpful, and often entertaining, officemate.

I want to express my deep gratitude to the STEM group in LPS, Orsay, for their hospitality, for their guidance, for their dedication, and because they always seem to schedule the parties so that I will be there when they take place. I would like to thank everybody in STEM group for making me feel like one of them at all occasions, and especially Prof. Christian Colliex, Dr. Mike Walls and Franciso de la Peña, with whom I worked more closely, and from whom I have learnt so much.

An equally deep gratitude to the SuperSTEM laboratory in Daresbury, for trusting me with operating a really expensive machine unsupervised, and for the freedom they gave me. To Prof. Andrew Bleloch, for allowing me to spend time in the laboratory, and for helping me understand aberration-corrected STEMs in greater depth. To Dr. Mhairi Gass, Dr. Budhika Mendis, Dr. Kassim Sader, Dr. Bernhard Schaffer, Dr. Peng Wang, Dr. Linshu Jiang, Iain Godfrey, Marg Robinshaw and the rest of the staff for their scientific support and for letting me borrow a bicycle and a helmet, trying to teach me how to play golf, giving me rides home, taking me to the pub and taking me to a conference by a Nobel Laureate, in no particular order.

Thanks also to the group of Prof. Marie-Jo Casanove at CEMES in Toulouse for having me for a short stage of a few days to learn about tripod sample preparation, and to the group of Gustav van Tendeloo at EMAT, for accepting me for a short stage that had to be finally cancelled.

I want to thank our collaborators who provided the samples that have been characterized in this thesis, first of all because it would not have been possible without them, and, just as importantly, because of our interesting scientific interactions. The groups of Prof. Anna Fontcuberta in EPFL (Lausanne) and Prof. Martin Eickhoff in Walter Schottky Institut, (München), who are carrying out their investigations in the field of semiconducting nanowires. The group of Dr. Alfonso Cebollada in IMM (Madrid), involved in the field of magnetic materials. Dr. Sven Barth, presently at University College (Cork), and his coworkers -especially Prof. Sanjay Mathur at Department of Inorganic Chemistry in Würzburg University- with whom I have very little personal contact but a very fluid e-mail interaction. Dr. Marta Estrader at ICN and her coworkers, as we seem to find ourselves at the beginning of a very promising collaboration. Dr. Esther Alarcón at ICTJA, and my former colleagues Dr. Albert Tarancón, Álex Morata and Dr. Eva Pellicer -I had a great time in the TEM sessions I shared with all of them. Dr. Llibertat Abad, Dr. Lluís Balcells and Prof. Benjamín Martínez at ICMAB, for their interesting samples and enlightening discussions. Xavier Martí and Franco Rigato also at ICMAB, for our always challenging collaboration. Dr. Ingrid Cañero Infante, now in CNRS-Thales (Palaiseau), with whom I worked quite closely during her PhD. at ICMAB, and whose scientific knowledge, enthusiasm and determination are so very impressing. Dr. Gervasi Herranz, Dr. Florencio Sánchez and Prof. Josep Fontcuberta, at

ICMAB, with whom I have spent quite some time discussing experimental data, for all the physics I have learnt from them in the process. This is some long list of collaborators, let us hope it only gets longer with time.

To my fellow organisers of the "Encontres amb el Tercer Cicle", present and past, for keeping me connected with science beyond EELS and the microscope. To my friends and colleagues at the Department of Electronics, Luis, Dani, Olga, Román, Paco, Teresa, Xavi, Cristian, Maria, Marta, Sergi, Pablo –yes, I will have that coffee later, and no, I am not a workaholic.

To Dr. Emma Rossinyol, now at Servei de Microscòpia de la Universitat Autònoma, who preceded me as a PhD. student working on TEM in the Department of Electronics, and who has helped me a great deal whenever I have used the facilities in Universitat Autònoma. To my colleague Sònia Conesa, now carrying out her PhD. on HRTEM of semiconducting nanowires. And, of course, to Josep M. Rebled, who has recently begun his PhD., with whom I have been closely collaborating these past few months.

I would like to thank all the senior researchers in Electronics Department for their help and advice, and especially our Head of Department, Prof. Albert Cornet. In particular, I would like to thank Prof. Alejandro Pérez for helping me understand the subtleties of the Thesis submission process.

Thanks to my co-advisor, Dr. Jordi Arbiol, for teaching me how to use a microscope, how to prepare a sample, and how to present the results of a TEM characterization, and for the many hours spent together at the J2010F.

I would like to express my gratitude to my advisor, Dr. Francesca Peiró for always challenging my conclusions and always respecting my views; for helping me tirelessly when facing any problem and refusing to take much credit for any good result; for the many things I have learned from her, regarding TEM sample preparation, TEM observation, data analysis, materials science, scientific communications and even teaching skills; for her excellent advice, which I have not always followed. Oh, and for putting up with my star trek jokes in our thesis meetings. Her energy, honesty and rigour have been a constant example for me.

On a more personal note, I would like to thank my family and partner for their support and understanding, and I would also like to acknowledge my father for all the effort he has put in supporting physics in Catalunya and the use of Catalan in the field of physics.

Index

1. Introduction

1.1. An Introduction To EELS

1.1. An introduction to EELS

1.1.1 EELS in a nutshell

In the Transmission Electron Microscope (TEM), an incident electron suffers both elastic and inelastic scattering by the solid state thin sample that is being characterised. In the event of inelastic scattering, the incident electron gives a part of its energy to the electrons in the sample. The amount of lost energy can then be measured by a magnetic filter at the end of the column, and a plot displaying how many electrons have lost what amount of energy will give us an Electron Energy Loss (EEL) Spectrum. Thus, in an EEL Spectrum the ordinate axis corresponds to the number of electrons, or counts, and the abscise corresponds to the Energy Loss.

Notice that most electrons shall not suffer any inelastic scattering whatsoever. As a consequence, the greatest contribution to the spectrum is due to these electrons having lost zero energy, giving rise to the so-called zero loss peak (ZLP). As for those electrons having lost a certain amount of energy, they may lose it to ionization of specimen electrons, transitions from occupied core states to unoccupied core states or to conduction band states, to interband transitions or excitations of collective vibrations of conduction band electrons.

Incident electrons carry a given momentum, and it is worth keeping in mind that in an inelastic scattering event not only energy, but also momentum, may be transferred. In fact, this is the reason why it is not straightforward to compare EELS results with those obtained by means of optic spectroscopies.

EELS detectors can provide an energy resolution down to the order of the 0.1 eV. In addition, incident electrons can be tuned by TEM optics, making it possible to get spectroscopic information from an extremely constrained area, and to combine EEL Spectroscopy with TEM imaging.

1.1.2 The Physics of EELS

1.1.2.1 Understanding inelastic scattering

Whenever an incident beam interacts with a solid state specimen in the TEM, a number of signals are generated, as schematically displayed in figure 1.1.1.

A scattering event is inelastic if the incident fast electron suffers a detectable energy loss. Elastic scattering can be viewed as being billiard-ball-like, with very little energy loss implied. Yet, Rutherford scattering may cause appreciable displacement damage to the sample, with an energy interchange in the order of the tens of eV.

Single scattering refers to one single scattering event; plural scattering, to a string of several (countable) scattering events suffered by the incident electron; finally, multiple scattering refers to a string of scattering events which are too numerous to keep track of them, and, thus, to implement accurate calculations.

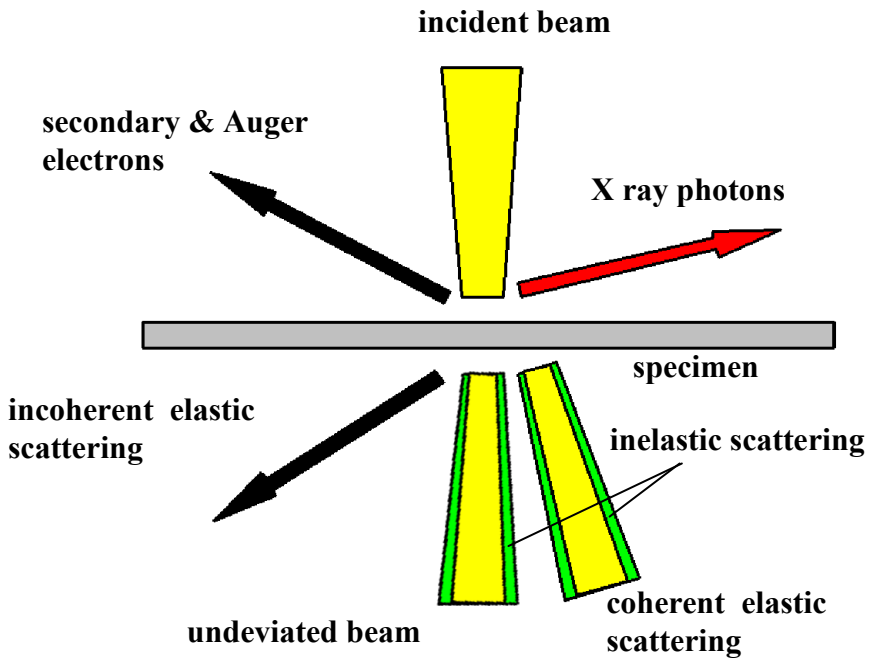

Figure 1.1.1: *Signals generated from the beam/specimen interaction in the TEM.*

The probability for a scattering event to take place is described by its cross section. The cross section is the apparent area each atom makes available in relation to the event. In order to understand this definition, it is important to keep in mind that, if the number of atoms per unit volume in the solid state sample is n_a, then, the probability that a scattering event X, described by a cross section σ_X, takes place in a differential thickness dy is: $\text{Prob}(X) = n_a\sigma_X dy$ [1.1]. Alternatively, we can define the mean free path (mfp) λ as the average distance travelled before the event takes place, thus $\lambda = 1/n_a\sigma_X$.

The cross section may be a function of angle, and of the energy lost by the incident electron in the case of an inelastic event, and, in this sense, the differential cross section per unit solid angle $\frac{d\sigma_X}{d\Omega}$ and the double differential cross section $\frac{d^2\sigma_X}{d\Omega dE}$ are usually referred to.

A simplistic description of **elastic scattering** is given by assuming Rutherford scattering from the whole atom. In this case, $\frac{d\sigma}{d\Omega} = \frac{4\gamma^2 Z^2}{a_0^2 q^4}$ [1.2] where Z is the atomic number, $\gamma = \left(1 - \frac{v^2}{c^2}\right)^{-1/2}$, $a_0 = 0.529 \cdot 10^{-10}\,\text{m}$ is the Bohr radius and q is the scattering vector $q = 2k_0\sin(\theta/2)$, with $\vec{q}$ being the momentum transferred to the nucleus in $\hbar$ units. Notice that formula [1.2] implies a strongly forward peaked scattering.

Rutherford scattering does not take into account the screening of the nucleus potential by localised electrons, overestimates scattering at low angles and, if integrated over all angles, yields an infinite cross section.

In order to take the screening into account, a Yukawa potential with a screening radius r_0 can be considered: $V(r) = \frac{Ze}{4\pi\varepsilon_0 r}\exp(-r/r_0)$ [1.3]

Then, the obtained differential cross section is of the form: $\frac{d\sigma}{d\Omega} = \frac{4\gamma^2 Z r_0^4}{a_0^2}\left(\frac{Z}{q^2 r_0^2 + 1}\right)^2$ [1.4]

We will later discuss the physics of **inelastic scattering** in detail.

Inelastic scattering can promote a number of excitations in the specimen. Phonons are the lowest form of life in the desexcitation chain, as everything else dies by exciting a phonon. Their energy is yet too low (less than 0.1 eV) to be detected in the EELS spectrum.

Collective oscillations of the free electrons, ejections of a single valence electron (single electron excitation) and ejections of a single atom core electron (core-loss) will be present in the EELS spectrum.

1.1.2.2 Lentz formalism of atomic inelastic scattering

Let us consider the inelastic scattering of an electron by a single atom. This event is described by a differential cross section $d\sigma_i/d\Omega$.

Lentz modification of Morse's theory of elastic scattering gives an expression for the inelastic differential cross section of the form:

$$\frac{d\sigma_i}{d\Omega} = \frac{4\gamma^2 Z}{a_0^2 q^4}\left[1 - \frac{1}{(1+(qr_0)^2)^2}\right] \qquad [1.5]$$

where again the electrons in the atom are described by a screening radius r_0 (in a Thomas-Fermi model, r_0 can be assumed to be $r_0 = a_0 Z^{-1/3}$). $\vec{q}$ is the scattering vector $\vec{q} = \vec{k}_f - \vec{k}_0$, where $\vec{k}_f, \vec{k}_0$ are the final and initial momentum of the incident electron respectively (see figure 1.1.2).

q^2 can be written as $q^2 = k_0^2\left(2 - 2\sqrt{1-2\theta_E}\cos\theta - 2\theta_E\right)$ [1.6], where θ is the scattering angle (i. e.: the angle between $\vec{k}_f$ and $\vec{k}_0$, as shown in figure 1.1.2), and θ_E is the characteristic scattering angle $\theta_E = \frac{E}{2E_0}$, with E_0 being the initial energy, and E, the energy loss.

Using a Taylor expansion for $\sqrt{1-2\theta_E}$ and $\cos\theta$ up to second order in θ_E and θ, we obtain

$$q^2 \approx k_0^2\left(\theta^2 + \theta_E^2\right)$$

[1.7]

Substituting in the differential inelastic cross section expression, we obtain:

$$\frac{d\sigma_i}{d\Omega} \approx \frac{4\gamma^2 Z}{a_0^2 k_0^4}\frac{1}{(\theta^2+\theta_E^2)^2}\left[1-\frac{\theta_0^4}{(\theta^2+\theta_E^2+\theta_0^2)^2}\right]$$

[1.8]

where $\theta_0 = \frac{1}{k_0 r_0}$.

Equation [1.8] contains the information relative to the angular distribution of the scattered electrons. Notice that the largest part of the scattering falls between θ_E and θ_0, where the differential inelastic cross section is roughly proportional to θ^{-2}.

One can be interested in the total cross section integrated up to a certain angle β. In this case,

$$\sigma_i(\beta) \approx \frac{8\pi\gamma^2 Z}{k_0^2}\ln\left[\frac{(\beta^2+\theta_E^2)(\theta_0^2+\theta_E^2)}{\theta_E^2(\beta^2+\theta_0^2+\theta_E^2)}\right]$$

[1.9]

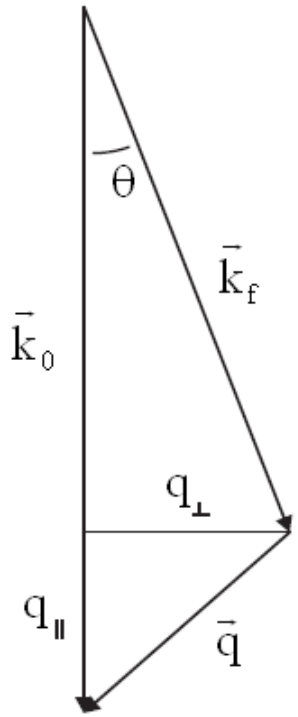

Figure 1.1.2: *Geometric construction of the scattering vector.*

1.1.2.3 The quantum mechanical approach: Bethe Theory

Let us now consider a sample, consisting of one atom for simplicity (we will later see how accurate this simplification is), as being described before and after the inelastic scattering event by its wavefunctions, ψ_0 and ψ_n. ψ_0 will then be the ground state of the atom and ψ_n a certain excited state.

If we can regard the interaction with the atom as a perturbation for the fast electron, which we can reasonably do in any practical EELS experiment, we can use the first order Born approximation to obtain a differential cross section of the form

$$\frac{d\sigma_n}{d\Omega} = \left(\frac{m_0}{2\pi\hbar^2}\right)\frac{k_f}{k_0}\left|\int V(\vec{r})\psi_0\psi_n^* e^{i\vec{q}\vec{r}}\,d\tau\right|^2 \qquad [1.10]$$

Again, $\vec{q}$ is the scattering vector, and, thus, $\hbar\vec{q} = \hbar(\vec{k}_0 - \vec{k}_f)$ is the moment transferred to the atom. $\vec{r}$ is the coordinate of the fast electron, $V(\vec{r})$ is the interaction potential and, finally, $d\tau$ is a differential volume element within the atom.

The explicit form for $V(\vec{r})$ is given by

$$V(\vec{r}) = \frac{Ze^2}{4\pi\varepsilon_0 r} - \frac{1}{4\pi\varepsilon_0 r}\sum_{j=1}^{Z}\frac{e^2}{\left|\vec{r} - \vec{r}_j\right|} \qquad [1.11]$$

where $\vec{r}_j$ is the position of the j-th electron in the atom.

Notice that the interaction potential is not a proper potential. In fact, it is related to the electrostatic potential ϕ as $V = e\phi = -U$, where U is the potential energy of the fast electron.

Also notice that the atomic nucleus contribution to V amounts to zero when integrated, because of its symmetry. In physical terms, we could say that the nucleus mass is by no means comparable to the mass of the incident electron, and thus no inelastic scattering is allowed. **Inelastic scattering is an electron-electron event.**

Integrating, $\frac{d\sigma_n}{d\Omega} = \left(\frac{4\gamma^2}{a_0 q^4}\right)^{(a)} \frac{k_f}{k_0}\left|\varepsilon_n(q)\right|^2$ [1.12]

where (a) is the Rutherford cross section for a single electron, and ε_n is the dynamical structure factor

$$\varepsilon_n = \left\langle \psi_n \left| \sum_j \exp(i\vec{q}\vec{r}_j) \right| \psi_n \right\rangle = \int \psi_n^* \sum_j \exp(i\vec{q}\vec{r}_j)\psi_n d\tau$$

[1.13]

It is then convenient to define the **generalized oscillator strength** (GOS) as

$$f_n(q) = \frac{E_n}{R}\frac{\left|\varepsilon_n(q)\right|^2}{(qa_0^2)}$$

[1.14]

where E_n is the energy lost in the transition (finally appearing in an explicit form) and R is the Rhydberg energy $R = \frac{m_0 e^4/2}{(4\pi\varepsilon_0\hbar)^2} = 13.6\text{eV}$.

Substituting in [1.8], we obtain $\frac{d\sigma_n}{d\Omega} = \frac{4\gamma^2 R}{E_n q^2}\frac{k_f}{k_0} f_n(q)$ [1.15]

It is worth noticing that in the $q\to 0$ limit, $f_n(q) = f_n$, with f_n being the dipole oscillation strength –**optical absorption is governed by the dipole oscillation strength.**

As we are interested in the E dependence of the differential cross section, we can now define

$$\frac{d^2\sigma}{d\Omega dE} = \frac{4\gamma^2 R}{Eq^2}\frac{k_f}{k_0}\frac{df}{dE}(q,E)$$

[1.16]

As $\frac{k_f}{k_0} = \sqrt{\frac{E_0 - E}{E_0}}$*, and* $E_0 >> E$*, we can assume* $\frac{k_f}{k_0} \approx 1$.

Recovering equation [1.7], we then obtain $\frac{d^2\sigma}{d\Omega dE} \approx \frac{4\gamma^2 R}{Ek_0^2}\left(\frac{1}{\theta^2 + \theta_E^2}\right)\frac{df}{dE}$ [1.17]

This formalism applies to single atoms or gas specimens, but TEM experiments are supposed to deal with solid state samples. Is this the wrong approach? Not really. The formalism still applies to the inner atomic shells of atoms in a solid, and, even if solid state effects modify df/dE, it can be treated as a perturbation. A scheme of an inelastic scattering event in a crystal is given in figure 1.1.3.

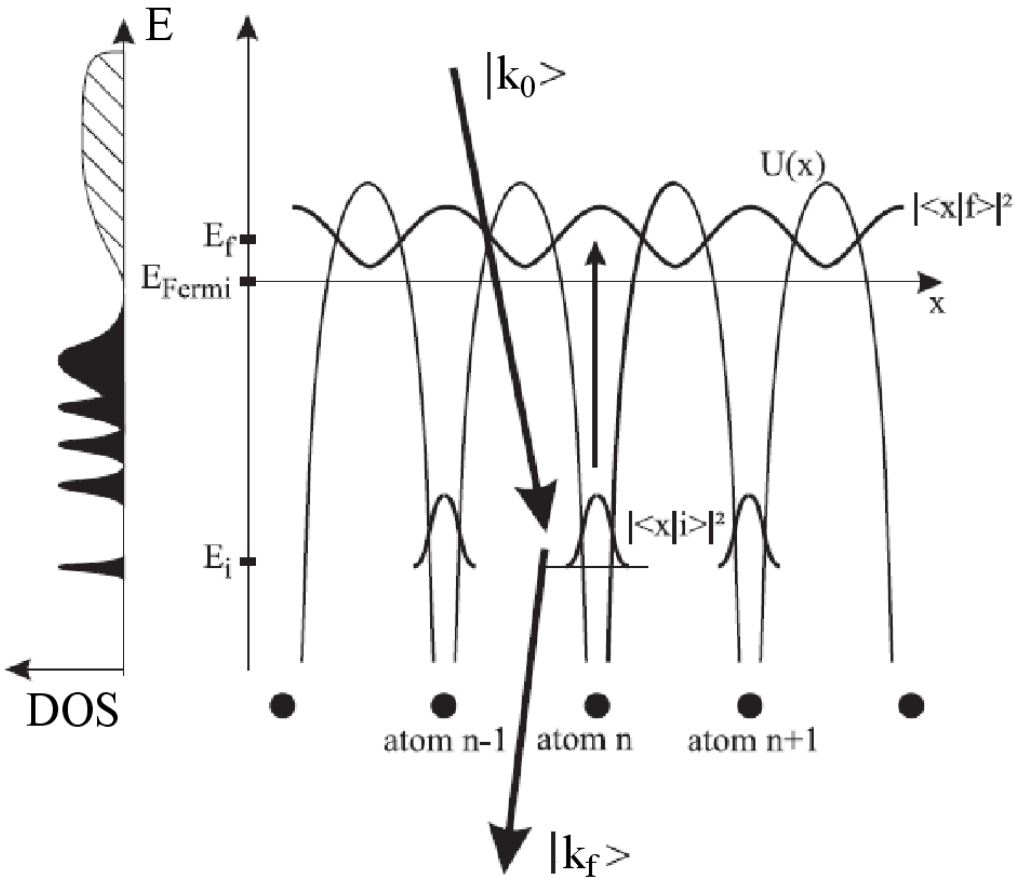

Figure 1.1.3: *Scheme of an inelastic scattering event in a crystal.*

As for outer shell electrons, their wavefunctions are modified by chemical bonding, and collective effects cannot be ruled out.

1.1.2.4 GOS calculations

In order to calculate the GOS, mainly two atomic models are considered, the hydrogenic model and Hartree-Slater.

1.1.2.4(a) Hydrogenic model

In the hydrogenic model, and effective Zs nuclear charge is used in an hydrogen-like model to solve the Schrödinger equation.

In the case of K shell excitations (where K shell refers to the initial state of the specimen electron involved in the transition), the second 1s electron screens the nucleus, reducing its effective charge by $0.3\,q_{e^-}$, so that Zs = Z – 0.3. In the case of L shell excitations, the two K shell electrons and seven L shell electrons are taken into account, the first reducing the effective nucleus charge by $0.85\,q_{e^-}$, the latter, by $0.35\,q_{e^-}$. Thus, Zs = Z – (2·0.85) – (7·0.35) = Z – 4.15

The generalized oscillator strength for a K-edge of carbon in the hydrogenic approximation (E_0=300 kV)[6] is given in figure 1.1.4.

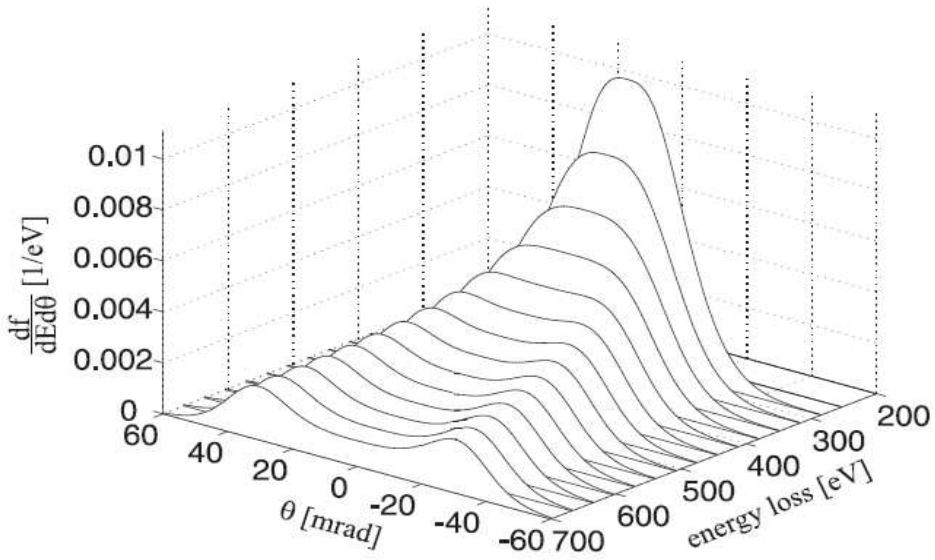

Figure 1.1.4: *Generalized oscillator strength for a K-edge of C in the hydrogenic approximation (E_0=300 kV)*

1.1.2.4(b)Hartree-Slater

Hartree-Slater is just a simplification of Hartree-Fock assuming a spherically symmetric field within the atom.

This means describing the wavefunction of the several electrons in an atom by a Slater determinant containing the N wavefunctions of the N electrons, each of which is an eigenfunction of the Hartree-Fock operator, which takes into account the potential created by the nucleus and by all the other electrons in the atom.

1.1.2.5 Naming the core-loss edges

The atomic shell of the initial state of the sample electron involved in an inelastic scattering event gives its name to the corresponding core-loss edge in the EEL spectrum. In order to keep in mind the quantum numbers and the degeneracy of each electronic shell, we explicitly give them in table 1.1.1.

Edge	State	N	l	j	Degeneracy
K	1s1/2	1	0	1/2	2
L_1	2s1/2	2	0	1/2	2
L_2	2p1/2	2	1	1/2	2
L_3	2p3/2	2	1	3/2	4
M_1	3s1/2	3	0	1/2	2
M_2	3p1/2	3	1	1/2	2
M_3	3p3/2	3	1	3/2	4
M_4	3d3/2	3	2	3/2	4
M_5	3d5/2	3	2	5/2	6
N_1	4s1/2	4	0	1/2	2
N_2	4p1/2	4	1	1/2	2
N_3	4p3/2	4	1	3/2	4
N_4	4d3/2	4	2	3/2	4
N_5	4d5/2	4	2	5/2	6
N_6	4f5/2	4	3	5/2	6
N_7	4f7/2	4	3	7/2	8

Table 1.1.1: *EELS edge, and state, quantum numbers and degeneracy of the initial state of the sample electron involved in the transition.*

1.1.2.6 EELS in the dielectric description

We can also look at our sample from a completely different point of view. Instead of considering the atoms that constitute it, we can take the solid as a medium characterized by a dielectric function ε. ε can be calculated from first principles in many cases, and can be deduced from optical properties.

An electron in a point $\vec{b}$ moving with a velocity $\vec{v}$ will suffer a work

$$W(\vec{b}) = q_{e-} \int_{-\infty}^{\infty} \vec{v}\vec{E}_{ind}(\vec{r}_{e-}(t), t)dt \qquad [1.18]$$

where q_{e-} is the electron charge, $\vec{E}_{ind}$ is the induced electric field, and $\vec{r}_{e-}(t)$ is the electron position at a given time.

We can define $\omega = \frac{E}{\hbar}$, then $W(\vec{b}) = \int_0^{\infty} \hbar\omega\left(P(\omega, \vec{b})\right)^{(a)} d(\hbar\omega)$ [1.19], where (a) is the amount of energy lost by the incident electron at position $\vec{b}$ as an $\hbar\omega$ energy package.

For a bulk sample, $P(\omega) = Im \int_0^{k_y(max)} -\frac{1-\varepsilon\beta^2}{\varepsilon\nu} dk_y$ [1.20], considering that the incident electron is moving along the y axis.

$\beta = \frac{v}{c}$, and $\nu = \sqrt{k_y^2 + \frac{\omega^2}{v^2}(1-\varepsilon\beta^2)}$. Notice that $\varepsilon = \varepsilon(\omega)$.

In the quasistatic limit, $P \propto Im\left(-\frac{1}{\varepsilon}\right)$. P is referred to as the **loss function**.

1.1.2.6(a) The Drude model

In order to find the explicit form of ε(ω) for metals, we can apply the Drude model. The Drude model assumes that the metal contains immobile positive ions and an electron gas of classical, non-interacting electrons of density n, with effective mass m, each of whose motion

is damped by a frictional force due to collisions of the electrons with the ions, characterized by a dampening coefficient γ:

$$m\ddot{\vec{x}} + m\gamma\dot{\vec{x}} = -q_{e^-}\vec{E} \qquad [1.21]$$

The solution to equation [1.21] would then yield $\vec{x} = \frac{q_{e^-}\vec{E}}{m(\omega^2 + i\omega\gamma)}$ [1.22]

Keeping in mind that the polarisation density would then be $\vec{P} = -q_{e^-}n\vec{x} = \varepsilon_0\chi\vec{E}$ [1.23], with χ being the electric susceptibility, then

$$\chi = -\frac{nq_{e^-}^2}{m\varepsilon_0(\omega^2 + i\omega\gamma)} \qquad [1.24]$$

Finally, as ε = 1+ χ,

$\varepsilon = 1 - \frac{\omega_0^2}{(\omega^2 + i\omega\gamma)}$ [1.25] expressed in ε_0 units, where $\omega_0 = \sqrt{nq_{e^-}^2 / \varepsilon_0 m}$

The Drude model can be generalized to insulators (Drude – Lorentz model) by adding n_{it} bound electrons behaving as simple harmonic oscillators. In this case,

$\varepsilon = 1 + \frac{\omega_0^2}{(\omega_{it}^2 - \omega^2) - i\omega\gamma}$ [1.26]; $\omega_{it} = \frac{E_{it}}{\hbar}$, where E_{it} is the characteristic energy of the interband transition

1.1.2.6(b) Kramers-Kronig transformations

For a complex function $\chi = \chi_1(\omega) + i\chi_2(\omega)$ of the complex variable ω, analytic in the upper half plane of ω and which is such that $\chi \to 0$ when $|\omega| \to 0$, the **Kramers–Kronig transformations** allow to obtain $\chi_1(\omega)$ from $\chi_2(\omega)$ and vice versa:

$$\chi_1(\omega) = \frac{1}{\pi} P \int_{-\infty}^{\infty} \frac{\chi_2(\omega')}{\omega' - \omega} d\omega'$$

[1.27]

$$\chi_2(\omega) = -\frac{1}{\pi} P \int_{-\infty}^{\infty} \frac{\chi_1(\omega')}{\omega' - \omega} d\omega'$$

[1.28]

where *P* denotes the Cauchy principal part of the integral, avoiding the pole at $\omega' = \omega$. It is worth noticing that this allows the full function to be reconstructed given just one of its parts.

In the case that $\chi_1(\omega)$ is an even function and $\chi_2(\omega)$ is odd,

$$\chi_1(\omega) = \frac{2}{\pi} P \int_{-\infty}^{\infty} \frac{\omega' \chi_2(\omega')}{\omega'^2 - \omega^2} d\omega'$$

[1.29]

$$\chi_2(\omega) = -\frac{2\omega}{\pi} P \int_{-\infty}^{\infty} \frac{'\chi_1(\omega')}{\omega'^2 - \omega^2} d\omega'$$

[1.30]

As $\varepsilon(\omega)$ fulfils all of the above mentioned conditions, Kramers-Kronig transformation allows to obtain $\mathrm{Re}\left(\frac{1}{\varepsilon}\right)$ from $\mathrm{Im}\left(-\frac{1}{\varepsilon}\right)$:

$$\mathrm{Re}\left[\frac{1}{\varepsilon(\omega)}\right] = P \int_0^{\infty} \mathrm{Im}\left[\frac{-1}{\varepsilon(\omega')}\right] \frac{\omega'}{\omega'^2 - \omega^2} \hbar d\omega'$$

[1.31]

and thus to reconstruct $\varepsilon(\omega)$ from $\mathrm{Im}\left(-\frac{1}{\varepsilon}\right)$.

1.1.2.6(c) Geometric considerations

For interfaces or nanostructures, P(ω) must be calculated taking into account the geometry of the problem. To illustrate this point, we can recall it has been reported that, for a plane parallel to the trajectory of the incident electron[8], P is expected to be of the form $P \propto \mathrm{Im}\left(\frac{\varepsilon-1}{\varepsilon+1}\right)$ and, for a nanosphere[9] of the form $P \propto \mathrm{Im}\left(\frac{\varepsilon-1}{\varepsilon+2}\right)$; in these cases, the response function P is not the loss function but the polarizability, and in the Drude model an effective ω_0 must be introduced, of the form $\omega_{\mathrm{eff}} = \omega_0/\sqrt{2}$ and $\omega = \omega_0/\sqrt{3}$ respectively. It has also been reported that for an interface parallel to the trajectory of the incident electron between materials A and B[8], $P \propto \mathrm{Im}\left(-\frac{2}{\varepsilon_A+\varepsilon_B}\right)$.

1.2.2.6(d) Plasmons

In the case of no dampening, Re(ε) =0 and $\mathrm{Im}\left(-\frac{1}{\varepsilon}\right)$ is maximum at $\omega = \omega_0$. This corresponds to the characteristic energy of resonance of the plasma (the resonance of the electron gas density). The resonance can also be described as a pseudoparticle, the Plasmon, with energy $E_P = \hbar\omega_0$. To generalize this concept to insulators, we can think that the electrons which are given an energy above that of the bandgap, keep an "extra" energy invested in the collective oscillation. In this case $E_P^{\mathrm{eff}} \approx E_P^2 + E_{\mathrm{it}}^2$, as deduced from equation [1.26].

Dampening is yet an important effect. On one hand, the fact that the Plasmon has a finite lifetime makes it broader. A relaxation time of τ ($\tau = 1/\gamma$) will give a full width at half maximum (FWHM) of $\Delta E = \hbar/\tau$ to the Plasmon. On the other hand, equation [1.21] indicates that the Plasmon maximum position will be shifted with respect to the energy determined for the case in which no dampening was taken into account, as $(E_P^{\mathrm{damp}})^2 = E_P^2 - (\Delta E)^2$.

1.1.2.7 Poisson distribution

As every inelastic scattering event suffered by an incident electron can be considered independent to any other previous or subsequent inelastic scattering event, the probability P_n of n scattering events happening follows a Poisson distribution: $P_n = \frac{k^n e^{-k}}{n!}$ [1.32] where k is the expected number of events. If the specimen thickness is t, then the expected number of events will be $k = t/\lambda$.

In the EELS spectrum, P_n will represent the fraction of the whole integrated intensity due to n-scattering processes. In the case of no scattering (n = 0), then

$$P_0 = \frac{I_{ZLP}}{I_{tot}} = e^{-t/\lambda} \qquad [1.33]$$

where I_{ZLP} is the ZLP integrated intensity and I_{tot} is the integrated intensity of the whole spectrum.

Notice that, in order to assume $k = t/\lambda$, scattering angles must be small, so that the same t can be assumed for all n. If several (j) layers were to be taken into account, then, quite trivially $k = \sum_i^j t_i / \lambda_i$, as the scattering probabilities are additive.

1.1.2.7(a) Fourier-log deconvolution

We can also try to use equation [1.32] to determine the intensity of a single scattering event as a function of energy $S_1(E)$. It is then necessary to define $Z(E) = I_0(E) = I_0R(E)$, where Z(E) is the zero event intensity as a function of energy, and R(E) is an instrumental response function with FWMH coincident with that of the ZLP and area equal to unity.

Following equation [1.32], $I_1 = \int S(E)dE = I(t/\lambda)e^{-t/\lambda} = I_0(t/\lambda)$ [1.34].

The experimental one event spectrum will not be given by S(E), but by $J^1(E) = R(E) * S(E)$, where * denotes a convolution between functions Y(x) and Z(x) as defined by

$$Y(x) * Z(x) = \int_{-\infty}^{\infty} Y(x - x')Z(x')dx' \qquad [1.35]$$

Then, if we define $J^n(E)$ as

$$J^n(E) = n!\,(I_0)^{(n-1)}\,R(\underbrace{E) * S(E) * \ldots * S}_{n}(E) \qquad [1.35]$$

the total intensity J(E) will be given by

$$J(E) = \sum_n J^n(E) \qquad [1.37]$$

Let us recall that the Fourier transform $\overline{Y}(f)$ of function Y(x) is given by

$$\overline{Y} = \int_{-\infty}^{\infty} Y(x)e^{i2\pi fx}dx \qquad [1.38]$$

If we take the Fourier transform of equation [1.37] we obtain

$$\overline{J}(f) = \sum_n \overline{J}^0(f)\left[\overline{J}^1(f)\right]^n /(n!I_0{}^n) = \overline{Z}(f)e^{\overline{S}(f)/I_0} \qquad [1.39]$$

Thus, $\overline{S}(f) = I_0 \ln\left[\overline{J}(f)/\overline{Z}(f)\right]$ [1.40]

Yet, we do not want to take the inverse Fourier transform of equation [1.40], as S(f) would be masked by high frequency noise. From a physical point of view, we would be trying to recover features that lay under the actual resolution of the experiment, so we would get a nonsensical result. Instead, we can consider

$$\overline{J}^1(f) = \overline{R}(f)\overline{S}(f) = \overline{Z}(f)\ln\left[\overline{J}(f)/\overline{Z}(f)\right] \qquad [1.41]$$

and take the inverse Fourier transform of equation [1.41].

1.1.3 Experimental conditions. Collection angle. Convergence angle

1.1.3.1 Effect of the collection angle

As the electrons that have lost a certain amount of energy to the specimen are not collected from the whole solid angle, but up to a given collection semiangle β (see figure 1.1.5), the cross sections one has to consider to perform an elemental quantification will not only depend on the primary energy of the incident beam, but also on the collection semiangle β.

Following equation [1.34], for a given core-loss EELS edge e of an element X,

$$I_1^e = I_0(t/\lambda_e) = NI_0\sigma_e \qquad [1.42]$$

where N is the areal density of the element X, N = ρt.

If we introduce a collection semiangle β, equation [1.42] becomes

$$I_1^e(\beta) = NI_0\sigma_e(\beta) \qquad [1.43]$$

Now, we can consider that elastic scattering is to cause a certain number of electrons to fall out of the collection semiangle, and, thus, be left out of the EELS spectrum. In a simplistic approximation, the fraction of left out electrons is the same for electrons having and having not lost the characteristic amount of energy of core-loss transition, so that, if $I_0(\beta)$ is the observed intensity corresponding to no inelastic scattering, we can assume

$$I_1^e(\beta) = NI_0(\beta)\sigma_e(\beta) \qquad [1.44]$$

We can regard the effect of the Plasmon excitation as a redistribution of intensity towards higher energies both at the zero event and the one event peaks. Thus, we can take the effect of Plasmon excitation into account by modifying equation [1.44] into

$$I_1^e(\beta) = NI_{LL}(\beta)\sigma_e(\beta) \qquad [1.45]$$

1.1.3.2 Effect of the convergence angle

If the incident electrons are condensed using a large convergence semiangle α (see figure 1.1.5), in order to obtain the angular distribution of the core-loss scattered electrons, one has to convolute the core-loss angular distribution of a given edge $\frac{dI_1^e(\alpha=0)}{d\Omega}$ by the incident electron angular distribution $\frac{dI_i}{d\Omega}$.

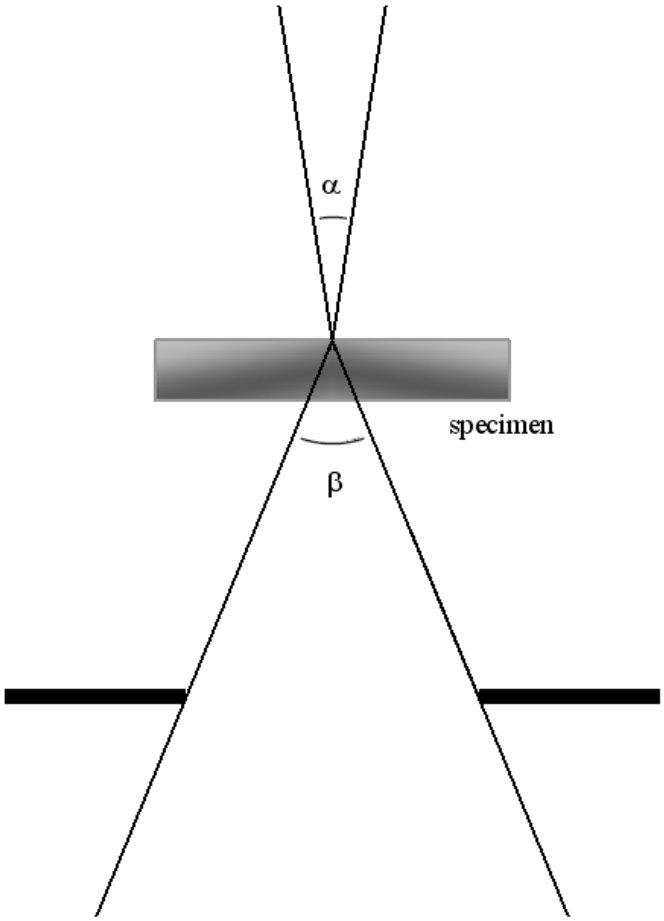

Figure 1.1.5: *Convergence (α) and collection (β) angles.*

If we assume $\frac{dI_1^e(\alpha=0)}{d\Omega}$ to be a Lorentzian function of width $\theta_E = \frac{< E_e >}{2E_0}$, with E_0 being the initial energy, and $< E_e >$ the mean energy loss of the integration region for the given edge, then

$$I_1^e \propto \int_{\theta=0}^{\beta} 2\pi\theta d\theta \int_{\theta'=0}^{\alpha} \theta' d\theta' \int_{\phi=0}^{2\pi} \frac{dI_0}{d\Omega} \frac{1}{\theta^2 + \theta'^2 - 2\theta\theta'\cos\phi + \theta_E} d\phi$$

[1.46]

Generally, $I_i(\alpha)$ is assumed to be a step function with intensity equal to I_0 up to a semiangle α and 0 for bigger angles. In this case,

$$\frac{I_1^e}{I_1^e(\alpha=0)} = F_0 = \frac{2}{\alpha^2 \ln\left(1+(\beta/\theta_E)^2\right)} \int_{\theta=0}^{\beta} \theta d\theta \ln\left[\frac{\psi^2 + \sqrt{\psi^4 + 4\theta^2\theta_E^2}}{\theta_E^2}\right]$$

[1.47]

with $\psi^2 = \alpha^2 + \theta_E^2 - \theta^2$

Notice that the correction accounting for α depends on the edge.

As for low-loss scattering $\theta_E/\beta << 1$, then $\frac{I_{LL}}{I_{LL}(\alpha=0)}$ is close to unity if $\alpha < \beta$ and approximately proportional to the area of the beam disk which falls into the collection aperture if $\alpha > \beta$. Then,

$$I_1^e(\alpha,\beta) = FNI_{LL}(\alpha,\beta)\sigma_e(\beta)$$

[1.47]

with factor F being $F \approx F_0$ for $\alpha \leq \beta$ and $F \approx (\alpha/\beta)^2 F_0$ for $\alpha \geq \beta$.

Finally, the equivalent $\sigma(\alpha,\beta)$ can be defined as $\sigma(\alpha,\beta) = F\,\sigma(\beta)$ [1.48].

1.1.3.3 Choosing your experimental conditions

Following equation 1.17, it is possible to demonstrate that for energies not much higher than the edge characteristic energy the incident electron having suffered and inelastic scattering event is strongly forward peaked . Yet, for energies significantly higher than the edge energy, the maximum intensity is found at angles $\pm\theta_R$, with $\theta_R \approx \sqrt{2\theta_E}$. These maxima are known as the Bethe ridge.

From a physical point of view, the intensity is peaked at those angles corresponding to the incident electron having given all of its momentum to the now free specimen electron. Yet, as the specimen electrons do not necessary have an initial zero momentum, these peaks are rather broad.

As the tail of one core-loss edge will contribute to the background of the following one, it is then clear that a small (5-10 mrad) collection angle will improve the edge/background ratio, making the edge somehow sharper. Yet, choosing a small collection angle will lower the overall signal, which can be problematic specially for edges lying at very high energies. Nevertheless, it can be proved that for collection angles over 20 mrad, considerably increasing of the collection angle leads to negligibly increasing the collected signal.

It is important not to choose angles which are near those of the specimen Bragg spots, as the equivalent σ calculated for those angles will no longer apply given the abnormal rise in elastic scattering signal, leading to considerable quantification errors.

In the case of a small probe, and, thus, of a large α, it is advisable to choose $\beta > \alpha$, as, else, a significant amount of signal will be lost.

1.1.4 What do we learn from an EELS spectrum?

In the present section, a general overview of the utility of the different available informations in the EEL spectrum is given. Their applications will be addressed in further detail in the following chapters.

1.1.4.1 Zero Loss Peak. Thickness determination

The ZLP is the most prominent feature in the low-loss region (and in the whole spectrum). Although it obviously does not contain any energy loss information, it does contain relevant information. Quite trivially, it allows to calibrate the energy scale. In addition, the FWHM of the ZLP gives a good estimation of the resolution of the EELS experiment being conducted.

It is possible to determine the local thickness of the specimen from the EELS spectrum. Although other methods exist, the most straight forward one for doing so is the so-called log-ratio method, which takes advantage of the relation stated in equation [1.33]:

$$t/\lambda = \ln (I_{ZLP}/ I_{tot}) \qquad [1.49]$$

where, again, I_{ZLP} is the ZLP integrated intensity and I_{tot} is the integrated intensity of the whole spectrum. λ can either be calculated or determined from a reference sample.

1.1.4.2 Low-loss region

The low-loss region of the EELS spectrum corresponds to energy losses under about 100eV, as, typically, core-loss edges are found over 100 eV (in the *core-loss region*).

In the case of an insulator specimen, valence band excitations can be observed. These are excitations of a valence band electron to a free state, and, thus, interband transitions. This, of course, requires a suitable experimental resolution. On the other hand, for a thin specimen (and all functional specimens need to be thin) the zero-loss peak is very intense when compared to the actual energy-loss features, as illustrated in figure 1.1.6., and thus the low energy losses are superposed on a background which must be estimated and subtracted, and

which is especially important if the point-spread function of the electron detector has extended tails[10]. A background correction needs to be carried out to extract the tail of the zero-loss peak from the spectrum. Methods to extract the ZLP include assuming symmetry and subtracting the negative tail to the positive energy side; modelling the ZLP by a Gaussian (or Lorentzian) function and subtracting the fitted function from the spectrum; subtracting the normalized ZLP obtained in the void from the normalized spectrum obtained at the specimen; fourier-log deconvolution of the low-loss spectrum. In the case where the spectrum is only used to measure the band gap of the material (and not for further processing in order to derivate its optical properties), a power-law function has been reported[11] to be a good local fit of the tail of the zero-loss peak.

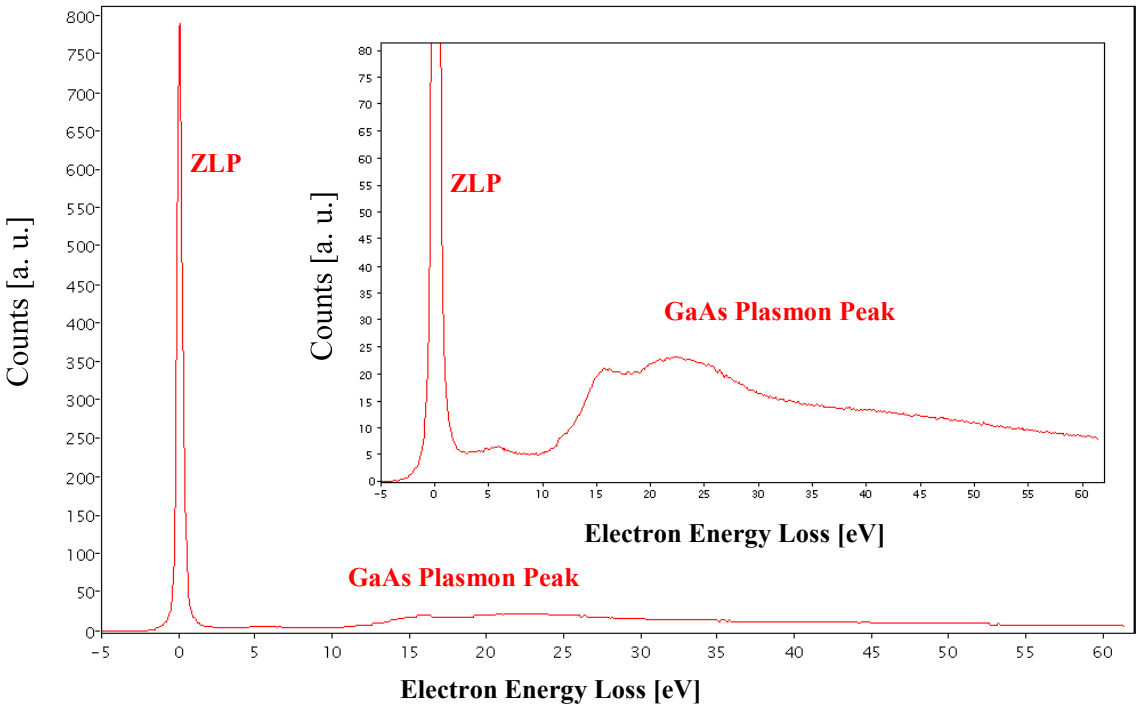

Figure 1.1.6: *Low-loss EELS spectrum of a GaAs nanowire, including the ZLP. Inset: detail of the low-loss spectrum.*

As the dielectric function ε depends on specimen composition, the Plasmon position is widely used to discriminate compounds. In addition, as the width of the Plasmon peak is given by its lifetime, a broadening of the Plasmon Peak can be linked to a greater density of desexcitation modes (for instance at defects). As multiple scattering will lead to an increased intensity towards the high-energy end of the Plasmon (giving it one or several hump-like features), it is possible to determine specimen thickness from the Plasmon shape. Fine structure of the Plasmon could be used in phase identification of compounds by comparison with reference

samples (fingerprinting), although fine structure of Plasmons can be easily blurred by thickness effects.

Some core-loss edges do appear in the low-loss region, namely N and O peaks (n=4,5) are found at low energies. Superposition of low-loss features makes it very difficult to extract any quantitative information from these edges.

Sometimes, a low-loss EELS spectrum is acquired in order to use it as a deconvolution function for a core-loss spectrum. In this case, the low-loss is considered the instrument function on itself, and deconvolution is carried out by dividing the Fourier transform of the core-loss spectrum by that of the low-loss region. This is the so-called fourier-ratio deconvolution method.

1.1.4.3 Core-loss region

The core-loss region consists of excitations from core sates of atoms in the sample. As already said, they are typically found from 100 eV on in the EELS spectrum, and can be observed up to a very optimistic upper limit of 4000 eV –for higher energy losses, the signal-to-noise ratio would be too low.

Core states of atoms can be regarded as eigenvalues rather than energy bands. It is straightforward to identify core-loss edges, by simple comparison of their energy position with a reference table.

Once the specific edges of the elements constituting a compound have been identified, one can try and quantify their relative compositions.

1.1.4.3(a) Quantification

Following equation [1.43], the relative composition of elements A and B will be given by

$$\frac{N_A}{N_B} = \frac{I_A / \sigma_A}{I_B / \sigma_B} = \frac{I_A}{I_B} k_{AB} \qquad [1.50]$$

where I_X is the integrated intensity corresponding to the X element edge, and where k_{AB} contains the information relative to the GOS of elements A and B in the given compound, and of the geometric conditions of the microscope.

It is most convenient to obtain k_{AB} from a reference sample of a similar compound with controlled stoichiometry observed in the same experimental conditions. If this is not possible, σ_X can be calculated for the given geometric conditions.

In order to obtain I_X, first it is convenient to deconvolute the low-loss spectrum from the core-loss spectrum using the fourier-ratio method. Then, it is necessary to fit a function to the background extending in the some 50 eV prior to the peak (usually a function of the form Ae^{-rE} is used, with E being the energy loss and A and r the free fitting parameters) and subtract it from the edge. Then, a numerical integration of the edge intensity will give I_X. A schematic representation of this method is given in figure 1.1.7.

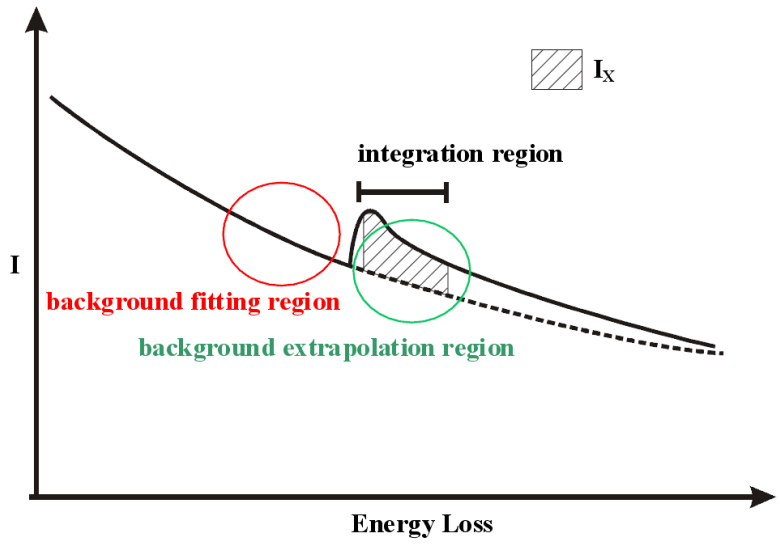

Figure 1.1.7: *Schematic representation of the I_X calculation method.*

If a pathological situation is encountered (if, for instance, peaks overlap) a model fitting approach can be preferable to peak integration, either by employing a weighted sum of reference spectra or a parameterized simulation of the experimental spectrum.

1.1.4.3(b) Oxidation state determination

The shape and onset of an EELS edge can be slightly modified by solid-state contributions. In some favourable cases it is possible to use these changes to determine the oxidation state of the studied element. Carbon K edge[1], oxygen K edge and manganese $L_{2,3}$ edges[12] in different compounds are given in figure 1.1.8.

This can be done by comparing the fine structure of the peak with reference spectra for the expected electronic configurations (fingerprinting) or with simulations of the fine structure for the expected configurations. Notice that fine structure is separated in energy loss near edge (ELNES) and extended energy loss fine structure (EXELFS, starting some 50 eV after the edge onset) contributions. ELNES is a probe of the unoccupied local density of states, and does contain information regarding the electronic structure of the material, whereas EXELFS contains information related to bond lengths.

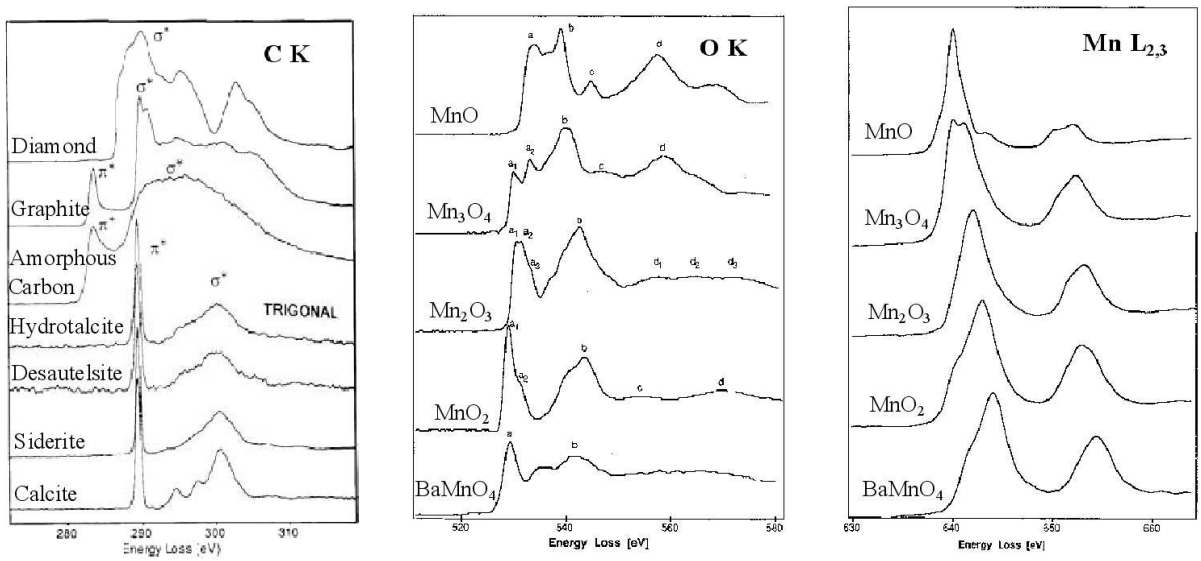

Figure 1.1.8: *Carbon K edge, oxygen K edge and manganese $L_{2,3}$ edges in different compounds.*

It may also be possible to determine the changes in the edge onset if the experimental resolution allows to do so, and to correlate them with the oxidation state of the element. This changes are of the order of a few eV and are usually referred to as chemical shifts.

Other properties of the edge can be correlated to the oxidation state for some elements, such as the splitting of the Fe L_3 peak, or the L_3/L_2 intensity ratio for Mn.

1.1.5 The data cube

As was it was previously stated, it is possible to combine EELS with TEM imaging. Combining spatial and spectroscopic information, we can consider the data cube displayed in figure 1.1.9 (a). Figure 1.1.9 (a) must be interpreted keeping in mind that each δxδyδE box contains a given number of counts.

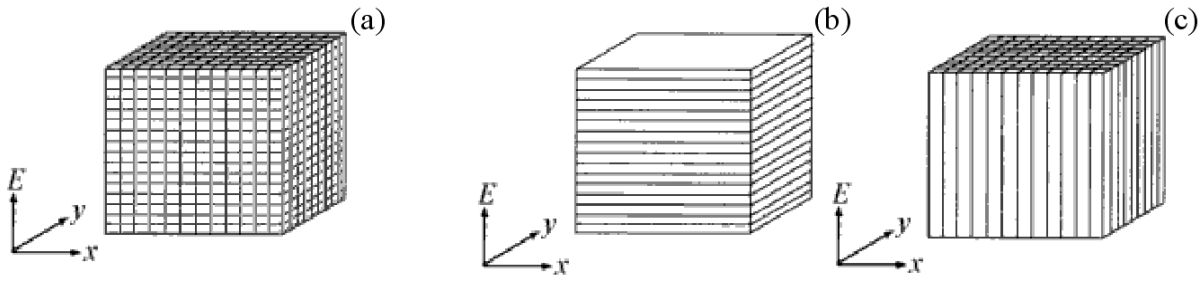

Figure 1.1.9: *(a) Data cube combining imaging and spectroscopy information. Energy filtered TEM (b) and Spectrum image (c) approaches to the data cube.*

1.1.5.1 Energy filtered TEM

Energy filtered TEM (EFTEM) is an imaging technique based on EELS, where the spectrometer is no longer used to determine how many electrons have lost which amount of energy, but as a band-pass filter to form an image only with electrons that have lost an energy amount ranging between E_0 and $E_0+\delta E$. This way we are getting a slice of the data cube which is δE thick (figure 1.1.9 (b)).

This can be used to improve contrast and resolution by getting rid of inelastic scattering, and, thus, chromatic aberration (zero-loss filtering), or to create images which will put in sharp contrast the zones in the sample which contain a given EELS edge and, thus, a given element.

To obtain elemental distribution information from an EFTEM image, it is necessary to get rid

of the background. In order to do so, a two-area method is usually employed: two images are taken at adjacent pre-edge energy ranges; if the intensity due to background in the edge image in a given pixel is I_{bg}, and assuming that the intensities of the pre-edge images are solely due to background, then, for the given background model Ae^{-rE},

$$I_{bg} = \frac{A}{1-r}\left(E_0^{1-r} - (E_0 + \delta E)^{1-r}\right) \qquad [1.51]$$

with $r \approx \frac{2\log(I_{p1}/I_{p2})}{\log((E_{0p2} + \delta E_{p2})/E_{0p1})}$ [1.52]; $A = \frac{(1-r)I_{p2}}{E_{0p2}^{r-1} - (E_{0p2} + \delta E_{p2})^{r-1}}$ [1.53]

where I_{px} are the intensities of the pre-edge images in a given pixel, and E_{0x} and δE_x their initial energies and energy slit widths respectively. Thus, for each pixel of the obtained image, the corrected intensity will be given by $I_c(x,y) = I(x,y) - I_{bg}(x,y)$.

EFTEM is a fast and straightforward method for obtaining a two-dimensional distribution map of a given element. In addition to this, by combining the images obtained for different edges is it possible to create maps of analytic information -elemental maps of the specimen.

1.1.5.2 Spectrum Imaging

Of course, in the EFTEM approach, there is no access to the actual spectrum, so no precise deconvolution or model fitting processing can apply. The alternative approach consists on dividing the area of interest of the specimen in a string of points separated from each other by a vector $\delta x\vec{i} + \delta y\vec{j}$, and acquiring a complete EELS spectrum at each of these points. The obtained result is called a spectrum image (SI) (fig 1.1.9 (c)). The obtained data cube can then be conveniently processed and filtrated in energy.

Accurate control of the beam size and position of the probe are of the utmost importance in a SI experiment, making it a STEM technique.

For the same acquisition time, either the area of interest or the spatial resolution can be demonstrated to be always lower for a SI experiment than for an EFTEM experiment[7].

It is quite common to choose an area of interest consisting of a straight line (for instance, if

the specimen is homogeneous along one direction in the plane, but inhomogeneous along the other). In this case, a spectrum line (SL) is obtained. A SL is a slice of the data cube perpendicular to those obtained in the EFTEM images.

SI information is usually combined with HAADF imaging. HAADF contains complementary chemical information as in HAADF intensity is roughly proportional to the Z^2 of characterized the material.

An example of a SL and HAADF image of a Si NW where Ga interdiffusion from the catalytic has taken place is given in figure 1.1.10

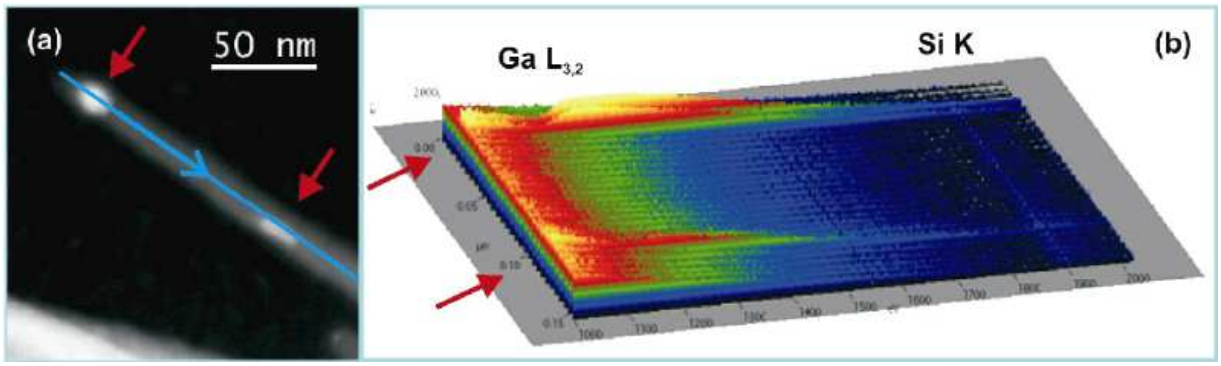

Figure 1.1.10: *(a) HAADF image of a Si nanowire. (b) EEL spectra obtained in the nanowire along the line indicated in (a), which demonstrate the presence of gallium segregation along the nanowire.*

1.1.6 Some orders of magnitude. Some limits

1.1.6.1 Some orders of magnitude

As already mentioned, Plasmons are collective oscillations of free electrons in the specimen. Their characteristic energy is usually in the 10-30 eV range. The mean free path of the interaction is usually of about 100-500 nm.

The interband transitions obviously yield the characteristic energy of the bandgap of the studied compound, which is, for the more favourable semiconducting materials, of the order of a few eV. The mean free path of the interaction is of about 100 nm.

Accessible core-loss edges usually lie in the 100-4000 eV range, as previously stated. In this case, the mean free path of the interaction can be significantly large, in the order of the μm.

Table 1.1.2 shows the first and last chemical element (in terms of atomic number) for which a given edge is available.

Edge	K	L_1	L_2	L_3	$M_{3,2}$	$M_{5,4}$	$N_{3,2}$	$N_{5,4}$
from	He (2)	Al (13)	Ca (20)	Ne (10)	Ti (22)	Ge (32)	Sr (38)	Sb (51)
to	Zn (30)	Ru (44)	Ru (44)	Ru (44)	Ru (44)	U (92)	Xe (54)	Lu (71)

Table 1.1.2: *First and last element (atomic number indicated in brackets) for which a given edge is available in the EELS spectrum.*

1.1.6.2 Energy resolution and energy dispersion

The energy dispersion of an EELS experiment is the range of energy loss included in each channel of the spectrometer. As stated above, the FWHM of the ZLP gives a good estimation of the resolution of an EELS experiment. The overall energy resolution depends on the energy spread of the incident electrons ΔE_0, the quality of the electron optics of the spectrometer, described by a spectrometer resolution ΔE_S, and the relationship between the spatial resolution of the spectrometer s and the energy dispersion D. Egerton[1] considers these factors

to be independent, and thus, the experimental energy resolution would be given by

$$\Delta E^2 = (\Delta E_0)^2 + (\Delta E_S)^2 + (s/D)^2 \quad [1.54]$$

The fact that ΔE_S is not independent from the energy loss means that the actual energy resolution may be worse for the chosen spectrum region than the one measured as the ZL FWHM.

Figure 1.1.11 displays the Low Loss EELS spectra of the same region of a GaAs nanowire, at a 1.0 eV energy dispersion and at a 0.3 eV energy dispersion. The energy resolution is 5.4 eV and 0.8 eV respectively.

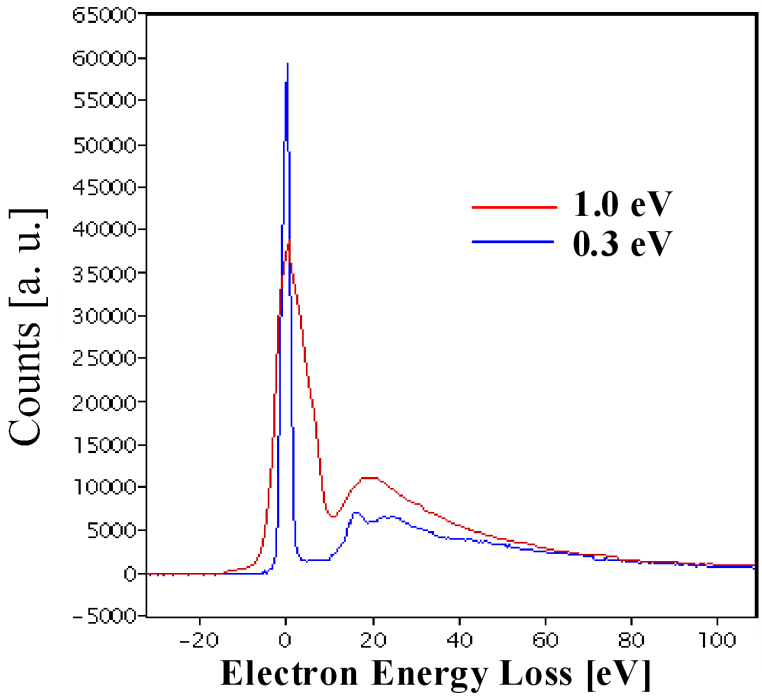

Figure 1.1.11: *Low Loss EELS spectra of a GaAs nanowire, at a 1.0 eV dispersion and at a 0.3 eV dispersion. The energy resolution is 5.4 eV and 0.8 eV respectively.*

1.1.6.3 Detection limits, a matter of moderate optimism

EELS detection of low concentration elements can be difficult, especially if the available peaks are not sharp features in the spectrum. Following Colliex[13], we must distinguish between two unfavourable cases: (a) that we have an element homogeneously distributed in a

given matrix in a low concentration, in which case we would be interested in the minimum detectable mass (MDM), or (b) that we have an element segregated into a matrix, in which case we would be interested in the minimum detectable number of atoms (MDN).

Then[13], the equation relating the detectable concentration C to the signal to noise ratio (SNR) of the available peak is:

$$C = \frac{SNR}{d} \frac{1}{\left(\frac{S}{B} PD \frac{\tau}{T}\right)^{1/2}} \qquad [1.55]$$

Where d is the probe diameter.

S/B is the signal to background ratio and P the probability ($P = \sigma nt$) of core edge excitation of the available peak from a pure foil of the studied element of thickness equal to the actual sample thickness t.

D is the irradiation dose D = JT, with J the probe current density ($J = I/d^2$, being I the total probe current), and T the irradiation time. τ is the recording time.

Equation [1.55] indicates that in the case where we have an homogeneous distribution of low concentration atoms, it is advisable to use large, intense probes.

The detectable number of atoms is given by $N = Cntd^2$ [1.56].

Thus, if we want to detect an element segregated into a matrix, we need thin specimens and a probe with high current density.

In general, a ~5% is considered the minimum detectable concentration for conventional EELS. Yet, it is worth noting that single atoms embedded in biological structures[14], interdiffused atoms at interfaces[15] or catalyst atoms in nanostructures[16] have been detected by EELS. In the last two cases, aberration corrected STEM-EELS allowed even to locate the impurity atoms in the structure.

1.1.6.4 Spatial resolution and delocalisation

Spatial resolution of an EELS experiment is limited by two factors: instrumental broadening of the signal and delocalisation. Delocalisation of inelastic scattering is described in a simplistic, classic way, by the impact parameter b of the incident electron. The smaller the impact parameter, the greater the electrostatic interaction, and the greater the scattering angle. Thus, already the earlier works by Howie et al[17]. suggested the use of an off-axis detector to minimise the delocalisation.

Following Bohr's adiabatic criterion, it is possible to define b_{max} as the maximum impact parameter before the sample electrons are dynamically screened $b_{max} = v / \omega$ [1.57], where v is the velocity of the incident electron and ω describes the energy loss. Muller and Silcox[18] extended this concept to a quantum mechanical model and suggested that b_{max} gives the measured decay length for inelastic scattering. This means that the given delocalisation depends on the energy loss, and that delocalisation should be a greater problem in low-loss experiments than in core-loss experiments. Yet, in the right experimental conditions, delocalisation should be limited to a subnanometric HWFM, even for low-loss.

More recent works in aberration corrected microscopes have proved that EELS can reach atomic resolution. For instance, Pennycook[19] demonstrated core-loss EELS atomic resolution in an aberration corrected STEM, and Grogger[20] et al. achieved subnanometric resolution in an aberration corrected TEM with a monocromator in low-loss EFTEM experiments.

1.1.6.5 Orientation. Channelling. Magic angles

If one solves the Scrödinger equation for an electron in a crystalline potential, the resulting wavefunctions are Bloch waves. When a number of Bragg beams are excited, the same number of Bloch waves propagate in the crystal.

In the most simple case, in the weak beam condition, two Bloch waves are present: one that is peaked at the specimen atoms (type 1) and one that is peaked at half way between the atoms (type 2), both with the same intensity. When tilting the specimen out of the exact Bragg

condition, if the beam-crystal plane angle is reduced, type 1 wave is enhanced, and, if the aforementioned angle is increased, then, the type 2 wave is enhanced.

The orientation dependence of Bloch waves amplitude is a generalised phenomenon and may affect the relative intensity of the EELS edges, depending on the position of the different atoms in the unit cell respective to the exact Bragg plane, which can be used to determine the polarity of a thin film or nanostructure[21].

When in exact zone axis, the Bloch wave description may not be the most suitable one. It is well established that, when a crystal is viewed parallel to the atom columns, the obtained high resolution images may show a one-to-one correspondence with the actual atom positions, if the balance between the resolution of the instrument and the atomic distance is favourable enough; thus, in this case, the exiting wave function mainly depends on the projected structure, and the physical explanation for this to happen has been proposed by van Dyck[22] to be the channelling of the electrons along the atom columns parallel to the beam direction: through the positive electrostatic potential of the atoms, a column acts as a channel for the electron, within which it can scatter dynamically without leaving the column.

This elastic and highly directed incident electron–atom interaction may strongly reduce the EELS signal, so that it is advisable to work slightly off the zone axis to collect EELS data, if possible. Yet, when working in aberration-corrected microscopes, one does want to keep the zone axis condition in order to allow for the chemical analysis of a given atomic column. In this case, electron channelling may give rise to further experimental problems. Artefacts may be encountered, especially if the sample is thick enough. If an inelastic scattering event is suffered by an electron channelling down an atomic column, there is a non-null probability of this electron swapping to the next atomic column and, thus, giving some chemical information about the *wrong* atomic column.

When studying the fine structure of a given edge in an anisotropic crystal, one finds that its shape is strongly dependent on sample orientation. The C K edge fine structure seems to be the most studied such case[23]. It can be proved[23] that a collection angle (or an effective collection angle if convergence angle effects must be taken into account) exists, for which this orientation dependence is lost. It is the so-called magic angle.

1.1.6.6 Sample requirements

In EELS, transmitted electrons are analyzed, so it is obvious enough a requirement that samples should be electrotransparents. Furthermore, spectra obtained from samples thicker than 50 nm will present striking thickness effects that may mask the actual information. Very thin samples may result in very little inelastic scattering to collect, but this can be overcome by taking spectra for a longer time (if possible –if the sample is robust under the beam and there are no drift issues) or by summing up the spectra taken at several equivalent zones. In general, the thinner the better, specially when trying to perform high spatial resolution experiments. It is also advisable to work with a sample which presents a constant thickness, as comparing spectra from zones with different thicknesses may lead to misinterpretations of the obtained data.

Obviously enough, it is nonsensical to characterize a sample containing carbon (or from which it is intended to collect a low-loss spectrum with the interesting plasmon peaks found around 24 eV) lying on holey carbon.

1.1.7 A word on spectrometers.

In the present Thesis, several EELS spectrometers were used, all of them post-column magnetic filters. Post-column filters can be mounted below an existing (S)TEM, without altering the optical elements of the microscope. Other filter typologies include the Castaing Henry and Omega filters which are in-column filters.

A magnetic filter can be understood as being analogous to a glass prism dispersing a beam of white light. Electrons travel down (up if we are in a DSTEM geometry) the spectrometer and are deflected over 90º by an existing magnetic field. Electrons with lower energy (greater energy loss), are further deflected than those having higher energy (smaller energy loss), according to Lorentz force. The spectrum is formed in the dispersion plane as a number of counts vs. energy loss. In addition, electrons travelling in any direction having lost the same amount of energy are focused at the same point of the dispersion plane. The spectrometer acts as a lens and thus *has to be focused*, and aberrations have to be taken care of as well.

The general strategy for focusing the spectrometer and getting rid of its stigmatism is to try to minimise the FWHM of the ZLP. This can be achieved by directly observing it in real time as the adjustments are made. Yet, it is advisable to take a look at the raster image of the low loss spectrum first to make sure the ZLP has the right 2-dimensional shape (as thin as possible and as straight as possible –as opposed to "banana-shaped"). As the focusing conditions do vary on the energy loss, it may be wise to refocus the spectrometer when observing the region of interest in the spectrum by sharpening the studied edge, or, if many, the more central one.

1.1.8 The actual instrumentation

In the present work (S)TEM-EELS characterization has been mainly carried out using a Jeol 2010F (S)TEM with a Gatan GIF spectrometer, a Philips CM30 TEM and a Jeol 2100 (S)TEM.

Additional experiments have been carried out using a VG 501 dedicated STEM with Gatan Enfina Spectrometer at Laboratoire de Physique dels Solides (LPS) in Orsay (France), a VG 501 dedicated STEM with a Nion aberration corrector and a Gatan Enfina Spectrometer at SuperSTEM in Daresbury (UK), and an aberration corrected Nion UltraSTEM 100 with a Gatan Enfina spectrometer, both at LPS and SuperSTEM.

A comparative of the characteristics of these instruments is given in table 1.1.3

Microscope	Type	Beam energy	EELS Spectrometer	Point-to-point resolution / probe size (*)	Energy Resolution
J2010F	(S)TEM	200 keV	GIF	0.19 nm	0.8 eV
CM30	TEM	300 keV	-	0.23 nm	-
J2100	(S)TEM	200 keV	-	0.23 nm	-
VG501	STEM	100 keV	Enfina	0.50 nm*	0.3 eV
Aberration corrected VG501	STEM	100 keV	Enfina	0.10 nm*	0.3 eV
UltraSTEM	STEM	100 keV	Enfina	0.05 nm*	0.3 eV

Table 1.13: *Characteristics of the used instruments*

1.1.9 References

1. Egerton, R. F., "Electron Energy Loss in the Electron Microscope" (2nd ed.), Plenum Press (1996)
2. Williams, D. B. and Carter, C.B., "Transmission Electron Microscopy: A Textbook for Materials Science Basics", Plenum Press (1996)
3. Goodhew, P. J., Humphreys, J., Beanland, R., Electron Microscopy and Analysis (3rd ed.), Taylor & Francis (2000)
4. Bransden, B. H. ; Joachain, C. J., "Quantum mechanics" (2nd ed.), Pearson Education, (2000)
5. Kittel, C., "Introducción a la física del estado sólido" (3a ed.), Reverté (1993)
6. Verbeek, J., Thesis, Antwerp University (2002)
7. Schaffer, B., Thesis, Graz University (2006)
8. Aizpurua, J., Howie, A., García de Abajo, F. J., Physical Review B 60, 11149 (1999)
9. García de Abajo, F. J., Howie, A., Physical Review Letters 80, 5180 (1998)
10. Egerton, R. F., Micron 34, 127 (2003)
11. Erni, R. and Browning, N. D., Ultramicroscopy, 104, 176 (2005)
12. Kurata, H., Colliex, C., Physical Review B, 48, 2102 (1993)
13. Colliex, C., Microscopy Microanalysis Microstructures, 2, 403 (1991)
14. Leapman, R. D., Journal of Microscopy 210, 5 (2003)
15. Muller, D. A., Fitting Kourkoutis, L., Murfitt, M., Song, J. H., Hwang, H. Y., Silcox, J., Dellby, N., Krivanek, O. L., Science, 319, 1073 (2008)
16. Allen, J. E., Hemesath, E. R., Perea, D. E. , Lensch-Falk, J. L., Li, Z. Y., Yin, F., Gass, M. H., Wang, P., Bleloch, A. L, Palmer, R. E., Lauhon, L. J., Nature Nanotechnology 3 168 (2008)
17. Ritchie, R., Howie, A., Philosophical Magazine A 58 753 (1988)
18. Muller, D. A., Silcox, J., Ultramicroscopy 59, 195 (1995)
19. Allen, J. L., Findlay, S. D., Lupini, A. R., Oxley, M. P., Pennycook, S. J., Physical Review Letters, 91, 105503 (2003)
20. Grogger, W., Varela, M., Ristau, R., Schaffer, B., Hoffer, F., Krishnan, K. M., Journal of Electron Spectroscopy and Related Phenomena, 143, 139 (2005)
21. Wang, Y., Xu, Q. Y., Du, X. L., Mei, Z. X., Zeng, Z. Q., Xue, Q. K., Zhang, Z., Physics Letters A, 320, 322 (2004)

22. Van Aert, S., Geuens, P., Van Dyck, D., Kisielowski, C., Jinschek, J. R., Ultramicroscopy, 107, 551 (2005)
23. Daniels, H., Brown, A., Scott, A., Nichells, T., Rand, B., Brydson, R., Ultramicroscopy, 96, 523 (2003)

2. Low-loss EELS

1.2 EELS as a tool for materials science

1.2. EELS as a tool for materials science

1.2.1 Why EELS?

1.2.1.1. The right scale

Some twenty years ago, scientists interested in EELS had to overcome the impression that "EELS [was] a playground for physicists and of little help for solving materials science problems"[1]. Nowadays, given the eventual reduction in scale of the problems at hand and the progressive instrumental advances that have taken place in microscopy in general and in EELS in particular, it seems clear that EELS has become a most crucial tool in materials science and even the life sciences[2,3].

As EELS is performed in the Transmission Electron Microscope (TEM), it benefits from the very high spatial resolution that can be achieved with electron optics, which can focus the electron beam to form a subnanometric probe. In particular, if a field emission gun is used, sufficient current can be obtained for a 1 nm probe. Within aberration corrected instruments, this figure can be reduced to 0.1 nm. In addition, EELS can be easily combined with structural information as obtained from the TEM imaging and diffraction modes, and even with complementary X-ray energy-dispersive spectroscopy (EDXS) if needed.

There is a fundamental limit to the minimum lateral resolution that can be achieved by EELS, irrespective of the electron optics. As commented in chapter 1.1, this limit is given by the delocalisation produced in inelastic scattering, and depends on the energy loss (the lower the loss, the greater the delocalisation)[4]. Yet, fortunately, this limit does not prevent from getting EELS signal from single atom columns at core-loss[5] or subnanometric resolution in low-loss experiments[6].

1.2.1.2. EELS compared to other spectroscopies

1.2.1.2(a) EDXS

The two main spectroscopies used in the TEM are electron energy loss spectroscopy (EELS) and energy-dispersive X-ray spectroscopy (EDXS). The first is based upon measuring the amount of energy given by the incident electron to the sample, and the second one upon detecting the X-rays generated in the subsequent desexcitation process.

Despite the poor energy resolution, EDXS is often preferred to EELS because quantification requires less sophisticated methods. When it is installed and adjusted, the EDXS silicon diode detector requires no further tuning from the operator. Acquisition of the X-ray spectra is straightforward and elemental-quantification software produces elemental ratios, also in a straightforward manner, but accuracy can rarely be considered better than 10%[7]. EDXS becomes more problematic for low Z elements as for them the main desexcitation mechanism is Auger (the X-ray fluorescence yield is below 1% for $Z < 10$)[7] and the detection of low-energy X rays is considerably affected by absorption effects in the specimen and in the detector window. Moreover, EDXS spectrometers have a small collection solid angle (at most a few tenths of a steradian), limited by the size of the detector crystal and the specimen–detector distance.

Using calibration specimens, it was showed as early as 1993 that EELS can detect smaller amounts of an element than EDX spectroscopy for elements below sodium ($Z < 11$) based on K-shell excitation, or below iron ($Z < 26$) using L excitation, given that cross section elemental ratios were experimentally obtained from controlled stoichiometry samples (as opposed to calculated from a physical model)[8].

1.2.1.2(b) XAS

X-ray absorption spectroscopy (XAS) gives an information which is physically equivalent to that obtained in EELS -absorption edges are the equivalent of ionization edges, and can be used to identify and measure the present elements, while the near-edge and extended fine

structure (NEXAFS, EXAFS) allows structural analysis[7]. In this technique X rays can be focused and made to go through a small part of the specimen, as one does with electrons in the TEM. Spatial resolution is worse (down to 30 nm) but energy resolution is significantly better (down to 100 meV) when compared to EELS. As in the case of EELS, avoiding specimen damage is one of its main constraints.

1.2.1.3. Recent developments

With the recent advances in instrumentation (spherical aberration correctors, electron monochromators, new energy filters and CCD detectors) EELS experiments can now be performed with a spatial resolution well below 0.1 nm and an energy resolution better than 0.2 eV.

One of the instrumental highlights in the history of TEM is the recent introduction of systems to compensate for spherical and even chromatic aberrations[9,10,11]. One way of achieving spherical aberration (C_s) correction is based upon the use of two hexapoles where the second order aberrations from the first hexapole are compensated by the second hexapole element. As the two hexapoles additionally induce a third-order spherical aberration which is rotationally symmetric and proportional to the square of the hexapole strength, and is of the opposite sign to that of the objective lens, the spherical aberration of the entire system can be compensated by appropriately controlling the strength of the hexapoles[9]. Alternatively, spherical aberration correction can be achieved through quadrupole-octupole (QO) corrector[10,11]. Schemes of the three multipole lenses are given in figure 1.2.1[11]. The QO corrector uses a quadrupole to put a line focus along the negative spherical aberration axis of an octupole, a further two quadrupoles to produce a line focus in the perpendicular direction in a second octupole, and a fourth quadrupole to reform a round beam (figure 1.2.2)[11]. The two octupoles add a negative spherical aberration in x and y, but also cause some four-fold distortion of the beam. A third octupole, acting on a round beam, is used to correct that distortion. A potential advantage of a QO corrector over a hexapole corrector is the possibility of also correcting the first-order chromatic aberration[11]. Spherical aberration, parasitic second-order axial aberrations, coma and threefold astigmatism, and the non-spherical axial third-order aberrations, star aberration and fourfold astigmatism need to be compensated at the same time by adequately changing the intensity of all the involved lenses. This is achieved by software assisted recursive

measuring and compensation of the aberrations. All kinds of instabilities must be suppressed for the corrector to perform adequately[9,10,11]. Using aberration corrected microscopy, an electron probe smaller than 1 Å can be achieved, which allows imaging of single atoms, clusters of a few atoms, and atomic columns.

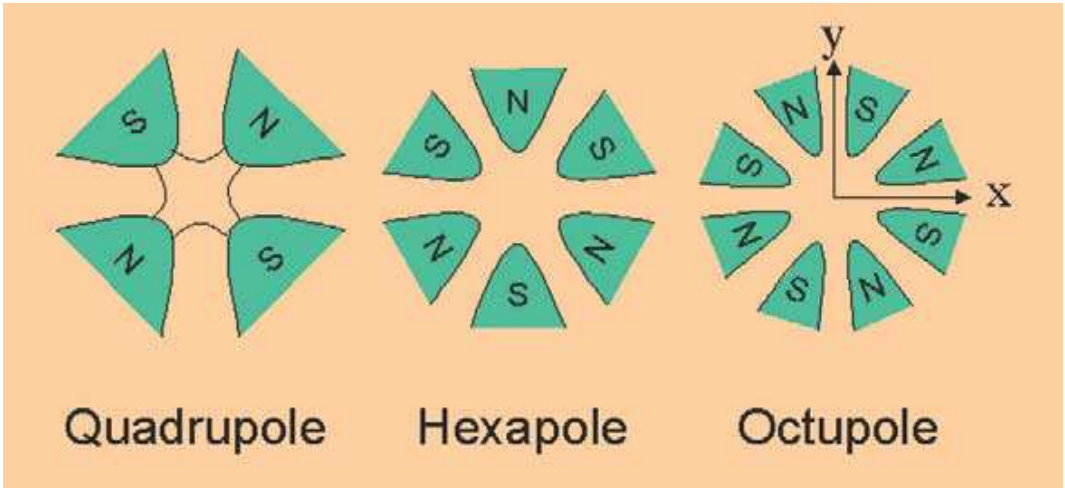

Figure 1.2.1: *Multipole lenses. The z-axis, along which the electrons travel, is into the page. The geometry of the field lines is sketched in on the quadrupole.*

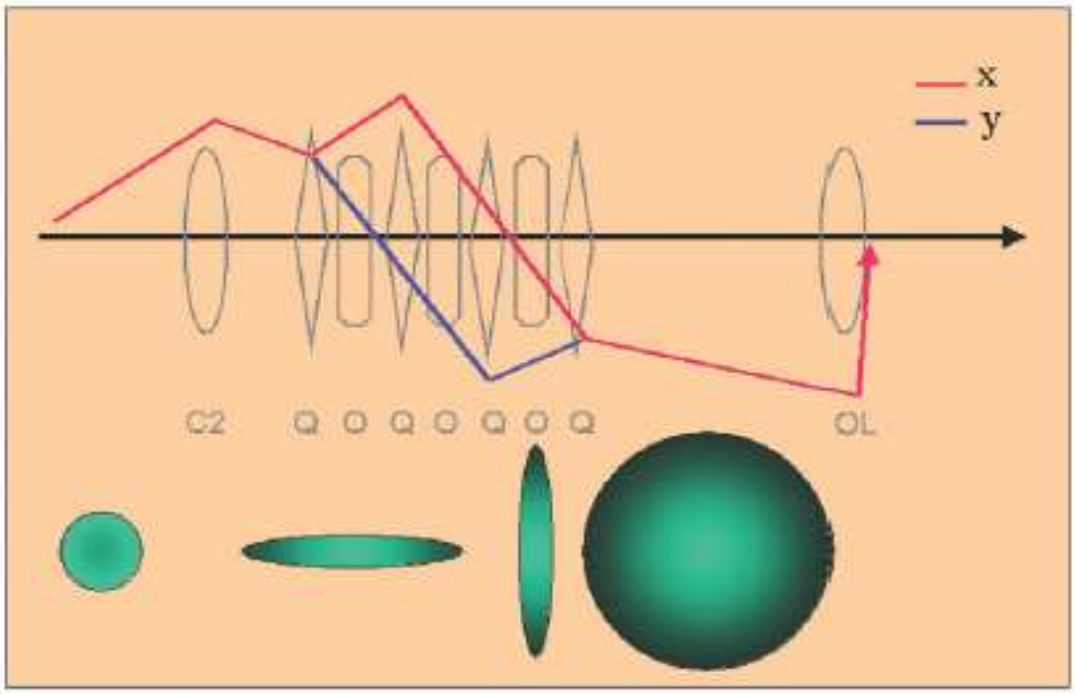

Figure 1.2.2: *Schematic trajectories of axial rays in x and y through the QO aberration corrector (z is along the optic axis). C2 is the final condenser lens and OL is the objective lens. The beam cross section is shown below at four places through the corrector.*

A multipole corrector built into the illumination system of a STEM (figure 1.2.3) increases the image resolution and allows more current to be focused in a given probe. This is of great importance for spectroscopy, as both lateral resolution and signal-to-noise ratio are enhanced.

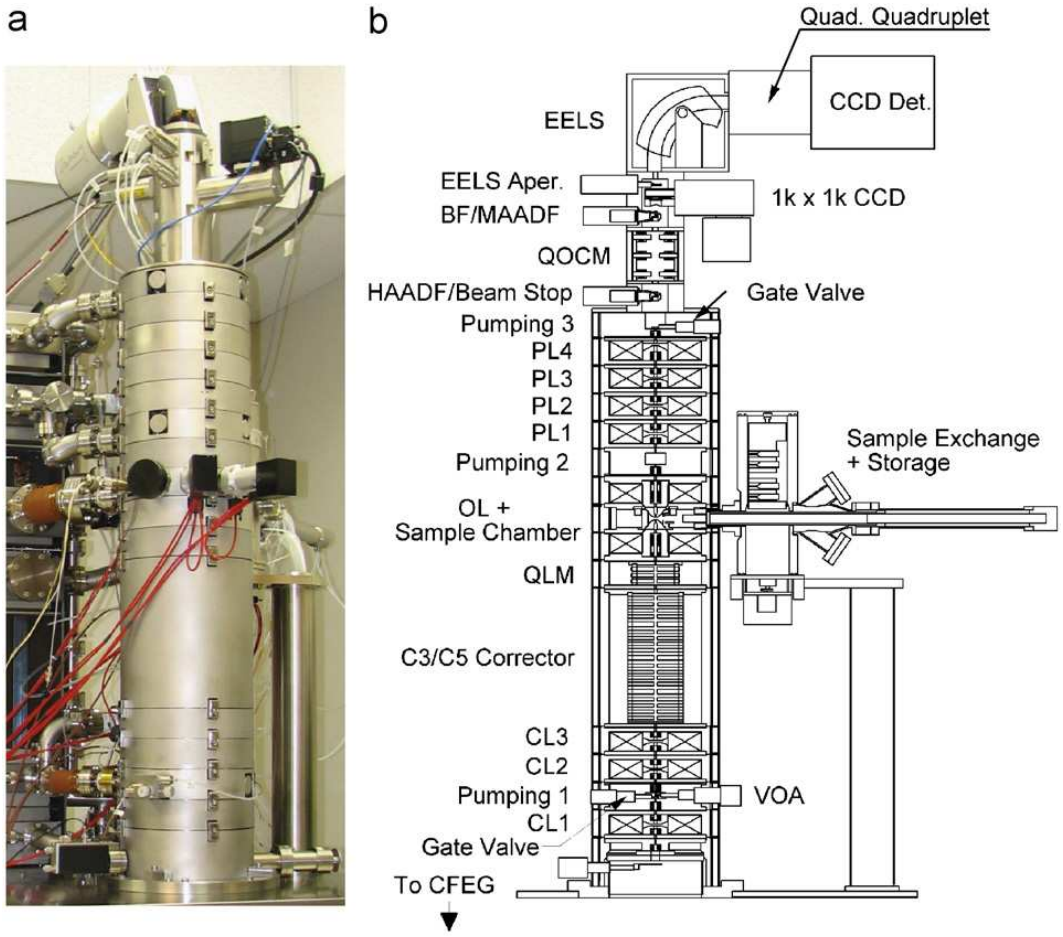

Figure 1.2.3: *Aberration corrected Nion Ultrastem STEM (a) column and (b) schematic cross-section of the column.*

If EELS presents a lower energy resolution when compared to other spectroscopies as XAS, the limitation does not lie in the capabilities of the spectrometers, but in the energy width of the electron source. This energy dispersion is typically 1–2 eV for a thermionic source and 0.5–1 eV for a Schottky or field-emission tip. For a cold FEG, this figure can go down to 0.3 eV. For comparison, synchrotron X-ray sources and beam-line spectrometers commonly provide a resolution below 0.1 eV for absorption spectroscopy, and even below 1 meV in certain cases[12].

In order to reduce the source energy spread, monochromators have been recently introduced. There are two main approaches: the electromagnetic Wien filter and the electrostatic Omega filter. Both types improve the energy width to about 0.2 eV. Yet, they both produce an energy spectrum of the electron source at a dispersion plane, where a narrow energy-selecting slit selects a small fraction of the electron distribution. As a result, many electrons are absorbed by the slit -the beam current at the specimen is reduced by a factor at least equal to the fractional improvement in energy resolution[12]. Nowadays, the monocromators yield a beam current in the order of several 100 pA[12].

The single Wien filter limits the probe size to about 2 nm, whereas there is no such limitation in the case of the Omega filter[13]. In some Wien filter designs[14], the dispersion is compensated and the beam reduced to its original size by using second monochromator section which produces an achromatic image of the electron source (double Wien filter).

1.2.2 Solving problems with EELS

1.2.2.1. Low-loss applications

Bulk plasmon peak position can be used as an indirect compositional measure, and has been extensively used as a local chemical characterization tool, especially in the case of semiconductors. It can be primarily used as an identification tag for determining which compound is there at a given region of the studied specimen[15, 16]. As the plasmon peak position depends on the lattice parameter (as well as the bandgap energy and the dielectric constant) it can also give an indirect measure of structural properties[17, 18].

The need for characterization techniques that provide precise information regarding the bandgap and general optical properties at high spatial resolution seems to be out of question, given the scaling down that has taken place in the field of materials science and the rapidly widening use of nanostructures. In this sense, standard optical techniques such as vacuum ultra-violet spectroscopy do not provide the spatial resolution required to probe a material on the nanometer scale. Low-loss EELS seems to be a most fitting technique for the local characterization of optoelectronic properties at the nanoscale.

For insulators or semiconductors with a sufficiently wide bandgap (that can be less than 1 eV using a monochromated STEM[19]), interband transitions can be observed in the EELS spectrum. It is possible to identify through EELS the bandgap energy of given nanostructures[20,21,22]. It is also possible to assess the existence of localized states within the bandpgap, which may be due to the presence of dislocations or other kinds of defects, for instance[23, 24], which create new energy levels in the local DOS.

A most promising EELS capability is in characterizing the local optical properties of semiconductors through Kramers-Kronig analysis of low-loss data. In 1999, experiments carried in a cold FEG VG 501 STEM demonstrated the possibility to access the local dielectric function of several semiconducting nitrides at the nanoscale through EELS[25]. The reliability of the result directly depends on the quality of the EELS data, mostly concerning the accuracy of the EELS intensity measurement at very low energy. Surface modes of excitation of small particles and nanotubes (in the range of 12-18 eV) have also been studied

through EELS in a cold FEG VG 501 STEM. They have been shown to highly depend on the anisotropy of the nanostructure[26]. Yet, surface plasmons of nanostructures often occur at energy losses below 10 eV and are often poorly resolved, even for very thin specimens. A low energy spread (and hence the use of a monochromator) can greatly benefit the characterization of such surface modes, which mostly describe their optic properties. In this sense, a very recent work by Schaffer et al.[27], demonstrated high resolution EFTEM mapping of gold nanoparticles surface plasmons using a monochromator. On the other hand, Nelayah et al[28]. showed that optical properties can be analyzed in the nearinfrared/visible/ultraviolet domain (energy loss under 3 eV) without a monochromator. A Richardson–Lucy algorithm and customized acquisition process were used to enable the observation of very low energy surface plasmon peaks. This method was applied to an equilateral Ag nanoprism with 78-nm-long sides and allowed the observation of three plasmon resonance modes centered at 1.75, 2.70 and 3.20 eV, corresponding respectively to wavelengths of 709, 459 and 387 nm.

1.2.2.2. Core-Loss EELS elemental identification and quantification. Single atom detection

Maybe the most common question that is addressed using EELS as a characterization tool is which elements, and in what proportion, are found, locally, in a given specimen. Problems such as interdiffusions at interfaces, or elemental distributions in nanostructures, sometimes specifically require EELS because the involved scales exceed the spatial resolution otherwise available.

Elemental identification is straight forward, but quantification is problematic. EELS quantification of a spectrum involves background removal and intensity conversion to chemical concentration through the appropriate, energy dependent, experimental geometry dependent, single-atom cross-section. Quite a lot of discussion has been centered on the optimal way of extracting the background[29,30,31], and a great deal of effort has been devoted to the calculations of EELS cross-sections[32,33,34]. Nowadays, both background fitting and extraction and cross-section calculations are generally carried out using the EELS quantification tools in the Gatan Digital Micrograph software. Although this is a robust and reliable tool, it is also extremely user-dependent, and may give rise to biased or plain nonsensical results depending on their level of expertise (no matter how badly the

quantification is made, the software will always produce a number). In order to avoid the problems associated with this usual quantification procedure, Verbeeck and coworkers[35,36,37] proposed the use of a C based software package (EELSmodel) to carry out a model based quantification of EELS spectra. The EELSmodel program works starting from a series of parameters which are introduced by user, and through a choice of different possible statistical tools, tunes these parameters to finally reach the model which better matches the experimental spectrum. A python model based quantification program (EELSlab) is currently being implemented by de la Peña and coworkers in STEM Group in Orsay.

Recent applications of EELS elemental quantification include the characterization of semiconducting nanostructures[38,39], thin films with applications in spintronics[40,41], or shape memory alloys[42].

As has been previously stated, the incorporation of monochromators and aberration correctors for transmission electron microscopes (TEM) has much helped improve the spatial and energetic resolution of EELS. Yet, best energy and best spatial resolution are not found in the same experimental configurations[43]. Best energy resolution (about 0.1 eV), achieved with monochromators, and most useful for low-loss EELS, comes with a spatial resolution in the order of the 1 nm. In an aberration corrected STEM, where energy resolution is about 0.4eV can achieve a spatial resolution in the order of the Armstrong. Such configuration is best for the core-loss chemical analysis of atomic columns and the localisation of individual atoms in nanostructures.

In this sense, Kimoto and coworkers[44] demonstrated atomic-column imaging of a crystal using core-loss EELS. In particular, the atomic columns of La, Mn and O in manganite $La_{1.2}Sr_{1.8}Mn_2O_7$ were visualized as two-dimensional images, using the La $N_{4,5}$, O K, Mn $L_{3,2}$ and La $M_{5,4}$ edges signal.

Muller and coworkers succeeded in quantifying the vacancy concentrations in $SrTiO_3$ (STO) at atomic scale through core-loss EELS[45]. Varela and coworkers detected a single La dopant atom in $CaTiO_3$, through HAADF intensity and La $M_{5,4}$ edge signal[46]. Recently, single Au atoms were observed in Si nanowires grown using Au as a catalyst[47].

1.2.2.3. Core-Loss EELS atomic coordination and oxidation state determination

In compounds where there is a coordinate bonding, information of the kind of bonding which is present is of the utmost importance to gain insight into the compound structure. The energy loss near edge structure (ELNES) of an EELS edge is given by the local density of states (LDOS) of the atom suffering the inelastic scattering, and, thus, contains information on its bonding. Coordination determination from ELNES fingerprinting is a standard technique from as soon as the mid 1980s[48]. As energy resolution is improved, so is the level of detail in ELNES of EELS edges. In this sense, many efforts have been recently devoted to theoretical calculations of ELNES, which allow the use of theoretical references to compare to actual EELS spectra, and further comprehension of the individual features in the ELNES[49,50].

The shift of the threshold energy of a given edge is a measure of charge transfer but also of coordination number[4]. Chemical shift can thus be used as a fingerprint to determine to which compound belongs the atom giving rise to the observed transition. A thoroughly studied classic case is that of the chemical shift of Si $L_{2,3}$ edge, that has been correlated to the electronegativity of nearest neighbour atoms for Si alloys[51], or to the mean Si-O bond lengths in Si oxides[52], for instance.

White lines ($L_{2,3}$ edges of transition metals and $M_{4,5}$ edges of rare earths) appear in the shape of two sharp peaks, with an energy separation given by the spin-orbit splitting of the initial states. The relative intensity of those peaks, yet, does not correspond to the number of electrons in the initial state, as it would be intuitive. This is so because of a spin selection rule. The final white-line intensity ratio depends on Z number and on the oxidation state[4]. Oxidation state quantification via white line intensity ratio has been demonstrated, for instance, for Co[53] or Fe[54]. We will address the case of Mn in greater detail in the following section.

1.2.2.4. Mn oxidation state determination

Kurata and Colliex, in their 1993 paper[55], gave a very accurate report of both the chemical shift and ELNES of O K edge and the Mn L_3 peak onset, L_3/L_2 intensity ratio and normalized L_2+L_3 total intensity for several manganese oxides. These experiments allowed manganese oxidation state determination by comparing experimental results with the references given, usually by obtaining Mn L_3 peak onset and L_3/L_2 intensity ratio, as they seem to be the most accurate, especially the latter.

Further works studied the electron beam induced reduction of manganese and offered very similar standards for EELS determination of manganese oxidation state[56]. Up to our knowledge, the last great effort to offer trustworthy references for comparison with experimental Mn L_3 peak onset and L_3/L_2 intensity ratio (as well as for Fe L_3 peak onset and L_3/L_2 intensity ratio) was made by Schmid and Mader in 2006. Again, they do not importantly differ from previous references, although they suggest that L_3/L_2 intensity ratio may have been slightly overestimated for Mn^{2+} in the past[54].

Manganese oxidation state determination through EELS has given the opportunity to locally assess phase separation in manganites[40,57,58]. This is of the outmost importance, as phase separation in mixed-valence ferromagnetic manganite films has been suggested to be the most likely microscopic explanation of the macroscopic negligible room-temperature magnetoresistance in magnetic tunnel junctions[59]. Other techniques, such as NMR, can indicate average deviations from the expected $Mn^{3+/4+}$ oxidation state in these compounds, but only EELS seems to be capable of determining where, and ideally why, these deviations are produced.

Local Mn oxidation state determination through EELS is also crucial in many other kinds of systems. Recent applications include fuel cell technology[60], large-scale integrated devices[61] or mineralogy[62].

A very recent work by Varela and coworkers[63] addressed Mn oxidation state quantification in atomically resolved core-loss EELS. In this case, surprisingly enough, edge onset variation seems to be the most accurate measure of Mn oxidation state. Mn valence can still be

quantified through white lines intensity ratio, but it oscillates dependent on Mn lattice site. In particular, best results are obtained when the electron beam is on the Mn-O column, for reasons that are not yet fully understood. New possibilities and new questions are thus now opened.

1.1.3. Aim of this work

In the present work, EELS will be applied to solving several materials science problems.

- Low-loss EELS will be used to characterize compositional and structural modulations in semiconductors.

- Interdiffusions at interfaces of thin films will be assessed through core-loss EELS.

- Oxidation state quantification of Fe and Mn in different nanostructures with magnetic applications will be addressed.

- Finally, EELS elemental quantification and EELS determination of Mn oxidation state will be applied to a thorough investigation of $La_{2/3}Ca_{1/3}MnO_3$ (LCMO) thin layers.

1.1.4. References

1. Colliex, C., Microsc. Microanal. Microstruct., 2, 403 (1991)
2. Pan, Y., Sader, K., Powell, J. J., Bleloch, A., Gass, M., Trinick, J., Warley, A. , Li, A., Brydson, R., Brown, A., Journal of Structural Biology 166, 22 (2009)
3. Calvert, C. C., Brown, A., Brydson, R., Journal of Electron Spectroscopy and Related Phenomena, 143, 173 (2005)
4. Egerton, R. F., "Electron Energy Loss in the Electron Microscope" (2nd ed.), Plenum Press, 1996.
5. Allen, J. L., Findlay, S. D., Lupini, A. R., Oxley, M. P., Pennycook, S. J., Phys. Rev. Lett., 91, 105503 (2003).
6. Grogger, W., Varela, M., Ristau, R., Schaffer, B., Hoffer, F., Krishnan, K. M., J. Elec. Spectroscopy and Rel. Phen., 143, 139 (2005).
7. Egerton, R. F. and Malac, M., Journal of Electron Spectroscopy and Related Phenomena, 143, 43 (2005)
8. Hofer, F. and Kothleitner, G., Microsc. Microanal. Microstruct., 4, 539 (1993)
9. Haider, M., Uhlemann, S., Schwan, E., Rose, H., Kabius, B. Urban, K., Nature 392, 768 (1998)
10. Batson, P. E., Dellby, N., Krivanek, O. L., Nature 418, 617 (2002)
11. Bleloch, A., Lupini, A., Materials Today 7, 42 (2004)
12. Egerton, R. F., Micron 34, 127 (2003)
13. Sigle, W., Annual Review of Materials Research, 35, 239 (2005)
14. Tsuno, K., Microsc. Microanal. 6, 142 (2000)
15. Topuria, T., Browning, N. D., Ma, Z., Applied Physics Letters, 83, 4432 (2003)
16. Irrera, A., Iacona, F., Franzò, G., Boninelli, S., Pacifici, D., Miritello, M., Spinella, C., Sanfilippo, D., Di Stefano, G., Fallica P. G., Priolo, F., Optical Materials 27, 1031 (2005)
17. Shen, Y. G., Mai, Y. W., McKenzie, D. R. , Zhang, Q. C., McFall, W. D., McBride, W. E., Journal of Applied Physics, 88, 1380 (2000)
18. Sanchez, A. M., Beanland, R., Papworth, A. J., Goodhew, P. J., Gass, M. H., Applied Physics Letters, 88, 051917 (2006)
19. Erni, R. and Browning, N. D., Ultramicroscopy, 104, 176 (2005)
20. Kuykendall, T., Ulrich, P., Aloni, S., Yang, P., Nature Materials 6, 951 (2007)

21. Iakoubovskii, K., Mitsuishi, K., Furuya, K., Nanotechnology 19, 155705 (2008)
22. Arenal, R., Stéphan, O., Kociak, M., Taverna, D., Loiseau, A., Colliex, C., Microscopy and Microanalysis, 14, 274 (2008)
23. Batson, P. E., Kavanah, K. L., Woodall, J. M., Mayer, J. M., Phys. Rev. Lett. 57, 2719 (1986)
24. Xin, Y., James, E. M., Arslan, I., Sivananthan, S., Browninga, N. D., Pennycook, S. J., Omnes, F., Beaumont, B., Faurie, J., Gibart, P., Applied Physics Letters, 76, 466 (2000)
25. Lakner, H,, Raferty, B., Brockt, G., Journal of Microscopy, 194, 79 (1999)
26. Kociak, M., L. Henrard, L., Stéphan, O., Suenaga, K., Colliex, C., Physical Review B, 61, 13936 (2000)
27. Schaffer, B., Hohenester, U., Trügler, A., Hofer, F., Physical Review B, 79, 041401 (2009)
28. Nelayah, J., Kociak, M., Stéphan, O., de Abajo, F. J. G., Tencé, M., Henrard, L., Taverna, D., Pastoriza-Santos, I., Liz-Marzán, L. M., Colliex, C., Nature Physics 3, 348 (2007)
29. Su, D. S. and Zeitler, E., Physical Review B, 47, 14734 (1993)
30. Liu, D. R. and Brown, L. M., Journal of Microscopy, 147, 37 (1987)
31. Pun, T., Ellis, J. R., Eden, M., Journal of Microscopy, 137, 93 (1985)
32. A. Weickenmeier; H. Kohl, Philosophical Magazine Part B, 60, 1463 (1989)
33. Hofer, F., Microsc. Microanal. Microstruct., 2, 215 (1991)
34. Potapov, P.L., Jorissen, K., Schryvers, D., Lamoen, D., Physical Review B, 70, 045106 (2004)
35. Verbeek, J., Thesis, Antwerp University, 2002.
36. Verbeeck, J. and Van Aert, S., Ultamicroscopy, 101, 207 (2004)
37. Verbeeck, J, Van Aert, S., Bertoni, G., Ultamicroscopy, 106, 976 (2006)
38. Schade, M., Heyroth, F. Syrowatka, F., Leipner, H.S., Boeck, T., Hanke, M., Applied Physics Letters 90, 263101 (2007)
39. Lari, L., Murray, R.T., Bullough, T.J., Chalker, P.R., Gass, M., Chezec, C., Geelhaar, L., Riechert, H., Physica E 40 2457 (2008)
40. Samet, L., Imhoff, D., Maurice, J.-L., Contour, J.-P. Gloter, A., Manoubi, T., Fert, A., Colliex, C., European Physical Journal B 34, 179 (2003)
41. Simon, J., Walther, T., Mader, W., Klein, J., Reisinger, D., Alff, L., Gross, R.,

Applied Physics Letters 84, 19 (2004)
42. Yang, Z.Q., Schryvers, D., Materials Science and Engineering A 481, 214 (2008)
43. Browning, N. D., , Arslan, I., Erni, R., Idrobo, J. C., Ziegler, A., Bradley, J., Dai, Z., Stach, E. A., Bleloch, A., Journal of Physics: Conference Series 26, 59 (2006)
44. Kimoto, K., Asaka, T., Nagai, T., Saito, M., Matsui, Y., Ishizuka, K., Nature, 450, 702 (2007)
45. Muller D. A., Nakagawa, N., Ohtomo, A., Grazul, J. L., Hwang, H. Y., Nature 430, 657 (2004)
46. Varela, M., Findlay, S. D., Lupini, A. R,, Christen, H. M., Borisevich, A. Y., Dellby, N., Krivanek, O. L., Nellist, P. D., Oxley, M. P., Allen, L. J., Pennycook, S. J. Physical Review Letters, 92, 095502 (2004)
47. Allen, J. E., Hemesath, E. R., Perea, D. E., Lensch-Falk, J. E., Li Z. Y., Yin, F., Gass, M. H., Wang, P., Bleloch, A. L., Palmer, R. E., Lauhon, L. J., ature Nanotechnology 3, 168 (2008)
48. Garvie, L. A., Craven, A. J., Brydson, R., American Mineralogist, 79, 411 (1984)
49. Eustace, D. A., McComb, D. W., Docherty, F. T., Craven, A. J., Microscopy and Microanalysis,13, 1276 (2007)
50. Mauchamp, V., Boucher, F., Ouvrard, G., Moreau, P., Physical Review B, 74, 115106 (2006)
51. Auchterlonie, G. J., McKenzie, D. R., Cockayne, D. J. H., Ultramicroscopy, 31, 217 (1989)
52. Garvie, L. A. J., and Buseck, P. R., American Mineralogist, 84, 946 (1999)
53. Wang, Z. L., Yin, J. S., Mo, W. D., Zhang, Z. J., Journal of Physical Chemistry B, 101, 6794 (1997)
54. Schmid, H. K., Mader, W., Micron 37, 426 (2006)
55. Kurata, H., Colliex, C., Physical Review B, 48, 2102 (1993)
56. Garvie, L. A .J., Craven, A. J., Ultramicroscopy 54, 83 (1994)
57. F. Pailloux, D. Imhoff, T. Sikora, A. Barthélémy, J.-L. Maurice, J.-P. Contour, C. Colliex , A. Fert, Phys.Rev. B 66, 14417 (2002)
58. Maurice, J.-L., Imhoff, D., Contour, J.-P., Colliex, C., Philosophical Magazine, 15, 2127 (2006)
59. Viret, M., Drouet, M., Nassar, J., Contour, J. P., Fermon, C., Fert, A., European Physical Letters, 39, 545 (1997)
60. M. Backhaus-Ricoult, Solid State Ionics, 177, 2195 (2006)

61. Koike, J., Haneda, M., Iijima, J., Otsuka, Y., Sako, H., Neishi, K., Journal of Applied Physics, 102, 043527 (2007)
62. Buatier, M. D., Guillaume, D., Wheat, C. G., Hervé, L., Adatte, T., American Mineralogist, 89, 1807 (2004)
63. Varela, M., Oxley, M. P., Luo, W., Tao, J., Watanabe, M., Lupini, A. R., Pantelides, A. R., Pennycook, S. J., Physical Review B, 79, 085117 (2009)

2.1 Composition modulation in InAlAs tensile buffer layers

2.1 Composition modulation in InAlAs tensile buffer layers

2.1.1 Introduction

Much attention has been centred on the spontaneous formation of lateral superlattices induced by lateral ordering processes or by phase separation in III-V semiconducting layers[1-7]. As a matter of fact, many nanostructures of great fundamental and technological interest, based on III/V semiconductors, have been recently reported to benefit from compositional modulation at an InAlAs layer[8-10], for instance by improving the uniformity of the nanostructures or by enabling to better control their sizes or their positions.

In addition, TEM-assessed segregation phenomena in III-V semiconductors are the object of an ongoing controversy. Evidence has been given in the sense that self-segregation and diffusion processes take place during growth of these materials, depending on the growth conditions and on the concentrations of the different species[11–13]. Yet, the possibility of inducing additional modifications in the structures through beam-damage during TEM or STEM observations is still the subject of an intense debate[14-16].

Tey and coworkers[8] studied the impact of varying the thicknesses of InAlAs in a combined two-level InAlAs–InGaAs capping layer on a structure of InAs/GaAs quantum dots grown for advanced laser applications. STEM and core-loss (Al $L_{2,3}$ edge) EFTEM were used to characterise the studied system. An increase in the height of the quantum dots was observed when the thickness of the InAlAs capping layer was increased. In addition, evidence was found of lower aluminium signal near the top of the quantum dots, with aluminium atoms migrating to the periphery of the quantum dots. Indium segregation within the InAlAs layer, giving rise to an In-rich zone over the QDs, was proposed as a mechanism to understand the increased height of InAs quantum dots with increasing InAlAs capping layer thickness.

Lei and coworkers[9] considered some uniformly distributed InAs nanostructures embedded in InAlAs grown on (001) InP. These nanostructures, with applications in long wavelength semiconductor lasers and photodetectors, were characterized through weak beam field TEM. It was found out that by changing the As overpressure during the molecular-beam epitaxy growth of InAs layers, quantum wires (under higher As overpressure) or elongated InAs quantum dots (under lower As overpressure) were formed. Interestingly, spatial correlation changed from vertical anti-correlation in quantum wire superlattices to vertical correlation in

quantum dot superlattices. This could be explained by the different alloy phase separation in the InAlAs spacer layers triggered by the InAs nanostrcutures. It was observed that the alloy phase separation in InAlAs in quantum dot superlattices could extend a long distance along the growth direction, indicating the vertical correlation of QD superlattices could be kept in a wide range of spacer layer thickness.

In a subsequent work[10], the same authors then contemplated the possibility to use a misoriented substrate to enhance phase separation in InAlAs. In particular, the self-organized growth of InAs/InAlAs quantum wires on a nominal (001) InP substrate and (001) InP substrates misoriented by 2°, 4°, and 8° towards both (−110) and (110) directions were considered. Samples were again characterized through weak beam TEM. Compared with those grown on nominal (001) InP substrate, the density of InAs/InAlAs quantum wires grown on misoriented InP (001) substrates was found to be enhanced. A strong lateral composition modulation effect was observed in the InAlAs buffer layers grown on misoriented InP substrates with large off-cut angles, which induced a nucleation template for the first InAs quantum wires and greatly improved the size distribution of the following ones. Best results were achieved with a 8° off cut towards (−110) substrate, in terms of size homogeneity and photoluminescence intensity.

In spite of the great number of investigations carried out in these systems, a quantitative EELS characterization of In-rich and Al-rich regions in InAlAs layers was never fully addressed, maybe because neither Al $L_{2,3}$ (at 73 eV) nor Al K (at 1560 eV) appear to be convenient to carry out an elemental quantification.

It is well known[17] that, except for some pathological cases, plasmon energies vary with composition in a quasi-linear manner. Keeping in mind that AlAs plasmon is found in at 16.1 eV and that InAs plasmon is found at 13.8 eV, a periodic variation of the plasmon position towards higher energies in Al-rich regions and towards lower energies in In-rich regions is expected. Moreover, for an $In_{1-x}Al_xAs$ composition, plasmon energy P is expected to be $P \approx 13.8\ eV\ (1 + 2.3x)$. Plasmon position location thus seems a most suitable way to assess the periodic variations in local chemistry of InAlAs layers.

In particular, in this chapter, plasmon position (together with HAADF imaging) will be used to characterize the local chemistry of an InAlAs buffer layer in an InGaAs /InAlAs /(100)InP

system with InP substrate misoriented 4º towards (111). These InAlAs layers had already been characterized by conventional TEM[2], and two beam experiments had shown white-dark domains inside the InAlAs buffer under g=022. Compositional modulation is thus expected.

2.1.2 Experimental details

The general structure of the analyzed samples is 5 nm GaAs / 50 nm $In_{0.52}Al_{0.48}As$ / 18 nm $In_{0.53}Ga_{0.47}As$ / 2 μm $In_yAl_{(1-y)}As$ buffer layer / InP substrate, where y_{In} = 50% for sample I and y_{In} = 48% for sample II. The samples were grown by molecular beam epitaxy on (100) InP substrates which were 4° misoriented towards (111). The InP substrates were cleaned for 20 min in UV ozone, which removes organic contaminants and results in a surface oxide. Oxide desorption was accomplished by heating InP at 530 °C under an As_2 flux of equivalent pressure $2.2x10^{-5}$ Torr. The growth rates were about 1 μm/h for all the layers and the As_2 flux was fixed at $2.2x10^{-5}$ Torr. Since composition variations in InAlAs appear at high growth temperatures (T_g), the InAlAs buffer layers have been grown at 580 °C. However, in order to avoid problems related to As-P exchange at the interface, the first 200 nm were grown at T_g =530 °C. Studied samples were grown by A. Georgakilas (Foundation for Research and Technology-Hellas), C. Wood and A. Christou (University of Maryland) in the frame of a Spanish-Greek bilateral cooperation project.

2.1.3 Previous PV and XT TEM results

In previous works[2], PV observation had revealed a quasi-periodic contrast modulation along [011]. These contrast fringes along [011] were observed in strong contrast for g = 022 and mean modulation wavelength had been determined to be λ = 125-135 nm. It is worth noticing that there was an extinction of the contrast of the bands for g = 0-22 (figure 2.1.1). When observing the samples from free surface towards interface, contrast vanished as approaching the substrate, modulation was observed down to a distance of about 200nm from InP.

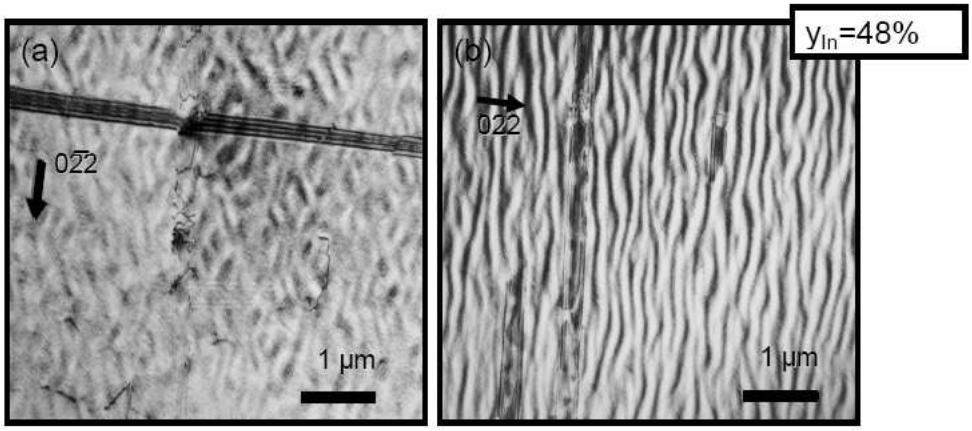

Figure 2.1.1: *Two-beam images with excitations g= 02-2 (a) and g = 022 (b) of y = 48% structure in PV geometry.*

No dislocation nucleation was found in the case of lower mismatch (y = 50%) and reduced dislocation density was found for higher mismatched (y = 48%) sample. In the more mismatched sample, misfit dislocations were observed at the buffer/substrate interface and at 200 nm from the interface. Some dislocations loops glided on (111) planes between both regions as was observed in (100) plan views.

In XT geometry, white-dark domains were observed inside the InAlAs buffer under g=022. These domains started to appear at about 200 nm from the interface in the sample with y_{In}=50% (figure 2.1.2), suggesting they were triggered by the change in T_g. Contrast bands were oriented at 13-15º from [100] direction. The trace of these domains on (100) plane is [011]. The stereographic projection indicated that the domains were limited by {122} and {133} planes. There was a correspondence of domains with ripples and valleys at the top surface.

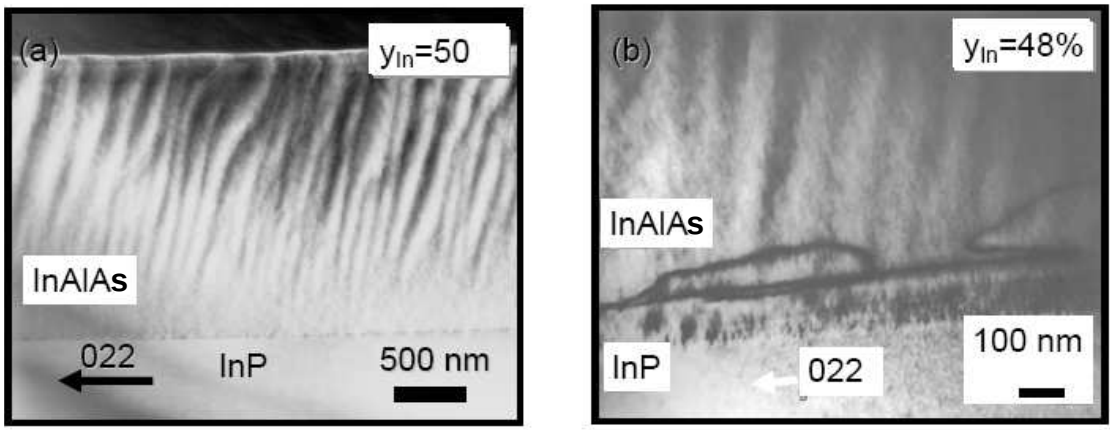

Figure 2.1.2: *Two images with excitation g=022 of y = 50% structure (a) and y = 48% structure (b), both in XT geometry.*

2.1.4 Plasmon Analysis

2.1.4.1 Plasmon position location

In order to find the local plasmon energy from a low-loss spectrum image in an automated way, a short Matlab script was written. Many are the advantages of having a routine find the plasmon position instead of determining it by direct observation of the EELS data; quite obviously, the repetitivity and rigor of the measure is increased. Also, one can take advantage of the shape of the plasmon to refine the plasmon energy location, instead of simply localizing the maximum –i. e: reconstructing the whole plasmon shape from a number of points and then calculating its centre rather than just locating the highest intensity point. Finally, if a spectrum image containing many spectra is considered, an automated routine can be fairly time-saving.

The Matlab script reads a spectrum image saved in .txt format (with no fixed energy range, but including a non-saturated ZLP), it separates the individual spectra and saves them, numbered, in case one may want to plot a given spectrum. Then, for each spectrum, it adjusts a Gaussian function to the ZLP, recalibrates energy scale by situating the centre of the ZLP at 0, fits a second Gaussian function to the plasmon peak and saves its centre. A file containing the plasmon position as a function of the spectrum ordinal in the spectrum image is then created, and can be plotted right away or exported as ASCII (for instance, to Origin).

In fact, the procedure is not much different from that that could be implemented directly in Digital Micrograph. There, one would fit a Gaussian to the ZLP of one of the spectra via NLLS fitting, would apply the model to the parent spectrum image and keep the ZLP vs spectrum ordinal plot. Then, one would use that plot as reference data to correct zero-loss centring. Finally, one would fit a Gaussian to a plasmon peak in one of the spectra and apply the model to the parent spectrum image. If the plasmon peak was heavily displaced in energy from one spectrum to the next, then one would have to do a new Gaussian fitting.

Some important advantages make the Matlab routine preferable, the most important one being the fact that the routine first finds the plasmon maximum and then fits the Gaussian function

around it, so that if the plasmon peak is heavily displaced in energy from one spectrum to the next, this is not a problem. Besides, the fitting window is not user-defined here. A user-defined window can lead to non-repetitive or biased results. From a practical point of view, it is also less time consuming, and the final result can be easily plotted in Matlab entourage. The only problem may be that for users different from the programmer, the whole plasmon positioning procedure may look like a black box.

The EELS data from the InAlAs buffer layer were treated both with the Matlab routine and with Digital Micrograph. Not surprisingly, the results were very coherent. From now on, the displayed results will be those obtained using the Matlab routine.

2.1.4.2 Plasmon analysis results

STEM image and EELS spectroscopy experiments have been carried out to directly correlate the observed contrast modulation with a possible composition modulation. In STEM BF images, we can already observe the dark-light fringes as seen in conventional TEM, especially for y = 50%. As for HAADF, contrast is enhanced, suggesting a composition contrast. Figure 2.1.3 displays BF STEM and HAADF images of the y = 50% and the y = 48% structures. Intensity profiles in HAADF are given in the inset. Notice that In-rich regions -Z(In) = 49- should be seen with higher intensity than Al-rich regions -Z(Al) = 13.

When studying intensity profiles, we conclude that intensity fringes observed by HAADF present an average spatial wavelength of about 130 nm, which is in good agreement with the above mentioned wavelength figure as deduced from conventional TEM observation. In order to further confirm the compositional modulation hypothesis, EELS 1 dimensional spectrum images (spectrum lines) have been obtained along [011] direction, in order to quantitatively correlate the contrast fringes with compositional data. As already mentioned, neither Al $L_{2,3}$ (at 73 eV) nor Al K (at 1560 eV) are very favourable edges to carry out an elemental quantification. Al K could still have been considered, a priori, but given the great energy distance separating it from In $M_{4,5}$ peak (at 443 eV), relative quantification would be seriously affected by the poor signal to noise ratio of the Al K peak when obtaining both peaks in the same spectrum. Thus, it was definitively wiser to use the plasmon peak to carry out the EELS analysis.

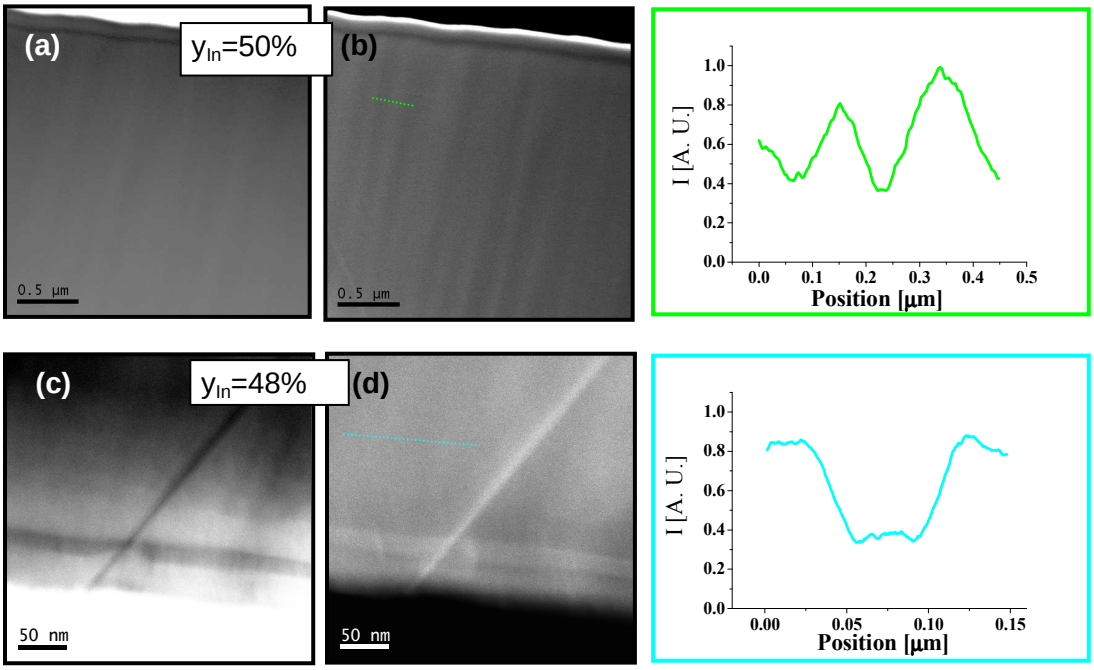

Figure 2.1.3: *BF STEM (a) and HAADF (b) images of y=50% structure. Intensity profile along highlighted line (inset). BF STEM (c) and HAADF (d) images of y=48% structure. Intensity profile along highlighted line (inset).*

Keeping in mind that AlAs plasmon is found in at 16.1 eV and that InAs plasmon is found at 13.8 eV, we expect a periodic variation of the plasmon position along [011] direction with spatial wavelength of about 130 nm, towards higher energies in Al-rich regions (darker contrast in HAADF) and towards lower energies in In-rich regions, with a plasmon energy mean value which is expected to be 14.95 eV for y = 50% and 14.99 eV for y = 48%. The latter values will be used as sanity check figures in our experiment.

The plasmon maximum position as a function of the acquisition point is given in figure 2.1.4 for the y = 50% sample and in figure 2.1.5 for y = 48% sample. Plasmon position has shown the expected variation, coherent with contrast variation, and, again, significantly more pronounced for y = 50%. Mean plasmon maximum position has been found to be in good agreement with the expected values for both considered samples.

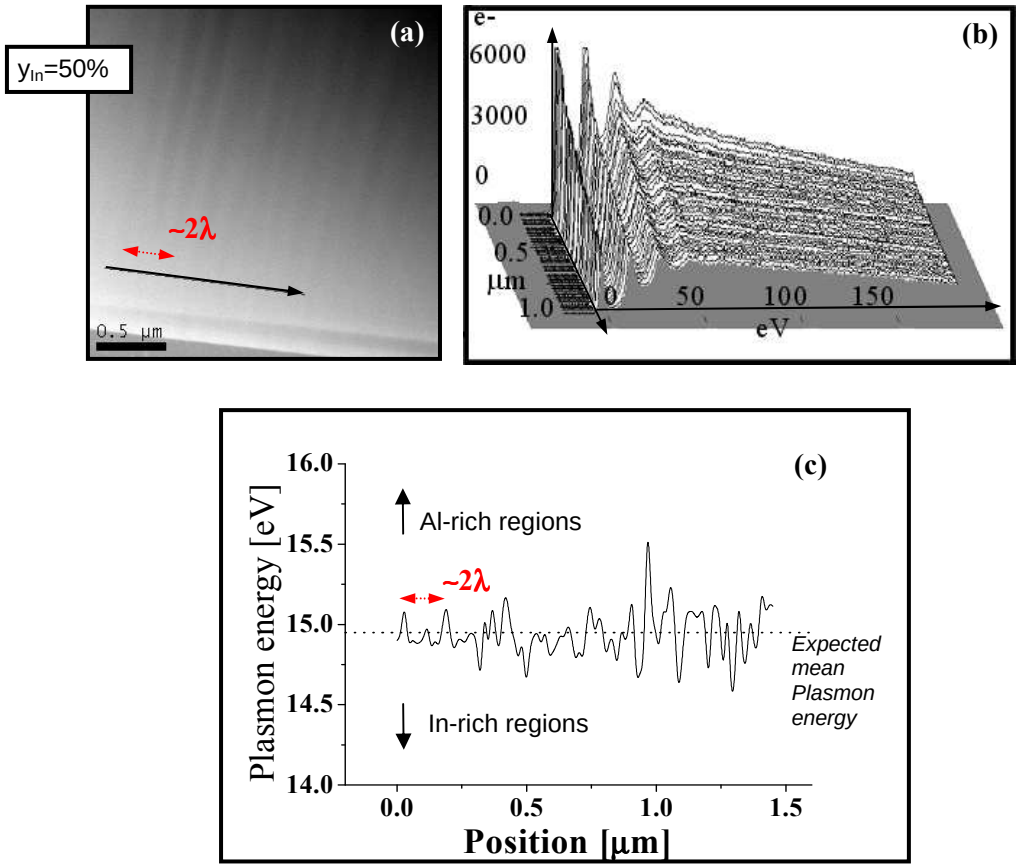

Figure 2.1.4: *HAADF image of y=50% structure (a), and EELS spectra series (b) and plasmon energy evolution (c) along the highlighted line.*

In the case of the y = 50% sample, plasmon maximum position varies between extreme values 15.5 eV and 14.6 eV. At a first order approximation, as already explained, we can consider that plasmon position varies in a linear manner with composition. Thus, the composition would vary between y_{min} = 26% and y_{max} = 65 %.

The plasmon position variation in the y = 48% sample is clearly more moderate, with extreme values of 15.1 eV and 14.9 eV. In this case, again as a first approximation, composition would vary between y_{min} = 43% and y_{max} = 52 %.

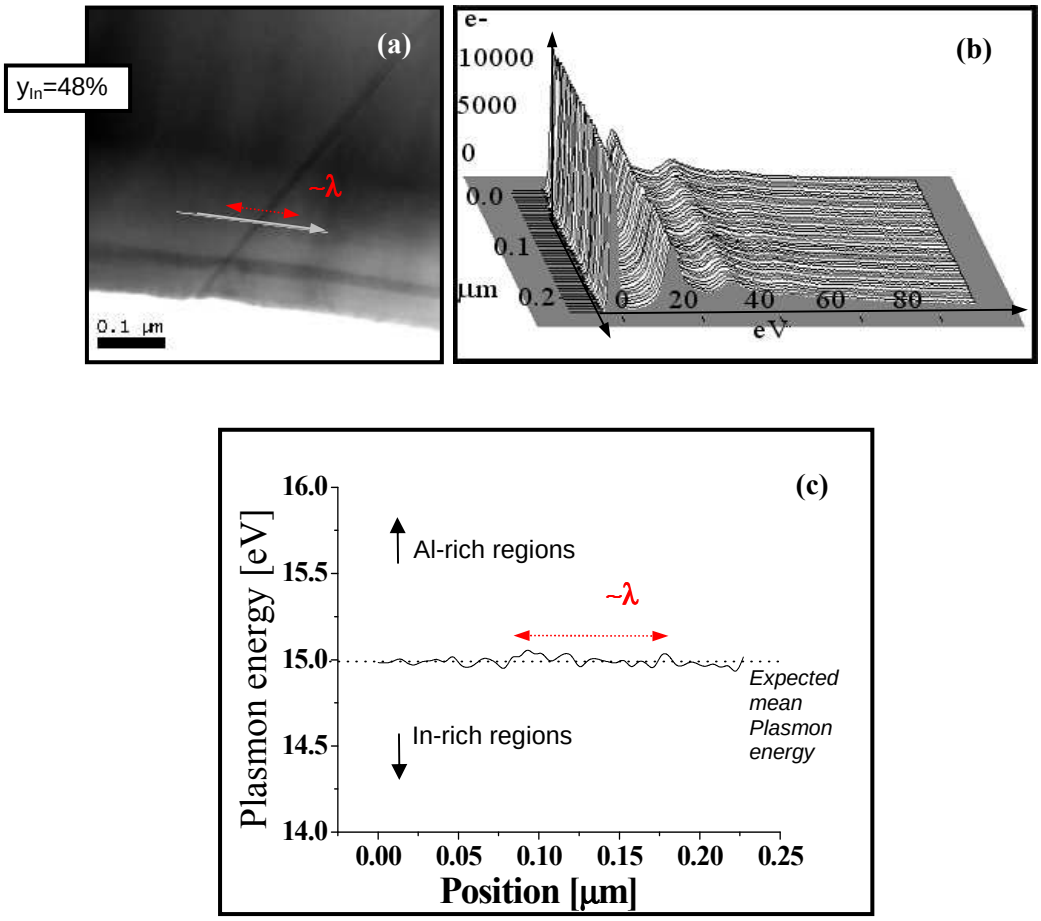

Figure 2.1.5: *BF STEM image of y=48% structure (a), and EELS spectra series (b) and plasmon energy evolution (c) along the highlighted line.*

2.1.5 Conclusions

Examination by two-beam BFTEM of InGaAs/InAlAs buffer (tensile)/InP structures using excitation g = 022 revealed quasiperiodic strong contrast modulation fringes perpendicular to the (002) direction, which seemed to indicate the presence of In-rich and Al-rich regions. HAADF observation has shown the same quasiperiodic contrast, thus confirming the hypothesis of compositional-related contrast.

EELS spectra analysis has shown a plasmon position variation, according to contrast variation as observed in HAADF, more pronounced for y_{In}=50% than for y_{In}=48%, where contrast variation was also more evident. EELS results are, thus, in good agreement with HAADF observations, and strongly suggest composition modulation.

Furthermore, the use of a Matlab script to determine the local plasmon energy from a low-loss spectrum image, in an automated and reliable way, has been demonstrated.

2.1.6. References

1. Tsuchiya, M., Petrov, P., Coldren, L., Applied Physics Letters 54, 1690 (1989)
2. Peiró, F., Cornet, A., Morante, J., Georgakilas, A., Wood, C., Christou, A., Applied Physics Letters 66, 2391 (1995)
3. Guyer, J. and Voorhees, P., Journal of Crystal Growth 187, 150 (1998)
4. Bortoleto, J., Gutiérrez, H., Cotta, M., Bettini, J., Applied Physics Letters 87, 013105 (2005)
5. Shiojiri, M., Čeh, M., Šturm, Chuo, C. C., Hsu , J.T., Yang, J. R., Saijo, H., Journal of Applied Physics 100, 013110 (2006)
6. Fetzer, C. M., Lee, R. T., Jun, S. W., Stringfellow, G. B., Lee, S. M., Seong, T. Y., Applied Physics Letters 78, 1376 (2001)
7. Zhao, F. A., Chen, Y. H., Ye, X. L., Jin, P., Xu, B., Wang, Z. G., Zhang, C. L., Journal of Physics: Condensed Matter 16, 7603 (2004)
8. Tey, C. M, Liu, H. Y., Cullis, A. G., Ross, I. M., Hopkinson M., Journal of Crystal Growth 285, 17 (2005)
9. Lei, W., Chen, Y. H., Jin, P., Ye, X. L., Wang, Y. L., Xu, B., Wang , Z. G., Applied Physics Letters 88, 063114 (2006)
10. Lei, W., Wang, Y. L., Chen, Y. H., Jin, P., Ye, X. L., Xu, B., Wang , Z. G., Applied Physics Letters 90, 103118 (2007)
11. Lin, Y.S., Ma, K.J., Yang, C.C., Weirich, T.E., Journal of Crystal Growth 242, 35 (2002)
12. Narukawa, Y. Kawakami, Y., Funato, M., Fujita, S. Fujita, S., Nakamura, S., Applied Physics Letters 70, 981 (1997)
13. Kisielowski, C., Liliental-Weber, Z., Nakamura, S., Japanese. Journal of Applied Physics 36, 6932 (1997)
14. O'Neill, J.P., Ross, I.M., Cullis, A.G., Wang, T., Parbrook, P.J., Applied Physics Letters 83, 1965 (2003)
15. Smeeton, T.M., Kappers, M.J., Barnard, J.S., Vickers, M.E., Humphreys, C.J., Applied Physics Letters 83, 5419 (2003)
16. Bartel T.P., Kisielowski, C., Specht, P., Shubina, T.V., Jmerik, V.N., Ivanov, S.V., Applied Physics Letters 91, 101908 (2007)

17. Egerton, R. F., “Electron Energy Loss in the Electron Microscope” (2nd ed.), Plenum Press, (1996)

2.2 Local electronic properties of Mg doped GaN NWs

2.2 Local electronic properties of Mg doped GaN NWs

2.2.1 Introduction

In recent years much attention has been focused on the growth of quasi-one-dimensional (1D) nanostructures for the controlled fabrication of nanodevices[1-5]. In particular, III-nitrides (InN, GaN, AlN and their alloys) have shown promising properties. Their direct band gap can be controlled from 0.7 eV (InN) to 3.4 eV (GaN) and to the deep UV spectral range of 6.0 eV (AlN). This makes them excellent candidates for the fabrication of heterostructures for optoelectronic applications, such as light emitting diodes, laser diodes, or quantum well infrared photodetectors as well as high electron mobility transistors. The synthesis of p-type 1D nanostructures based on these III-nitrides is still a challenging topic. To exploit these material properties also in nanoscaled devices, catalyst-induced processes like the vapour liquid solid (VLS) mechanism[6,7], using metal droplets like Au, Ni[8], or Fe[9] as catalysts have been developed for the growth of GaN nanorods (NRs) or nanowires (NWs) with vertical orientation with respect to the substrate, with horizontal orientation, or as free structures. GaN NWs grown by laser assisted catalytic growth have been reported and heterodiodes have been realized by deposition of n-type GaN NWs on p-type Si substrates[10]. However, for the integration of more complex structures such as p–n junctions or quantum wells, and in order to avoid the negative effects of catalysts in group III–V NRs or NWs, molecular beam epitaxy (MBE) is the growth method of choice[11,12]. As mentioned above, for the realization of nanoelectronic devices doping is one of the most important issues. In the case of Mg doped (p-type) GaN NRs and NWs, only a few studies have been devoted to analyze their optoelectronic[13-17], transport, and electronic properties[15,18,19]. Some of these works have provided limited information on the morphology[14] and crystal structure[15,19,20] of the Mg doped GaN NRs and NWs. To this end, a systematic and detailed study of the correlation of the structural and morphological modifications originated by Mg doping with the resulting local electronic properties of GaN is of the utmost importance. In this sense, low-loss EELS can be used to probe the local electronic configuration of a semiconductor[21,22] at a sub-nanometric scale and correlate it with the local structural changes observed by (S)TEM in the same region.

2.2.2 Experimental details

Gallium nitride nanowires were grown using plasma assisted molecular beam epitaxy (PAMBE). Nitrogen radicals were supplied by an Oxford Applied Research RF-plasma source whereas for Ga and Mg thermal effusion cells were used. Low resistivity n-type Si(111) substrates were etched in 5% hydrofluoric acid for 10 s to remove the surface oxide layer prior to transfer into the load lock chamber. For all samples a substrate temperature of 790 ºC, a nitrogen pressure of 2.7×10−5 mbar and a Ga beam equivalent pressure (BEP) of 3.3×10^{-7} mbar was used. The substrates were exposed to the nitrogen plasma at a temperature of 790 ºC for 2 min directly before GaN growth. For the magnesium doped samples the Mg effusion cell temperature was varied between 205 ºC and 355 ºC, corresponding to a BEP of 1×10^{-11} mbar to 2×10^{-8} mbar, respectively. Growth duration was 90 min unless mentioned otherwise. Samples were grown by Florian Furtmayr, Christoph Stark, Martin Stutzmann and Martin Eickhoff (Walter-Schottky-Institut, Technische Universität München) and Andreas Laufer (I Physikalisches Institut, Justus-Liebig-Universität).

2.2.3 TEM characterization

In order to analyze the influence of the Mg doping on the atomic structure of the Mg NWs, selected area electron diffraction (SAED) patterns were obtained on several samples, prepared in XTEM geometry (figure 2.2.1).

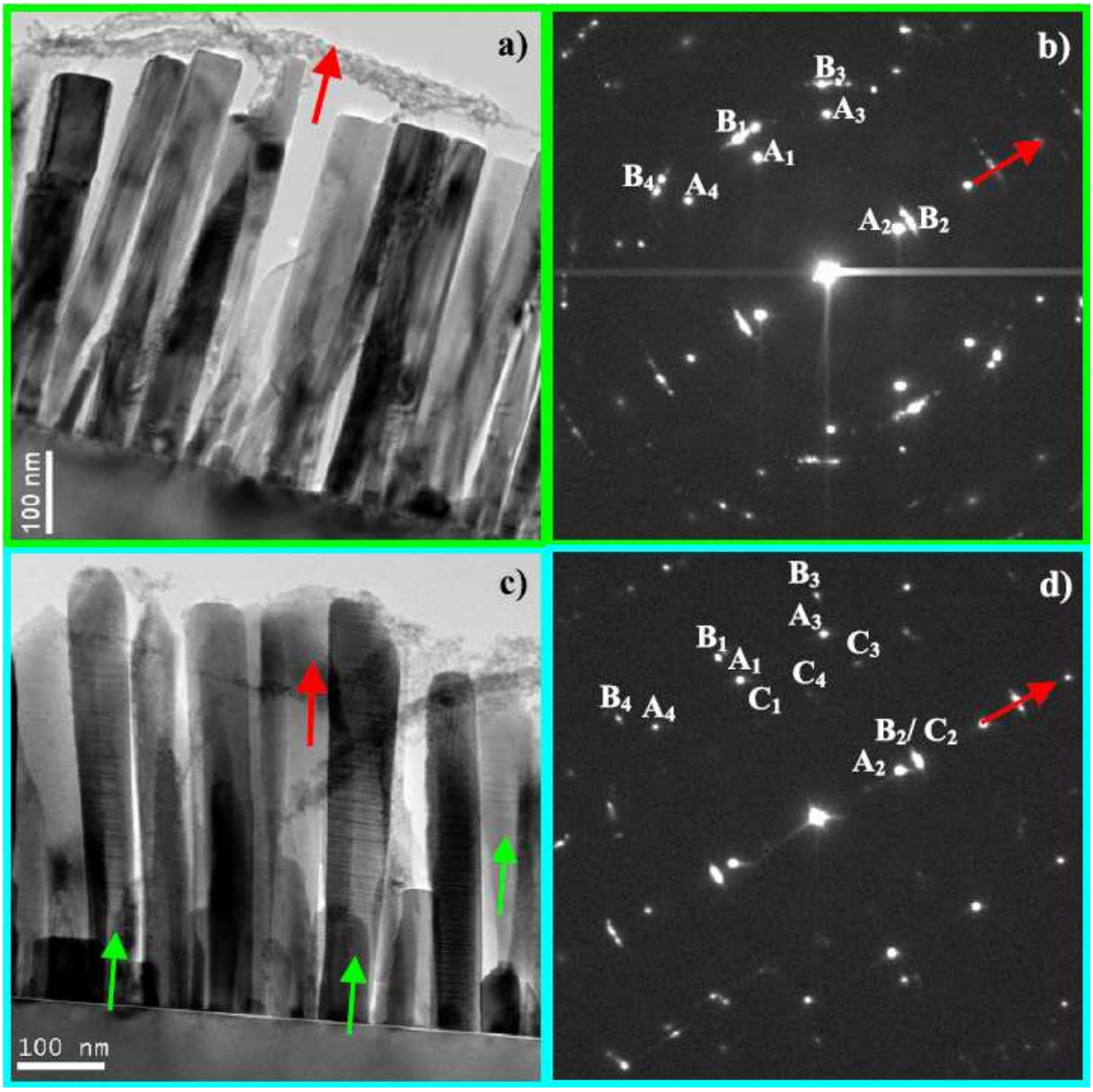

Figure 2.2.1: *(a) BFSTEM general view of the undoped GaN NWs. (b) SAED pattern of the region displayed in (a). (c) BFSTEM general view of the highly Mg doped (TMg = 355 ◦C) GaN NWs. Some of the NWs present twin defects (marked with green arrows). (d) SAED pattern of the region displayed in (c). A new crystal orientation appears in this case, that has been related to the twinned NWs (spots labelled as C). Top arrows (red) are pointing to the same equivalent growth direction in SAED patterns and BFSTEM micrographs.*

After this analysis (see the corresponding indexation in table 2.2.1) it was observed that GaN NWs follow a preferential epitaxial relationship versus the Si substrate, namely: (0001)[0-110] GaN // (111)[-1-12] Si. Undoped GaN NWs appear to be defect-free, whilst Mg doped samples present some NWs with twin (T) defects along the growth axis, as shown in figure 2.2.1(a) and (b) -some twinned NWs have been marked with green arrows in figure 2.2.1(c). When a SAED pattern of a NW region populated with few twinned NWs is obtained, a new orientation relationship superimposed to the one found for undoped samples can be observed. As shown in figure 2.2.1(d), the new spots –indexed in table 2.2.1-, labeled as C_n, are rather weak. The presence of these weak spots can be attributed to the presence of Ts in the NWs. The new epitaxial relationship which is found is: (0001)[1-210]GaN // (111)[-1-12]Si. The twinned NWs still grow along the [0001] direction; however, they are rotated 30º along the growth axis with respect to the non-twinned NWs.

Spot #	d (nm)	(deg) versus spot A_1	Indexation
A_1	1.92	—	(2-20)
A_2	3.13	90	(111)
A_3	1.64	31	(3-11)
A_4	1.64	31	(1-3-1)
Zone axis: [-1-12] Si			

Spot #	d (nm)	(deg) versus spot B_1	Indexation
B_1	1.55	—	(-2110)
B_2	2.59	90	(0002)
B_3	1.30	32	(-2112)
B_4	1.30	32	(-2112)
Zone axis: [0-110] GaN			

Spot #	d (nm)	(deg) versus spot B_1	Indexation
C_1	2.76	—	(-1010)
C_2	2.59	90	(0002)
C_3	1.89	43	(-1012)
C_4	2.44	62	(-1011)
Zone axis: [0-110] GaN			

Table 2.2.1: *Indexation of the diffraction spots in Figure 2.2.1.*

The density of twins dramatically increases with increasing Mg concentration and, thus, the formation of twins can be directly correlated to the increasing presence of Mg. Twin defects along the growth axis have been commonly observed in some other one-dimensional semiconductor nanostructures such as in III–V NWs[10,23–26], or even in Si NWs[27,28].

On the other hand, an amorphous layer between the substrate and the GaN NW is apparent in figure 2.2.1(a) and (c). Core-loss EELS quantification along the interface was carried out to find out the chemical nature of this amorphous layer. As Si $L_{2,3}$ and Ga $M_{2,3}$ edges overlap, quantification was not carried out in the usual manner –computing background subtracted integrated signals for each element, sigma correcting them and dividing them by each other-, but rather treating the overlapping region as a linear combination of the Si and Ga edges. This way, it was found that the amorphous layer contained 50 ± 5 % of Si, 50 ± 5 % of N and no Ga (figure 2.2.2). This Si nitride layer was very likely created during the nitridation process that occurred during the first growth steps.

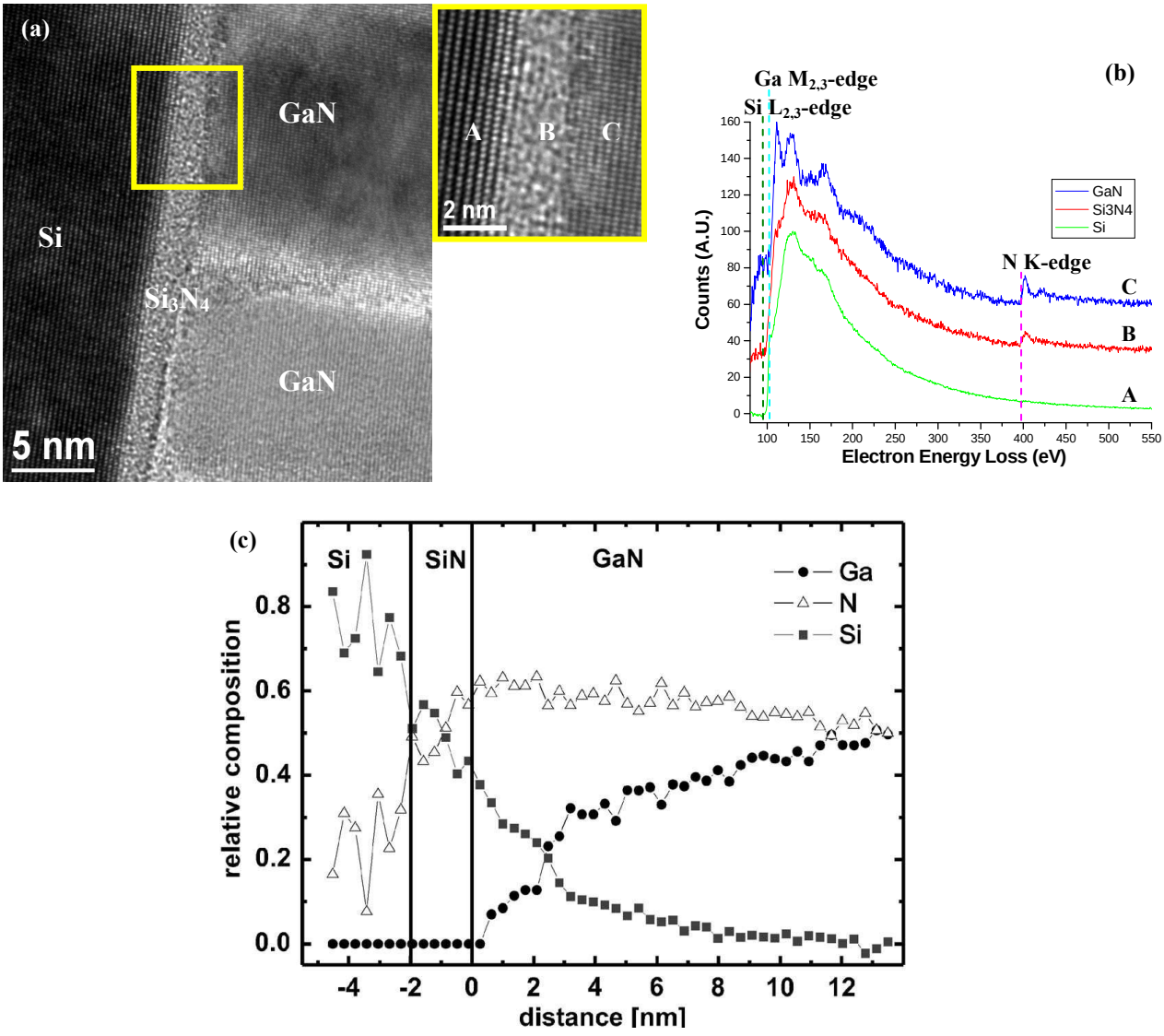

Figure 2.2.2: *(a) HRTEM image of the interface. (b) EEL Spectra at the indicated points in (a). (c) Quantification profile along the interface.*

Figures 2.2.3(a)–(c) show an HRTEM analysis which confirms that NWs with Ts grow in the (0002)[1-210]GaN // (111)[-1-12]Si orientation and are rotated 30º from the defect-free NWs. As shown in figure 2.2.3(e), red arrows are pointing towards GaN(0001) wurtzite planes, while the cyan ones are pointing to the GaN twinned planes -in particular to a triple-twin region. As observed, the stacking of the planes is different in the twinned regions.

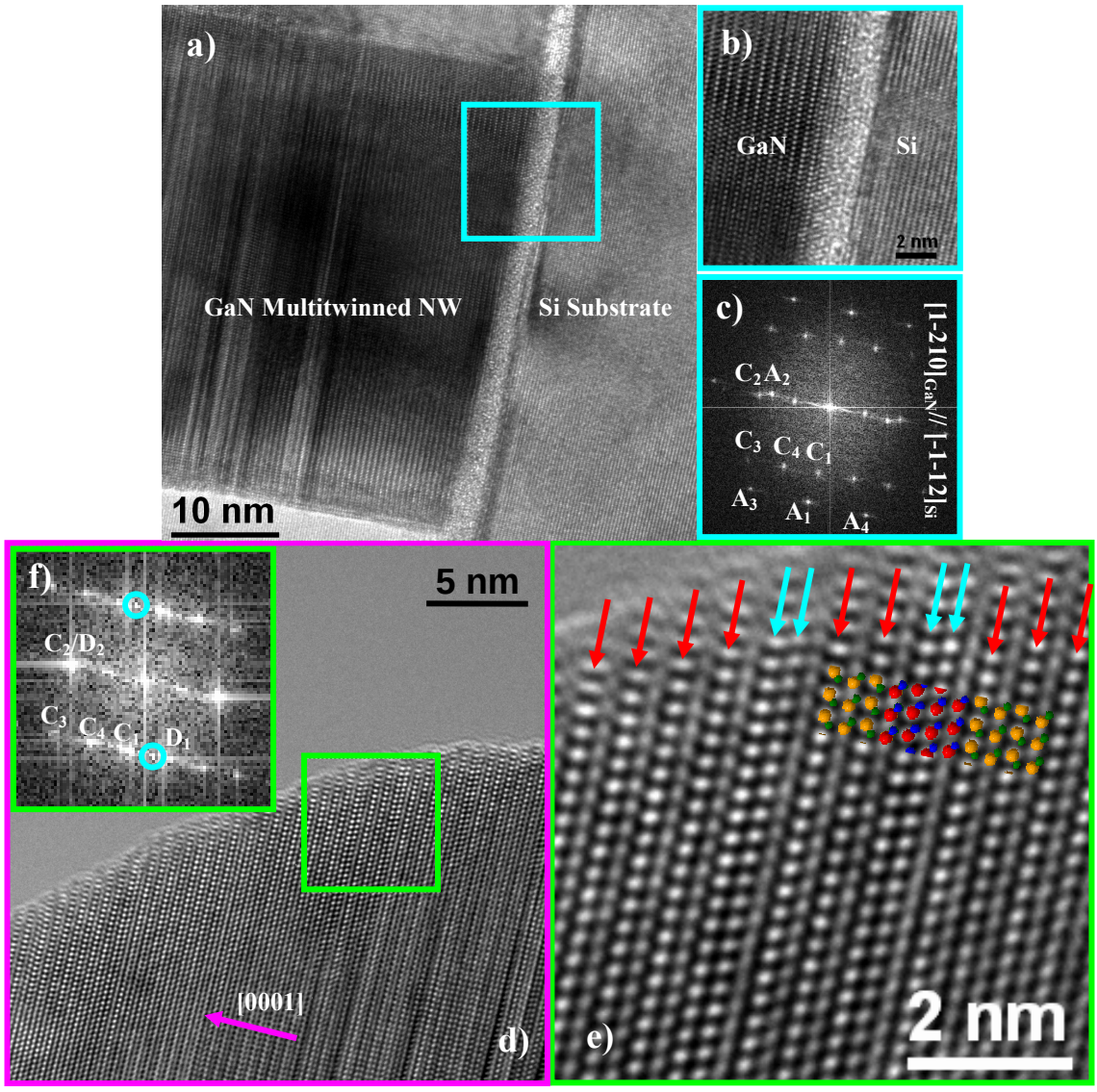

Figure 2.2.3: *(a) HRTEM image of a twinned Mg highly doped GaN NW (355 ºC). (b) Magnified detail of the squared region in (a). (c) Power spectrum of (b). (d) HRTEM micrograph of the top part of a highly doped NW showing its stepped surface. (e) HRTEM detail of the twinned region squared in (d); red arrows correspond to (0001) GaN wurtzite planes, while cyan arrows are pointing to (111) GaN zinc-blende planes. (f) Power spectrum obtained in (e), Cn spots correspond to the wurtzite phase while Dn corresponds to the zinc-blende phase (D1 and D2 spots correspond to the (-11-1) and (111) GaN zinc-blende planes, respectively).*

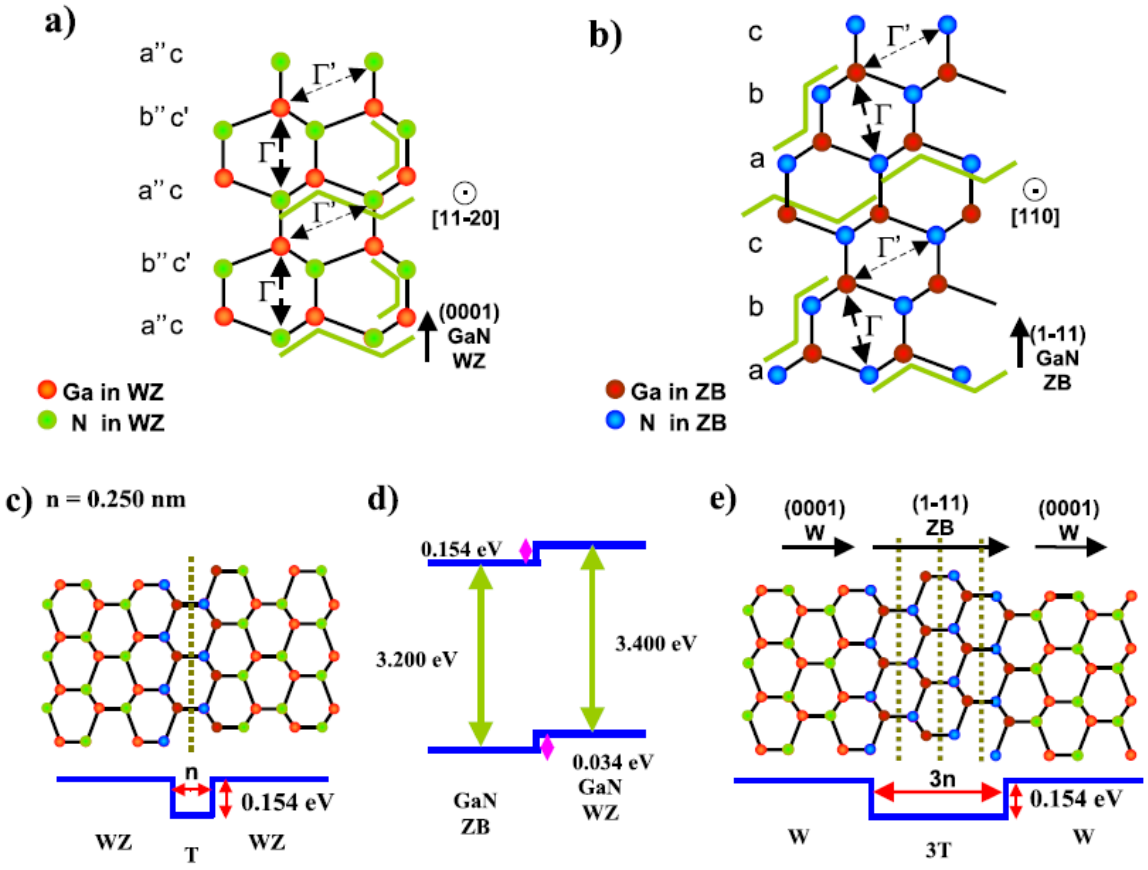

Figure 2.2.4: *(a) Atomic scheme of the GaN wurtzite (W) structure (b) Atomic scheme of the GaN zinc-blende (ZB) structure. (c) Conduction band potential profile and the corresponding QW thickness for a single twin in GaN (equivalent to a single ZB unit). The twinned plane is marked with a dashed line. (d) Band alignment between GaN ZB and GaN WZ according to Murayama and Nakayama[37]. (e) Conduction band potential profile and the corresponding QW thickness for a triply-twinned domain equivalent to three ZB cells (twin planes have been marked with dashed lines).*

In figure 2.2.4, a scheme of the twin formation is shown. Figure 2.2.4(a) represents the conventional GaN wurtzite (WZ) structure, while in figure 2.2.4(c) the formation of a single twin, equivalent to a 60º rotation in the WZ structure around the [0001] growth axis, is shown. It is important to point out that the consecutive stacking of [0001] axial twins leads to the formation of the GaN zinc-blende (ZB) structure, which is cubic instead of hexagonal (see figure 2.2.4(b) for a scheme of the GaN ZB structure). In particular, in figure 2.2.4(e), it is displayed how a triple-twin creates a three-cell ZB domain (see figure 2.2.3(e)). In this way, in the power spectrum shown in figure 2.2.3(f), the D1 spot corresponds to the (-11-1) GaN ZB plane, while the D2 spot is the (111) plane. The appearance of alternating wurtzite and zinc-

blende structures due to the presence of twins has been widely reported for III–V NWs[28-30] and the change of crystal phases in 1D nanostructures due to twinning is a widespread phenomenon in several materials[31]. In addition, the formation of wurtzite and zinc-blende heterostructures in a chemically homogeneous nanowire material is a hot scientific topic as it is opening up new possibilities for band-structure engineering [28,32,33].

These heterostructures can have dramatic implications on the electronic properties of the NWs, as a change in the crystal structure also implies a variation in the density of states and thus on the carrier transition energy. In a recent work, Bao et al.[32] showed how the presence of twinned planes between WZ quantum domains in InP NWs (they attributed it to WZ–ZB alternance) could influence their photoluminescence properties.

2.2.4 Local optical properties addressed through EELS

2.2.4.1 Plasmon position and structural considerations

Initially, low-loss spectra were acquired along the doped NWs using a GIF2001spectrometer coupled to a JEM2010F microscope. The plasmon position was found to remain constant along the NW. Now, the plasmon position depends on bandgap, but it also depends on other factors that may cancel out. In particular, it is possible to assume that plasmon position depends on the composition and the distance to the first neighbouring atom, which are the same for W and ZB regions in the NWs, so that even if the bandgap changes, the plasmon energy remains the same. In other words, the unchanging plasmon position does not need to correspond to unchanging bandgap energy. This affirmation will be further substained by ab-initio simulations in the following section. On the other hand, it is clear that EELS spectra with a better energy resolution are needed to access the bandgap energy.

2.2.4.2 Bandgap estimation

Aberration-corrected STEM, and EELS spectra with a 0.3 energy resolution were used to move one step further and locally analyze the atomic scale modifications in the local density of states that occur in the interface between the tripletwin (3T) planes (ZB) and the WZ GaN heterostructure. Experiments were performed on a dedicated VG HB 501 STEM retrofitted with a Nion quadrupole–octupole corrector (SuperSTEM 1) at Daresbury.

Cs-corrected HRHAADF STEM micrographs, where the displayed bright spots directly correspond to the actual atomic positions, corroborate the proposed structural model for the 3T domains (figure 2.2.5 (a)).

EEL spectra maps of the NWs were obtained with a zero loss peak (ZLP) energy FWHM of 0.3 eV and a probe size of about 0.1 nm. The much reduced probe size allowed us to obtain atomic-column resolved EELS spectrum images in the wurtzite and 3T regions (see square blue and red marks in figure 2.2.5 (a) for the EELS selected areas). Then, the spectra obtained at the exact atomic positions in the wurtzite and the 3T regions were processed and analyzed. These spectra are displayed in figure 2.2.5(b). It is generally accepted that the ZLP shape is

Gaussian[34], and thus that it contributes to the low-loss signal as A exp(−rx^2), where x is the energy loss. In the present work, it was subtracted from the low-loss region by fitting an A exp(−rx^2) function to the positive tail of the ZLP.

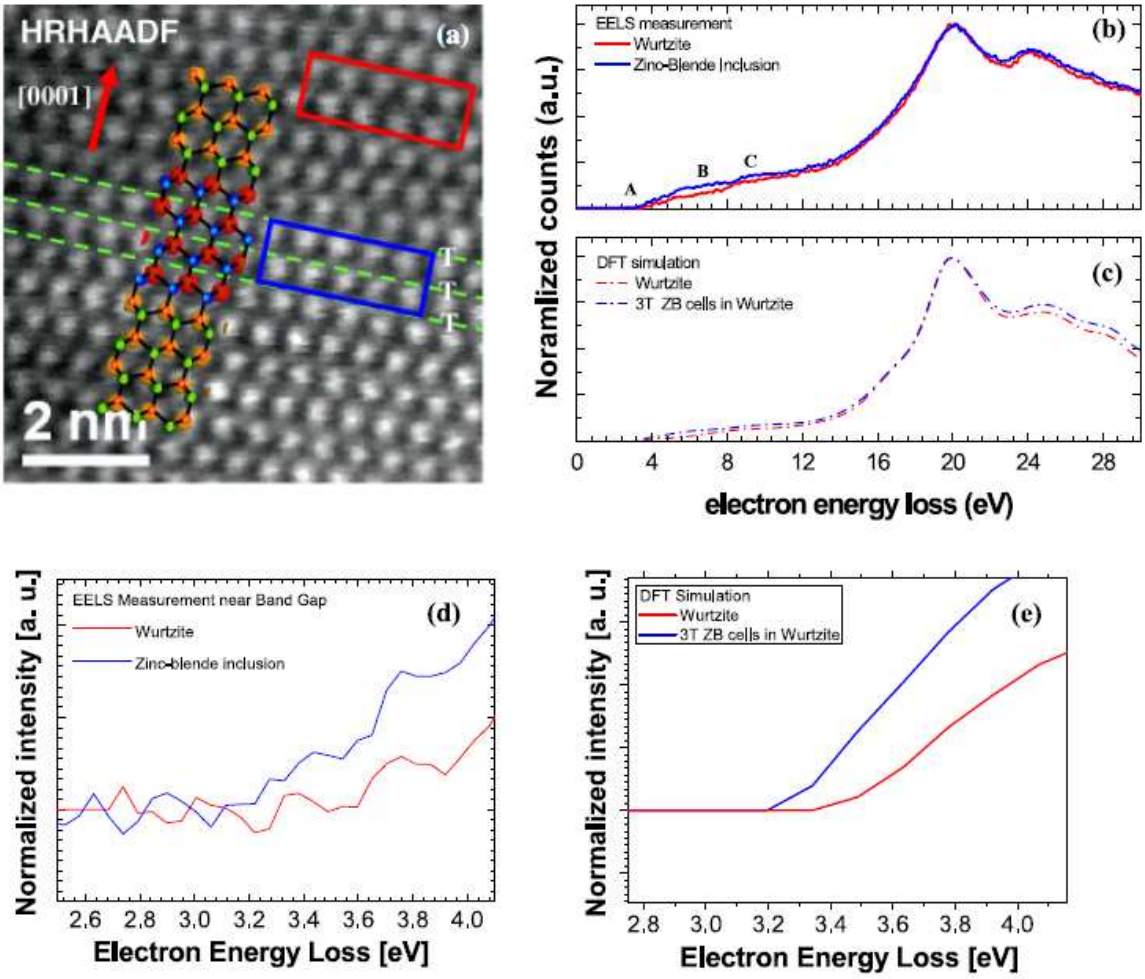

Figure 2.2.5: *(a) Cs -corrected high resolution HAADF image of a twinned Mg highly doped GaN NW (355 ºC). (b) Low-loss EEL spectra corresponding to wurtzite (red) and triply-twinned (ZB) (blue)—highlighted in (a)—regions of the W, after ZLP subtraction; (c) ab initio simulations of the loss function from wurtzite and from a three monolayer (ML) Zinc-blende inclusion in wurtzite. (d) Detail of the band gap region of the ZLP subtracted low-loss spectra. (e) Ab initio simulation of the same energy region. All spectra have been normalized to the maximum of the plasmon peak in (b) and (c).*

The resulting spectra (figure 2.2.5(b)) show several interesting features –before analyzing the low-loss spectra, it should yet be noticed that the peak observed at about 24 eV is in fact the Ga 3d transition. The obtained band gap is found to be higher for the WZ region (measured to be 3.4 eV) than for the 3T region (measured to be 3.2 eV). The values are comparable to the band gap measurements for WZ and ZB phases obtained by EELS in literature[35,36] but, interestingly,

lower than the values obtained using optic spectroscopies[37]. On the other hand, features B and C in figure 2.2.5 (b) are found at higher energies for zinc-blende GaN than for wurtzite GaN. These peaks were expected, from first principles calculations[38], to arise from transitions from the three upper valence bands to the third and fourth conduction bands (B), and from the same bands to the fifth and upper conduction bands (C), occurring at higher energies for ZB GaN than for WZ GaN. Finally, the higher intensity of the EELS spectrum in the region <15 eV and the broadening of the plasmon peak for the faulty region can be related to the occurrence of surface modes[34,39] corresponding to the WZ–ZB–WZ interface.

Specific ab initio simulations of the EELS spectra of pristine bulk wurtzite and defective bulk wurtzite (triply-twinned inclusion) were carried out (figures 2.2.5(c) and (e)) in order to corroborate the origin of these experimental features.

Ab initio calculations were carried out by J. D. Prades (Departament d'Electronica, UB) using the SIESTA[40] code, which combines density functional theory (DFT), normconserving pseudopotentials, and local basis set functions. We used the generalized gradient approximations (GGAs) with the Perdew, Burke, and Ernzerhof (PBE) parameterization[41]. For Ga and N atoms, the double ζ local basis set was used with polarization. Additional d-electrons were included in the valence electron set of Ga. Well converged spectra were obtained with a real space mesh cut-off of 250 Ryd and Monkhorst–Pack sets larger than 34 × 34 × 18 for wurtzite structures. Experimental HRTEM lattice parameters were used to build all crystal models. Atomic positions were determined by performing structural relaxations using conjugate gradient minimization of the energy, until the forces on all the atoms were smaller than 0.04 eV $Å^{-2}$. In the relaxation of the models, lattice dimensions were kept constant (in accordance with the experimental values) and no constraints were imposed on the atomic positions within the supercell. To model the planar defects, defective inclusions were embedded in pristine bulk wurtzite. Eight [0001] layers of Ga–N dimers were used to separate the periodic images of the defects. Variations in the electronic structure of less than 0.2% were observed for 16 spacing layers. The loss functions were obtained using first-order time-dependent perturbation theory to calculate the dipolar transition matrix elements between occupied and unoccupied single-electron eigenstates, as implemented in SIESTA 2.0. The optical matrix elements were calculated including the corrections due to the nonlocality of the pseudopotentials[42], which were then used to obtain the dielectric function $\varepsilon(\omega)$ and the loss function $\mathrm{Im}\{-1/\varepsilon(\omega)\}$ that is directly comparable with the EELS spectra.

It is well known that electronic structure calculations within DFT-GGA generally underestimate the band gap of semiconductors[43]. In this case, the calculated band gap for the pristine wurtzite phase was EW g(GGA) = 2.42 eV, clearly lower than the experimental value EW g(exp) = (3.4 ± 0.1) eV. We followed the most common procedure in the literature to circumvent this difficulty that is to apply scissor operators[44,45] that rigidly shift the conduction band in order to match the position of the main peak of the calculated and experimental EELS spectra (located at 20.1 eV in figures 2.2.5(b) and (c)). Figures 2.2.5(c) and (e) show the simulated spectrum of the pristine wurtzite bulk and the local spectrum of the 3T cells embedded in wurtzite. These calculations not only reproduce the main features (A, B, C in figure 2.2.5(b)) of both situations but also predict the experimental band gap change (figures 2.2.5(d) and (e)). Notice that all spectra have been normalized to the maximum of the plasmon peak in figures 2.2.5(b) and (c).

2.2.5 Conclusions

EELS has been applied to characterize the features caused by the Mg doping in GaN nanowires grown by plasma assisted molecular beam epitaxy to obtain p-type nanostructures and their effects on the nanowire. As observed by (S)TEM, the presence of Mg results in the formation of triple-twin (3T) defects, which increase with increasing Mg concentration. The high concentration of misplaced atoms gives rise to local changes in the crystal structure equivalent to three non-relaxed atomic cells of zinc-blende (ZB), which define quantum wells (QW) along the wurtzite (WZ) nanowire growth axis. Local EEL spectra obtained on the 3T and wurtzite planes show modifications in the local density of states, in which the band to band electronic transition energies change from 3.4 eV (for the wurtzite band gap) to 3.2 eV in the 3T lattice regions, the latter being in good agreement with the band gap measured in GaN ZB structures by EELS. These results are confirmed by specific ab initio atomistic simulations of these two situations. EELS assessment of the optoelectronic properties of the given nanostructures at a subnanometric scale has been successfully demonstrated.

2.2.6. References

1. Hochbaum, A. I., Chen, R., Diaz Delgado, R., Liang, W., Garnett, E. C., Najarian, M., Majumdar, A., Yang , P., Nature 451, 163 (2008)
2. Nesbitt, D. J., Nature 450, 1172 (2007)
3. Stern, E., Klemic, J. F., Routenberg, D. A., Wyrembak, P. N., Turner-Evans, D. B., Hamilton, A. D., LaVan, D. A., Fahmy, T. M., Reed, M. A., Nature 445, 519 (2007)
4. Hernandez-Ramirez, F., Tarancon, A., Casals, O., Arbiol, J., Romano-Rodriguez, A. Morante, J. R., Sensors and Actuators B 121, 3 (2007)
5. Arbiol, J., Cirera, A., Peiró, F., Cornet, A., Morante, J. R., Delgado, J. J., Calvino, J. J., Applied Physics Letters 80, 329 (2002)
6. Wagner, R. S., Ellis, W. C., Applied Physics Letters 4, 89 (1964)
7. Fontcuberta i Morral, A., Arbiol, J., Prades, J. D., Cirera, A., Morante, J. R., Advanced Materials 19, 1347 (2007)
8. Kim, T. Y., Lee, S. H., Mo, Y. H., Shim, H. W., Nahm, K. S., Suh, E-K.,Yang, J. W., Lim, K. Y., Park, G. S., Journal of Crystal Growth 257, 97 (2003)
9. Chen, C-C., Yeh, C-C., Chen, C-H., Yu, M-Y., Liu, H-L., Wu. J-J., Chen, K-H., Chen, L-C., Peng, J-Y., Chen, Y-F., Journal of the American Chemical Society 23, 2791 (2001)
10. Huang, Y., Duan, X., Cui, Y., Lieber, C. M. Nanoletters 2, 101 (2002)
11. Calleja, E., Sánchez-García, M. A., Sánchez, F. J., Calle, F., Naranjo, F. B., Muñoz, E., Jahn, U., Ploog, K., Physical Review B 62, 16826 (2000)
12. Fontcuberta i Morral, A., Spirkoska, D., Arbiol, J., Morante, J. R., Abstreiter, G., Small 4, 899 (2008)
13. Furtmayr, F., Vielemeyer, M., Stutzmann, M., Laufer, A., Meyer, B. K., Eickhoff, M., Journal of Applied Physics 104, 074309 (2008)
14. Park, Y. S., Na, J. H., Taylor, R. A., Park, C. M., Lee, K. H., Kang, T. W., Nanotechnology 17, 913 (2006)
15. Zhong, Z., Qian, F., Wang, D. Lieber, C. M., Nanoletters 3, 343 (2003)
16. Lai, F-I., Kuo, S. Y., Chang, Y. H., Huang, H. W., Chang, C. W., Yu, C. C., Lin, C. F., Kuo, H. C., Wang, S. C., Journal of Vacuum Science and Technology B 24, 1123 (2006)
17. Pal, S., Ingale, A., Dixit, V. K., Sharma, T. K., Porwal, S., Tiwari, P. Nath, A. K, Journal of Applied Physics 101, 044311 (2007)

18. Park, Y. S., Park, C. M., Park, C. J., Cho, H. Y., Lee, S. J., Kang, T. W., Lee, S. H., Oh, J-E., Yoo, K-H., Son, M-S, Applied Physics Letters 88, 192104 (2006)
19. Cheng, G., Kolmakov, A., Zhang, Y., Moskovits, M., Munden, R., Reed, M. A., Wang, G., Moses, D., Zhang, J. Applied Physics Letters 83, 1578 (2003)
20. Cimpoiasu, E., Stern, E., Klie, R., Munden, R. A., Cheng, G., Reed, M. A., Nanotechnology 17, 5735 (2006)
21. Batson, P. E., Kavanah, K. L., Woodall, J. M., Mayer, J. M., Phys. Rev. Lett. 57, 2719 (1986)
22. Xin, Y., James, E. M., Arslan, I., Sivananthan, S., Browninga, N. D., Pennycook, S. J., Omnes, F., Beaumont, B., Faurie, J., Gibart, P., Applied Physics Letters, 76, 466 (2000)
23. Karlsson, L. S., Dick, K. A., Wagner, J. B., Malm, J. O., Deppert, K., Samuelson, L., Wallenberg, L. R., Nanotechnology 18, 485717 (2007)
24. Mikkelsen, A., Sköld, N., Ouattara, L., Borgström, M., Andersen, J. N., Samuelson, L., Seifert, W., Lundgren, E. Nature Matererials 3, 519 (2004)
25. Johansson, J., Karlsson, L. S., Svensson, C. P. T., Martensson, T., Wacaser, B. A., Deppert, K., Samuelson, L., Seifert, W., Nature Materials 5, 574 (2006)
26. Davidson, F. M., Lee, D. C., Fanfair, D. D., Korgel, B. A., Journal of Physical Chemistry C 111, 2929 (2007)
27. Arbiol, J., Kalache, B., Roca i Cabarrocas, P., Morante, J. R., Fontcuberta i Morral, A., Nanotechnology 18, 305606 (2007)
28. Arbiol, J., Fontcuberta i Morral, A., Estradé, S., Peiró, F., Kalache, B., Roca i Cabarrocas, P., Morante, J. R., Journal of Applied Physics 104, 064312 (2008)
29. Banerjee, R., Bhattacharya, A., Genc, A., Arora, B. M., Philosophical Magazine Letters 86, 807 (2006)
30. Ihn, S-G., Song, J-I., Kim, Y-H., Lee, J. Y. Applied Physics Letters 89, 053106 (2006)
31. Arbiol, J., Comini, E., Faglia, G., Sberveglieri, G., Morante, J. R., Journal of Crystal Growth 310, 253 (2008)
32. Bao, J., Bell, D. C., Capasso, F., Wagner, J. B., Martensson, T., Trägardh, J. Samuelson, L. Nanoletters 8, 836 (2008)
33. Algra, R. E., Verheijen, M. A., Borgstrom, M. T., Feiner, L-F., Immink, G., van Enckevort, W. J. P., Vlieg, E.Bakkers, E. P. A. M., Nature 456, 369 (2008)
34. Egerton, R. F., "Electron Energy Loss in the Electron Microscope" (2nd ed.), Plenum Press, 1996.

35. Lazar, S., Botton, G. A., Wu, M-Y., Tichelaar, F. D., Zandbergen, H. W., Ultramicroscopy 96, 535 (2003)
36. Bangert, U., Harvey, A., Davidson, J., Keyse, R., Dieker, C., J. Appl. Phys. 83, 127726 (1998)
37. Ramirez-Flores, G., Navarro-Contreras, H., Lastras-Martinez, A., Powell, R.C., Greene, J.E., Physical Review B, 50, 8433 (1994)
38. Gavrilenko, V. I., Wu, R. Q., Applied Physics Leters 77, 3042 (2000)
39. Erni, R. and Browning, N. D., Ultramicroscopy, 104, 176 (2005)
40. Soler, J. M., Artacho, E., Gale, J. D., Garcia, A., Junquera, J., Ordejon. P., Sanchez-Portal, D., Journal of Physics: Condensed Matter 14 2745 (2002)
41. Perdew, J. P., Burke, K., Ernzerhof, M., Physical Review Letters 77, 3865 (1996)
42. Read, A. J., Needs, R. J. Physical Review B 44, 13071 (1991)
43. Jones, R. O., Gunnarsson, O., Review of Modern Physics 61, 689 (1989)
44. Levine, Z. H., Allan, D. C., Physical Review Letters 63, 1719 (1989)
45. Hughes, J. L. P., Sipe, J. E., Physical Review B 53, 10751 (1996)

3. Elemental identification through core-loss EELS

3.1 Temperature induced V migration into FePd layers

3.1 Temperature induced V migration into FePd layers

3.1.1 Introduction

In the present section, core-loss EELS will be applied to assess the possible interdiffusions taking place at the FePd layer / V buffer layer interface in a FePd/V/MgO system.

Binary FePt and FePd alloys are of great fundamental and technological interest, as they exhibit large perpendicular magnetic anisotropy (PMA), namely $K_u \sim 10^7$ J/m^3 in FePt and $K_u \sim 10^6$ J/m^3 in FePd[1], when in their chemically ordered phase ($L1_0$). Chemical order means in this case that pure Fe and Pd (or Pt) atomic planes alternate along a pseudocubic (001) growth direction. In fact, as a consequence of this ordering, the cubic symmetry is broken and a tetragonal distortion appears, that makes the growth direction the easy magnetization axis. In other words, chemically ordered $L1_0$ films grown along the (001) direction exhibit PMA.

On the other hand, in magnetic nanoparticle systems the thermal stability of the magnetization in individual nanoparticles scales with the anisotropy constant (K_u) and the nanoparticle volume[2]. As a consequence, the presence of such high magnetic anisotropy allows to strongly reduce the nanoparticle size while avoiding the so called superparamagnetic limit.

These considerations clearly show that layers of those FePt(Pd) nanoparticles can be considered excellent candidates to develop ultrahigh density magnetic media with naturally separated and stable bits[3,4].

Yet, as the onset of the described chemical order and, therefore, of the large magnetic anisotropy in FePd and FePt binary alloys is only achieved at high enough deposition or annealing temperatures, namely ~400 °C for FePd[5] and ~600 °C for FePt[6], the production of technological devices based on those alloys remains a challenging issue. In this sense, alternative methods used in recent years to obtain PMA in alloys grown at a lower temperature and with a smaller chemical ordering degree include the addition of third elements[7], artificial multilayering[8], ion irradiation[9], monoatomic layer control[10], compositional changes[11], and use of a buffer layer[12].

In particular, the introduction of a buffer layer between the substrate and the binary alloy is generally used to increase the flatness of the initial growing surface and to decrease the

existent lattice mismatch. It has been demonstrated that the nature[5,10–17], thickness[5], and deposition temperature[13] of the buffer layer strongly affect the ordering degree of the binary alloy.

A large variety of materials has been considered for use in such buffer layers. In this chapter, we will focus on the influence of a V buffer layer. V had never been used as a buffer layer for the epitaxy of FePt and FePd alloys before, in spite of the high flatness and crystalline quality of V (100) thin films grown on MgO (001) substrates[18] –displaying an interfacial roughness between 1 and 3 Å.

The structure, morphology and composition of FePd films sputter deposited, at temperatures between room temperature (RT) and 700 °C, on monocrystalline V (001) buffer layers grown on MgO (001) substrates will be assessed through TEM and EELS and correlated with their magnetic, and magneto-optical (MO) properties.

3.1.2 Experimental Details

Studied samples were provided and magnetically characterized by C. Clavero (Instituto de Microelectrónica de Madrid-IMM) and coworkers and optomagnetically characterized by L. Balcells (Institut de Ciència de Materials de Barcelona-CSIC). FePd films of 22 nm in thickness were obtained by triode sputtering codeposition from Fe and Pd targets at $4x10^{-4}$ mbar Ar pressure in an ultrahigh-vacuum chamber with a base pressure in the low 10^{-9} mbar range. The alloys were grown at different deposition temperatures, ranging from RT up to 700 °C at a deposition rate of 0.24 Å/ s. Prior to FePd deposition, a 40 Å buffer layer of V was deposited by sputtering at 400 °C on MgO (001) substrates at a deposition rate of 0.07 Å/ s, optimum conditions for the growth of high crystalline quality, and low surface roughness epitaxial V films[18]. Subsequently to the FePd deposition, a 50 Å thick protective capping layer of Pd was deposited at RT also by sputtering.

Magnetization measurements were carried out by using a RF-SQUID magnetometer from Quantum Design at RT in applied fields up to 20 kOe. The MO behavior of the samples was studied by means of transverse and polar MOKE loops. Transverse loops were measured with a 633 nm HeNe laser system at RT in 45° incidence angle geometry; the change in reflectance was registered; in the case of polar Kerr loops, 530 nm light in normal incidence also at RT was used and the Kerr rotation angle was measured.

TEM samples were prepared in cross section geometries by dry flat polishing down to 50 μm, followed by a dimpling down to 25 μm and a final Ar+ bombardment at V=5 kV with an incident angle of 7° using a PIPS-Gatan equipment. TEM-EELS measurements were carried out in a Jeol JEM 2010F at 200keVs with a GIF spectrometer. Notice that all the EELS data in the present chapter were obtained *before* the STEM unit was installed in the TEM.

3.1.3 Results and discussion

SQUID magnetometry has been used to obtain the saturation magnetization (M_S) of the samples. A value close to that of the stoichiometric phase at RT (1280 emu/cm^3)[14] is found in the samples grown at lower temperatures (from RT to 300 °C), while a strong reduction is observed in the samples grown at higher temperature (400, 500, 600, and 700 °C), as displayed in figure 3.1.1(a).

Hysteresis loops for out-of-plane and in-plane fields have been measured by polar and transverse MOKEs; in figure 3.1.1(b), a complete characterization is shown: polar loops on the left column and the corresponding transverse loops on the right one.

The samples grown at RT and 100 and 200 °C present in-plane magnetic anisotropy; they have a small in-plane coercitive field and saturation field, and high out-of-plane saturation field. They also exhibit a fourfold anisotropy, with easy (100) directions and hard (110) ones (shown in the transverse loops in 3.1.1(b). The sample grown at 300 °C is similar, but in this case the fourfold anisotropy has disappeared. Again, the sample grown at 400 °C separates two different behaviour regions in the magnetic response as it did in the saturation magnetization. The in-plane coercitive field increases from 6 to 150 Oe. The increase of the out-of-plane coercive field and the big reduction of the out-of-plane saturation field indicate the presence of perpendicular anisotropy. Also in SQUID measurements where a higher field is applied and the sample gets saturated, an enormous increase of the in-plane saturation field (6 kOe) is observed in this sample, confirming the presence of a phase with perpendicular anisotropy. The samples grown at 500, 600, and 700 °C show a similar response as the one grown at 400 °C, with decreasing in-plane and out-of-plane coercivities. Also, a decrease of the in-plane and an increase of the out-of-plane saturation fields are observed, indicative of a PMA phase.

The magnetic anisotropy constant (K_u) calculated for the samples exhibiting PMA from the SQUID hysteresis loops measured along the in-plane direction reaches values of $5.2\text{x}10^4$ J/m^3 for the 400 °C sample and $2.34\text{x}10^4$ and $1.25\text{x}10^4$ J/m^3 for the 500 and 700 °C samples, respectively.

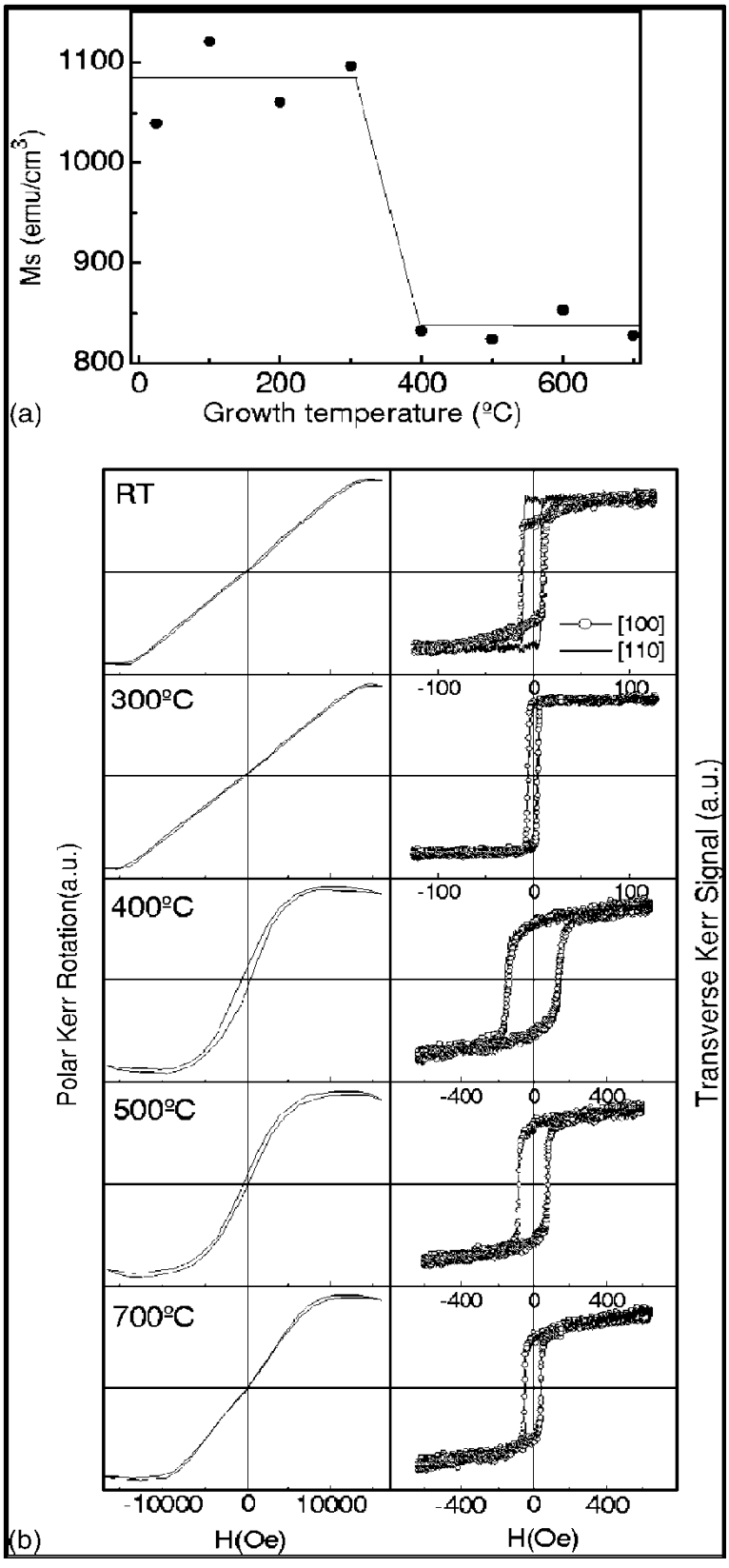

Figure 3.1.1: *(a) Saturation magnetization of the samples as a function of the deposition temperature - the line is just a guide for the eyes. (b) Evolution of the polar (left) and transverse (right) Kerr loops with temperature. For the transverse loops, two curves are shown, one obtained for the (100) direction and the other for the (110) direction. Please note the different scales in the transverse loops.*

The MO spectral response of all the samples was investigated with polar Kerr spectroscopy in the photon energy range from 1.4 to 4.3 eV. In Fig. 3.1.2, the evolution of the Kerr rotation spectra as a function of deposition temperature is shown. While the samples grown at low temperature (RT and 100, 200, and 300 °C) show almost identical spectra, a strong change is observed in the sample grown at 400 °C, with an overall reduction of the Kerr rotation intensity and an even stronger reduction of the intensity of the 4 eV Kerr rotation peak in the sample grown at 700 °C.

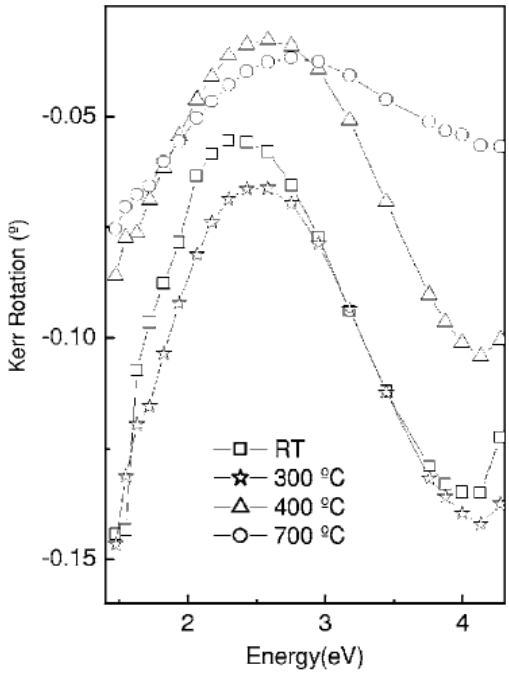

Figure 3.1.2: *Polar Kerr rotation spectra of the samples grown at different temperatures.*

It does thus seem clear that important changes take place in the microstructure and/or local chemistry of the layers when increasing deposition temperature, giving rise to two well-defined deposition temperature regimes of the macroscopic properties of the layers, namely, saturation magnetization, magnetic anisotropy and Kerr rotation intensity. TEM-EELS characterization of the layers is bound to identify what these changes are.

At low FePd deposition temperatures (100, 200, and 300 °C) very flat alloy layers are observed, with a well defined layered structure and clear interfaces: MgO, V, and FePd layers

can be easily distinguished. At 400ºC, the free surface of the alloy layer is still flat, but the V-FePd interface starts getting diffuse. At 500-700ºC, V-FePd interface remains diffuse, and an important layer roughness (of 70% at 500ºC and of 110% at 700ºC) appears, suggesting 3-dimensional growth. Figure 3.1.3 displays an overview of the layer morphology in the 100-700ºC range.

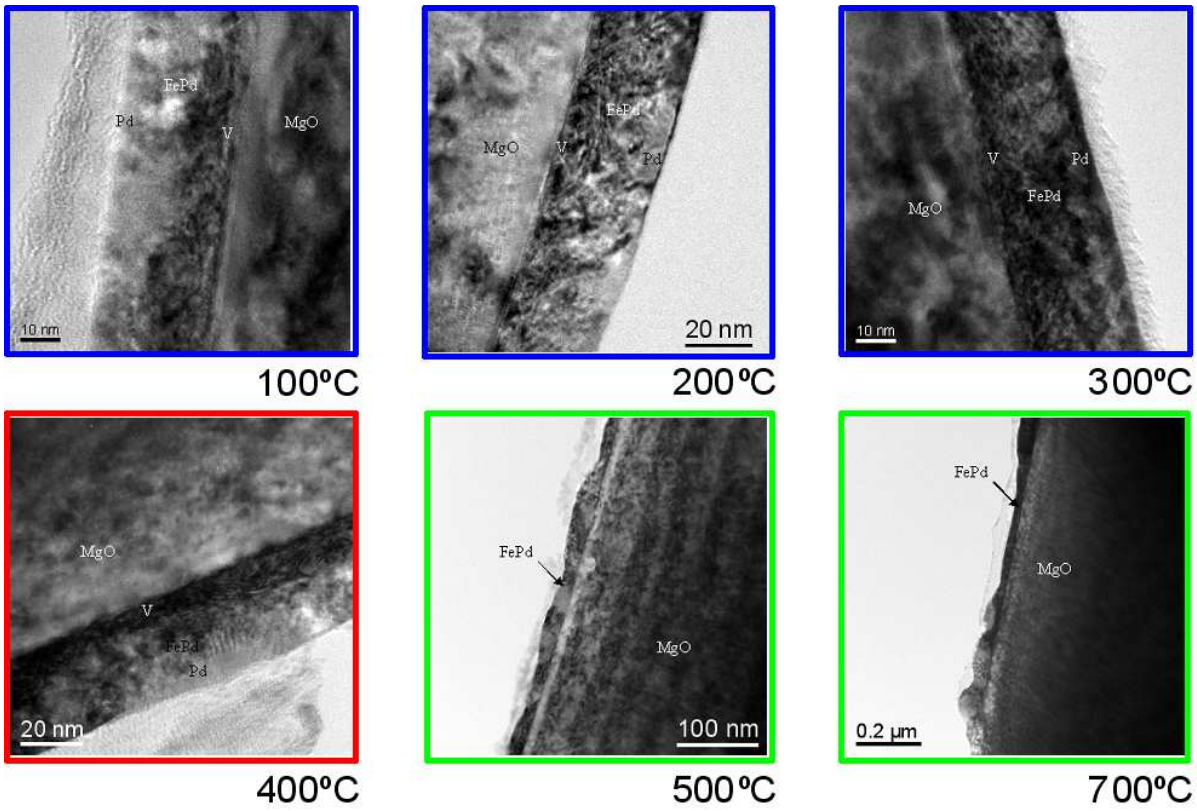

Figure 3.1.3: *Low magnification TEM images of the Pd/FePd/V/MgO system grown at 100-700ºC*

Diffraction patterns were obtained for samples in the 100-700ºC temperature range and allowed to establish the epitaxial relationship between V and MgO, found to be (0 0 1) [1 1 0] V // (0 0 1) [1 0 0] MgO. As for the FePd alloy, it is always (001)-textured, with a moderate degree of polycrystallinity, however, that is found to rise with deposition temperature (figure 3.1.4): no relevant mosaicity is found for 100-300 ºC samples, whereas, for 400 and 500 ºC samples, a mosaicity of about 8 and 11º, respectively, is encountered. No evidence of the ordered $L1_0$ phase is found when considering the microstructure of the FePd layers, irrespective of growth temperature.

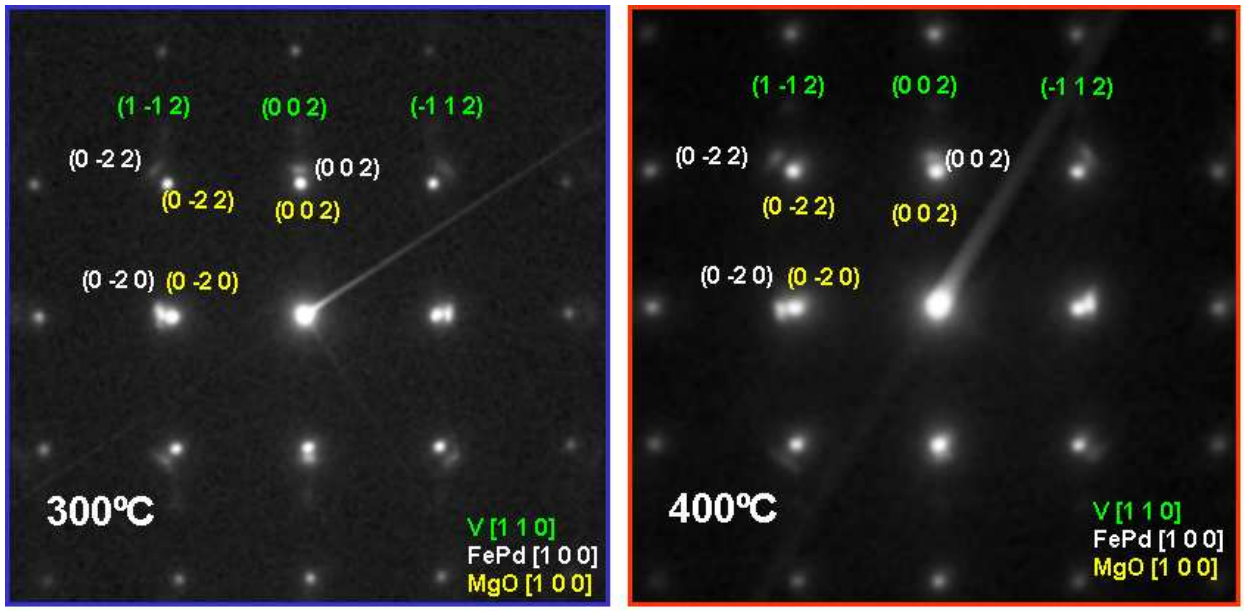

Figure 3.1.4: *Selected Area Electron Diffraction (SAED) patterns corresponding to the samples grown at 300 and 400ºC.*

In order to assess the local composition of the samples, EEL spectra were obtained from the substrate and increasingly deep into the layer. Because of the aforementioned instrumental limitations, EEL spectra were obtained discretely at relevant locations. The considered energy range was 250eV – 760 eV, where the Pd $M_{4,5}$ (335 eV), V $L_{2,3}$ (513 eV), O K (532 eV) and Fe $L_{2,3}$ (708 eV) edges can be found.

For the 100, 200 and 300ºC samples, EEL spectra in the FePd alloy do not display peaks corresponding to V –no V diffusion is detected for that growth temperature range. For the 400 and 500ºC samples, the EELS spectra in the FePd do show V peaks, with decreasing intensity as distance from FePd/V interface increases. Finally, for a 700ºC growth temperature, V is detected in the FePd layer, with constant intensity. It can be thus concluded that for temperatures up from 400ºC, there is a V diffusion into the FePd alloy. When the temperature is further increased to 700ºC, V is already homogeneously distributed along the layer. EEL spectra corresponding to chosen samples are displayed in figure 3.1.5.

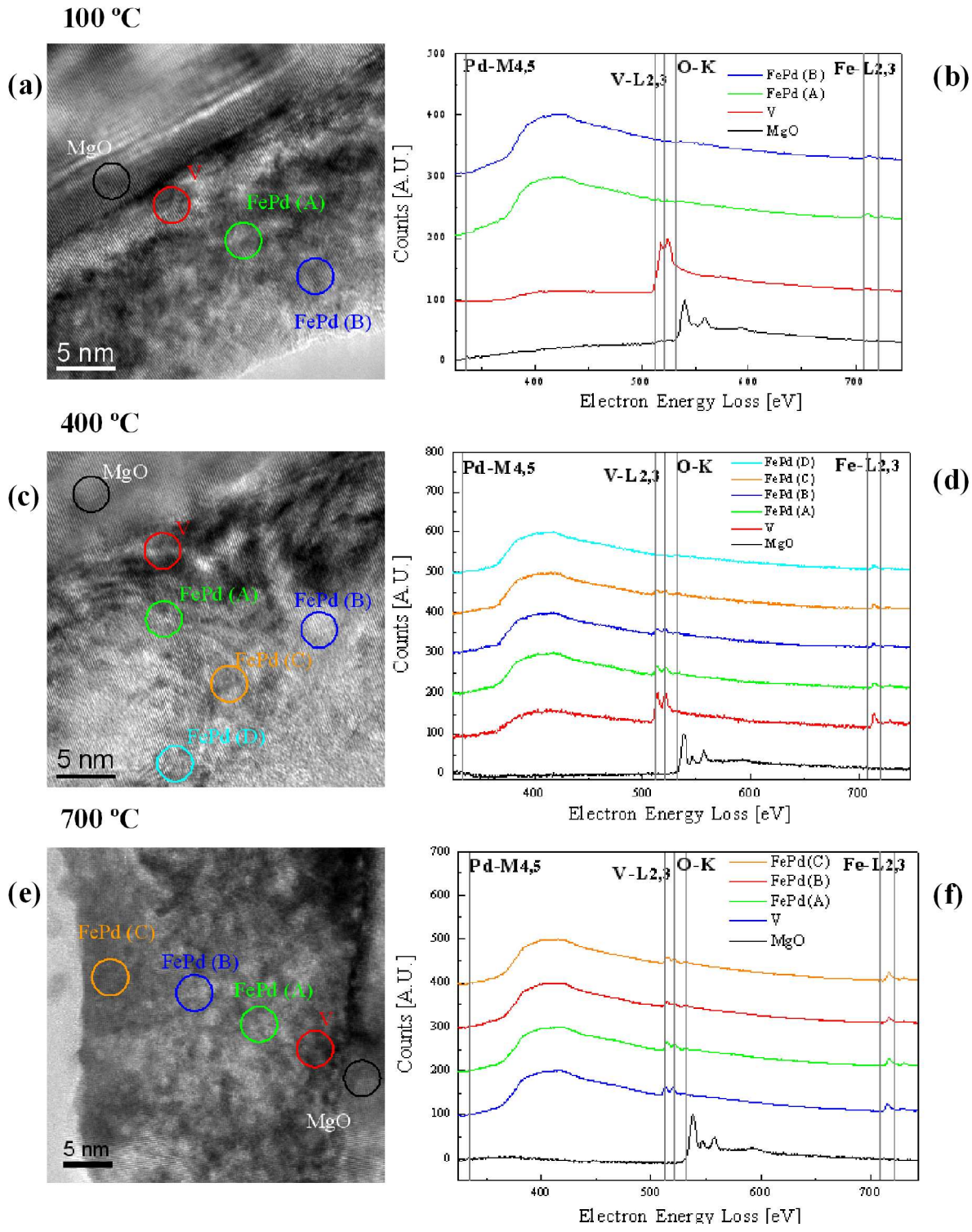

Figure 3.1.5: (a), (c), and (e) TEM micrographs of the samples grown at 100, 400, and 700 °C, respectively. (b), (d), and (f) EEL spectra for the aforementioned samples measured in the points marked in the images shown beside. The Pd $M_{4,5}$, V $L_{2,3}$, O K, and Fe $L_{2,3}$ edges are studied. Note the absence of V in the FePd layer in the 100 °C sample, how V appears in different points of the FePd layer in the 400 °C sample, and the constant concentration of V along the FePd layer in the 700 °C sample.

Changes in saturation magnetization appear in the sample grown at 400 °C, which is the lowest temperature for which the onset of V diffusion is observed by EELS. It has been demonstrated that, in Fe–V interfaces, V couples antiferromagnetically with Fe, giving rise to an induced magnetization in V (magnetic moment per V atom ranging from $0.3\mu_B$ to $1.5\mu_B$), and a 20% decrease in the magnetic moment of Fe interface atoms[19,20]. This reduction has been observed as well in FeV alloys, measuring a magnetization of $0.99\mu_B$ at. for Fe (55% reduction) in equiatomic alloys[21] or even a total extinction of the magnetization for high concentrations of V. On the other hand, in FePd the coupling is ferromagnetic and it has been calculated to have a magnetic moment of $3.04\mu_B$ at. for Fe (thus exceeding the Fe value $2.2\mu_B$ at.) and of $0.38\mu_B$ at. for Pd[22]. The diffusion of V into the FePd layer and the appearance of FeV alloy with a lower average magnetization moment can explain the decrease of the saturation magnetization.

In order to understand the magnetic response of the system we must keep in mind that two factors are competing: on one hand, the change in morphology from continuous films to three-dimensional islands as deposition temperature increases; and on the other hand, the FeV alloy formation between 400 and 700 °C as a consequence of the V interdiffusion.

Samples grown between RT and 300 °C show a typical behavior of continuous thin films[23]. The loss of fourfold anisotropy in the sample grown at 300 °C probably due to an already significant polycrystallinity that produces an additional configurational anisotropy which smears out the crystalline counterpart. The increase of coercitive field from 400ºC is mainly due to the high dispersion of crystalline plane orientation (mosaic spread), observed by SAED and TEM, in this sample. Yet, it is worth noticing that the encountered PMA phase cannot be ascribed to the three-dimensional (3D) growth, since the nanoparticles conforming the layer exhibit a disk-like shape with a maximum height/diameter ratio around 0.1 that is unlikely to promote perpendicular magnetization. In fact, the clear correlation between reduced M_s (induced by a FeV alloy formation) and PMA, simultaneously observed in all the samples grown between 400 and 700 °C, indicates that the presence of the FeV alloy is responsible for the PMA.

In FePd alloys, the Kerr rotation peak at 4 eV is related to the polarization of Pd induced by Fe[24]; thus, the reduction of the intensity of this peak as growth temperature is increased is

probably due to the presence of the FeV alloy. The V atoms will reduce the number of Pd atoms in contact with Fe and, therefore, their polarization, which will produce a reduction of the intensity of the Kerr rotation. The amount of FeV increases as deposition temperature increases due to the total diffusion of V in the FePd layers, as observed by EELS.

3.1.4 Conclusions

The structure, morphology and composition of FePd films sputter deposited, at temperatures between room temperature (RT) and 700 °C, on monocrystalline V (001) buffer layers grown on MgO (001) substrates have been assessed through TEM and EELS and correlated with their magnetic, and magneto-optical (MO) properties.

It is found that above 400 °C a strong V interdiffusion into the FePd layer and the formation of a FeV alloy is accompanied by a two-dimensional to three dimensional growth mode transition and an increase of the mosaic spread at these temperatures. A PMA phase is found in FeV–FePd films grown at temperatures above 400 °C in spite of the absence of long range chemical ordering, usually observed in FePd systems at high deposition temperature. The observed PMA is correlated with the V interdiffusion into the FePd layer assessed by EELS and the formation of a FeV alloy. Although in this case PMA is obtained at similar temperatures as in regular FePd alloys, this approximation, i.e., FePd–FeV mixed systems, can open alternative ways to obtain high anisotropy systems at lower temperatures and with lower chemical order.

3.1.5 References

1. Cebollada, A., Farrow, R. F. C. , Toney, M. F., Magnetic Nanostructures, ed. Nalwa, H. S., American Scientific Publishers, Los Angeles (2002).
2. Weller, D., Moser, A., IEEE Transactions on Magnetism 35, 4423 (1999)
3. Sun, S., Murray, C. B., Weller, D., Folks, L., Moser, A., Science 287, 1989 (2000)
4. Sun, S., Fullerton, E. E., Weller, D., Murray, C. B., IEEE Transactions on Magnetism 37, 1239 (2001)
5. Caro, P., Cebollada, A., Briones, F., Toney, M. F., Journal of Crystal Growth 187, 426 (1998)
6. Shima, T. Takanashi, K., Takahashi, Y. K., Hono, K., Li, G. Q., Ishio, S., Journal of Magnetism and Magnetic Materials 266, 171 (2003)
7. Maeda, T., Kai, T., Kikitsu, A., Nagase, T., Akiyama, J., Applied Physics Letters 80, 2147 (2002)
8. Endo, Y., Kikuchi, N., Kitakami, O., Shimada, Y., Journal of Applied Physics 89, 7065 (2001)
9. Ravelosona, D., Chappert, C., Bernas, H., Halley, D., Samson, Y., Marty, A., Journal of Applied Physics 91, 8082 (2002)
10. Shima, T., Moriguchi, T., Mitani, S., Takanashi, K., Applied Physics Letters 80, 288 (2002)
11. Seki, T., Shima, T., Takanashi, K., Takahashi, Y., Matsubara, E., Applied Physics Letters 82, 2461 (2003)
12. Hsu, Y. N., Jeong, S., Laughlin, D. E., Lambeth, D. N., Journal of Applied Physics 89, 7068 (2001)
13. Caro, P., Cebollada, A., Ravelosona, D., Tamayo, J., García, R., Briones, F., Acta Materialia 46, 2299 (1998)
14. Caro, P., Cebollada, A., Ravelosona, D., Briones, F., García, D., Vázquez, M., Hernando, A., Journal of Applied Physics 81, 5050 (1997)
15. Toney, M. F., Lee, W. Y., Hedstrom, J. A., Kellock, A., Journal of Applied Physics 93, 9902 (2003)
16. Halley, D., Gilles, B., Bayle-Guillemaud, P., Arenal, R., Marty, A., Patrat, G., Samson, Y., Physical Review B 70, 174437 (2004)
17. Takahashi, Y. K., Hono, K., Shima, T., Takanashi, K., Journal of Magnetism and

Magnetic Materials 267, 248 (2003)

18. Huttel, Y., Navarro, E., Cebollada, A., Journal of Crystal Growth 273, 474 (2005)
19. Izquierdo, J., Vega, A., Elmouhssine, O., Dreyssé, H., Demangeat, C., Physical Review B 59, 14510 (1999)
20. Fritzsche, H., Liu, Y. T., Hauschild, J., Maletta, H., Physical Review B 70, 214406 (2004)
21. Krause, J. C., Schaf, J., da Costa, M. I., Jr., Physical Review B 61, 6196 (2000)
22. García, D., Casero, R., Vázquez, M., Hernando, A., Physical Review B 63, 104421 (2001)
23. Cebollada, F., Hernando-Mañeru, A., Hernando, A., Martínez-Boubeta, C., Cebollada, A., Gonzalez, J. M., Physical Review B 66, 174410 (2002)
24. Armelles, G., Weller, D., Rellinghaus, B., Caro, P., Cebollada, A., Briones, F., Journal of Applied Physics 82, 4449 (1997)

3.2 Orientation dependence of Ti diffusion into NFO layers

3.2 Orientation dependence of Ti diffusion into NFO layers

3.2.1 Introduction

In the present section, core-loss EELS will be applied to assess the possible interdiffusions between layer and substrate for $NiFe_2O_4$ (NFO) layers grown on $SrTiO_3$ (STO) substrates.

Spinel ferrites had drawn a great deal of interest in the past, mainly to gain better insight into their magnetic properties, and due to their application to high-frequency devices[1]. Nowadays, $NiFe_2O_4$ (NFO) thin films are considered to be excellent candidates for more advanced applications, as the implementation of spintronics devices[2,3] as thin films display magnetic properties which are well above those of their bulk counterparts[4]. This behavior has been attributed to a partial change to normal spinel structure in thin films, triggered by the stress conditions. This change of the spinel structure should give rise to enhanced magnetic properties (for the inverse spinel structure, which is found in bulk NFO, a saturation magnetization of $M_s(Fe[NiFe]O_4)$ = 256 emu/cm^3 is expected, while for normal spinel structure, $M_s(Ni[Fe]_2O_4)$ = 1024 emu/cm^3 is expected).

Thus far, it has been reported that antiphase boundaries (APBs) may appear during the epitaxial growth of NFO thin films[4,5,6], but microstructural characterization of these nanostructures is not abundant in literature.

In the present section we consider the characterization of NFO spinel layers with nominal thicknesses of 6 nm and 30 nm, grown on perovskite STO (001) substrates, by High Resolution Transmission Electron Microscopy (HRTEM) and Electron Energy Loss Spectroscopy (EELS).

3.2.2 Experimental Details

Studied samples were provided and magnetically characterized by F. Rigato and coworkers at ICMAB-CSIC (Campus de Bellaterra, Barcelona). NFO layers were grown on STO substrates by RF magnetron sputtering at a substrate temperature of 600ºC, a total deposition pressure of 250 mTorr, an Ar/O2 Flux Ratio of 10:1, a target-substrate distance of 6 cm and an estimated growth rate of about 0.3 nm/min. TEM samples were prepared both in planar view and cross section geometries by flat polishing down to 50 μm, followed by a dimpling down to 25 μm and a final Ar+ bombardment at V=5 kV with an incident angle of 7° using a PIPS-Gatan equipment. (S)TEM-EELS characterization was performed in a Jeol 2010 FEG (S)TEM at 200kV with a Gatan GIF detector.

3.2.3 (001) STO vs. (001) MAO

XTEM characterization of the NFO/STO system shows that NFO first grows as islands some 10nm wide and some 8nm high (Fig. 3.2.1a,b), which are found to be perfectly epitaxed on the substrate (Fig. 3.2.1c). Closer investigation of these islands reveals the presence of a thin continuous layer with a lighter contrast and of about two unit cells right over the substrate on which the islands seem to grow (Fig. 3.2.1b). As the thickness of the films is increased, these islands reach coalescence. Fig. 3.2.1d-e display the thicker NFO layer, which is found to be about 27 nm thick.

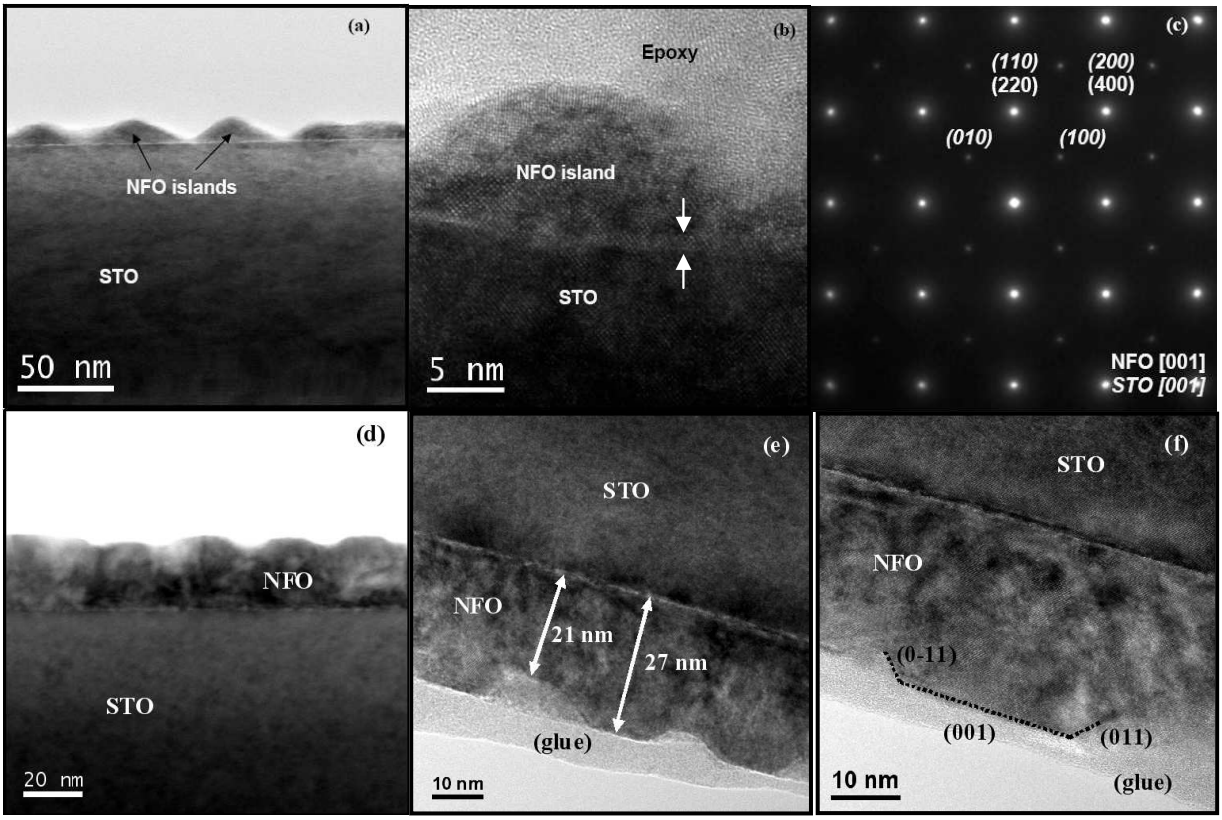

Figure 3.2.1: *XT TEM images of NFO islands in early stages of NFO growth on STO substrates (a, b). Diffraction pattern of the NFO islands / STO substrate system in PV geometry. Arrows indicate a continuous NFO layer of about 2 unit cells right over the substrate (c). XT TEM images of NFO 27 nm layer grown on STO (d-f).*

No APBs were observed in the continuous films. Yet, APBs were predicted in literature[5,6] for this growth mechanism: as NFO has roughly twice the lattice parameter of STO (NFO a =8.339 Å; STO a = 3.905 Å) and NFO is growing by island nucleation, when the islands grow together, the correct stacking sequence of the spinel structure should be just as probable as the stacking sequence being half a unit cell out of phase. Thus, a grain boundary would have a ½ probability to be, in turn, an APB as well. Yet, in this work no APB were detected. It seems that the islands have grown in contact with each other via the observed two unit cell continuous layer, effectively avoiding the possibility of a random stacking sequence of the coalescing grains. It is thus possible to grow NFO on STO without any APBs appearing in the layer.

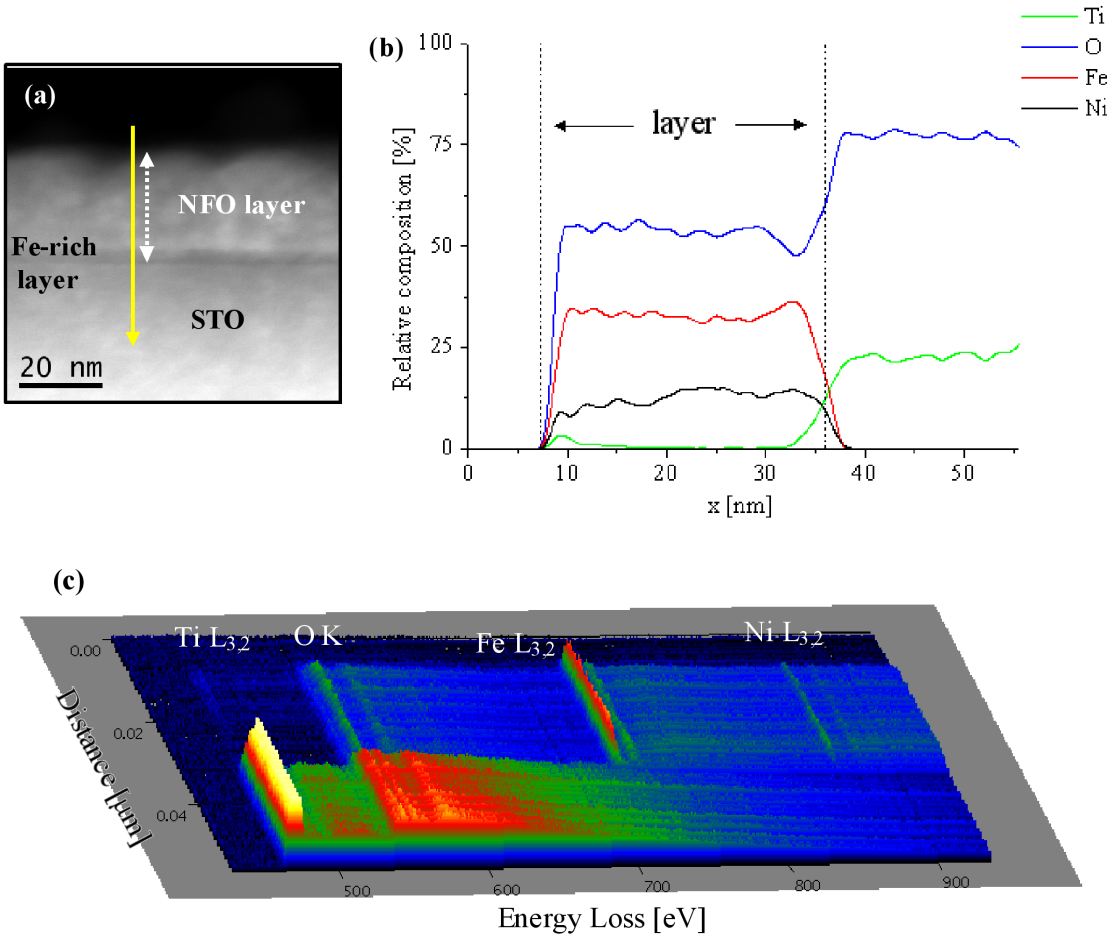

Figure 3.2.2: *(a) HAADF image of the 27 nm NFO layer grown on STO. (b) EELS Elemental quantification and (c) individual EEL spectra along the line displayed in (a).*

EELS spectra of NFO layers grown on STO showed the expected O K at 532 eV, Fe $L_{3,2}$ at 708 eV and Ni $L_{3,2}$ at 855 eV, but they also displayed an extra EELS edge, identified as Ti $L_{3,2}$ at 456 eV. In figure 3.2.2, the EEL spectra taken along the growth direction of a ~ 30 nm NFO layer on STO are given, as well as the corresponding elemental quantification. From figure 3.2.2, it is clear that Ti is present in the layer, especially near the free surfaces.

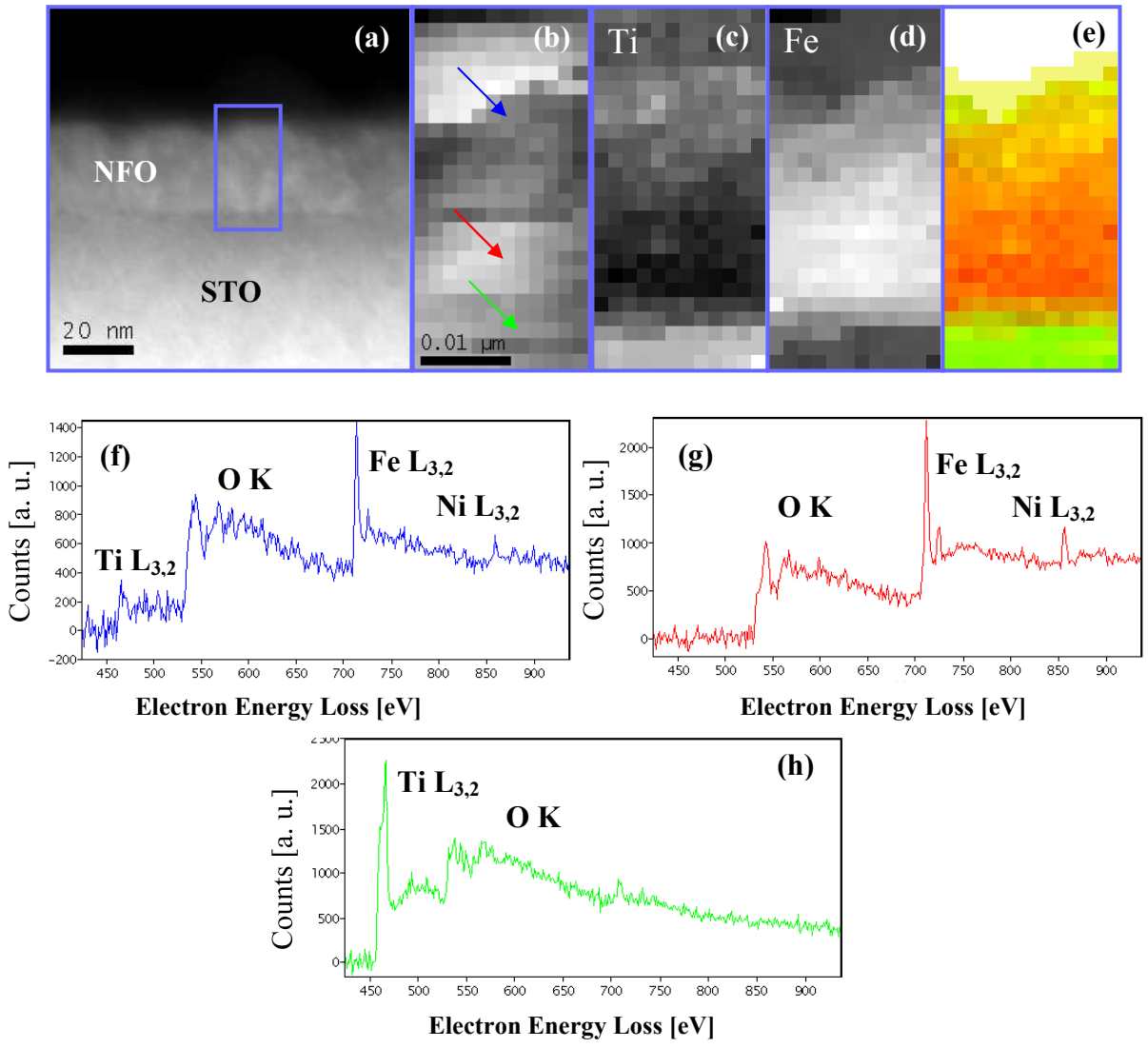

Figure 3.2.3: *(a) HAADF general image of the sample. (b) Spectrum image from the region highlighted in (a). (c,d) Ti, Fe signal from (b). (e) Ti (green) and Fe (red) distribution map. (f,g,h) Background subtracted EEL spectra obtained at the highlighted points in (b).*

In order to further illustrate this point, a two dimensional spectrum image of the layer was taken (figure 3.2.3 (b)), from which the Fe and Ti signals were obtained (figure 3.2.3 (c) and (d) respectively); a map of the spatial distribution of both species is displayed in figure 3.2.3 (e). Again, Ti is seen to be present at the layer, mostly near free surface. Recent ab-initio calculations[7] have shown that, in the case that Ti diffusion from the substrate into an oxide layer takes place, it may be energetically favourable for the system to accumulate the Ti near the free surface.

The presence of Ti in the NFO layers was confirmed by XPS and TOF-SIMS measurements (figure 3.2.4), and EELS quantification yielded about 5% of Ti.

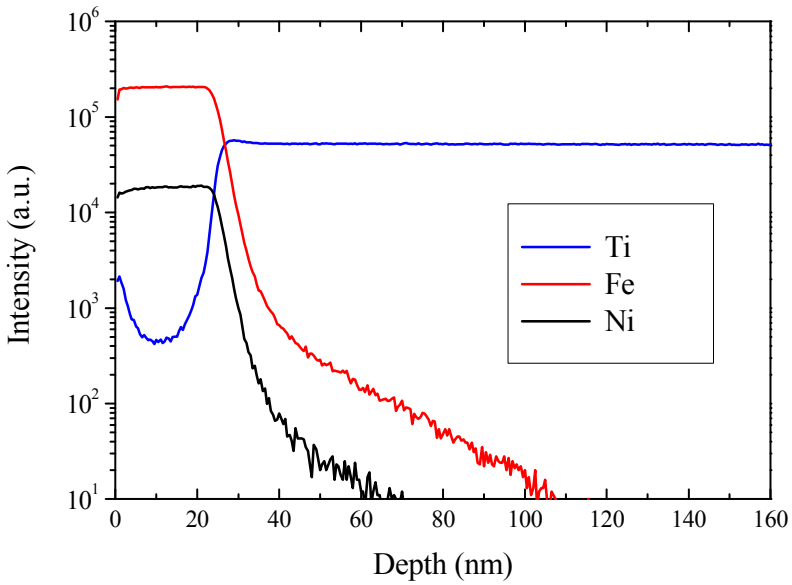

Figure 3.2.4: *TOF-SIMS elemental quantification from top of the 27 nm layer and into the substrate.*

Low magnification TEM observations both in XT and PV geometry revealed a surprisingly poor quality of the used STO substrates (Figure 3.2.5). Encountered defects correspond to both bubbles and dislocations, which have been reported in STO[8], and are believed to promote the observed Ti diffusion from the substrate into the layer. Furthermore, EEL spectra revealed the continuous layer between substrate and eventually coalescing islands to be Fe- and O-rich (see figure 3.2.2), thus probably some kind of Fe oxide.

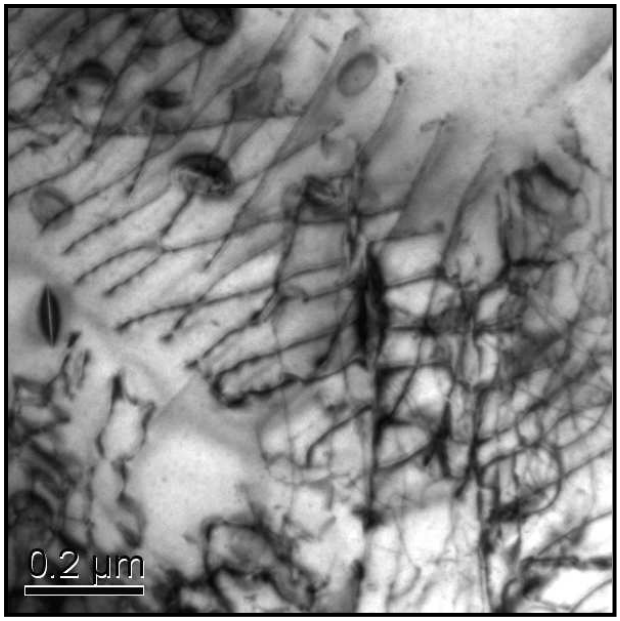

Figure 3.2.5: *PV low magnification TEM image of STO substrate.*

3.2.5 Conclusions

NFO films of various thicknesses grown (001) STO substrates were evaluated by TEM and EELS. It is observed that NFO first grows as islands that eventually reach coalescence to form a continuous layer. A thin continuous layer, probably some kind of Fe oxide, is observed to appear at the interface between the STO and the NFO, thus making it possible for the NFO film to grow on (001) STO without APBs appearing in the layer.

Poor quality of the STO substrate is observed to promote Ti diffusion into the (001) NFO layer. Interdiffusion of species from the substrate is often overlooked, but it may have important effects on the behaviour of the layers.

3.2.6 References

1. Kitamoto, Y., Kantake, S., Shirasaki, F., Abe, M., Naoe, M., Journal of Applied Physics, 85, 4708 (1999)
2. Seneor, P., Fert, A., Maurice, J.-L., Montaigne, F., Petroff, F., Vaurès, A., Applied Physics Letters 74, 4017 (1999)
3. Hu, G., Suzuki, Y., Physical Review Letters 89, 276601 (2002)
4. Lüders, U. , Bibes, M., Bobo, J., Cantoni, M., Bertacco, R., Fontcuberta, J., Physical Review B 71, 134419 (2005)
5. Margulies, D.T., Parker, F.T., Spada, F.E., Goldman, R.S., Li, J., Sinclair, R., Berkowitz, A.E., Physical Review B 53, 149175 (1996)
6. Arora, S. K., Sofin, D.T.I., Shvets, V., Luysberg, M., Journal of Applied Physics 100, 073908 (2006)
7. Wang, R., Zhu, Y., Shapiro, S.M., Physical Review Letters, 80, 2370 (1998)
8. Chen, H., Kolpak, A.M., Ismail-Beigi, S., Physical Review B 79, 161402(R) (2009)
9. Hu, G. Choi, J.H., Eom, C.B., Harris, V. G., Suzuki, Y., Physical Review B, 62, R779 (2000d)
10. Wakiya, N., Shinozaki, K., Mizutani, N., Applied Physics Letters 85, 1199 (2004)
11. Venzke, S., van Dover, R.B. Philips, J. M., Gyorgy, E.M., Siegrist, T., Chen, C.-H., Werder, D., Fleming, R.M., Felder, R.J., Coleman, E., Opila, R., Journal of Materials Research 11, 1187 (1996)
12. Suzuki, Y., van Dover, R.B., Gyorgy, E.M., Philips, J.M., Korenivksi, V., Wender, D.J., Chen, C.H., Cava, R.J., Krajewski, J.J., Peck, W. F., Do, K. B., Applied Physics Letters 68, 714 (1996)
13. Beach, G.S.D., Parker, F.T., Smith, D.J., Crozier, P.A., Berkowitz, A.E., Physical Review Letters 91, 267201 (2000)
14. Wiesendanger, R., Shvets, I.V., Burgler, D., Tarrach, G., Guntherodt, H.G., Coey, J.M.D., Graser, S., Science 255, 583 (1992)
15. Shvets, I.V., Berdunov, N., Mariotto, G., Murphy, S., Europhysics Letters, 63, 867 (2003)
16. Walz, F., Journal of Physics: Condens. Matter 14, R285 (2002)
17. Li, X.W., Gupta, A., Xiao, G., Qian, W., Dravid, V. P., Applied Physics Letters 73, 3282 (1998)

18. Arora, S. K., Sofin R.G.S., Shvets, I.V., Physical Review B 72, 134404 (2005)
19. Eerenstein, W., Palstra, T.T.M., Hibma, T., Celotto, S., Physical Review B 66, 201101 (2002)
20. Hong, J.P., Lee, S.B., Jung, Y.W., Lee, J.H., Yoon, K.S., Kim, K.W., Kim, C.O., Lee, C.H., Applied Physics Letters 83, 1590 (2003)
21. Ziese, M., Physical Review B 62, 1044 (2000)
22. Hibma, T., Voogt, F.C., Niesen, L., van der Heijden, P.A.A., de Jonge, W.J.M., Donkers, J.J.T.M., van der Zaag, P.J., Journal of Applied Physics 85, 5291 (1999)
23. Watts, S.M., Nakajima, K., van Dijken, S., Coey, J.M.D., Journal of Applied Physics 95, 7465 (2004)
24. Zeise, M., Hohne, R., Semmelhack, H.C., Reckentin, H., Hong, N.H., Esquinazi, P., European Physical Journal B 28, 415 (2002)
25. Reisinger, D., Schonecke, M., Brenninger, T., Opel, M., Erb, A., Alff, L., Gross, R., Journal of Applied Physics 94, 1857 (2003)

4. Quantitative core-loss EELS

4.1 FeOx nanowires

4.1 FeO nanowires

4.1.1 Introduction

In the present section, quantitative core-loss EELS will be applied to determine the composition of the iron oxide in FeO_x nanowires and SnO_2/FeO_x core-shell nanowires. The chemical spatial distribution map of the core-shell structure by MLLS fitting of reference spectra will also be carried out.

Binary metal oxides with strong magnetic and electronic correlations have attracted a great interest in recent years due to their possible applications to high temperature superconductivity[1], catalysis[2], magnetic data storage[3], and spintronics[4]. On the other hand, synthesis of nanostructures is a focus of current research, because of the new properties arising from their reduced size, such as the quantization of the density of states at the nanometer level and the surface-dependent number of active sites on crystal facets[5].

Therefore, metal oxide nanostructures are promising candidates for magnetic applications. In particular, the conversion of nanoscale mechanical energy into electrical energy by means of piezoelectric zinc oxide nanowire arrays has been proposed[6]. Spin-dependent electron transport has been demonstrated[7] in individual magnetite (Fe_3O_4) nanowires contacted with normal metallic electrodes –this device demonstrated a spin-filter effect: only the minority spin carriers could transport through the magnetite nanowire due to its negative spin polarization. An anomalous positive magnetoresistance of about 7.5% was observed at room temperature. Moreover, the magnetoresistance could be controlled via bias voltage.

In addition, metal oxide nanostructures have also been considered for biomedical applications such as drug delivery[8,9], gene therapy[8,10], hyperthermic cancer treatment[8,11], and contrast agents in magnetic resonance imaging (MRI)[8,12].

Literature concerning the growth of magnetic iron oxide nanostructures includes template based[13], hydrothermal[14], sol-gel[15], and pulsed laser deposition[16], methodologies, as well as reduction or oxidation processes of pre-grown hematite and metallic iron belts and wires[17]. The molecule based chemical vapor growth of nanostructured oxide coatings and nanowires has been reported to allow the synthesis of nanostructures with well-defined properties[18].

It is clear enough that understanding of the electromagnetic performance of such nanostructures requires assessment of any possible diffusion of the catalytic (generally Au) into the nanowires, determination of whether interdiffusion takes place in core-shell structures, and an estimation of the Fe/O proportion as to elucidate which oxide is being synthesized.

Given the reduced size of the studied nanostructures, EELS is apparent to be the most suitable technique to carry out these investigations. Yet, no careful EELS characterization of FeOx 1-dimensional nanostructures seems to have been reported thus far.

4.1.2 Experimental

The synthesis of the FeOx nanowires involved thermolysis of $[Fe(O^tBu)_3]_2$ in a cold-wall CVD reactor at a temperature of 825 °C on Au covered (~5 nm) polycrystalline alumina[19]. The vaporizing temperature of the iron(III)- tertbutoxide (500-750 mg) source was fixed at 95 °C and adjusted to obtain adequate feedstock in the gas phase for a growth time between 60-90 min.

Core-shell nanowires were formed by a two stage CVD process at 700 °C involving SnO_2 nanowire growth followed by magnetite shell formation by decomposition of $[Fe(OtBu)_3]_2$ for 5-10 min. Tin oxide nanowires were grown on gold-coated substrates (Si and Al_2O_3) by the vapor deposition of $[Sn(O^tBu)_4]$, which acts as a single delivery source for the Sn and O that are necessary for the formation of the SnO_2 phase. Under constant precursor flux, chemical vapour growth of one-dimensional structures was achieved in the range 550–750 ºC, whereas deposition of granular films was observed at lower temperatures (<525 ºC). The catalyst particles were produced by annealing sputtered Au layers.

The details of the nanowires growth were addressed in previous works[19,20]. FeOx and core-shell nanowires were provided by Dr S. Barth and coworkers, then at Department of CVD-Technology, Leibniz-Institute of New Materials (Saarbruecken). SEM characterization was carried out by Dr. F. Hernandez at UB.

Nanowires for (S)TEM-EELS observation were either mechanically transferred on carbon coated copper grids or prepared by FIB (FEI Strata DB 235) in a cross section geometry. FIB sample preparation by R. Jiménez and Dr. A. Romano (UB) is acknowledged. TEM-EELS measurements were carried out using a JEOL 2010F field emission gun (S)TEM, working at 200 kV with a point-to-point resolution of 0.19 nm, and a GIF spectrometer.

4.1.3 Iron oxide determination

FeOx nanowires were observed by (S)TEM. Their single crystalline nature was confirmed in HRTEM investigations. The analysis of the fast fourier tranforms of the HRTEM images and of the electron diffractions of the nanowires were found to correspond exclusively to a [111] zone axis and a wire growth direction [110] for all the investigated nanostructures. Figure 4.1.1 shows a HRTEM image of a FeOx nanowire and its corresponding diffraction pattern.

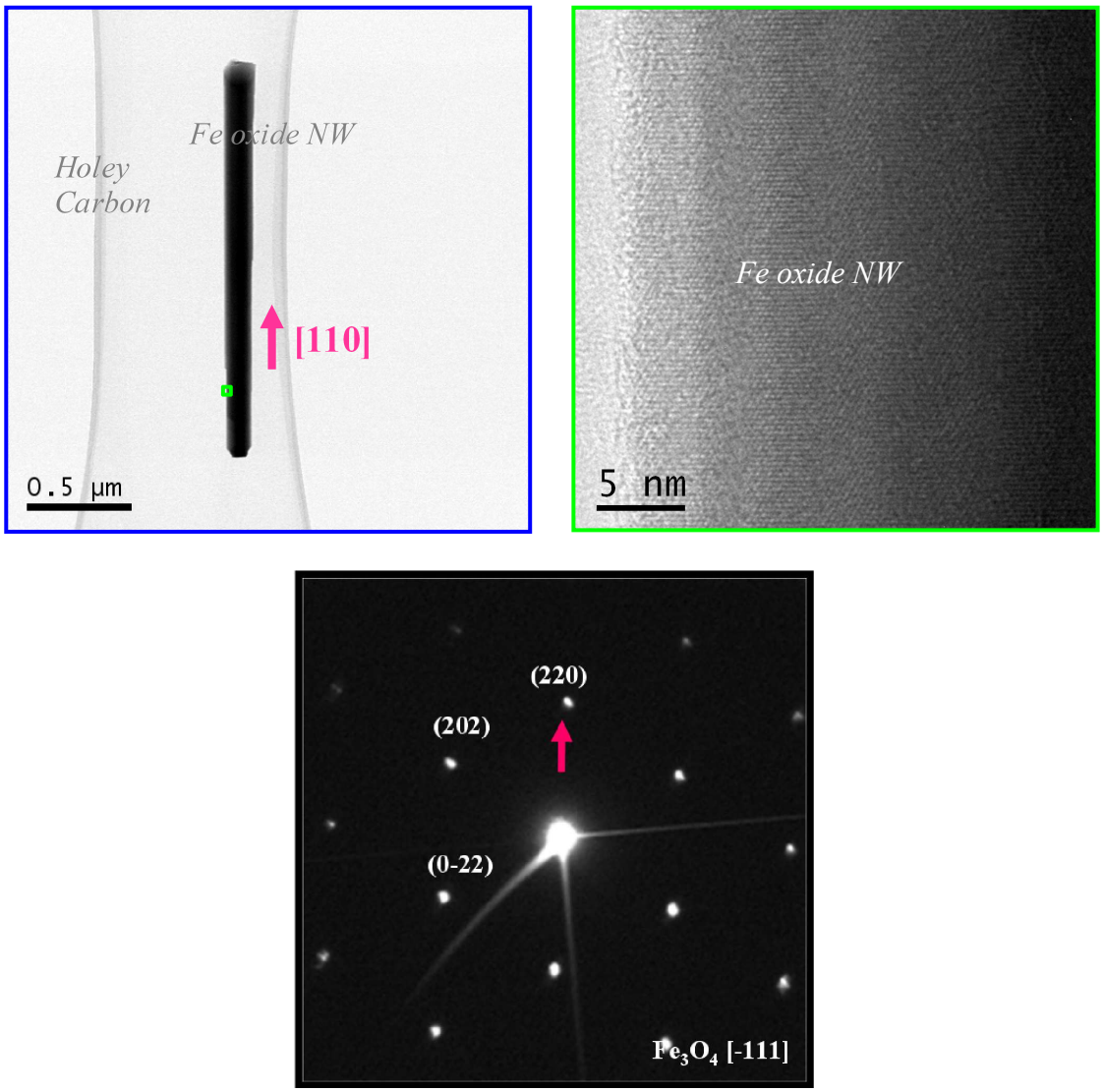

Figure 4.1.1: *General image of a FeOx nanowire, HRTEM micrograph of the highlighted region and diffraction pattern of the nanowire. Diffraction pattern can be indexed as magnetite with a [110] growth direction.*

For the face-centered cubic closed-packed inverse spinel structure of magnetite, the most stable surfaces are {111} <{110} < {211}[21]. Therefore, the formation of crystals in a gas phase process without any surfactant influence preferentially gives rise to {111}-faceted structures, as had been observed by SEM (figure 4.1.2).

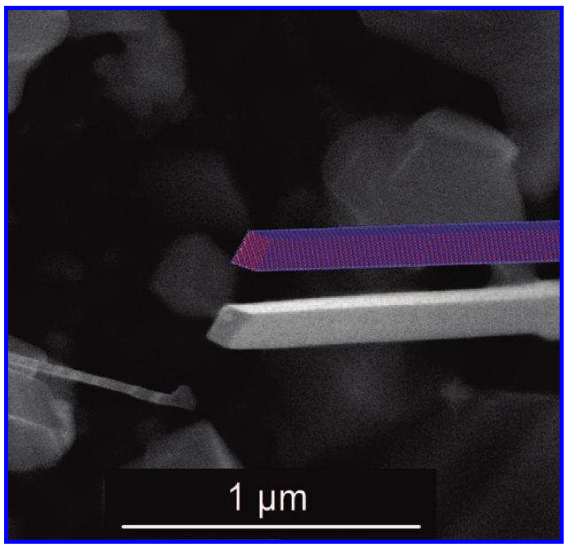

Figure 4.1.2: *SEM image of an individual magnetite nanowire displaying a wire with broken tip and a model showing {111} side facets in the (110) growth direction.*

Intensity profiles of HAADF images (figure 4.1.3 (a), (b)) provided further evidence of a symmetric structure with thinning at the edges and support the proposed model, which is illustrated in the schematic image in the [110] viewing direction (inset of figure 4.1.3b). However, brightness contrast observed in the HAADF images seemed to imply a compositional variation in the iron oxide nanowire material (Figure 4.1.3a). In this sense, Au interdiffusion from the catalytic was suspected. Individual EEL spectra obtained at a small particle at the surface of the nanowire and in the wire body were compared and effectively confirmed the existence of gold islands at the nanowire exterior (Figure 4.1.3c). This correlates with data obtained from different parts of the nanowire showing brightness contrast. The higher fraction of gold found in the thinner parts of nanowires implicates a surface diffusion process for the catalyst, which was recently described for the Si/Au system investigated by HAADF[22].

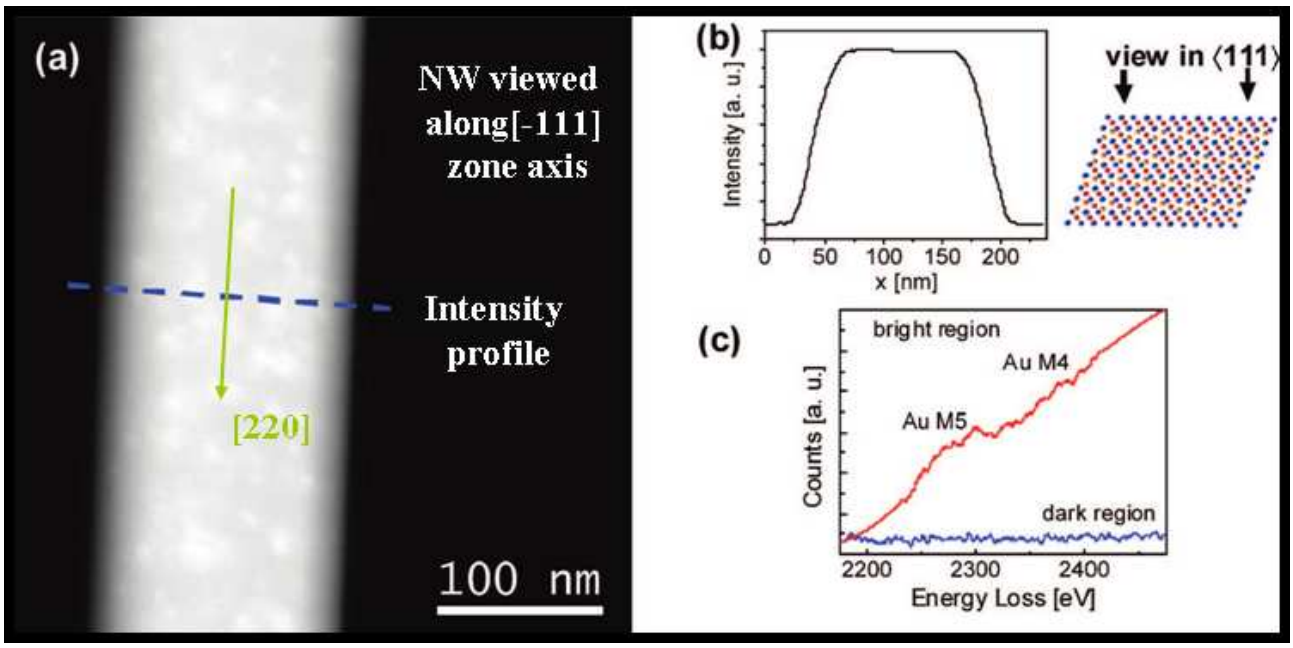

Figure 4.1.3: *(a) HAADF image of a magnetite nanowire showing brightness variation. (b) Cross-sectional intensity spectrum along the line in (a) and schematic image of a {111} surface-terminated nanowire in [110] zone axis. (c) EEL spectra of wire sections with different brightness contrasts indicate the presence of Au on the wire surface.*

The FeOx were carefully investigated through quantitative EELS. In the energy range of around 55 eV, several features attributed to iron $M_{2,3}$ could be found, which were not further studied because of marginal changes in the $M_{2,3}$ edges between different iron oxide phases.

The composition of the iron oxide wires could have been estimated by determining of the iron oxidation state through an adequate fitting of the Fe^{2+} and the Fe^{3+} associated features in the Fe L_3 peak. Yet, experimental energy resolution (0.8 eV) prevented us from following this procedure, which would have been the preferred one if a higher energy resolution had been available.

Determining an iron oxide stoichiometry via the direct Fe/O ratio is a rather controversial procedure that may lead to positively wrong results. Nevertheless, careful Fe/O ratio calculations using the Digital Micrograph program had been previously tested in the context of the 2007 Winter HAADF and EELS Workshop (WHEW) held in Orsay (France). There, EEL spectra corresponding to unknown specimens were quantified. Interestingly, the obtained

results were in good agreement with both the specimens nominal stoichiometry and the elemental quantification carried out by Dr. J. Verbeeck with his EELSmodel program[23]. This way of testing the method via a blind experiment was convincing enough to believe that a careful, error free Fe/O ratio estimation using Digital Micrograph yields a sound, reliable result. Of course, this method is extremely operator-dependent, especially when compared to the Fe L_3 fine structure analysis.

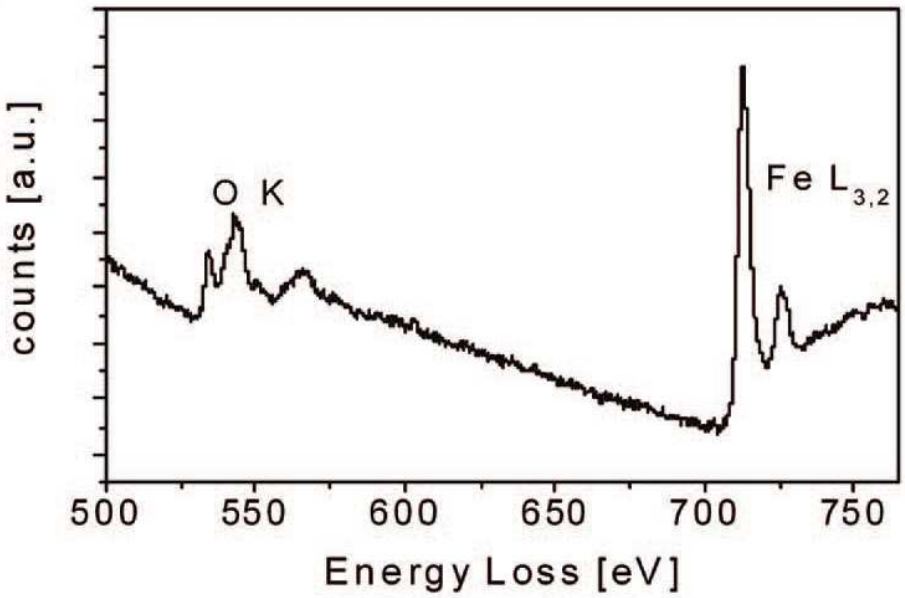

Figure 4.1.4: *Typical EELS spectrum from a FeOx nanowire. Fe / O ratio yielded a value of 0.78 ± 0.05, compatible with the intended compound (magnetite).*

Calculating the Fe/O ratio from the spectrum shown in Figure 4.1.4, a value of 0.78 ± 0.05 was obtained. Local variations in stoichiometry within the same nanowire (figure 4.1.5), and elemental ratio variations between nanowires both of the same and of different batches were found to lie below experimental resolution. The Fe/O ratio value for pure Fe_3O_4 is expected to be 0.75 which is in good agreement with the experimental data.

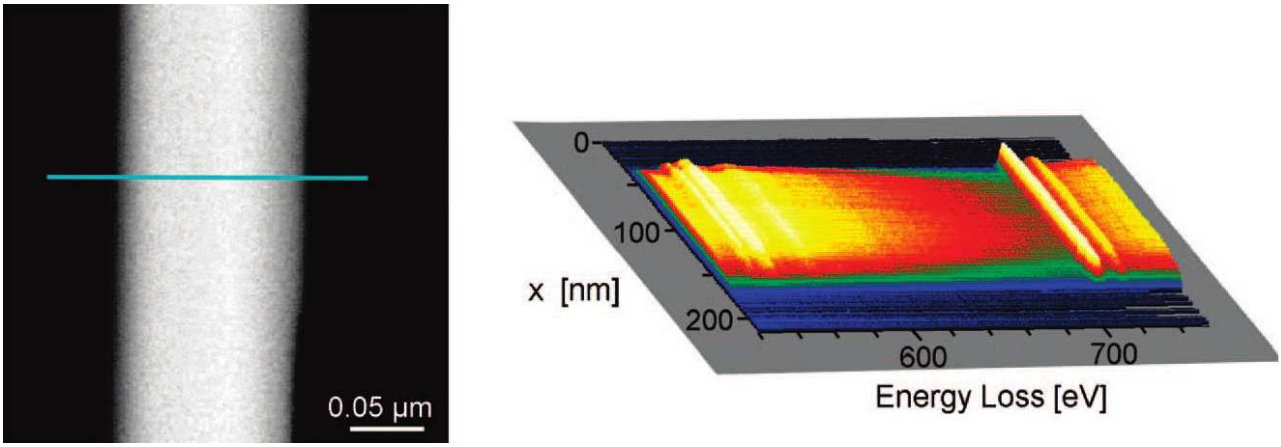

Figure 4.1.5: *EELS Spectrum Line from the region shown in the HAADF image.*

Further features in the EEL spectra were used as sanity checks of the obtained result. O K ELNES shape was found to be compatible with that reported in literature for magnetite[24,25]. Plasmon maximum position was determined to be 23.5 eV (figure 4.1.6) which is higher in energy than that reported for Fe_2O_3 (21.8 eV)[26]. Thus, according to Drude theory, valence state of our sample should be lower than 3+[27], which is also compatible with magnetite.

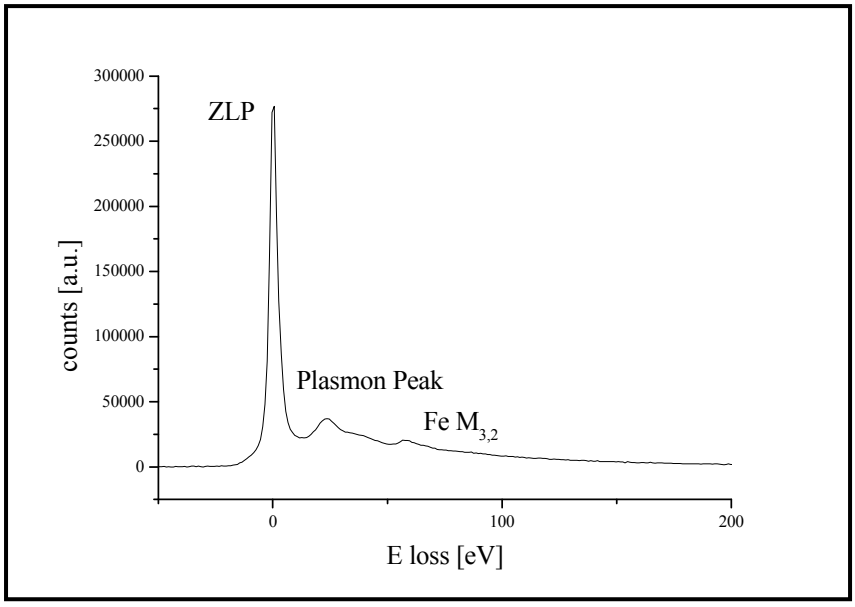

Figure 4.1.6: *EELS spectrum of Fe oxide NW, in the low-loss region.*

4.1.4 Core-shell nanowires

Core (SnO_2) – shell (FeO_x) nanowires were also characterized by (S)TEM-EELS. HAADF observation of the nanowire suggests that the structure does consist of an iron oxide layer that wraps around a tin oxide nanowire, however it does also show that the thicknesses of the FeO_x shell and the tin oxide core seem to vary noticeably (figure 4.1.7).

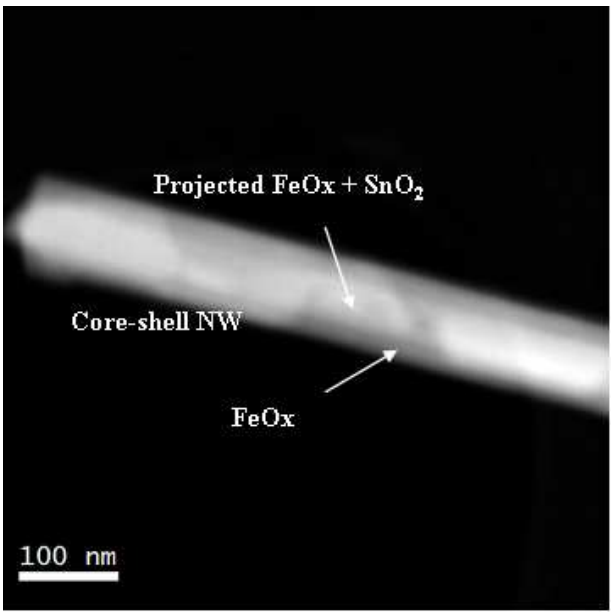

Figure 4.1.7: *HAADF image of core-shell nanowire. Notice than $Sn0_2$ (Z_{mean} = 22.0) appears brighter in HAADF image than Fe_3O_4 (Z_{mean} = 15.7).*

FeO_x does not appear to grow epitaxially on the SnO_2 core. Furthermore, the FeO_x layer is not monocrystalline either. It consists of several pieces or subunits that fuse together during growth. The subunits themselves are of single crystalline nature, which was confirmed by high resolution TEM images (inset in figure 4.1.8).

The tin oxide-core iron oxide-shell nanowires were investigated by EELS to determine the composition of the conducting iron oxide layer. In this sense, EEL spectra were obtained along one core-shell nanowire prepared in cross section geometry -so that the observation zone axis coincided with the growth direction of the nanowire- (figure 4.1.8). The Fe/O ratio of the magnetite shell yielded a value of 0.79 ± 0.05 without site-specific variations, which is in the same range of pure iron oxide wires grown at similar temperatures.

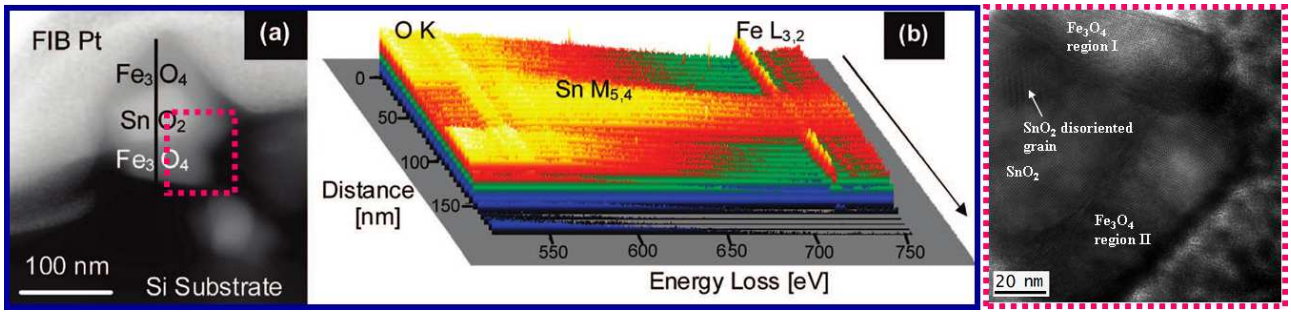

Figure 4.1.8: *HAADF image of a core-shell nanowire in XT geometry including a description of different sections. (b) EEL spectra along the drawn line in (a). HRTEM image of the highlighted region in (a). Notice that, in the case of the core-shell nanowires, the core, nor the shell, appear to be monocrystalline.*

A map of the SnO_2 and Fe_3O_4 distribution in a core-shell nanowire was obtained through multiple linear least-squares (MLLS) fitting of a spectrum image of the nanowire in cross-section geometry, using two previously obtained reference spectra in the SnO_2 and Fe_3O_4 regions of the sample (figure 4.1.9). These spectra were chosen because they corresponded to pure SnO_2 and Fe_3O_4, respectively. MLLS fitting interprets each individual spectrum in the spectrum image as a linear combination of the reference spectra, and returns the fitting coefficients of this linear combination. The spatial distribution of the fitting coefficients can thus be interpreted as a mapping of the compounds to which the reference spectra correspond.

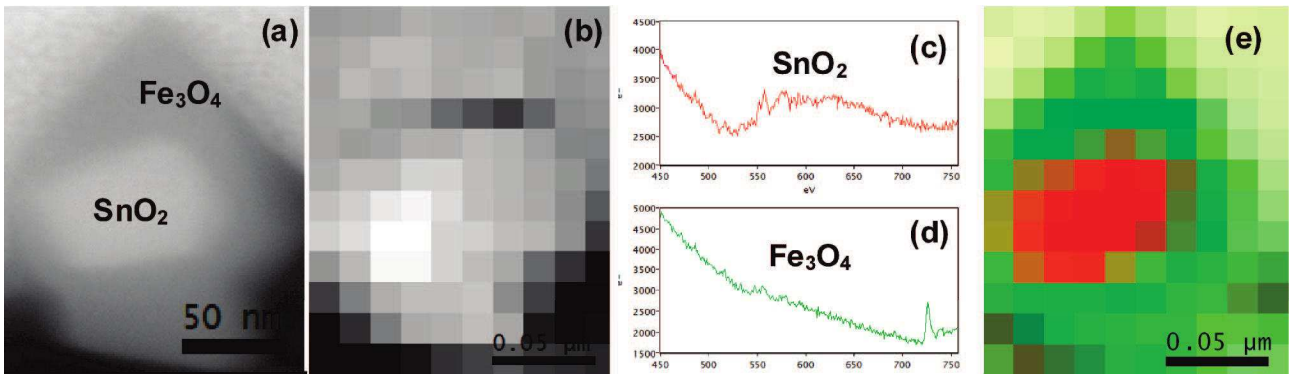

Figure 4.1.9: *(a) HAADF image of a coaxial SnO_2/Fe_3O_4 nanostructure in cross-section geometry. (b) EEL spectrum image from the region displayed in (a). Reference spectra, obtained on (c) SnO_2 and (d) Fe_3O_4 regions. (e) MLLS fitting of spectrum image (b), taking spectra (c) and (d) as reference spectra. Notice that (e) can be viewed as a composition map of the core-shell nanowire cross-section.*

Spectrum line in figure 4.1.8 and spectrum image in figure 4.1.9 suggest a complete wrapping of the SnO_2 interior by the iron oxide phase and do not point towards the existence of interdiffusion between the SnO_2 core and the Fe_3O_4 shell -at least at the studied point of the cross-sectionally thinned nanowire.

4.1.5 Conclusions

Iron oxide single crystal nanowires, grown by molecule-based CVD, were characterized by (S)TEM-EELS. The results of the EELS analysis of the iron oxide and of its HRTEM characterization were consistent with magnetite, as intended in the synthesis process - moreover, no chemical variations were found within the nanostructures. In particular, the Fe/O ratio yielded a value of 0.78 ± 0.05. This figure remained consistently invariant for various wires from different batches. Catalytic (Au) diffusion into the surface of the nanowires was observed through EELS and HAADF. A higher fraction of gold was found in the thin parts of NWs, which suggests a surface diffusion process for the catalyst.

Core shell SnO_2/Fe_3O_4 nanowires were also considered. Cross-sections of the coaxial nanostructures revealed polycrystalline magnetite shells on SnO_2 wires. No interdiffusion was observed between the SnO_2 shell and the magnetite core. EEL spectra were obtained along one core-shell NW in cross section geometry, and the Fe/O ratio of the magnetite shell yielded a value of 0.79 ± 0.05 without site-specific variations, which is in good agreement with the values corresponding to pure iron oxide wires grown at similar temperatures.

The successful application of several core-loss quantification methods has been demonstrated. In particular, the determination of the nature of an iron oxide via a careful Fe/O elemental quantification has been carried out. In addition, the spatial distribution mapping of a core-shell SnO_2/Fe_3O_4 structure by MLLS fitting of SnO_2 and Fe_3O_4 reference spectra has also been achieved.

4.1.6 References

1. Lee, P.A., Nagaosa, N., Reviews of Modern Physics 78, 17 (2006)
2. Kim, Y.J., Westphal, C., Yzunaga, R.X., Gallloway, H.C., Salmeron, M., Van Hove, M.A., Fadley, C.S., Physical Review B 55, R13448 (1997)
3. Zeng, H., Li, J., Liu, J.P., Wang, Z.L., Sun, S., Nature 420, 395 (2002)
4. Lei, B., Han, S., Zhang, D., Liu, Z., Zhou, C., Nanotechnology 18, 044019 (2007)
5. Tian, N., Zhou, Z.-Y., Sun, S.-G., Ding, Y., Wang, Z.L., Science 316, 732 (2007)
6. Wang, Z.L., Song, J.H., Science 312, 242 (2006)
7. Liao, Z.M., Li, Y.D., Xu, J., Zhang, J.M., Xia, K., Yu, D.P. Nano Letters 6, No. 6 1087 (2006)
8. Pankhurst, A.Q., Connolly, J., Jones, S.K., Dobson, J.J., Journal of Physics D: Applied Physics 36, R167 (2003)
9. Berry, C.C., Curtis, A.S.G., Journal of Physics D: Applied Physics 36, R198 (2003)
10. Shinkai, M., Yanase, M., Suzuki, M., Honda, H., Wakabayashi, T., Yoshida, J., Kobayshi, T., Journal of Magnetism and Magnetic Materials 194, 176 (1999)
11. Morishita, N., Nakagami, H., Morishita, R., Takeda, S., Mishima, S., Terazono, B., Nishijima, S., Kaneda, Y.;,Tanaka, N., Biochemical and Biophysical Research Communications 334, 1121 (2005)
12. Braehler, M., Georgieva, R., Buske, N., Mueller, A., Mueller, S., Pinkernelle, J., Teichgraeber, U., Voigt, A., Baeumler, H., Nano Letters 6, 2505 (2006)
13. Wang, J., Chen, Q., Zeng, C., Hou, B., Advanced Materials 16, 137 (2004)
14. Wang, J., Wu, Y., Zhu, Y., Materials Chemistry and Physics 106, 1 (2007)
15. Lian, S., Wang, E., Kang, Z., Bai, Y., Gao, L., Jiang, M., Hu, C., Xu, L., Solid State Communications 129, 485 (2004)
16. Ding, Y., Morber, J.R., Snyder, R.L., Wang, Z.L., Advanced Functional Materials 17, 1172 (2007)
17. Chang, M. T., Chou, L.J., Hsien, C.H., Chueh, Y.L., Wang, Z.L., Murakami, Y., Shindo, D., Advanced Materials 19, 2290 (2007)
18. Mathur, S., Barth, S., Small 3, 2070 (2007)
19. Mathur, S., Barth, S., Werner, U., Hernandez-Ramirez, F., Romano-Rodriguez, A., Advanced Materials 20, 1550 (2008)
20. Mathur, S., Barth, S., Shen, H., Pyun, J.-C., Werner, U., Small 1, 713 (2005)

21. Cornell, R.M., Schwertmann, U., The Iron-Oxides, VCH, Weinheim (1996)
22. Den Hertog, M.I., Rouviere, J.-L., Dhalluin, F., Desre, P., Gentile, P., Ferret, P., Oehler, F., Baron, T., Nano Letters 8, 1544 (2008)
23. Verbeeck, J. and Van Aert, S., Ultamicroscopy, 101, 207 (2004)
24. Colliex, C., Manoubi, T., Ortiz, C., Physical Review B 44, 11402 (1991)
25. Gloter, A., Douiri, A., Tencé, M., Colliex, C., Ultramicroscopy 96, 385 (2003)
26. Ahn, C.C., Krivanek, O.L., EELS Atlas, ASU HREM Facility and Gatan, Inc., Tempe (1983)
27. Erni, R., Browning, N.D., Dai, Z.R., Bradley, J.P., Micron 36, 369 (2005)

4.2 Transition metal oxide nanoparticles

4.2 Transition metal oxide nanoparticles

4.2.1 Introduction

In the present section, quantitative core-shell EELS will be applied to determine the composition of MnO_x/MnO_y, FeO_x/FeO_y and FeO_x/MnO_y nanoparticles, through the careful calculation of Mn/O and Fe/O ratios and the direct estimation of Mn oxidation state.

Exchange bias in nanoparticles has recently attracted quite a lot of attention because of its capability to enhance the performance of permanent magnetic materials by raising their coercivity[1,2] or to overcome the superparamagnetic limit in magnetic recording media[3,4].

The exchange bias phenomena can be described in terms of an alignment of the antiferromagnetic (AFM) spins at a ferromagnetic (FM) – AFM interface to be parallel to the FM spins, which takes place during the field cooling procedure. The coupling between the AFM and FM spins at the interface exerts an additional torque on the FM spins, which the external field has to overcome. According to this, two different competing behaviours can be predicted, depending on the strength of the AFM magnetic anisotropy. If the AFM anisotropy is large, a shift of the hysteresis loop should be observed, while for small AFM anisotropies, the only observed effect should be a coercivity enhancement (without any loop shift). Yet, both effects are generally simultaneously observed, due to, for example, structural defects or grain size distribution, which lead to local variations of the AFM anisotropy[5].

Many transition metal oxides are known to be AFM. In this sense, the most widespread approach to obtain exchange bias in nanoparticles is to partially oxidize transition metal magnetic particles. Some examples of this simple procedure are: Co–CoO, Co_3O_4[6,7], Ni–NiO[8,9], NiCo–NiCoO[10,11], FeCo–FeCoO[12,13], Fe–Fe_3O_4, γ-Fe_2O_3, α-Fe_2O_3, FeO (note that Fe_3O_4 and γ-Fe_2O_3 are ferrimagnetic)[14,15,16]. Thus, in these core–shell structures, the core is a magnetic transition metal and the shell is the AFM (or ferrimagnetic) transition metal compound. The original core diameter can be usually adjusted by the nanoparticles production techniques but in these systems the core and the shell cannot be controlled independently as the AFM shell grows at the expense of the FM core.

These nanoparticles are simple to produce but present several drawbacks. The main problem concerns the limited repertory of possibilities that can be obtained if the AFM shell must come

from a simple chemical modification of the core. Another drawback is that, due to the reduced size of the nanoparticles, the AFM shell usually grows highly disordered[17-19]. Furthermore, if the particles are overoxidized, the core could be exceedingly small, becoming superparamagnetic[20,21] and the exchange bias properties could be lost.

Studies of core-shell nanoparticles with AFM cores are thus far rather scarce. Yet, core-shell nanoparticles of MnO–Mn_3O_4, composed of an antiferromagnetic (AFM) core and a ferrimagnetic (FiM) shell[22-25], as well as FeO–Fe_3O_4[26] nanoparticles seem to be promising candidates.

On the other hand, the synthesis of hetero-core-shell systems, composed of different transition metal materials, opens the door to new degrees of freedom to control the magnetic properties of the nanoparticles and is thus of great interest[27].

The determination of the composition of MnO_x/MnO_y, FeO_x/FeO_y and FeO_x/MnO_y nanoparticles, which will be demonstrated in the present section, is a specially striking example of properties that need to be accessed through EELS because of the reduced sizes involved in the problems at hand.

For instance, as an illustration, it is clear if one aims for the synthesis of FeO_x/MnO_y onion-like nanoparticles and performs an X-ray analysis, even if that analysis yields Fe and Mn signals, it is impossible to determine whether the sample is made of FeO_x/MnO_y core-multi shell (onion) structures or, on the contrary, contains separate FeO_x and MnO_x nanoparticles in random configuration. EELS, on the other hand, can resolve the composition of individual nanoparticles at the nanoscale.

4.2.2 Experimental details

MnO_x/MnO_y and FeO_x/FeO_y nanoparticles were prepared by thermolysis of the corresponding metal organic salt leading to the AFM-core which is passivated under air yielding to the corresponding ferromagnetic shell[28].

The synthesis of onion FeO_x/MnO_y particles was carried out following a multi-step procedure where preformed iron oxide nanoparticles were used as seeds for the subsequent growth of manganese (II) oxide and its passivation. Briefly, the iron oxide seeds were prepared by thermolysis of the iron (III) oleate leading to an average particle size of 6.5 ± 1 nm. The manganese oxide layers were then laid on the iron oxide-based nanoparticles[29].

All nanoparticles were provided by Marta Estrader and coworkers at Institut Català de Nanotecnologia (Campus de Bellaterra), who are also to undertake a detailed structural and magnetic characterization of the nanoparticles.

Nanoparticles for (S)TEM-EELS were deposited on carbon coated copper grids. TEM-EELS measurements were carried out using a JEOL 2010F field emission gun (S)TEM, working at 200 kV with a point-to-point resolution of 0.19 nm, and a GIF spectrometer.

4.2.3 Results and discussion

4.2.3.1. MnO_x/MnO_y

The synthesis of narrowly size distributed MnO/MnO_y, nanoparticles of about 14 nm, with a MnO core of about 9 nm was aimed. MnO_y was supposed to be either Mn_3O_4 or γ-Mn_2O_3. The system should then be considered as double inverted since it would be composed of a MnO-AFM core with T_N = 122 K and a ferrimagnetic (FiM) shell with T_C = 43 K for Mn_3O_4 or T_C = 39 K for γ-Mn_2O_3 (i.e., $T_C < T_N$, as opposed to conventional exchange biased systems).

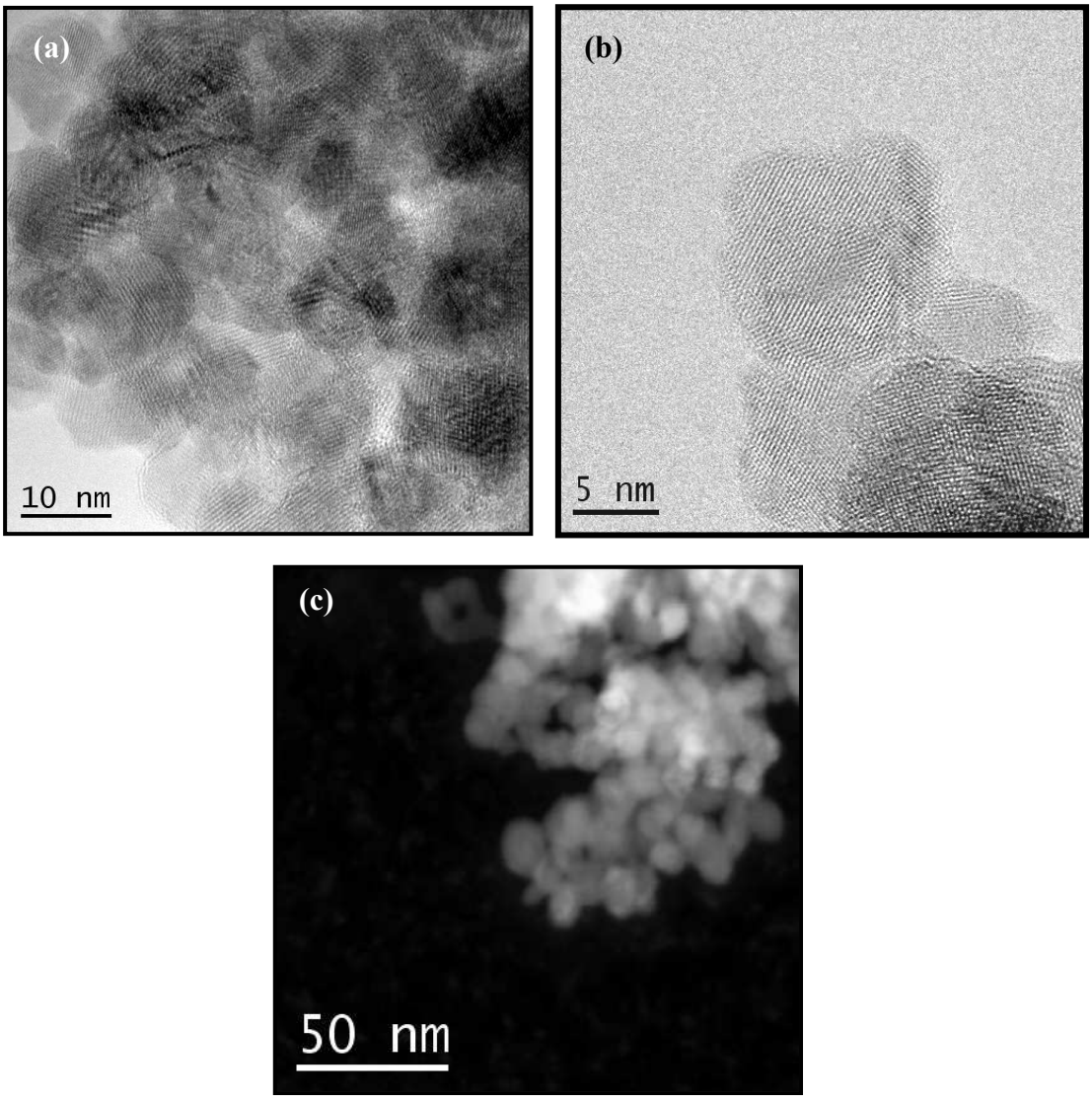

Figure 4.2.1: *HRTEM (a), (b) and HAADF (c) images of several core-shell nanoparticles.*

The nanoparticles were found by HRTEM and STEM (figure 4.2.1) observations to effectively be about 14 nm in size. It was of course not possible to distinguish between core and shell in HAADF images, as the difference between the mean Z of two Mn oxides is not enough to resolve it.

EEL Spectra were obtained along several nanoparticles. Mn oxidation state was determined from these EEL Spectra through a threefold procedure: first of all, Mn/O elemental ratio was calculated. Then, Mn oxidation state was deduced from the Mn L_3/L_2 peak intensity ratio and from the Mn L_3 peak onset. Those two observables have been reported[30-32] to be correlated to Mn oxidation state and were calculated using home-made program MANGANITAS[33-35]. The details of Matlab-based code MANGANITAS will be fully addressed in the next chapter of this Thesis.

Results corresponding to one of the studied particles are given in figure 4.2.2. The data concerning the Mn oxidation state of the different considered particles were found to be consistent with one another.

A MnO core is clearly observed (even if, when obtaining an EELS signal from the centre of a nanoparticle, the signal comes both from the core and the enveloping layer, making it impossible to obtain a pure MnO spectrum). As for the shell, it is apparent from EELS data that it consists of two parts: an inner Mn_2O_3 layer and a very thin outer MnO layer. It thus seems that the particles have a $MnO/Mn_2O_3/MnO$ radial structure. The central layer is clearly not Mn_3O_4, as the data in figure 4.2.2 strongly suggest the presence of a Mn^{3+} phase.

In order to gain further insight into the structure, we have calculated, from simple geometric considerations, the total projected EELS signal that would be obtained for MnO (r1 = 4.5nm)/ Mn_2O_3 (r2 = 1,5nm)/MnO (r3 = 0.5nm). As the calculated model does not correlate well with the experimental data, inner radius has been optimized. Best results are obtained for r1 = 2.5 nm.

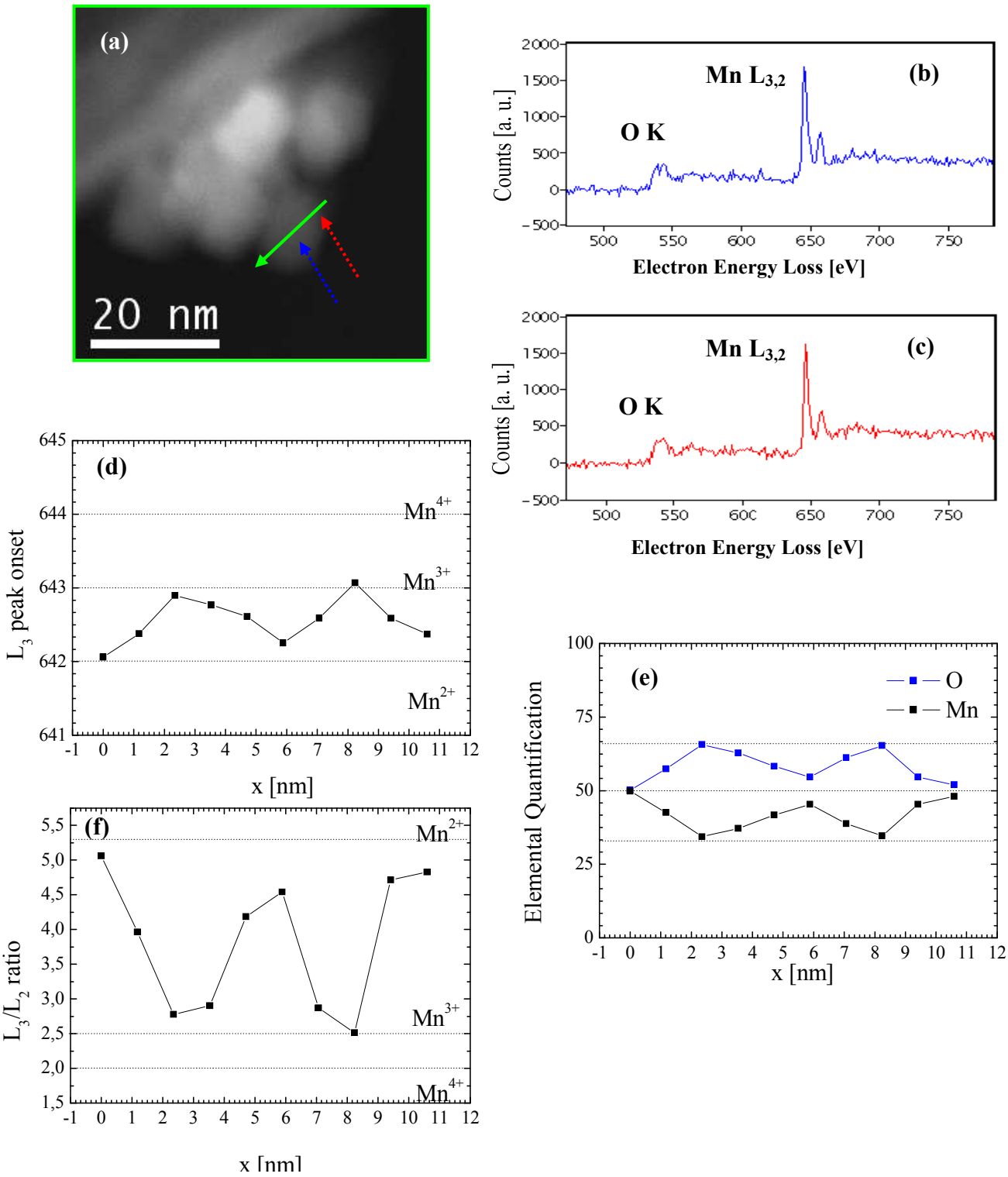

Figure 4.2.2: *(a) HAADF image of several nanoparticles. (b,c) Background-subtracted EEL Spectra obtained at the positions indicated in (a) –dashed arrows. (d) Mn L_3 peak position along the line highlighted in (a). (e) Elemental quantification along the line highlighted in (a). (f) Mn L_3/L_2 intensity ratio along the line highlighted in (a). Elemental quantification, L_3 peak chemical shift and L_3/L_2 intensity ratio are subjected to a relative error of about 5%.*

Taking into account that the nanoparticles do not seem to be perfectly spherical, an even better agreement with experimental data in figure 4.2.2 can be obtained when considering (a little arbitrarily) that the outer layers are half in thickness in the direction perpendicular to the beam compared to the in-plane directions (thus considering a flat particle). All these simple calculations are shown in figure 4.2.3.

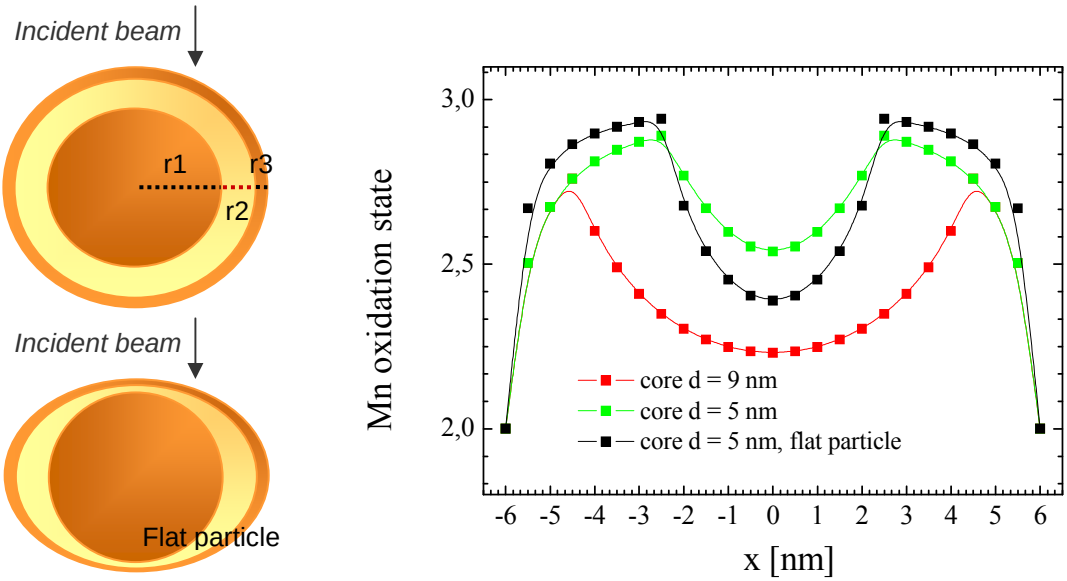

Figure 4.2.3: *Schematic representation of a nanoparticle, considered to be spherical (a), or flat (b). (c) Simulation of the spatial distribution of measured Mn oxidation state, for a spherical nanoparticle with a core diameter of 9 nm, and of 5 nm, and for a flat particle with a core diameter of 5 nm.*

4.2.3.2. FeO_x/FeO_y

The synthesis of monodispersed 11nm FeO/Fe_3O_4 particles with a 4 nm core was also intended. In this case $T_C(Fe_3O_4) > T_N(FeO)$, thus the system can be considered single inverted. STEM images of several nanoparticles are given in figure 4.2.4.

EELS analysis was carried out for several nanoparticles. Fe/O elemental ratio was calculated, and, from Fe/O ratio data, the presence of a Fe-rich core was hinted for all considered particles. In order to further analyse the EELS data, elemental quantification measurements were plotted together with the expected elemental quantification profiles in the case of no FeO core (thus in the case of a uniform Fe_3O_4 nanoparticle) and in the case of a 4 nm thick FeO core. These expected profiles were, once more, calculated from simple geometrical considerations.

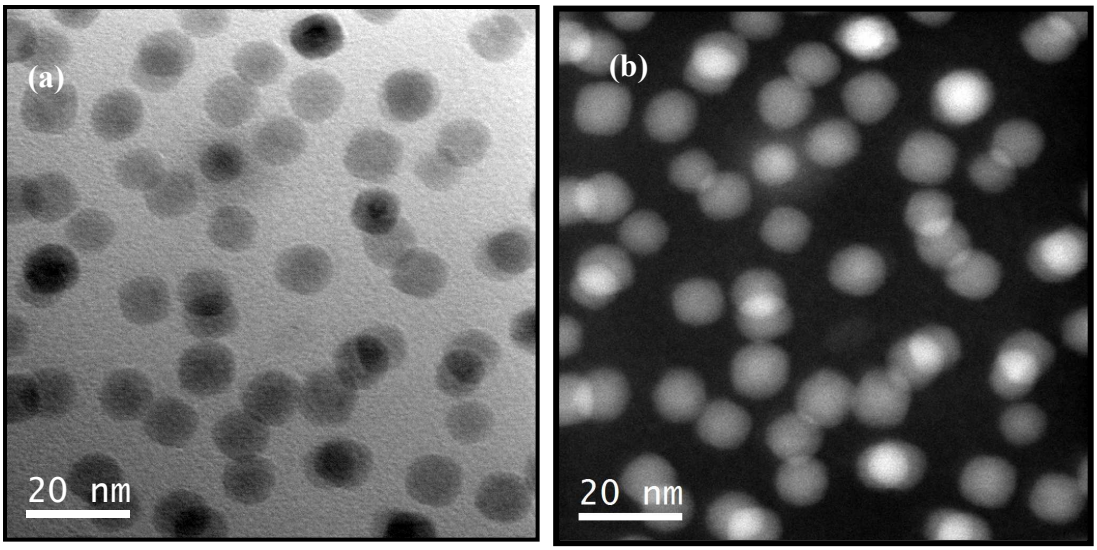

Figure 4.2.4: *STEM BF (a) and HAADF (b) images of several core-shell nanoparticles.*

Even if the detected Fe/O variation through the nanoparticles is not far from the experimental error, it is still clear that the obtained data are not compatible with uniform Fe_3O_4 nanoparticles, and that nanoparticles do show a Fe-rich core. The elemental quantification for three different nanoparticles, together with the expected elemental quantification for both a 4 nm thick FeO core / Fe_3O_4 shell nanoparticle and a uniform Fe_3O_4 nanoparticle are given in figure 4.2.5.

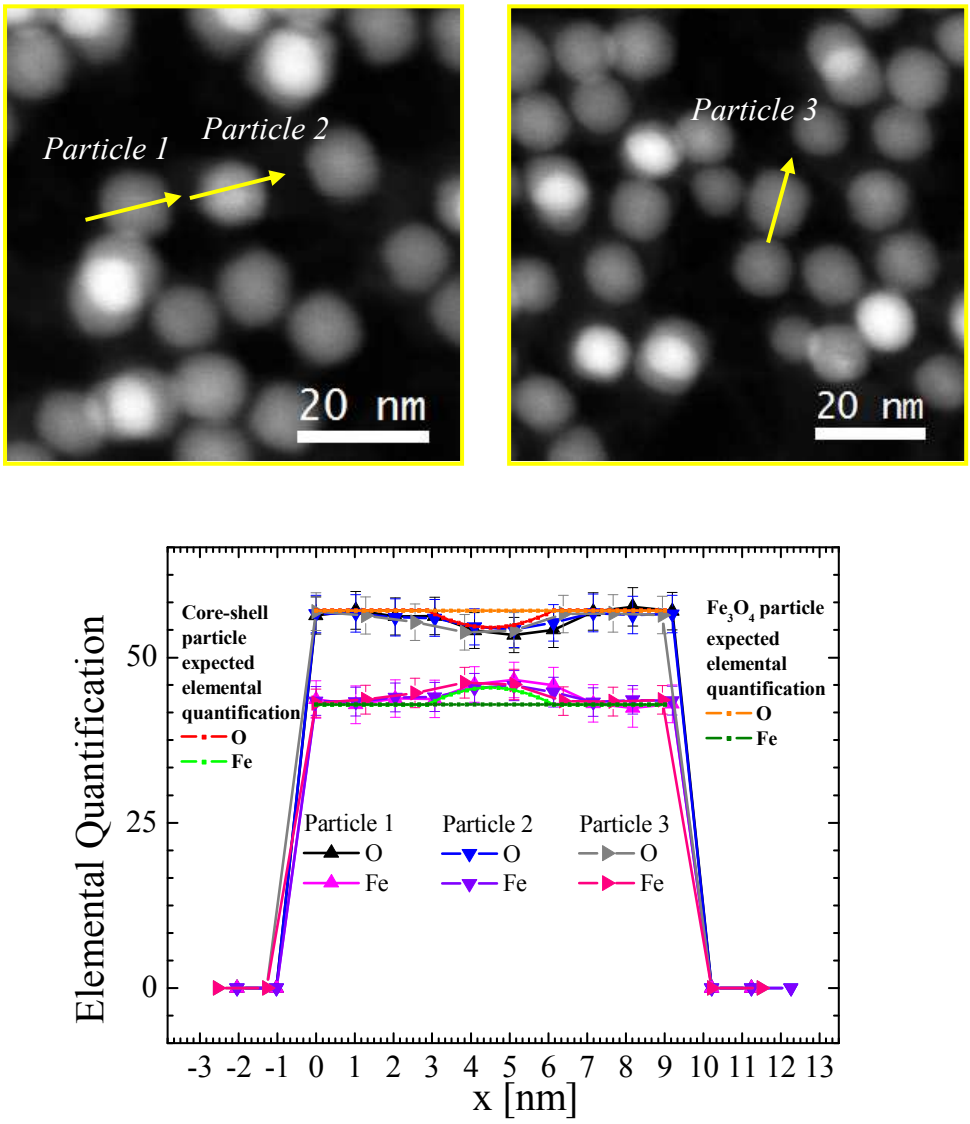

Figure 4.2.5: *HAADF images of several core-shell nanoparticles. Elemental quantification along the highlighted lines for the three considered nanoparticles and expected elemental quantification for both a 4 nm thick FeO core and a uniform Fe_3O_4 nanoparticle. As indicated by error bars, elemental quantification is subjected to a relative error of about 5%.*

4.2.3.3. FeO_x/MnO_y

Finally, FeO_x/MnO_y onion-like nanostructures were synthesised. In this case, nanoparticle size was found to be more variable, and HRTEM observation yielded a particle mean diameter of 7.9 nm, with a standard deviation of 0.7 nm. Several HRTEM images of the nanoparticles are given in figure 4.2.6.

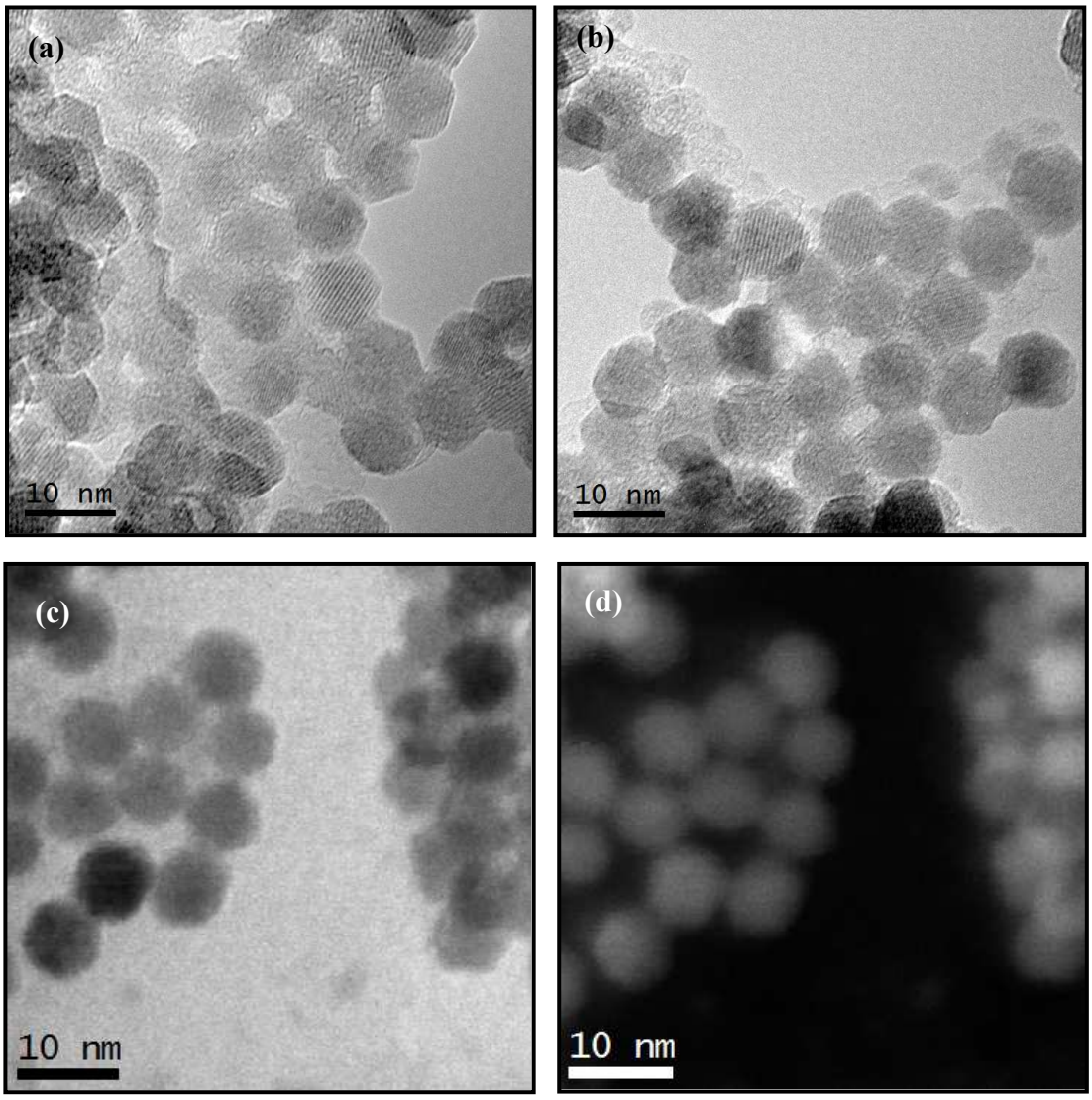

Figure 4.2.6: *HRTEM (a), (b), BF-STEM (c) and HAADF (d) images of several core-shell nanoparticles.*

BF-STEM and HAADF images of several nanoparticles are also given in figure 4.2.6. No diffraction contrast between core and shell is observed in BF STEM. As Mn and Fe have Z numbers Z = 25 and Z = 26, respectively, no contrast is found in HAADF either.

MLLS analysis of the EELS Spectrum Image of an onion nanoparticle is given in figure 4.2.7. The MLLS fitting makes it possible to distinguish between a shell, where only Mn signal is observed, and a core, where both (projected) Mn and Fe signals are found.

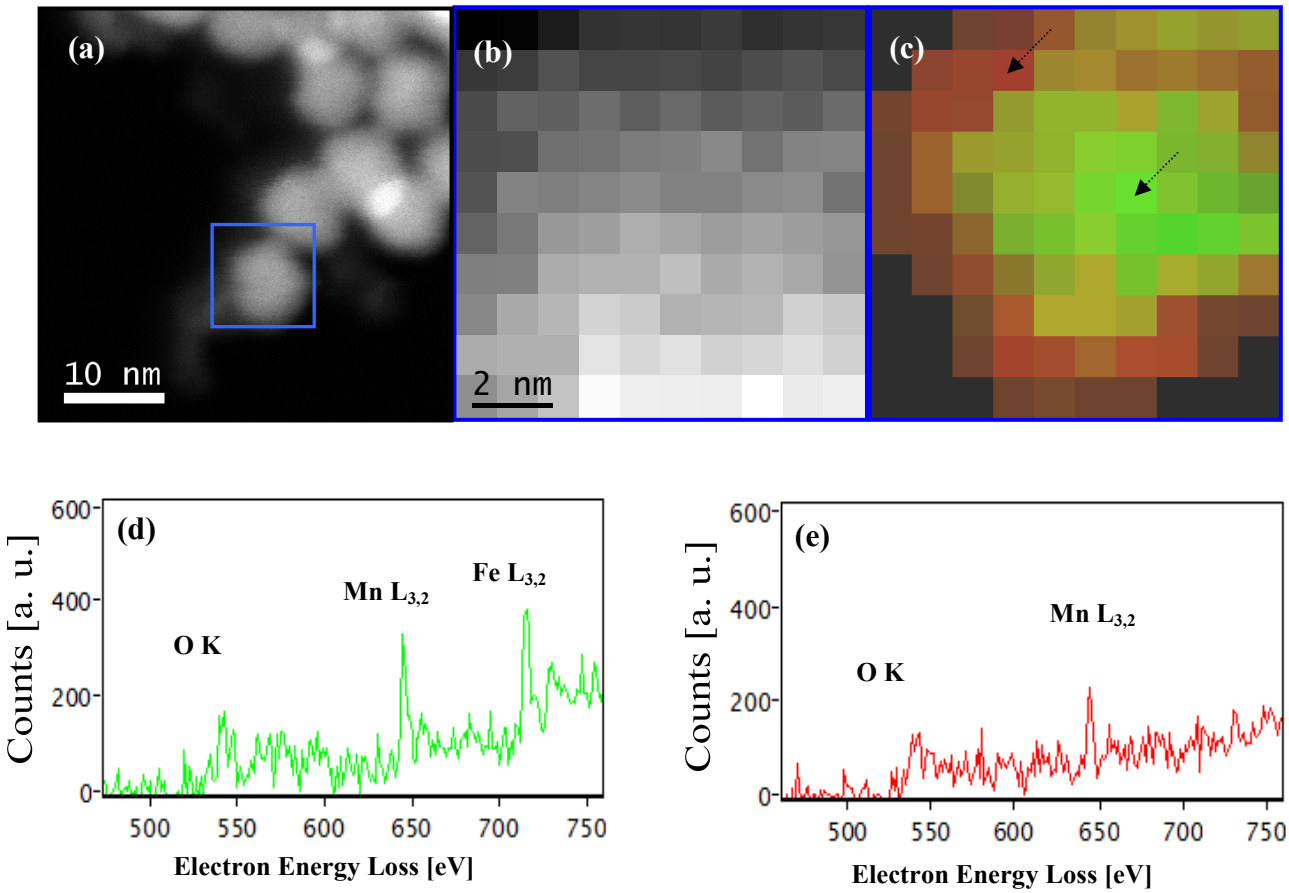

Figure 4.2.7: *(a) HAADF image of several core-shell nanoparticles. (b) Spectrum Image obtained in the highlighted zone in (a). MLLS fitting of (b) using spectra (d) and (e) as a reference –it can be understood as a mapping of the regions containing both Fe and Mn (green) and Mn only (red). (d), (e) EEL Spectra obtained at the indicated points in (c).*

Further quantitative EELS analysis has been carried out to better understand the structure of the nanoparticles. EELS data obtained from spectrum lines across several nanoparticles show that Mn oxidation state is 3+ at the outer part of the particles (i. e.: where no Fe signal is found) and decreases moderately towards the centre of the particles (figure 4.2.8). Mn, Fe and O elemental quantification through several nanoparticles (also given in figure 4.2.8) evidences the pure MnO_y outer layer to be about 1nm thick. In addition, it is clear from elemental quantification data that there must be some additional Mn in the core of the nanoparticles.

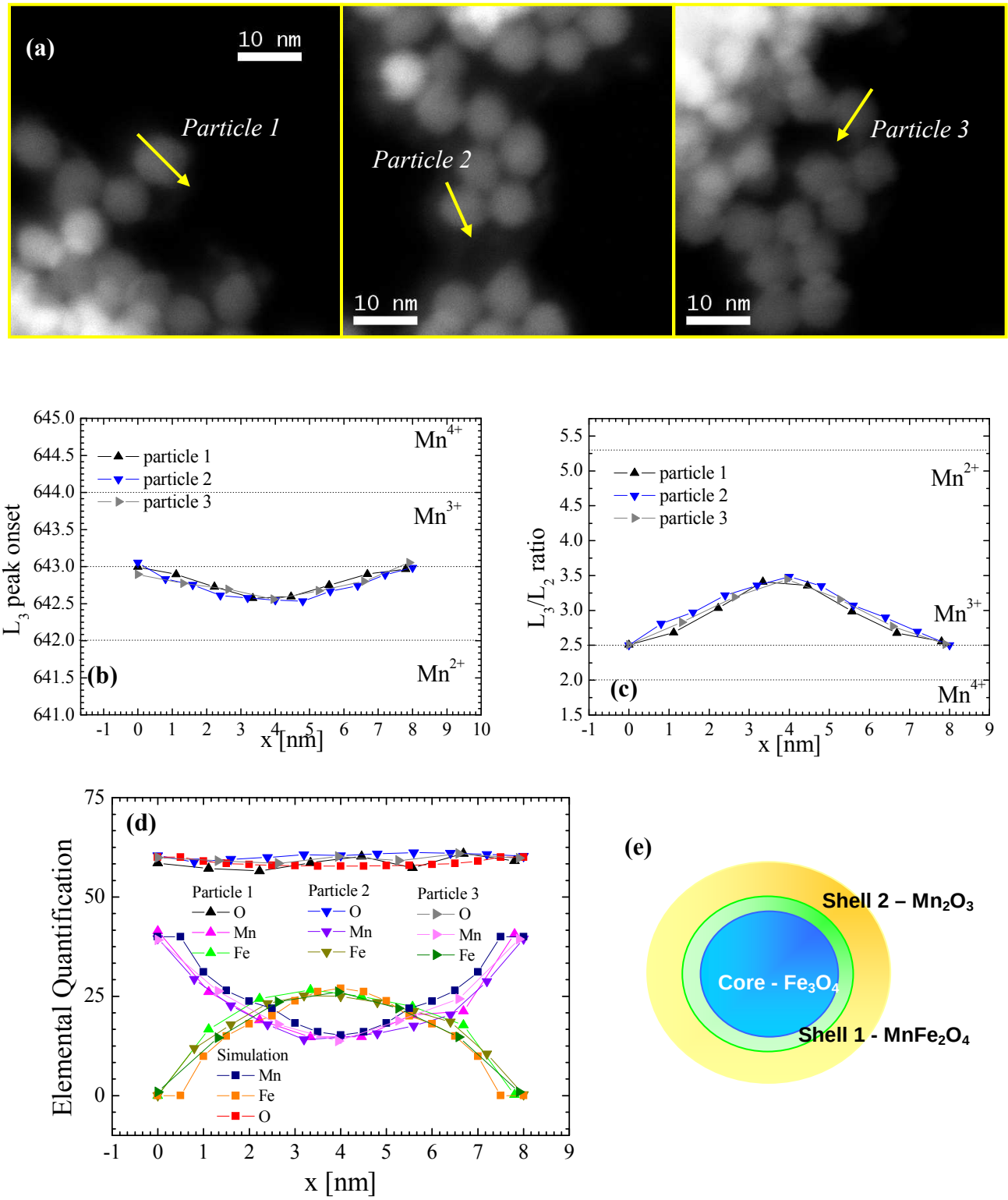

Figure 4.2.8: *(a) HAADF images of several core-shell nanoparticles. (b)L_3 peak position and (c) Mn L_3/L_2 intensity ratio along the lines highlighted in the HAADF images, for the three considered nanoparticles. (d) Elemental quantification for the three considered particles, and simulation considering a 2nm thick a $MnFe_2O_4$ spinel around a Fe_3O_4 core. L_3 peak chemical shift and L_3/L_2 intensity ratio, as well as elemental quantification are subjected to a relative error of about 5%. (e) Cartoon of the structure of a nanoparticle.*

In this sense, the presence of a mixed phase containing Mn, Fe and O must be considered. Both a $MnFe_2O_4$ and a $FeMn_2O_4$ middle layer seem plausible. Taking the composition and the thickness of the mixed phase and the composition of the Fe oxide as parameters to simulate, out of geometric considerations, the obtained, projected EELS data, the best fit of the elemental composition experimental data has been achieved for a $MnFe_2O_4$ spinel about 2 nm thick around a Fe_3O_4 core (figure 4.2.8).

The overall system would then correspond to tri-magnetic hetero-onion nanoparticles composed by core-Fe_3O_4 (FiM)/shell1-$MnFe_2O_4$ (FiM)/shell2-Mn_2O_3 (FiM).

4.2.4 Conclusions

The capability of EELS to determine the composition of MnO_x/MnO_y, FeO_x/FeO_y and FeO_x/MnO_y nanoparticles has been demonstrated. MnO/Mn_2O_3, with and additional MnO thin outer layer, and FeO/Fe_3O_4 core-shell particles were observed: in both systems the coupling between the AFM-core and FiM-shell is to lead to strong exchange bias effects. Nominal FeO_x/MnO_y onion-like structures were in fact found out to be tri-magnetic hetero-onion nanoparticles composed by core-Fe_3O_4 /shell1-$MnFe_2O_4$/shell2-Mn_2O_3.

4.2.5 References

1. Sort, J., Nogués, J., Suriñach, S., Muñoz, J.S., Baró, M.D., Chappel, E., Dupont, F., Chouteau, G.., Applied Physics Letters 79, 1142 (2001)
2. Sort, J., Suriñach, S., Muñoz, J.S., Baró, M.D., Nogués, J., Chouteau, G., Skumryev, V., Hadjipanayis, G.C., Physical Review B 65, 174420 (2002)
3. Skumryev, V., Stoyanov, S., Zhang, Y., Hadjipanayis, G., Givord, D., Nogués, J., Nature 423, 850 (2003)
4. Eisenmenger, J., Schuller, I.K., Nature Materials 2 437 (2003)
5. Nogués, J., Sort, J., Langlais, V., Skumryev, V., Suriñach, S., Muñoz, J.S., Baró, M.D., Physics Reports 422, 65 (2005)
6. Rivero, J.M., De Toro, J.A., Andrés, J.P., González, J.A., Muñoz, T., Goff, J.P., Applied Physics Letters 86, 172503 (2005)
7. Koch, S.A., Palasantzas, G., Vystavel, T., De Hosson, J.T.M., Binns, C., Louch, S., Physical Review B 71, 085410 (2005)
8. Löffler, J.F., Meier, J.P., Doudin, B., Ansermet, J.P., Physical Review B 57, 2915 (1998)
9. Seto, T., Akinaga, H., Takano, F., Koga, K., Orii, T., Hirasawa, M., Journal of Physical Chemistry B 109, 13403 (2005)
10. Jeyadevan, B., Chinnasamy, C.N., Perales-Perez, O., Iwasaki, Y., Hobo, A., Shinoda, K., Tohji, K., Kasuya, A., IEEE Transactions on Magnetism 38, 2595 (2002)
11. Luna, C., del Puerto Morales, M., Serna, C.J., Vázquez, M., Nanotechnology 15, S293 (2004)
12. Ennas, G., Falqui, A., Marras, S., Sangregorio, C., Marongiu, G., Chemistry of Materials 16, 5659 (2004)
13. Li, X.G., Murai, T., Saito, T., Takahashi, S., Journal of Magnetism and Magnetic Materials 190, 277 (1998)
14. Slawska-Waniewska, A., Roig, A., Gich, M., Casas, L., Racka, K., Nedelko, N., Molins, E., Physical Review B 70, 054412 (2004)
15. Zheng, R.K., Wen, G.H., Fung, K.K., Zhang, X.X., Physical Review B 69, 214431 (2004)
16. del Bianco, L., Fiorani, D., Testa, A.M., Bonetti, E., Signorini, L., Physical Review B 70, 052401 (2004)

17. Theil Kuhn, L., Bojesen, A., Timmermann, L., Fauth, K., Goering, E. Johnson, E., Meedom Nielsen, M., Zrup, S.M., Journal of Magnetism and Magnetic Materials 272–276, 1485 (2004)
18. Theil Kuhn, L., Bojesen, A., Timmermann, L., Meedom Nielsen, M., Zrup, S.M., Journal of Physics: Condensed Matter 14, 13551 (2002)
19. Bonetti, E., Savini, L., Deriu, A., Albanese, G., Moya, J., Journal of Magnetism and Magnetic Materiañs 262, 132 (2003)
20. Dormann, J.L., Fiorani, D., Tronc, E., Advances in Chemical Physics 98, 283 (1997)
21. Jönsson, P.E., Advances in Chemical Physics 128, 191 (2004)
22. Salazar-Alvarez, G., Sort, J., Suriñach, S., Baro, M.D., Nogues, J., Journal of the American Chemical Society 129, 9102 (2007)
23. Berkowitz, A.E., Rodriguez, G.F., Hong, J.I. An, K., Hyeon, T., Agarwal, N., Smith, D.J., Fullerton, E.E., Physical Review B 77, 024403 (2008)
24. Berkowitz, A.E., Rodriguez, G.F., Hong, J.I. An, K., Hyeon, T., Agarwal, N., Smith, D.J., Fullerton, E.E., Journal of Physics D: Applied Physics 41, 134007 (2008)
25. Djerdj, I., Arcon, D., Jaglicic, Z., Niederberger, M., Journal of Physical Chemistry C 111, 3641 (2007)
26. Kavich, D.W., Dickerson, J.H., Mahajan, S.V., Hasan, S.A., Park, J.-H., Physical Review B 78, 174414 (2008)
27. Liu, W., Zhong, W., Du, Y.W., Journal of Nanoscience and Nanotechnology 8, 2781 (2008)
28. Estrader, M., López-Ortega, A., Salazar-Alvarez, G., Tobia, D., Winkler, E., Estradé, S., Golosovsky, I., Sort, J., Arbiol, J., Peiró, F., Suriñach, S., Zysler, R.D., Baró, M.D., Nogués, J., Abstract, Trends in Nanotechnology (2009)
29. López-Ortega, A., Estrader, M., Salazar-Alvarez, G., Estradé, S., Sort, J., Arbiol, J., Peiró, F., Suriñach, S., Baró, M.D., Nogués, J., Abstract, Trends in Nanotechnology (2009)
30. Kurata, H., Colliex, C., Physical Review B, 48, 2102 (1993)
31. Garvie, L.A.J., Craven, A.J., Ultramicroscopy 54, 83 (1994)
32. Schmid, H.K., Mader, W., Micron 37, 426 (2006)
33. Estradé, S., Arbiol, J., Peiró, F., Abad, L., Laukhin, V., Balcells, L., Martínez, B., Applied Physics Letters 91, 252503 (2007).
34. Estradé, S., Arbiol, J., Peiró, F., Infante, I.C., Sánchez, F., Fontcuberta, J., de la Peña, F., Walls, M., Colliex, C., Applied Physics Letters 93, 112505 (2008).

35. Estradé, S., Rebled, J.M., Arbiol, J., Peiró, F., Infante, I.C., Herranz, G., Sánchez, F., Fontcuberta, J., Córdoba, R., Mendis, B.G., Bleloch, A.L., Applied Physics Letters, 95, 072507 (2009)

5. Quantitative core-loss EELS applied to manganites

5.1 Introduction

5.1 Introduction

5.1.1 The physics of manganites

The manganites are a family of perovskite oxides in which the composition of the A-site (and B-site as well) cations may be varied by using mixtures of trivalent rare-earth and divalent alkaline-earth elements. In La manganites, a correlation between doping-induced electrical conductivity and ferromagnetism can be observed. Whilst the three-component materials $LaMnO_3$ and $AMnO_3$, where A is a divalent alkaline-earth, are antiferromagnets (AFMs) with spins localized at the sites occupied by the manganese ions, the four-component manganites $La_{1-x}A_xMnO_3$ with intermediate compositions ($0.2<x<0.5$) not only become strong ferromagnets but also manifest conductivity of the metallic type, which is observed only below the Curie temperature T_C. The phase diagram of $La_{1-x}Ca_xMnO_3$ is given in figure 5.1.1.

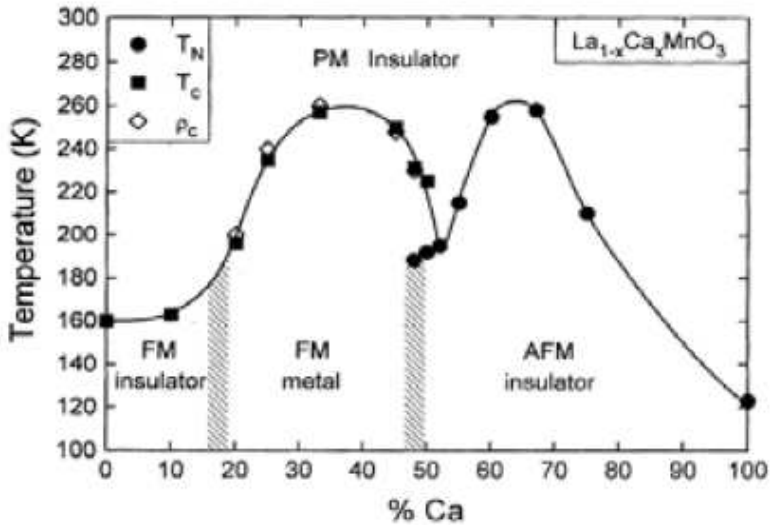

Figure 5.1.1: *Phase diagram of $La_{1-x}Ca_xMnO_3$[1]. Neel temperature T_N for the antiferromagnetic (AFM) phases, Curie temperature Tc for the ferromagnetic (FM) phases and insulator to metal transition temperature ρ_c are shown.*

Each manganese (Mn) ion in the perovskite is surrounded by an oxygen octahedron (figure 5.1.2). The 3d orbitals on the Mn-site are split into the lower-lying t_{2g} triplet and the higher-lying e_g doublet (figure 5.1.3)[6]. In the Mn^{3+} compounds, the Mn site has the following electronic configuration: $t^{3}_{2g}e^{1}_{g}$ (total spin number S = 2). The t_{2g} electrons, less hybridized with O 2p states and more stabilized by the crystal field splitting, are understood as being localized and as forming the local spin (S = 3/2), and the e_g electrons as the charge carriers. Yet, the e_g electrons are localized as the hopping interaction is relatively small. Even though the e_g states are more strongly hybridized with the O 2p states, there is still a strong electron correlation. In addition, the Jahn–Teller coupling of the e_g electron with the surrounding oxygen displacement also contributes to the electron localization (The Jahn–Teller coupling lifts the degeneracy of the e_g orbital by causing the deformation of the MnO_6 octahedra[7]). When the e_g band filling is close to 1, the individual Jahn–Teller distortions are cooperatively induced, leading to symmetry lowering of the lattice or a new superstructure. Thus, the orbital ordering in the manganites is always associated with the cooperative Jahn–Teller distortion.

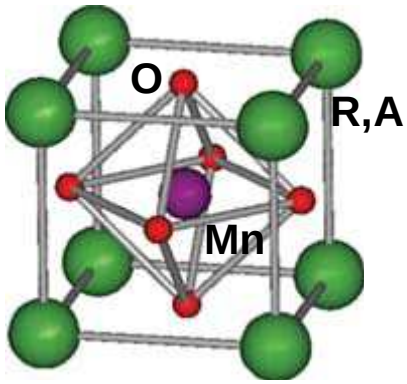

Figure 5.1.2: *Perovskite structure of doped manganites, (R,A)MnO_3, with trivalent (3+) rare-earth (R) ions and divalent (2+) alkaline-earth (A) ions at the perovskite A site and Mn on the perovskite B site.*

When electron vacancies or holes are created in the e_g orbital states of the crystal and escape from the long-range ordering, the e_g electrons can be itinerant and hence play the role of conduction electron. The latter hole-doping procedure corresponds to the creation of mobile Mn^{4+} species on the Mn sites (as it is achieved by doping a trivalent rare-earth manganite with a divalent alkaline-earth).

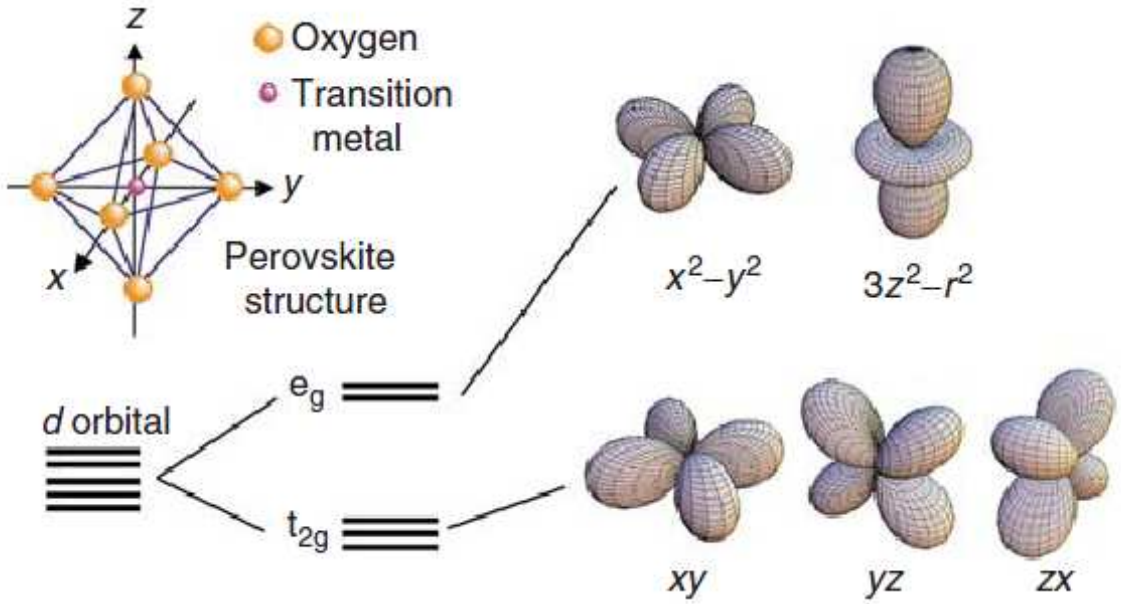

Figure 5.1.3: *Mn d-electron orbitals and level splitting when in octahedral coordination with O^{2-}.*

The important consequence of the separation of the 3d orbital into the local-spin and charge components is the strong coupling between the e_g conduction electron spin (S = 1/2) and the t_{2g} electron local spin (S = 3/2). This ferromagnetic coupling follows Hund's rule.

By creating electron-vacancy sites (or hole-doping) the e_g electron can hop depending on the relative configuration of the local spins. The ferromagnetic metallic state is stabilized by maximizing the kinetic energy of the conduction electrons. When the temperature is raised to near or above the ferromagnetic transition temperature (T_C), the configuration of the spin is dynamically disordered and accordingly the effective hopping interaction is also subject to disorder and is reduced on average. This would lead to enhancement of the resistivity near and above T_C. Therefore, a large (Colossal) MR can be expected around T_C, since the local spins are relatively easily aligned by an external field achieving a reduction of the randomness of the spin configuration. This is the intuitive explanation of the CMR observed for manganites around T_C in terms of the double-exchange (DE) model.

The hopping of the e_g electrons from Mn^{3+} to O^{2-} and finally to Mn^{4+} creates degenerate couples of $Mn^{3+/4+}$-O^{2-}- $Mn^{3+/4+}$, so that the overall Mn oxidation state is a mixture of Mn^{3+} and Mn^{4+} rather than a local alternation between Mn^{3+} and Mn^{4+}.

It is clear that the mobility of the e_g carriers is greatly dependent on the nature of the Mn-O-Mn bonding; in particular, the width of the e_g band depends on the Mn-O angle (with 180º being the optimal configuration) and on the Mn-Mn distance[8]. As a matter of fact, isolated Mn^{3+} and Mn^{4+} atoms are naturally antiferromagnetically coupled. If the e_g bandwidth is reduced, and the double exchange mechanism is weakened, ferromagnetism is easily lost in the material.

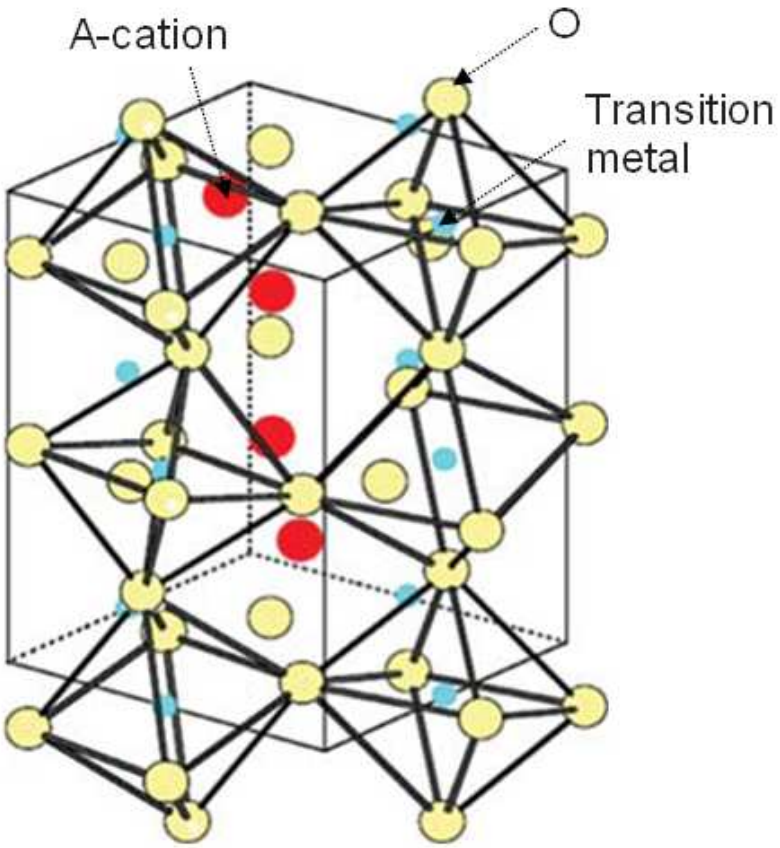

Figure 5.1.4: *Orthorhombically distorted (pseudocubic) perovskite structure.*

Bulk doped manganite perovskites may show lattice distortions -modifications from the cubic structure. Orthorombic distortion is shown in figure 5.1.4. These distortions may be due to the deformation of the MnO_6 octahedra arising from the Jahn–Teller effect as explained above. In these distorted perovskites, the MnO_6 octahedra show alternating buckling. Such lattice distortions quite trivially affect the Mn-O angle and the Mn-Mn distance, effectively reducing the e_g bandwidth. Of course, when growing these perovskites as thin films on a given substrate, additional lattice deformations may arise from strain conditions.

5.1.2 Functional applications of manganites and associated problems.

A number of functional devices using manganites have been successfully implemented[5]. Epitaxial tunnel junctions[9] made from FMM electrodes of (La,Sr)MnO_3 or (La,Ca)MnO_3 with an ultrathin $SrTiO_3$ barrier were reported in the mid 90s. Subsequent improvements[10,11] have achieved a magnetoresistance (MR) switching with a magnitude in the order of 1000%.

Recent improvements in performance are based on interface engineering[9-17]. The interface properties are tailored by choosing insulators of perovskite or rutile structure, by using perovskite insulators with different structural mismatch with the electrode or by varying the nominal charge of the electrode.

MR devices may also be obtained without a tunnel barrier, by growing a bilayer comprising a manganite and some other FMM material such as magnetite[18] or permalloy[19].

Additionally, MR devices may be obtained using FMM manganite electrodes widely separated by organic materials. This can be achieved because carbon has a low atomic number and therefore weak spin-orbit coupling, which allows spin-polarized electrons to get through the organic material without losing their magnetic information. For example, submicron layers of an organic semiconductor between $La_{0.67}Sr_{0.33}MnO_3$ and Co electrodes allow the implementation of devices that show a low-temperature giant magnetoresistance effects as large as 40%[20].

In this sense, carbon nanotubes (CNTs) have been reported to allow the transport of spin information over a distance of 1.5 μm between $La_{0.7}Sr_{0.3}MnO_3$ electrodes[21]. The conversion of magnetic information into large electrical signals corresponds to an MR of 61%, and represents the basis for a spin transistor if the nanotube can be suitably gated. The advantage of a spin transistor is that the use of a magnetic gate would permit nonvolatile information storage.

To integrate manganites in the aformentioned functional devices, the implementation of epitaxial thin films heterostructures of these materials is clearly a necessary condition. As a consequence, the physics of doped manganites cannot be fully taken advantage of, as the

properties of thin films of these materials are depleted when compared to their bulk counterparts. In particular, in thin films conduction, T_C and saturation magnetisation (M_S) are significantly reduced and both ferromagnetism and conductivity may be altogether suppressed[22-27].

In fact, the reasons for this strong degradation of magnetotransport properties remain mostly unknown and are believed to be manifold. For instance, the existence of a magnetic dead layer has been postulated[22]. MNR experiments have allowed correlating the reduced properties of manganite films to the nucleation of regions with different magnetic and electronic states, which make the film electronically and magnetically inhomogeneous[23,28-30]. The origin and nature of this electronic phase separation remain unclear. Both strain itself and elastic strain relaxation due to the substrate/film mismatch have been suggested as possible causes of the depleted magnetic properties, as, not surprisingly, greater lattice mismatch figures are correlated to a greater hindering of the films performance[31].

The thin films properties thus depend not only on the growth parameters (such as temperature, pressure, growth rate) but also on the employed substrate. The most commonly used substrates for $La_x(Ca,Sr)_{1-x}MnO_3$ manganites are cubic $SrTiO_3$ (STO, a = 0.3905 nm)[32-35], pseudocubic $LaAlO_3$ (LAO, a = 0.3788 nm)[36-38], and cubic MgO[39-40] (a = 0.4205 nm).

Lattice mismatch δ along the interface is defined by $\delta = (a_p \text{ substrate} - a_p \text{ bulk manganite})/a_p$ substrate, where a_p is the pseudocubic (or cubic) lattice parameter. Positive values of mismatch correspond to tensile strains (the cell is elongated in the film plane), whereas negative values correspond to compressive stresses (the cell is compressed in the film plane).

In this chapter, we will consider thin films of $La_{2/3}Ca_{1/3}MnO_3$ (LCMO) manganite, grown on STO and LAO substrates. LCMO is orthorhombic, with lattice parameters a = 0.5453nm, b = 0.7672 nm and c = 0.5447 nm. It can be considered pseudocubic, and the pseudocubic lattice parameter would then be $a_p = 0.3863 \text{ nm} \approx a/\sqrt{2} \approx c/\sqrt{2} \approx b/2$. Whereas LCMO on STO grows under a tensile, moderate strain (lattice mismatch ≈1.2 %) allowing to get a defect-free epitaxy, the LCMO on LAO, grows under a compressive, greater strain (lattice mismatch ≈ -1.8 %).

The substrate mismatch strain induces a lattice deformation in the layer, which is generally measured using x-ray diffraction (XRD) and reciprocal space maps (RSM)[31,41-43]. TEM can also be used to measure changes in lattice parameter[44,45]. In addition, TEM is generally used to assess the quality of the interfaces, investigate the presence of defects in the layer and observe whether local changes in crystal structure take place or not[46-49].

Moreover, if TEM is combined with EELS, then local deviations in stoichiometry can be detected[50-54], and the Mn oxidation state can be inferred from local EELS data[50-53]. The latter is of the outmost importance, as it gives a means to probe phase separation in manganites at the nanoscale, which can be correlated with their macroscopic magnetic behaviour.

In summary, the rich physics of manganites make them display unique conduction and magnetic properties and assign them the potentiality to become building blocks in the rapidly developing field of spintronics, but also make them behave in ways that are not yet fully understood, and in particular, make their properties highly dependent on substrate nature, film thickness and growth conditions. The combination of (S)TEM-EELS techniques allows to investigate the existence of crystalline defects or structural changes, the chemical composition and the Mn oxidation state at the nanoscale, and, in favourable cases, to correlate these nanoscale properties with the macroscopic behaviour of the considered materials. It is thus clear that careful (S)TEM-EELS characterization of manganite thin films seems bound to unveil relevant and (as it often seems happens when manganites are involved) surprising results.

5.2 EELS of Mn and Mn oxidation state determination

5.2 EELS of Mn and Mn oxidation state determination

5.2.1 Mn $L_{3,2}$ white lines

$L_{2,3}$ edges of transition metals (as well as $M_{4,5}$ edges of rare earths) consist of two so called white line peaks close to the ionisation energy[55]. The white line name is quite trivially due to the fact that, in the raster image of the EELS spectrum, the peaks appear as two vertical white lines.

The energy separation between the two peaks is given by the spin-orbit splitting of the initial (ground) states of the transition. On the other hand, one would expect their relative intensities to correspond to the number of electrons in the initial states provided that the matrix elements and final densities of states were the same for all electrons –this rather intuitive picture happens to be wrong. In fact, the influence of a spin selection rule results in a white line intensity ratio which depends on the number of electrons in the final 3d (or 4f) state. Thus, the white line intensity ratio varies with atomic number Z, and with the oxidation state in a quite non-trivial manner. In the case of Mn, the L_3/L_2 intensity ratio decreases with oxidation state, but not lineally.

The ionization threshold energy in EELS represents the difference in energy between the core-level ground state and the lowest energy final state. In the case of a compound, any increase in the binding energy of a core level, relative to its value in the pure element, gives rise to a change in threshold energy, and thus, to a chemical shift of the edge. Yet, other factors contribute to the magnitude of this chemical shift. Quite trivially, the energy of the lowest energy final state also depends on the nature of the studied compound. In addition, core-hole effects involved in the electron transition further complicate the whole picture.

The chemical shift is in the order of ~ 1 eV, in general. In the case of Mn, L_3 peak onset lies at 640 eV. Yet, in manganese oxides, L_3 peak onset is found between 642 and 644 eV, with a chemical shift that monotonously increases with increasing oxidation state. Mn $L_{3,2}$ edge spectra, obtained by Kurata and Colliex[56] for five different considered oxides, after deconvolution of multiple loss scattering and background substraction, are given in figure 5.2.1.

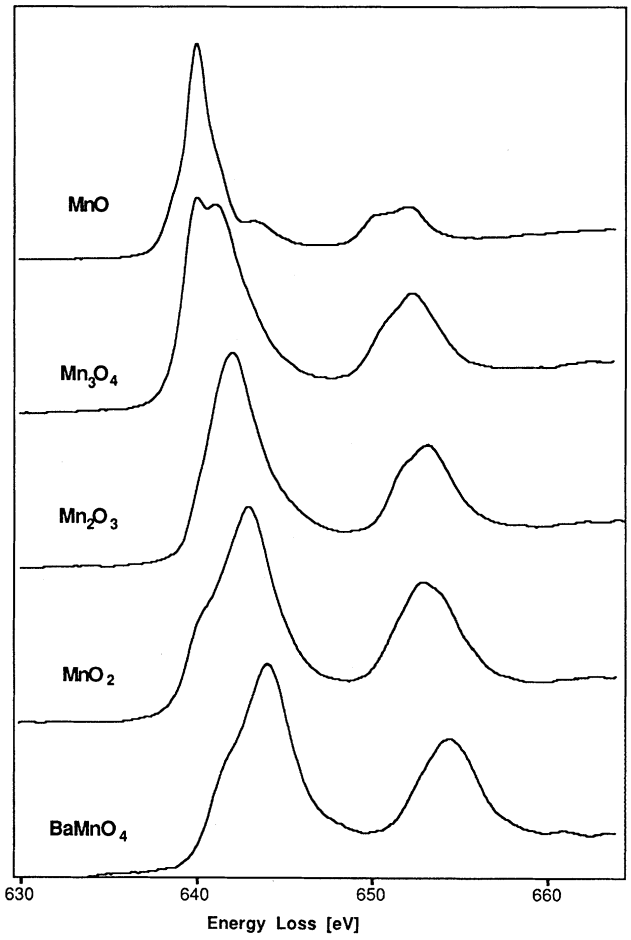

Figure 5.2.1: *Mn $L_{3,2}$ edge spectra, obtained by Kurata and Colliex[56] for five different considered oxides, after deconvolution of multiple loss scattering and background substraction*

One final remark: as Mn L_3 peak appears lower in energy than M L_2 peak, the Mn $L_{3,2}$ notation is usually preferred to the, in principle, more obvious, Mn $L_{2,3}$ one.

5.2.2 Mn oxidation state quantification

It is clear that both the Mn L_3 peak onset and the L_3/L_2 intensity ratio are measures of the Mn oxidation state. Yet, it is also clear that it is very difficult to correlate these measures with the actual Mn oxidation state from physical calculations. There are two ways around this difficulty: using specimens of well-known Mn oxidation state as standards, or comparing the experimentally obtained L_3 peak onsets and L_3/L_2 intensity ratios with the figures given in the literature for the different Mn oxidation states.

In fact, in a certain way, the two procedures were used in the present Thesis. Specimens of well-known Mn oxidation state (Mn oxidation state = 3.3) were considered for sanity-check experiments: if the values obtained for the Mn L_3 peak onset and the L_3/L_2 intensity ratio in this case were in good agreement with those given in the literature, then the procedure used to calculate the Mn L_3 peak onset and the L_3/L_2 intensity ratio from the EELS spectra was sound and could be used to obtain experimental data of problem samples that could then be compared with the values given in the literature.

The reference values for the Mn L_3 peak onset and the L_3/L_2 intensity ratio were taken from Kurata and Colliex[56], which are in good agreement with those given by Garvie and Craven[57], and mostly in good agreement also with those given much more recently by Schmid and Garvie[58]. Reference values of Mn L_3 peak onset and L_3/L_2 intensity ratio vs. Mn oxidation state are given in figure 5.2.2[59].

$La_{2/3}Ca_{1/3}MnO_3$ (LCMO) target material for the growth of LCMO layers was used for the sanity check experiments. The material was kindly provided by Dr. Llibertat Abad, then a PhD student at ICMAB. Several samples were prepared by mixing the LCMO powder with ethanol, dispersing it with ultrasounds and letting one drop of the dispersed mixture fall on a holey carbon grid. Quite nicely, the mean value of L_3/L_2 ratio was found to be 2.25, with a standard deviation of 0.11 and the mean value of L_3 onset was found to be 643.4 eV with a standard deviation of 0.5 eV.

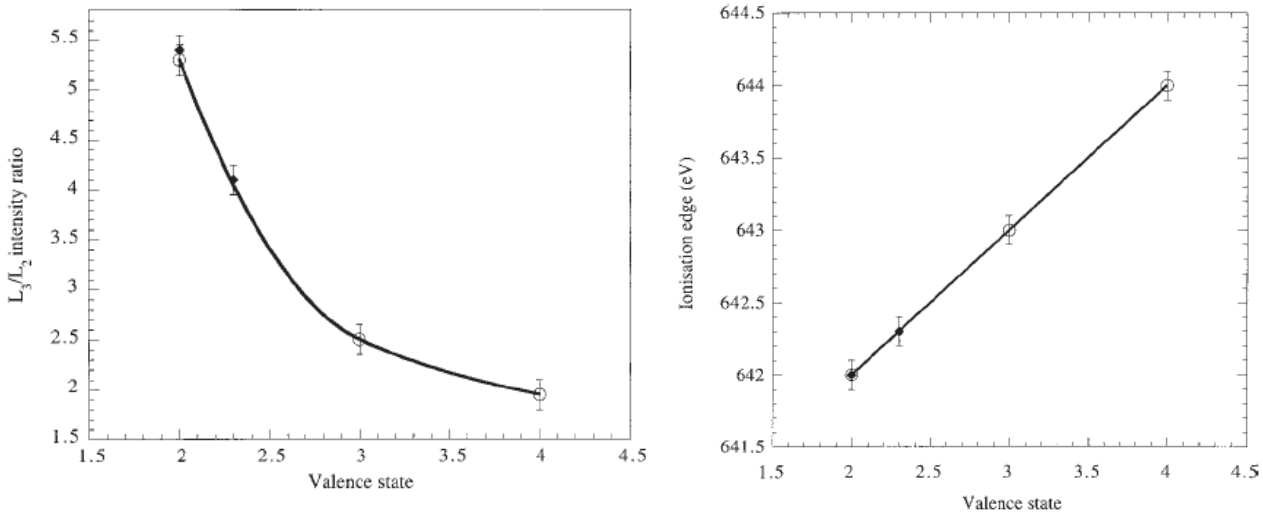

Figure 5.2.2: *Reference values of L_3/L_2 intensity ratio and Mn L_3 peak onset vs. Mn oxidation state.*

The procedure to determine the Mn oxidation state in a problem sample would be as follows: obtain a spectrum containing the Mn $L_{3,2}$ edges. Then obtain a low-loss spectrum of the very same region. Deconvolute the low-loss spectrum from the core-loss spectrum to get rid of multiple scattering. Correct the energy scale. Fit and subtract pre-peak background and continuum contributions. Find L_3 peak onset, and calculate L_3 and L_2 intensities. Compare the Mn L_3 peak onset and the L_3/L_2 intensity ratio with the values given in the literature.

There are quite a lot of calculations that should be carried out in a repetitive, systematic manner. Besides, this may be a tedious and thus error inducing procedure in the case of large spectrum lines or spectrum images. Thus, a software package to calculate the Mn L_3 peak onset and the L_3/L_2 intensity ratio was developed in the frame of the present work.

5.2.3 The MANGANITAS software

MANGANITAS is a Matlab-based software package. It deals with spectrum lines (or individual spectra) only. It was generalized in MANGANITAMatrix, which can operate with 2-dimensional spectrum images, but the generalization has been given little practical use so far because the studied manganite thin films happened to show no local variations in Mn oxidation state in the in-plane direction, and thus spectrum lines along the z direction seemed to be the most sensible data collection geometries.

MANGNITAS does not perform low-loss deconvolution, as Digital Micrograph does it quite easily, and quite fast. The low-loss deconvoluted experimental spectrum line file is to be saved as .txt and imported into the Matlab workspace. Then MANGANITAS can be called. MANGANITAS reads the .txt files, performs the appropriate calculations and returns posL and Ratio .out files. posL and Ratio contain the L_3 onset position and the L_3/L_2 intensity ratio as a function of spectrum ordinal, respectively.

As for the calculations themselves, the software locates a reference edge and recalibrates the energy axis of each individual spectrum using this edge as a reference (in the case of LCMO, La $M_{5,4}$ white lines appear to be a safer choice than O K, as in O K chemical shift may be significant). Then, it performs a fitting of the pre-peak background using a power-law fit function and subtracts it. Transitions to continuum are fitted via a step function and subtracted as well. Gaussian curves are fitted to both Mn L_3 and Mn L_2 peaks. Mn L_3 onset is established to be at half the height of the peak, as conventionally accepted. The area under the gaussian curves (I_3 and I_2) is integrated and I_3/I_2 is calculated.

5.3 LCMO/LAO

5.3 LCMO/LAO

5.3.1 Introduction

The strain conditions of manganite thin films can be tuned by choosing the appropriate substrate. Let us consider LCMO layers grown on (001) LAO substrates: as already explained, LCMO grows on LAO under a compressive strain of about -1.8%.

The present section will focus on the careful study of the microstructure and the local chemistry and Mn oxidation state of LCMO/LAO films prepared using RF-sputtering, as a function of thickness, both in as-grown (AG) and annealed samples.

5.3.2 Experimental details

LCMO layers were grown by RF-sputtering on top of (001) LAO substrates with nominal thicknesses ranging from 14 to 93 nm at a deposition temperature of 800ºC, a deposition pressure of 330 mtorr, and an O2/Ar pressure ratio of 1/4; afterwards, they were submitted to an in situ annealing process in an O_2 atmosphere at a pressure of 350 torr and at a temperature of 800ºC for 60 minutes[60]; every such sample was annealed at Ta=1000ºC, also keeping an as grown (AG) sample for comparison. Magnetic properties were measured by using a commercial SQUID magnetometer from Quantum Design.

Samples were provided by Llibertat Abad and coworkers at ICMAB (Campus de Bellaterra). They also carried out the XRD analysis and the magnetic measurements.

The samples, prepared in cross section geometry by flat polishing down to 50 μm, followed by a dimpling down to 25 μm and a final Ar+ bombardment at V=5 kV with an incident angle of 7° using a PIPS-Gatan equipment, were observed by HRTEM in a Jeol J2010F microscope, with field emission gun, operating at 200 keV. EELS spectra were obtained with a Gatan Image Filter (GIF) spectrometer. Notice that all the EELS data in the present chapter were obtained *before* the STEM unit was installed in the TEM.

Ca/La normalized relative concentration variations were obtained from EELS spectra by integrating the intensity corresponding to Ca and La peaks, getting the relative intensity for each studied point and dividing such figure by the value obtained in a reference position, that was chosen to be the one closest to the interface. Mn L_3 EELS peak edge and Mn L_3 / Mn L_2 peak intensity ratio were determined using the aforementioned software package MANGANITAS.

5.3.3 XRD and magnetic measurements data

As previously mentioned LCMO grows on LAO under compressive strain (~-1.8 %) leading to higher values of the out-of-plane lattice parameter, c, than would be found in the bulk material. XRD measurements (table 5.3.1) clearly show that out-of-plane c parameter decreases while in-plane a parameter increases, after annealing processes and/or when increasing film thickness, approaching bulk values as in-plane stress gradually relaxes.

	TEM determined c [Å]		*XRD determined c [Å]*		*TEM determined a [Å]*		*XRD determined c [Å]*	
t [nm]	*As grown*	*Annealed*	*As grown*	*Annealed*	*As grown*	*Annealed*	*As grown*	*Annealed*
14 n	*3.94*	*3.88*	*3.957*	*3.878*	*3.82*	*3.83*	*3.793*	*3.865*
48 n	*3.91*	*3.85*	*3.920*	*3.868*	*3.82*	*3.88*	*3.793*	*3.857*
90 n	-	*3.85*	*3.897*	*3.870*	-	*3.86*	*3.820*	*3.853*

Table 5.3.1: *In-plane, a, and out-of plane, c, LCMO lattice parameters of LCMO/LAO samples determined by TEM and XRD as a function of layer thickness t.*

The elongation of the unit cell along the z axis should induce an easy magnetization axis perpendicular to the film plane. The departure of the easy magnetization axis from perpendicular to film plane to parallel to plane has been observed as structural strain relaxes by increasing film thickness or by high temperature annealing processes, in good agreement with literature[61]. On the other hand, both saturation magnetization M_S, and T_C exhibit a clear dependence on sample thickness (figure 5.3.1). In this figure it is also shown that the high temperature annealing process substantially improves magnetic properties, and that this improvement is notoriously stronger in thinner samples. At first sight this evolution of T_C and M_S could be correlated with variations of structural strain; nevertheless, as pointed out by A. Biswas and coworkers[62,63], the LCMO/LAO system exhibits a 3D growth mechanism from the early stages leading to a granular character of the films and making it very difficult to obtain a homogeneously strained film. Besides, in-plane biaxial compression, as in LCMO/LAO system, should imply an expansion of the out-of-plane parameter because of the Poisson effect leading to a flattening of the Mn-O-Mn angle, thus promoting a reduction of the Jahn-Teller effect and the increasing of T_C[64], which is not observed in our case. Therefore, we should conclude that structural strain alone cannot account for the variations of T_C and M_S.

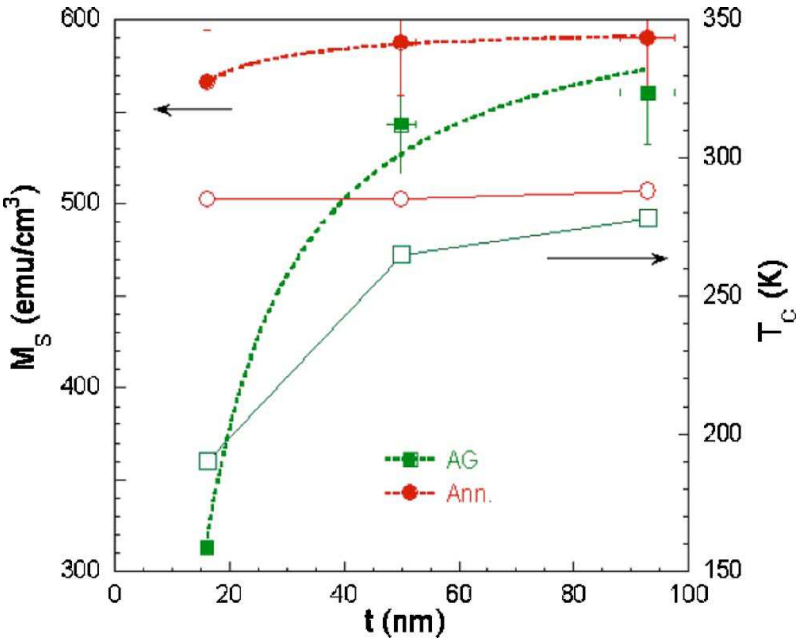

Figure 5.3.1: *Saturation magnetisation and dependence of the transition temperature, T_C, as a function of sample thickness for as-grown and annealed samples.*

5.3.4 Results and discussion

HREM images of AG (a) and annealed (b) 14 nm thick samples along [100] zone axis are shown in Fig. 5.3.2. Abrupt, flat and homogeneous interfaces between LCMO film and LAO substrate, and LCMO free surfaces were found in the thinnest AG samples (figure 5.3.2). Nevertheless, interfaces between LCMO film and LAO substrate, and LCMO free surfaces, were found to get slightly rougher as layer thickness increases and with the annealing treatment. The layers were determined to be homogeneous and defect-free at least in the studied region, with mosaicity increasing again with thickness and after annealing treatments.

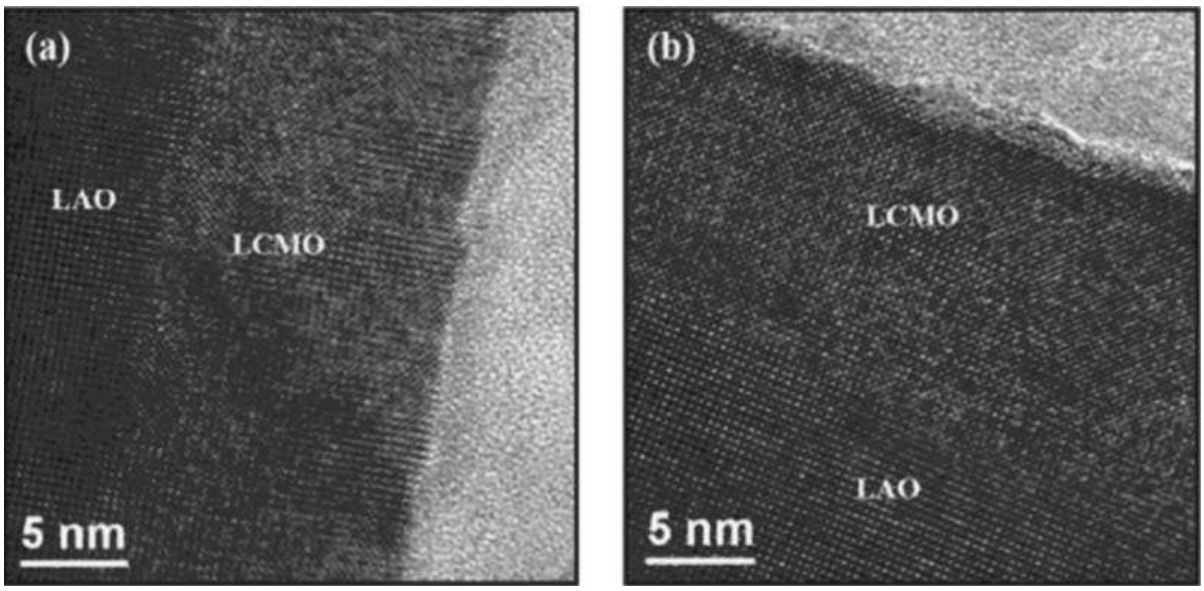

Figure 5.3.2: *High resolution images of as grown (a) and annealed (b) 14 nm thick samples along [100] zone axis.*

The nominal epitaxial relationship LCMO (001)[100]//LAO(001)[100] was found, by fast Fourier transform (FFT) of high resolution images of layer and substrate, for all studied samples. High resolution images were also studied by Gaussian fitting of intensities corresponding to atomic columns, as to locate their relative positions with high precision[65,66]; this method was used to determine lattice parameters instead of FFT. Lattice parameters as determined by TEM are in good agreement with those found by XRD (table 5.3.1)

Compositional profiles along sample thickness were obtained by EELS in cross sections of the different samples. Initially general spectra (between 325 and 870 eV) were acquired along

the direction perpendicular to the interface going from the substrate/film interface towards the free surface of the layer.

The evolution of the Ca/La ratios in LCMO layers were estimated from the general spectra and the corresponding results are displayed in figure 5.3.3. In all cases, a cationic segregation process leading to an increase of the La content while approaching film surface was detected, whilst the Ca/La variation rate slows down with annealing process and/or by increasing sample thickness.

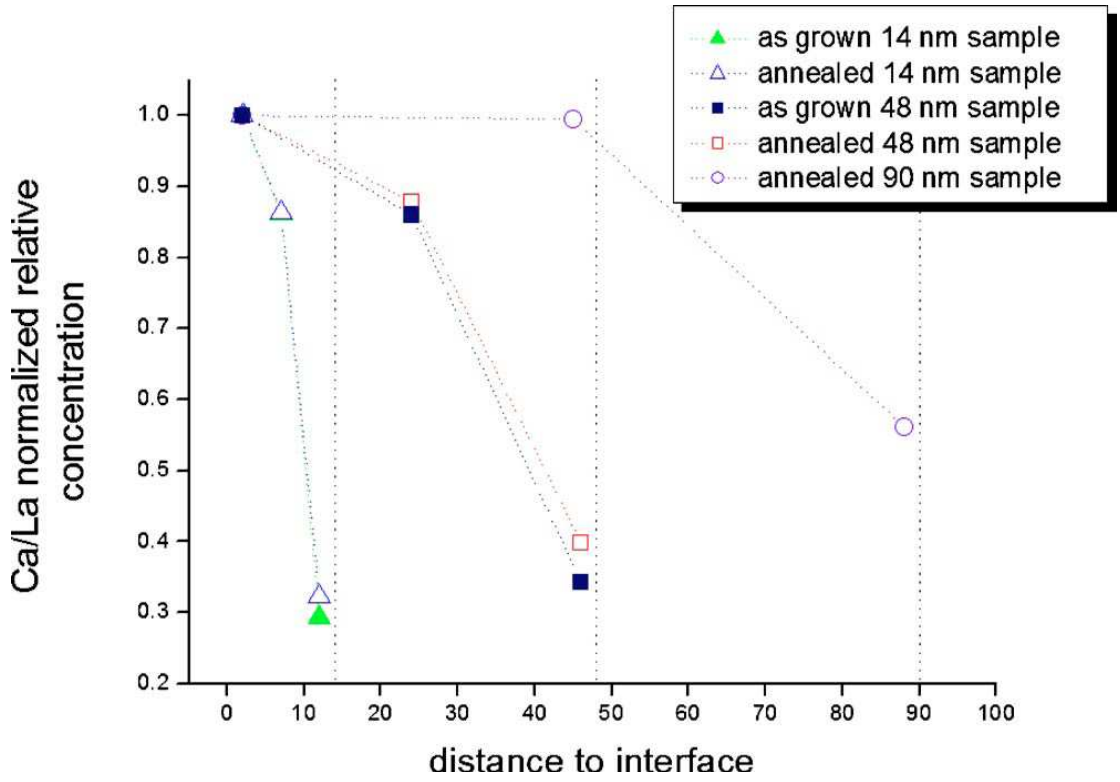

Figure 5.3.3: *Variation of the Ca/La relative intensity ratio for several as-grown and annealed LCMO/LAO samples having different thickness.*

EELS spectra in the energy loss range between 500 and 675 eV (in which the Mn $L_{3,2}$ peaks -640, 651 eV- and the O K edge -532eV- can be found) were also investigated. Once the position of the LCMO/LAO interface was fixed, a sequential acquisition of EELS spectra at different distances from the interface was carried out (figure 5.3.4). L_3 peak edge and Mn L_3 / Mn L_2 peak intensity ratio were determined from these spectra.

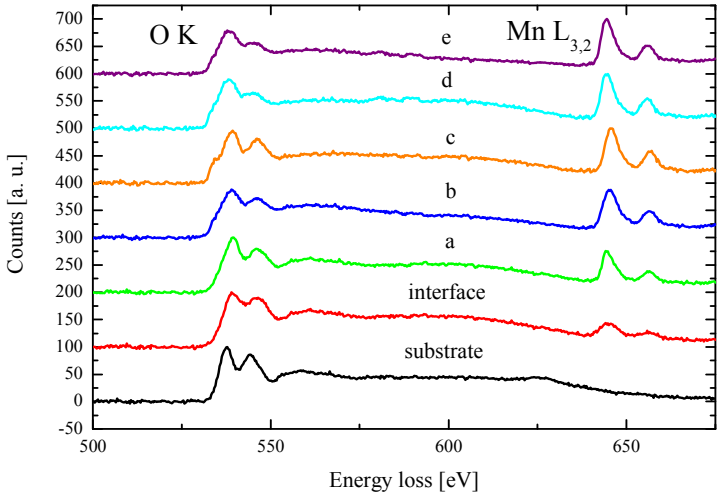

Figure 5.3.4: *Evolution of the EELS spectra, in the electron energy loss range between 500 and 675 eV, measured at several points of the cross section as a function of the distance to the interface for a 14 nm thick as grown sample.*

The experimental results are illustrated in figure 5.3.5 in comparison with the theoretical values found in literature[56-58] for the Mn oxidation states 2+, 3+ and 4+. The most relevant feature in figure 5.3.5 is a shift towards lower energies of the Mn $L_{3,2}$ peaks as well as a variation of the intensity ratio of these two peaks as the distance from the interface is increased, more important for thinner films, and less pronounced after annealing. This variation of the Mn oxidation state is compatible with the detected La diffusion towards the free surface of the films, as suggested by the observed variation of the Ca/La ratio.

Interestingly enough, the observed evolution of T_C and M_S clearly correlates with the segregation process of La ions towards the surface of the films. The formation of a La floating layer during LCMO thin film growth should lead to the appearance of a La-enriched layer of few nm close to the free surface of the films. This layer should exhibit strongly depressed magnetic properties in agreement with the existence of a surface magnetic dead layer as detected from magnetic measurements in LCMO/LAO thin films[67]. Since this La-rich layer is very thin (few nm) its effects are negligible for thick samples but critical for thin ones. This La segregation process would, in turn, imply a departure from the nominal composition (2/3-1/3) $Mn^{3+/4+}$ valence balance, thus becoming an efficient mechanism for the reduction of T_C and M_S.

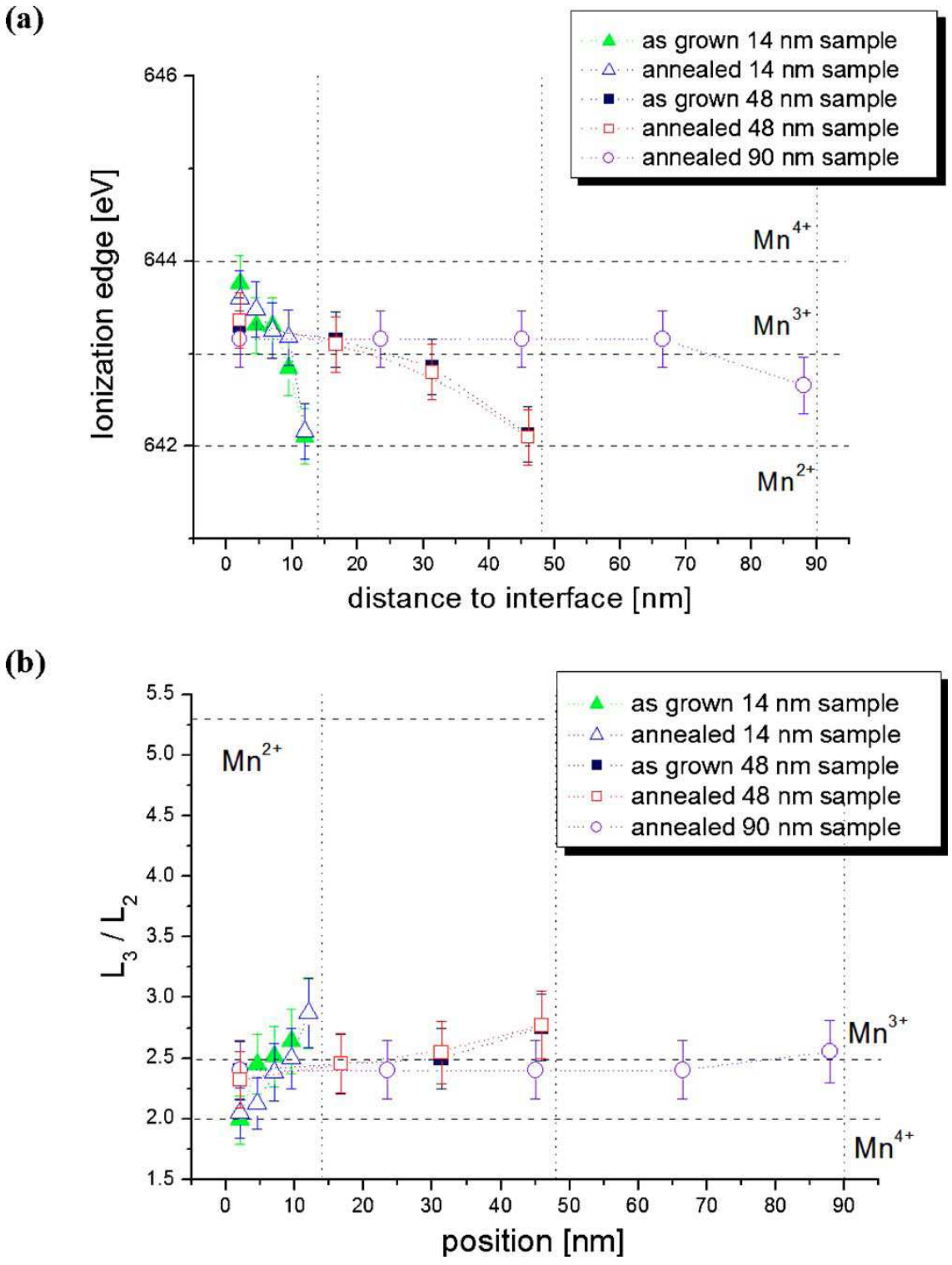

Figure 5.3.5: *Ionisation edge variation (a) and relative intensity variation (b) of the Mn L_3 and L_2 peaks along LCMO layers.*

Whereas depressed magnetic performances of LCMO thin films grown on LAO substrates had been usually explained in terms of the presence of microstructural defects[68,69] or strain conditions, it seems clear that La^{3+} cationic diffusion does play a major role in the observed degradation of the magnetic performances. Nevertheless, it should be mentioned that strain may be at the origin of this cationic migration since a way to accommodate structural strain in thin films could be by means of the segregation of ions with larger or smaller size. Cation migration is thus proposed as a strain reliving mechanism in manganite thin films.

On the other hand, high temperature annealing processes would promote a rediffusion of the La ions into the whole film which would moderate the effect of the cationic migration (as observed in figure 5.3.1) and concomitant Mn oxidation state variation (figure 5.3.5) and substantially improve both T_C and M_S, especially in the thinnest films, where the magnetic dead layer has a greater impact, as observed.

5.3.5 Conclusions

EELS has been applied to explore the local stoichiometry and Mn oxidation state of LCMO layers of various thicknesses grown on top of (001) LAO substrates. The EELS analysis has allowed assessing the existence of a cationic segregation process of La atoms towards free surface, as well as a Mn oxidation state variation through the layer thickness. La diffusion would lead to a Mn valence change and, in turn, to reduced magnetization, creating, in fact, a thin magnetic dead layer. This dead layer would have a higher impact on the properties of thinner films, as the volume fraction it would represent would be greater than for thicker layers. Finally, high temperature annealing processes seems to promote rediffusion of the La ions into the whole film, which would moderate the effect of the observed cationic migration.

5.4. LCMO / STO – orientation and layer thickness dependence

5.4 LCMO / STO – orientation and layer thickness dependence

5.4.1 Introduction

In section 5.3, La^{3+} migration towards the top layer surface in LCMO films grown compressively strained on $LaAlO_3$ substrates was assessed. These results clearly indicate that strain/stress conditions must be taken into account to understand chemical segregation in manganite films. In the present section, the (S)TEM-EELS characterization of LCMO grown on STO (001) and (110) substrates will be addressed.

Little attention has been paid, so far, to the chemistry and electronic structure of (110) LCMO films, even if, as will be shown, they display enhanced magnetic properties when compared to their (001) counterparts.

5.4.2 Experimental details

The (001) and (110) LCMO films with thicknesses (t) ranging from 3.5 to 82 nm, were grown by rf-sputtering at 800 °C, at 330 mtorr, with an O_2 /Ar pressure ratio of 1 / 4 and a growth rate of ~ 0.4 nm/min for thicker samples (~80 nm and ~40 nm) and ~ 0.3 nm/min for the thinner ones. After-growth, samples were in-situ annealed at 800 °C for 1 h in O_2 atmosphere at 350 torr.

X-ray diffraction (XRD) and reciprocal space maps (RSMs) were performed to determine the unit cell parameters. Magnetic properties were studied using a commercial superconducting quantum interference device (Quantum Design). Magnetic measurements were carried out with the magnetic field applied in plane for (001) samples being parallel to the [100] direction and for (110) ones parallel to [001] direction. Temperature dependences of magnetization for all films were recorded at 5 kOe and hysteresis loops were measured at 10 K with a maximum magnetic field of 30 kOe.

Samples were provided by Ingrid Cañero Infante and coworkers at ICMAB (Campus de Bellaterra). They also carried out the XRD analysis and the magnetic measurements.

TEM samples were prepared in cross section geometry (XTEM) by Focused Ion Beam (FIB) and in plan-view (PV) geometry by mechanical thinning down to 25 μm and Ar^+ bombardment at V=5 kV and 7° using a PIPS-Gatan. They were observed in a Jeol J2010F scanning (S)TEM microscope, with a hot field emission gun at 200 keV, coupled with a GIF spectrometer. Additional EEL spectra and STEM images were obtained using a VG 501 dedicated STEM in Orsay and a Nion UltraSTEM 100 aberration corrected dedicated STEM in Daresbury.

5.4.3 XRD and magnetic measurements data

The thickness dependence of the interplanar distances were evaluated from RSMs for the (110) and (001) films and are summarized in figure 5.4.1a. For the (001) LCMO, virtually no relaxation occurs for the in-plane interplanar distance, which remains clamped to the substrate. The out-of-plane distance displays a non-monotonic behaviour: it contracts for films up to a critical thickness t = ~ 20 nm and then expands slightly, remaining well below the bulk value, even for thickest layers. The persistence of a strained state in LCMO (and other manganites) epitaxial thin films has been reported earlier[23,29,70]. For the (110) LCMO, figure 5.4.1a reflects the gradual structural relaxation along both in plane directions [001] and [1−10] as well as along the out-of-plane [110] one. It is clear that the in-plane distances relax much faster than the corresponding in-plane distances in (001) films. Moreover, the relaxation along the [001] and [1−10] directions is different. The out-of-plane [110] direction distance displays a non-monotonic behaviour: it again contracts up to t = ~ 20 nm but then it expands markedly for a further increase of the film thickness, approaching the bulk value for thicker films.

Therefore, the response of (001) and (110) films to the identical lattice mismatch imposed by the substrate is quantitatively different; however, a common trend is identified, namely, the evidence of a critical thickness that separates the well-defined regions in the thickness dependence of the out-of-plane interplanar distance. The dashed areas in figure 5.4.1a indicate a range of thicknesses where the out-of-plane distances are substantially larger than could be expected from their monotonic variation observed above the critical thickness. The evolution of the unit cell volume with thickness is depicted in Fig. 5.4.1b. It is clear that the unit cell volumes of the (001) and (110) LCMO thinnest films are substantially larger than the bulk value; it is also clear that upon increasing thickness the (001) LCMO unit cell volume changes slightly, remaining above the bulk value even for the thickest films, whilst, for (110) LCMO a pronounced gradual reduction of the unit cell volume is observed. Data in figure 5.4.1b clearly illustrate that the assumption of a constant unit cell volume when describing strain effects is not supported by the experimental data. Moreover, they also reveal that for the films under the critical thickness value, the unit cell volume displays a rapid expansion which is more pronounced than what could be expected from a simple linear extrapolation toward $t \rightarrow 0$. Dashed areas in figure 5.4.1b illustrate these anomalous unit cell volume regions.

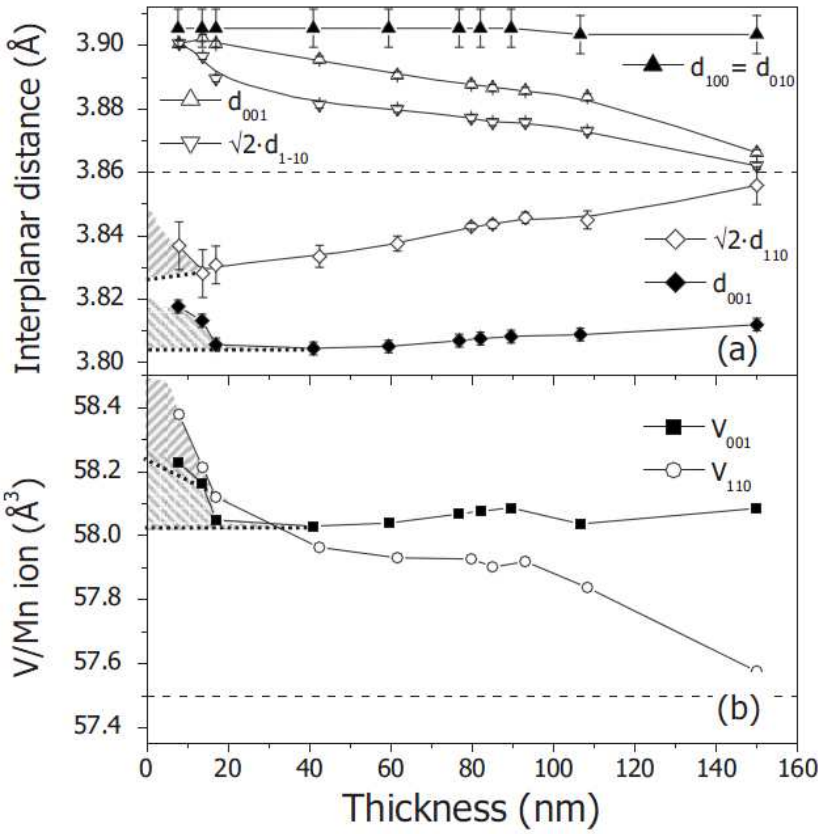

Figure 5.4.1: *(a) Out-of-plane and in-plane lattice parameters and (b) unit cell volume of (001) and (110) LCMO films as a function of the layer thickness.*

Exhaustive X-ray diffraction experiments[71] showed that the LCMO films grow on (001) and (110) STO substrates in a "cube-on-cube" mode with the following epitaxial relationships: LCMO (001) [100] // STO (001) [100] and LCMO (110) [001] // STO (110) [001] respectively.

Figure 5.4.2 displays the thickness dependence of T_C and M_S for all (001) and (110) films. For (001) LCMO, T_C decreases with layer thickness. This trend has been reported earlier for (001) films of LCMO[23,25,29] and other $R_{1-x}A_xMnO_3$ manganites[72-74] grown on different substrates. The same trend is displayed by (110) LCMO films. However, the decay of T_C when reducing thickness is much less pronounced for (110) films than for (001) ones. In addition, comparison of data for (001) and (110) films immediately evidences that the saturation magnetization M_S of the (001) films is smaller than that of the (110) films for a given layer thickness. Thus, (110) films do indeed present improved magnetic properties.

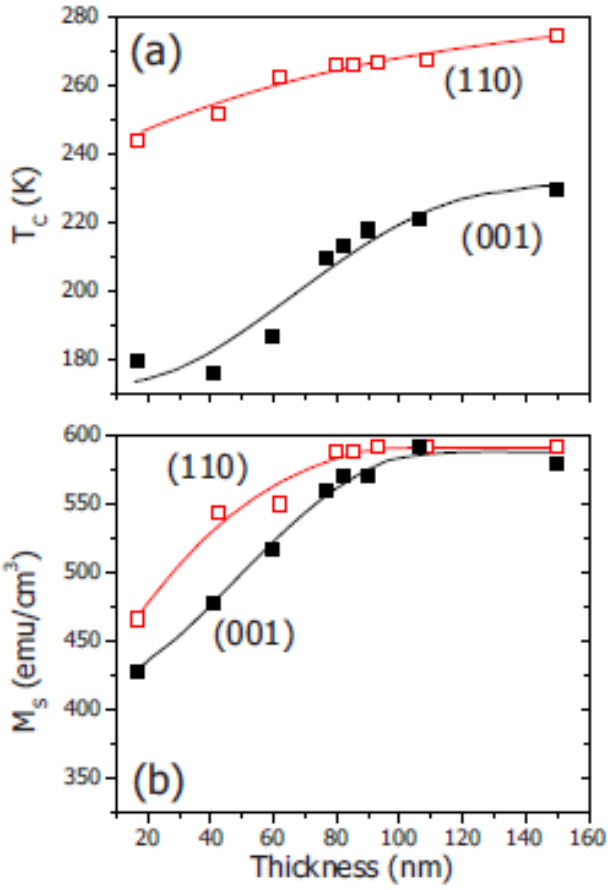

Figure 5.4.2: *(a) Curie temperature T_C and (b) saturation magnetization M_S of (001) and (110) LCMO films (closed and open symbols, respectively) as a function of film thickness.*

5.4.4 Results and discussion

PV TEM study of (001) samples shows no evidence of defects. This is in good agreement with XRD lattice parameter measurements, which indicated (001) film is fully and isotropically in-plane strained. Yet, for thick (~80, ~40nm) (110) films, g = (1-10) two beam observations show a highly periodic distribution of misfit dislocations running perpendicular to the [1-10] direction; g = (001) two beam observation shows a much lower density of dislocations, running perpendicular to (001). This is in also good agreement with XRD measurements of the (110) thick LCMO films that indicated an anisotropic partial in-plane relaxation. In figure 5.4.3, TEM planar view (PV) bright field two-beam images using g = (1-10) (a) and g = (001) (b) excitations of a ~ 80 nm thick (110) LCMO layer are given.

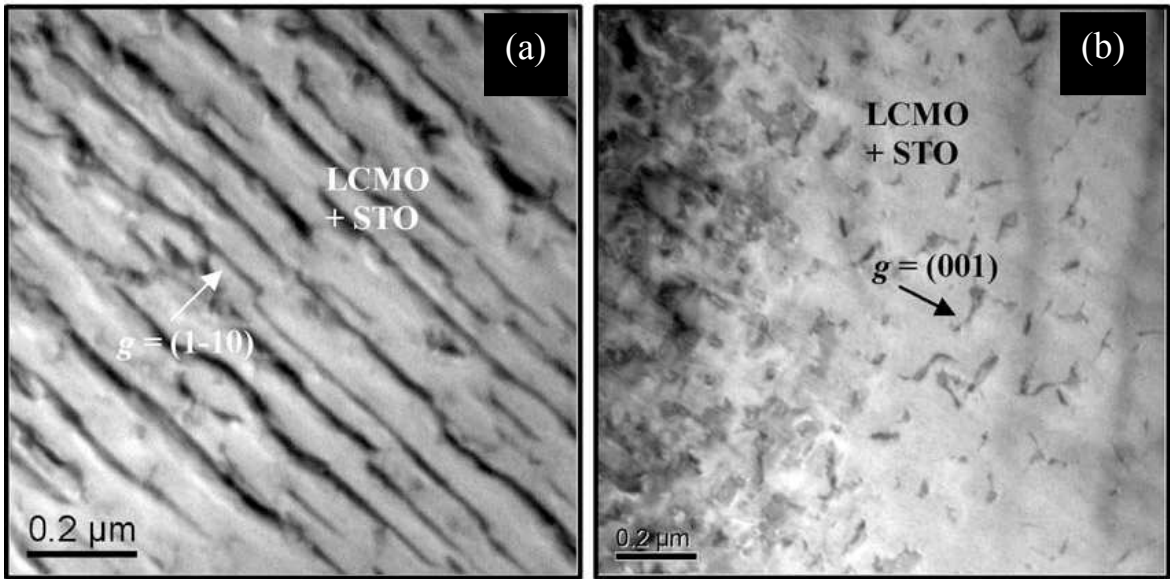

Figure 5.4.3: *(a) g = (1–10) and (b) g = (011) two beam images of ~ 80 nm (110) LCMO/STO in PV geometry.*

A misfit dislocations net is thus evident for (110) thicker (t > 20 nm) films. In contrast, PV images of the thinnest (t < 20 nm) (001) and (110) films yields no evidence of defects. It follows that t < 20 nm LCMO layers are dislocations free irrespective of their orientation. Moreover, TEM characterization of these thin films shows no crystal symmetry change with respect to thicker films (crystal symmetry changes in very thin films are mentioned in literature[74]). In figure 5.4.4 we show TEM planar view (PV) bright field two-beam images of

the t = 36 and 14 nm (110) LCMO films respectively. Insets in figure 5.4.4 display on-axis electron diffractions, corresponding to the 36 and 14 nm (110) films, in PV geometry.

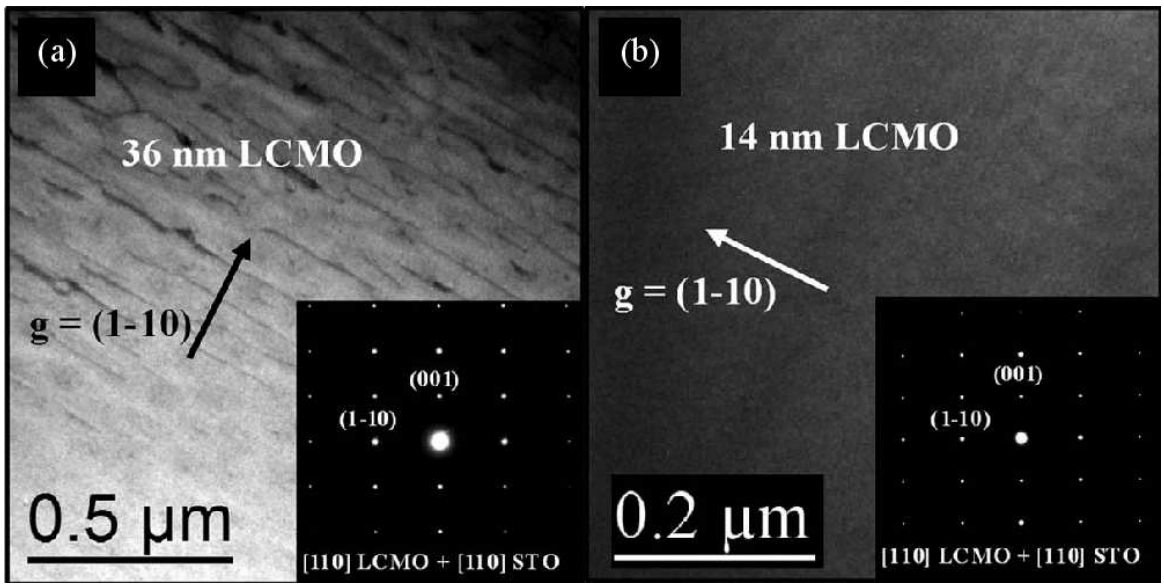

Figure 5.4.4: *g = (1–10) bright field two-beam images of (a) 36 nm and (b) 14 nm thick (110) LCMO films in PV geometry. Insets: on-axis electron diffractions corresponding to the 36 and 14 nm, respectively, (110) films in PV geometry.*

Composition profiles across film thickness were obtained by EELS from FIB lift-off cross section foils. In order to evaluate the suitability of the FIB lamellas for EELS experiments, foil thicknesses (ts) were estimated from low loss spectra via Log-ratio calculations. All ts were found to fall within the (20 ± 2) nm – (32 ± 3) nm range. General spectra (in the range of 325 to 870 eV) were acquired along the direction perpendicular to the substrate/film interface. Concentrations of the different elements at different positions were determined from these spectra. Ca and La σ-weighted intensities along the layers are depicted, for (001) and (110) films of various thicknesses, in figure 5.4.5. Depending on thickness two distinct regimes are evident. For t > 20 nm, (110) and (001) layers present a clearly different behaviour. Whereas in (110) films the Ca, and La concentrations are found to be constant and close to the expected values -0.33 and 0.66- across the whole film, this is not the case for the (001) films, where a monotonous reduction of the La intensity across film thickness is found, the interface being La enriched and the free surface, La deficient. Accordingly, the Ca intensity increases with distance to interface. In sharp contrast, for t < 20 nm, irrespective of layer orientation, the free surface gets progressively La rich (Ca deficient) as thickness is reduced. The effect is somewhat more pronounced in the (001) films than in (110). It is worth noticing that the total

[(Ca+La) / Mn] ratio remains constant, around the expected proportion of ~1, for all the considered samples. No overall cation deficiency is thus observed.

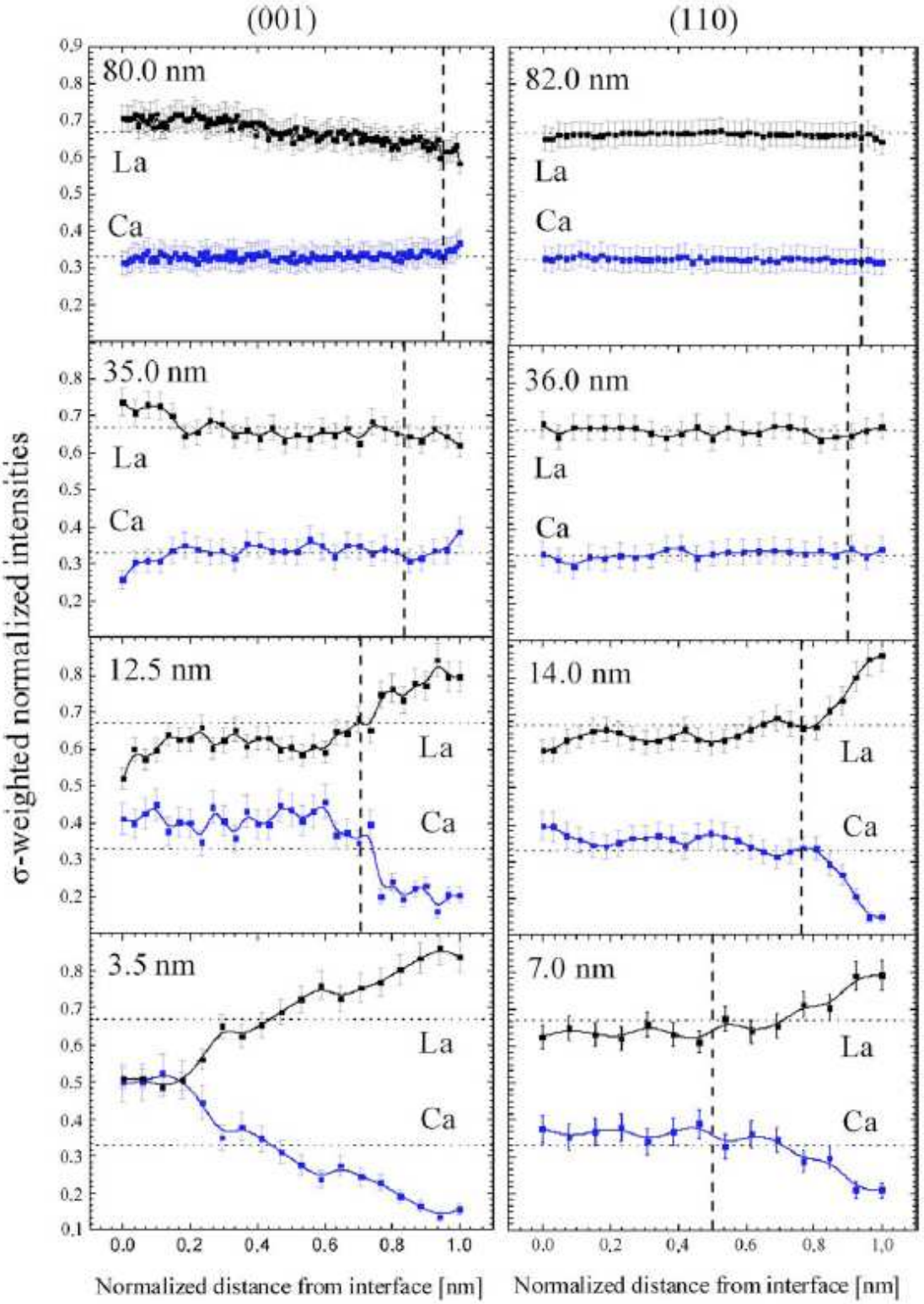

Figure 5.4.5: g = (1–10) Ca and La σ-weighted intensities as a function of normalized distance to interface for several film thicknesses for (001) and (110) LCMO films. Dashed lines indicate the outmost 3.5 nm of each film.

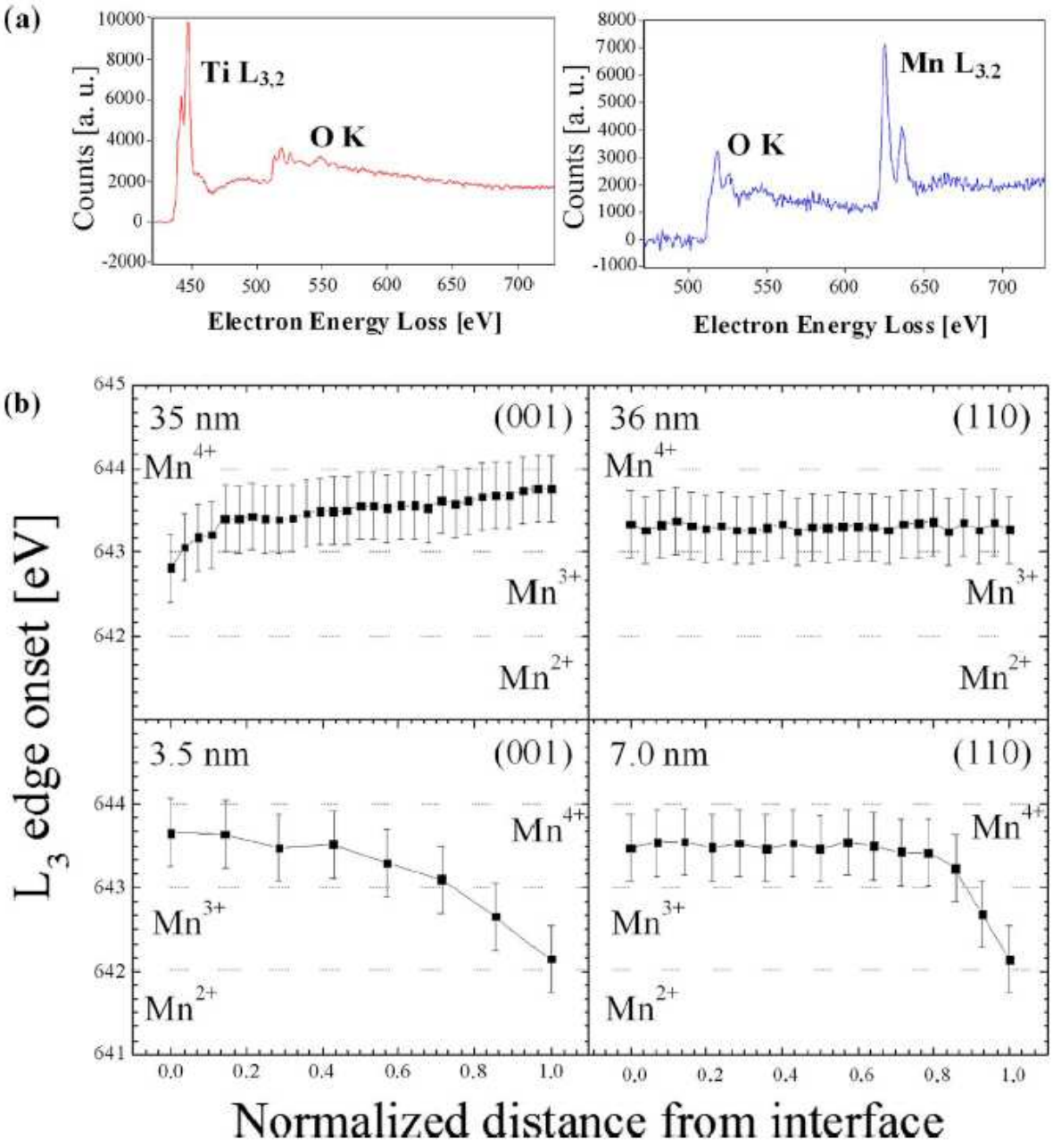

Figure 5.4.6: *(a) Representative individual EEL spectra obtained at the STO substrate (left panel) and at the LCMO layer. (b) Mn L_3 peak onset as a function of normalized distance to interface in representative (001) and (110) LCMO films.*

EELS spectra in the 400–750 eV energy-loss range, where Mn $L_{2,3}$ edges (640 and 651 eV respectively) and O K edge (532 eV) occur, were also recorded. In figure 5.4.6a, representative individual EEL spectra, from the layer and the substrate, are given for illustration purposes. Mn

L_3 peak onset and Mn L_3/L_2 intensity ratio were calculated using the MANGANITAS software. In figure 5.4.6b we report the Mn L_3 edge position along the layer (from interface to free surface) for (001) and (110) layers of different thicknesses. Dotted lines in figure 5.4.6b indicate the Mn L_3 edge positions reported in literature for Mn^{2+}, Mn^{3+} and Mn^{4+} ions[56-58]. Two thickness regimes are observed once more. For thicker (110) films, no significant variation is found to take place along the layer. Yet, the oxidation state of Mn^{m+} ions gradually changes in (001) thick films, with a progressive reduction in the Mn^{m+} species near the interface while free surface is overoxidized. This observation is consistent with the La^{3+} enrichment of the free surface described before. In contrast, figure 5.4.6b, it can be appreciated that for the thinnest samples the Mn^{m+} ions get progressively more reduced when approaching the free surface. Local Mn oxidation state as determined by L_3 / L_2 edge intensity ratio is coherent with the one obtained through L_3 onset position data for all samples. The observed variation in Mn^{m+} oxidation state in the thinnest (001) and (110) films is fully consistent with the detected La enrichment near the free surface. Yet, for thinner films, Mn seems to be more reduced than it should be expected from the Ca / La proportion data.

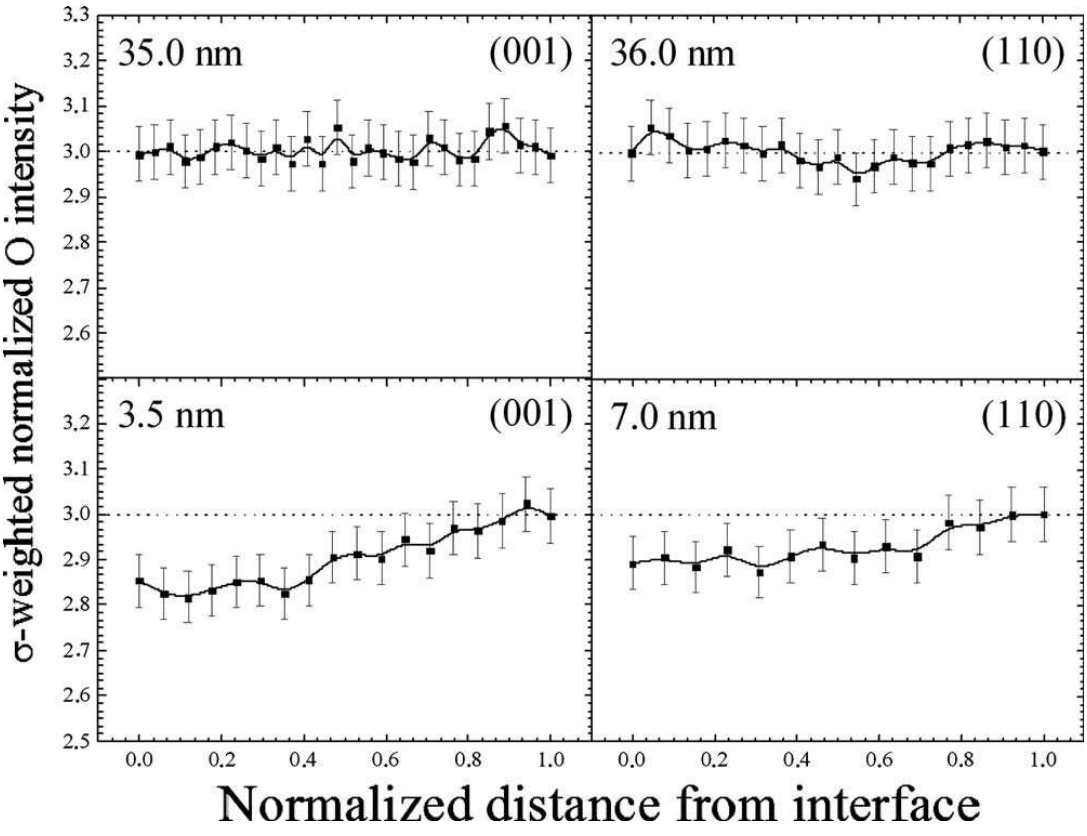

Figure 5.4.7: *O σ-weighted intensity as a function of normalized distance to interface in representative (001) and (110) LCMO films.*

In figure 5.4.7, the O σ-weighted intensity along the layers is depicted, for (001) and (110) films of various thicknesses. For thicker layers, the O intensity remains constant across the film; the [O/Mn] concentration ratio is found to be close to the expected value (~3). In contrast, for the thinner films, the oxygen concentration is not constant but a significant decrease is observed close to the substrate/film interface

In view of TEM, EELS and XRD results two different regimes are revealed. For the higher thickness regime, as stressed (001) sample does not exhibit plastic relaxation, it seems elastic strain accommodation has occurred via cation migration. These results are in good agreement with findings of Simon et al.[54], and have just been reproduced by Varela and coworkers for (001) cobaltites[76]. We notice that due to the larger ionic size of La^{3+} than Ca^{2+}, La^{3+} enrichment close to the STO interface provides a natural mechanism for cell-parameter matching to STO substrate. Comparison between the two encountered stress accommodation mechanisms, namely defect formation for (110) orientation and cation migration for (001) orientation, in two systems with the same layer/substrate mismatch and grown in the same conditions, strongly suggest that strain accommodation via cation migration is more detrimental to the magnetic performance than accommodation via defect creation, both because it is less effective (i.e: layers remain in higher strain conditions) and because it modifies the optimal hole doping (~1/3) in extensive regions of (001) films.

The self-adapting chemical variation related to strain-induced elastic energy is the prevalent mechanism for chemical-phase separation only for (001) films thicker than a critical value which is about ~ 20 nm for LCMO/STO. For thicknesses below this threshold, a different behaviour emerges: La migration towards free surface occurs in absence of plastic relaxation irrespective of LCMO orientation. Both this cation distribution and the apparition of O vacancies, mostly near the interface, determine the Mn^{m+} oxidation state. The presence of O vacancies would account for the abnormally large unit cell volume detected by XRD for the thinnest layers. For this ultra-thin regime for which elastic energy considerations should not be so determinant, kinetic factors such as cation incorporation rate, i.e: sticking coefficient and growth parameters, would determine the local chemistry of the layers.

5.4.5 Conclusions

Electron energy-loss spectroscopy has been used to map composition and electronic states in moderately thin LCMO films grown on STO (001) and (110) substrates. It is found that in partially relaxed (110) films cationic composition and valence state of $Mn^{3+/4+}$ ions are preserved across the film thickness. In contrast, in fully strained (001) films, the Ca/La ratio gradually changes across the film, being La rich at film/substrate interface and La depleted at free surface; Mn valence state changes accordingly. These observations suggest that a strongly orientation-dependent adaptative composition mechanism dominates stress accommodation in manganite films and provides microscopic understanding of their dissimilar magnetic properties.

For thicknesses below ~20 nm, a different behaviour emerges, as La migration towards free surface occurs in absence of plastic relaxation irrespective of LCMO orientation. It is thus clear that the properties of moderately thin LCMO films (t>20nm) cannot be extrapolated to the thinnest ones (t<20nm). For very thin samples, growth kinetic effects rather than equilibrium balances related to stored elastic energy seem to be determinant for the chemical inhomogeneities found across the layers. It thus follows that growth rate and growth mechanism should play a critical role in the properties of LCMO layers.

5.5. STO / LCMO / STO bilayers

5.5 STO / LCMO / STO bilayers

5.5.1 Introduction

The influence of the growth rate on the properties of LCMO layers was strongly hinted by the results presented in chapter 5.4. In the present chapter (001) and (110) LCMO layers about 40 nm thick, prepared at a much slower growth rate, will be investigated. Taking a further step towards the implementation of actual devices, the present chapter will also focus on the influence of growing STO insulating capping layers on the (001) and (110)-oriented manganite layers.

5.5.2 Experimental details

The (001) and (110) (STO/) LCMO films were grown by rf-sputtering at 800 °C, at 330 mtorr, with an O_2 /Ar pressure ratio of 1 / 4 and a growth rate of ~1.1 nm/min for the LCMO layers and of ~1.8 nm/min for the STO cappings. After-growth, samples were in-situ annealed at 800 °C for 1 h in O2 atmosphere at 350 torr.

Structural properties were studied by x-ray diffraction. Reciprocal space maps (RSMs) were obtained to evaluate the unit cell parameters. Magnetic properties were measured in a commercial superconducting quantum interface device (Quantum Design).

Samples were provided by Ingrid Cañero Infante and coworkers at ICMAB (Campus de Bellaterra). They also carried out the XRD analysis and the magnetic measurements.

TEM samples, were prepared for cross section view using a FEI Strata FIB. They were observed in a Jeol J2010F scanning (S)TEM microscope, with a hot field emission gun at 200 keV. Additional EEL spectra and STEM images were obtained in a Nion UltraSTEM 100 aberration corrected dedicated STEM in Orsay.

5.5.3 XRD and magnetic measurements data

RSMs data show the (001) LCMO electrode remains fully strained, whilst the (110) is partially (~0.7 %) relaxed. The temperature dependence of magnetization of bare electrodes and 4 nm STO capped ones is shown in figure 5.5.1. The magnetic field (5 kOe) was applied in-plane, along the [100] direction for the (001)-oriented samples and along the [001] one for the (110)-oriented samples. T_C of the bare electrodes is clearly dependent on the substrate orientation, being higher for the (110) one (T_C = 256K), and, thus, closer to LCMO bulk value (~270 K) than for the (001) electrode (T_C = 180 K). When depositing 4 nm thick capping layers, the T_C of the electrodes does not change appreciably, while the magnetization of the (001) samples is clearly reduced after the capping. On the contrary, no relevant decrease on magnetization is observed for the (110) samples. From magnetization curves vs. field, measured at 10 K, saturation magnetisation of bare electrodes M_S has been found to be M_S (001) = 543 emu/cm^3 and M_S (110) = 570 emu/cm^3, whereas for the capped electrodes M_S (001) = 488 emu/cm^3 and M_S (110) = 548 emu/cm^3.

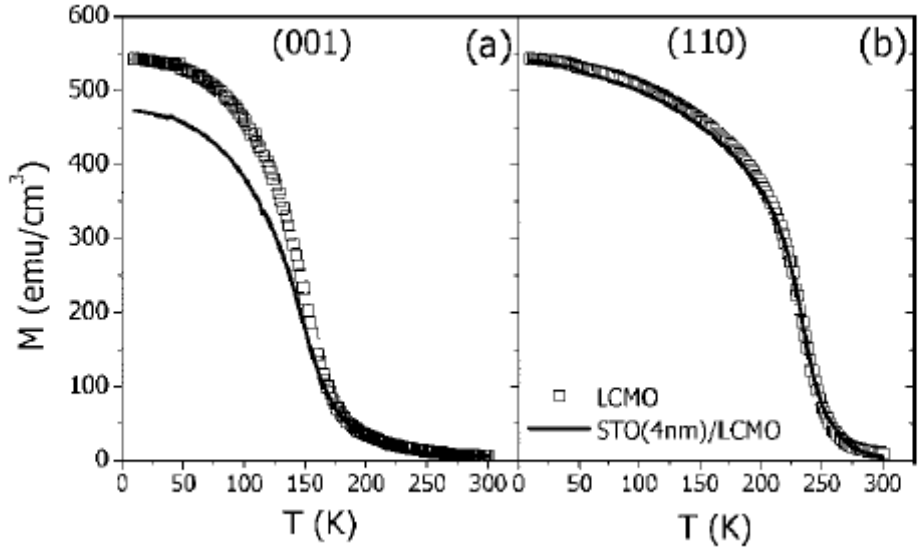

Figure 5.5.1: *Temperature dependence of the magnetization of LCMO electrodes (symbols) and 4 nm STO capped LCMO electrodes (lines): (a) (001) samples and (b) (110) samples.*

5.5.4 Growth rate considerations

Bare electrodes were first characterized through (S)TEM-EELS. From a morphological point of view, the (001) LCMO layers were found to be homogeneous and defect-free with a sharp interface and free surface. Figure 5.5.2 (a) and (b) show BF STEM images of the (001) electrode.

Composition profiles across the films were then obtained by EELS. General spectra (in the range of 325 to 870 eV) were acquired along the direction perpendicular to the substrate/film interface. Concentrations of the different species as a function of distance to interface were determined from these spectra. No local deviations from the nominal cation rate (<Ca> = <La>/2) were found for the (001) direction, as evidenced in figure 5.5.3 (a).

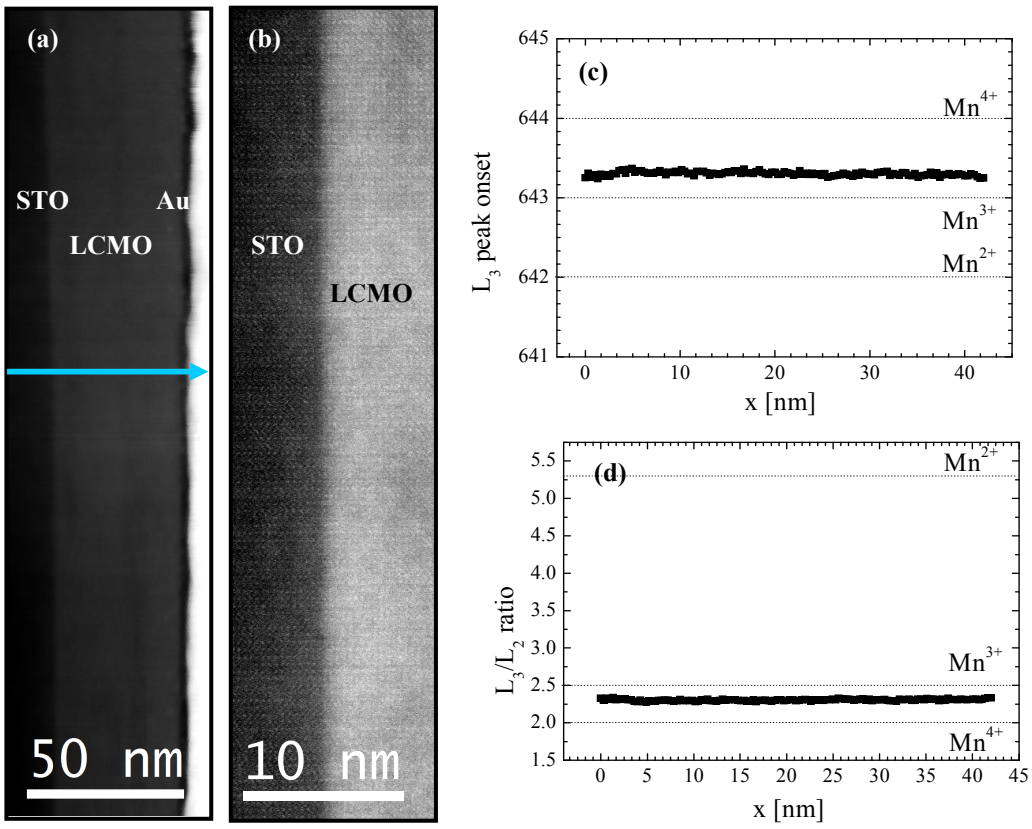

Figure 5.5.2: *(a) General HAADF image of the (001) LCMO/STO system. (b) HRHAADF image of the LCMO/STO interface. (c) Mn L_3 peak onset and (d) Mn L_3/ Mn L_2 relative intensity along the LCMO layer.*

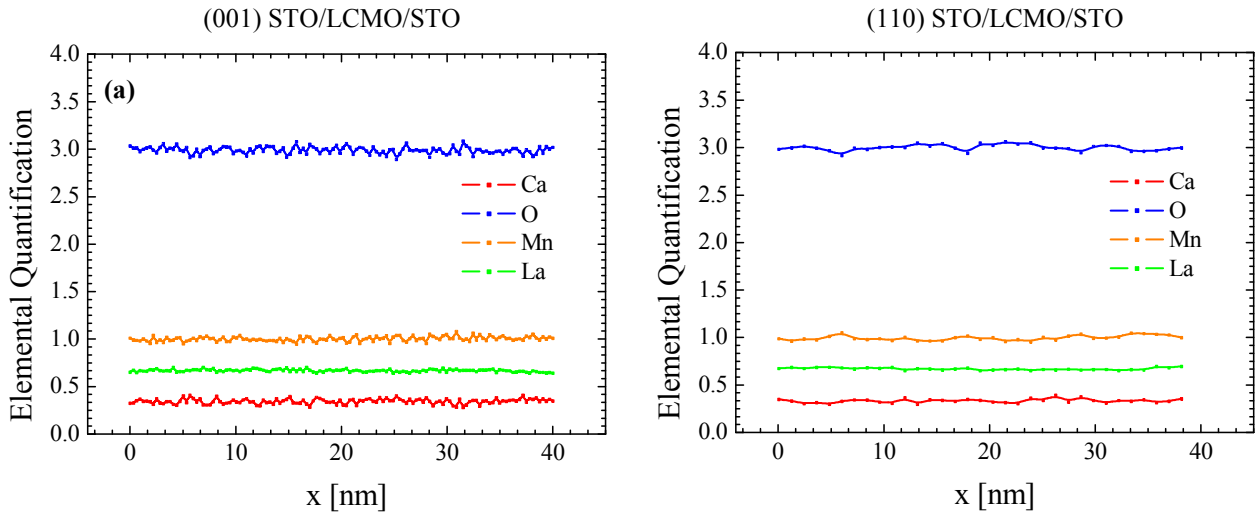

Figure 5.5.3: *EELS elemental quantification along the (001) (a) and (110) (b) LCMO layers.*

EELS spectra in the 500–675 eV energy-loss range, where Mn $L_{2,3}$ edges (640 and 651 eV respectively) and O K edge (532 eV) occur, were also recorded. The position of the Mn L_3 edge and the Mn L_3 /Mn L_2 edge intensity ratio are well known to be related to the Mn oxidation state[56-58]. In figures 5.5.2 (c) and (d) we report the Mn L_3 edge position and the Mn L_3 /Mn L_2 edge intensity ratio along the layer (from interface to free surface). Dotted lines indicate the values reported in literature[56] for Mn^{m+} ions in various oxidation states. No variations in Mn oxidation state were found for (001) LCMO in good agreement with the chemical distribution EELS data.

In contrast, the (110) LCMO layers present a sharp interface but a fairly irregular free surface. Figure 5.5.4(a) shows a g=(1-10) two beam BF image of the (110) LCMO layer, displaying what appears to be a number of defects, in good agreement with recent reports on the crystal quality of (110) LCMO thin films[77].

No local deviations from the nominal stoichiometry were detected in the case of the (110) sample either (figure 5.5.3 (b)). In figures 5.5.4 (b) and (c) we report the Mn L_3 edge position and the Mn L_3 /Mn L_2 edge intensity ratio along the layer: no variations in Mn oxidation state were found, in good agreement with the chemical distribution EELS data.

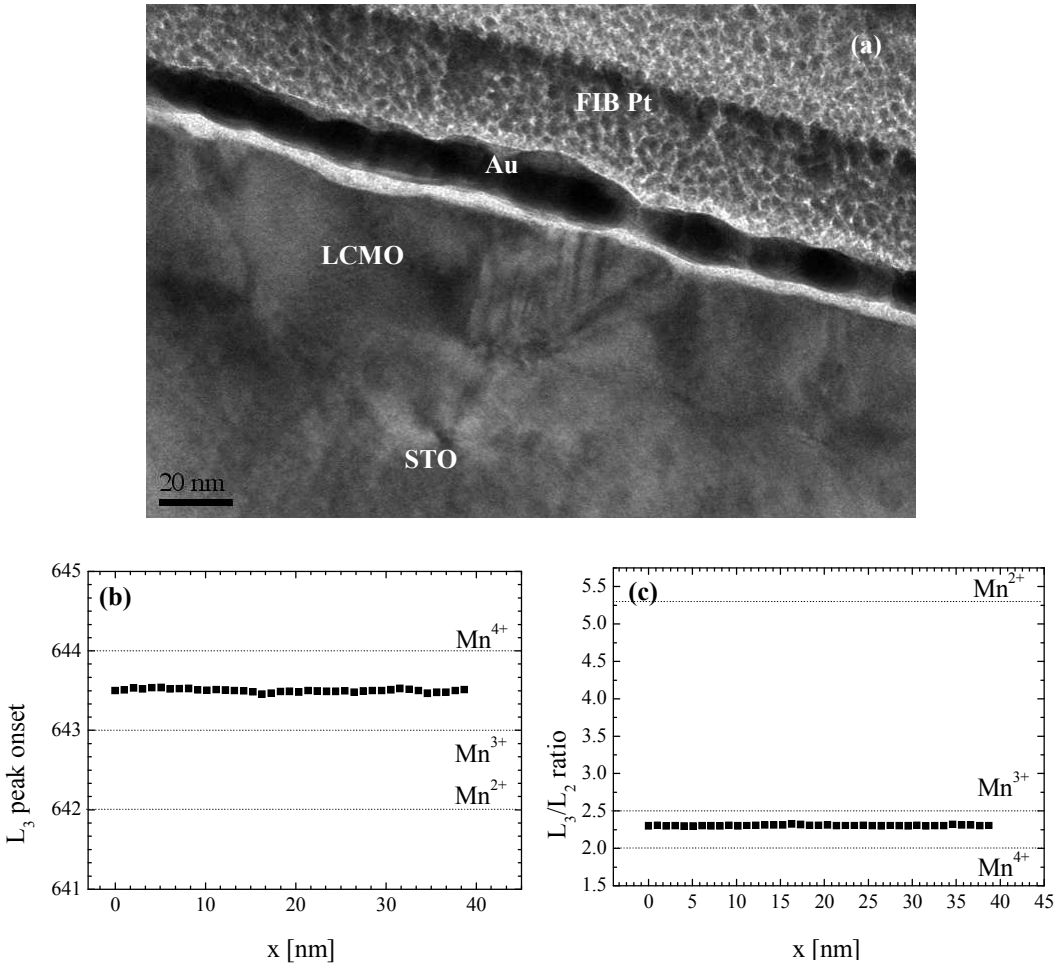

Figure 5.5.4: *(a) g=(1-10) two beam BF image of the (110) LCMO layer. (b) Mn L_3 peak onset and (c) Mn L_3/ Mn L_2 relative intensity along the LCMO layer.*

After a careful EELS characterization, it can be concluded that the defects in figure 5.5.4 (a) correspond in fact to a number of grains with a different composition inside the LCMO layer. These grains are visible all along the layer and separated some 50 nm from one another. The grains themselves are found by EELS experiments to be cation depleted; on the other hand these grains do contain Mn and O. Inside the grains, Mn oxidation state is determined to be 4+. Thus, these grains seem to correspond to a MnO_2 phase.

It seems clear that strain conditions greatly influence the magnetic properties of electrodes. Partially relaxed (110) LCMO films, even if containing MnO_2 grains, still display better magnetic properties than their chemically homogeneous (001) counterparts.

5.5.5 Effect of the capping

In order to study the effect of a STO capping on the electrodes, 4 nm and 5 nm STO layers were grown on the (001) and (110) LCMO.

The STO was observed to grow epitaxially on the LCMO, as seen in figures 5.5.5 and 5.5.6, displaying HRTEM images of both interfaces (STO-layer/LCMO and LCMO/STO-substrate) of the (001) and (110) bilayers, respectively. Figure 5.5.5 shows a (001) STO / (001) LCMO / (001) STO epitaxial relationship for the STO / LCMO / (001) STO system, observed along the [100] zone axis; figure 5.5.6 shows a (110) STO / (110) LCMO / (110) STO epitaxial relationship for the STO / LCMO / STO system, observed along the [1-10] zone axis.

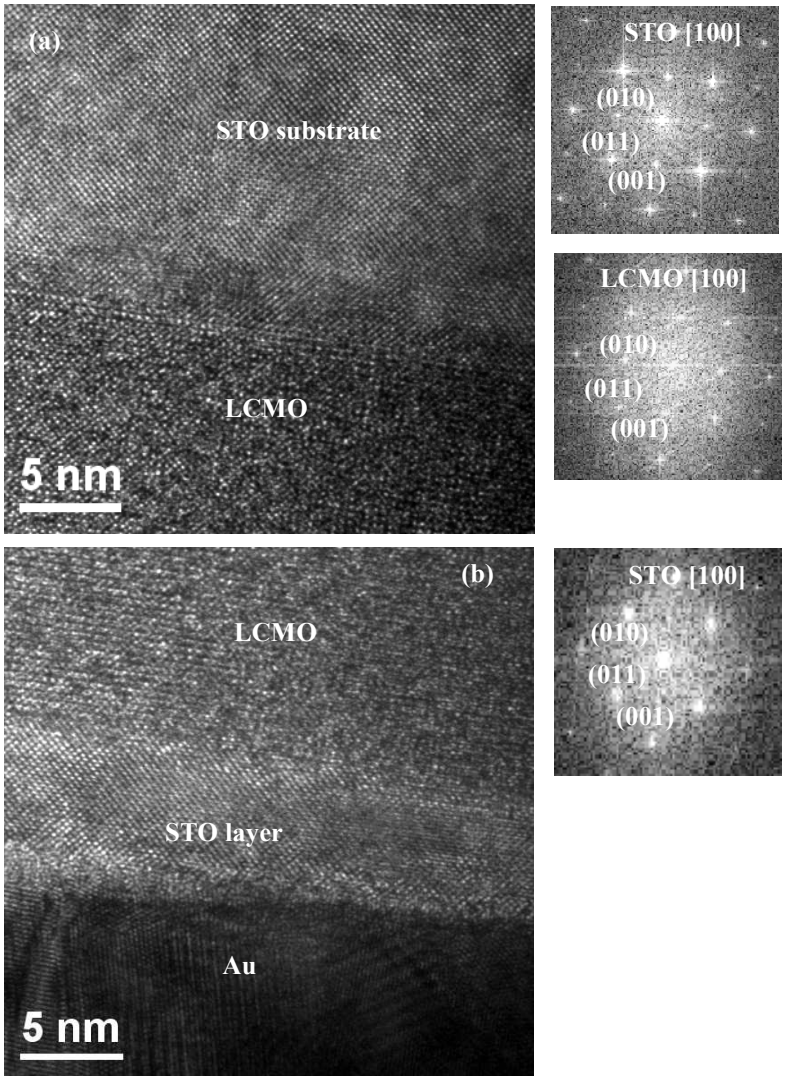

Figure 5.5.5: *(a) LCMO/STO (substrate) interface and corresponding FFTs and (b) STO/LCMO interface and STO layer FFT of the (001) 5 nm STO/LCMO/STO system.*

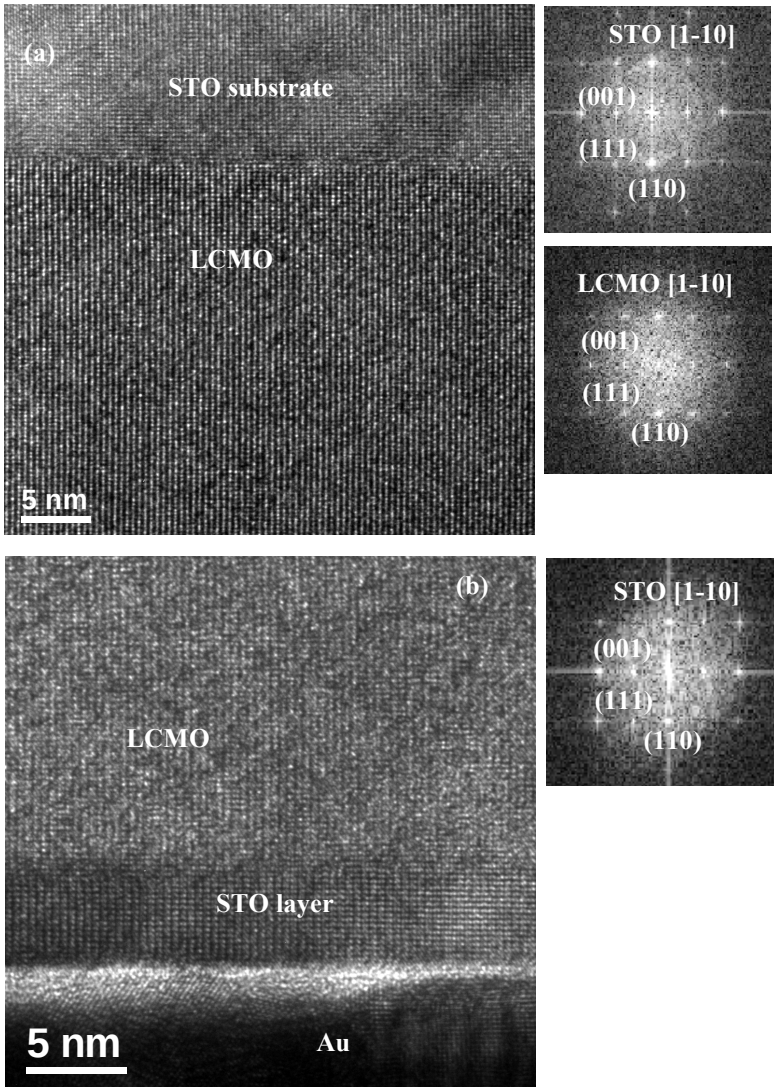

Figure 5.5.6: *(a) LCMO/STO (substrate) interface and corresponding FFTs and (b) STO/LCMO interface and STO layer FFT of the (110) 5 nm STO/LCMO/STO system.*

In order to further characterize the interfaces of the (001) and (110) STO/LCMO/STO systems, atomic resolution EELS experiments were performed.

Figure 5.5.7 displays a HRHAADF image of the lower interface and atomically resolved chemical maps at this interface. In figure 5.5.8, we show a HAADF general image of the (001) 5 nm STO/LCMO/STO system (a), a HRSTEM image of the upper interface (b) and atomically resolved Mn, La and Ti maps at this interface (c). Figure 5.5.8 clearly indicates that interdiffusion is limited to a maximum of 1 monolayer (probably less) across the interface. In figure 5.5.9 we show a HAADF general image of the (110) 5 nm STO/LCMO/STO system, a HRSTEM image of the lower

interface and atomically resolved Mn, La and Ti maps at this interface. In this case, interdiffusion is also seen to be limited to a maximum of 1 monolayer across the interface. An analogous chemical map could not be obtained at the (110) upper interface, because the upper surface of the LCMO layer is irregular -as this surface is not flat, contributions from both the LCMO layer and the STO capping layer are encountered in the beam direction.

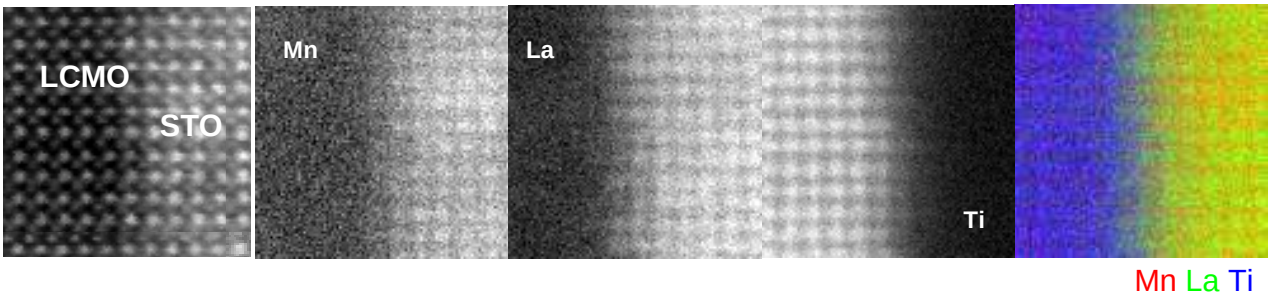

Figure 5.5.7: *HRSTEM image of the (001) 5 nm STO/LCMO/STO system lower interface, and Mn, La and Ti maps at this interface.*

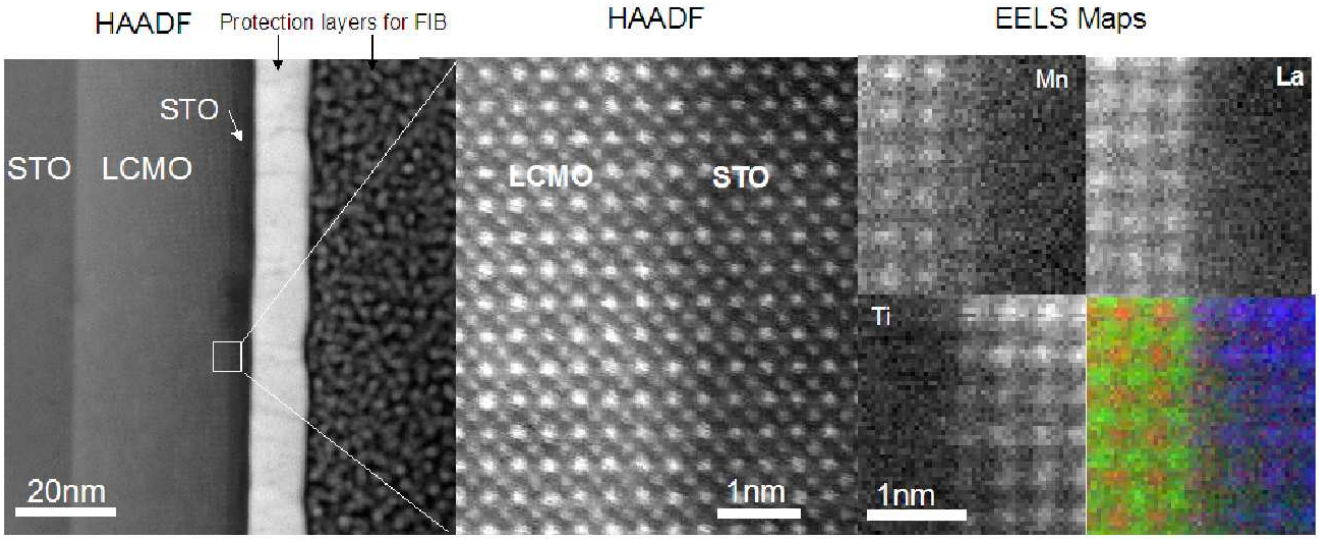

Figure 5.5.8: *HAADF general image of the (001) 5 nm STO/LCMO/STO system. HRSTEM image of the upper interface, and Mn, La and Ti maps at this interface.*

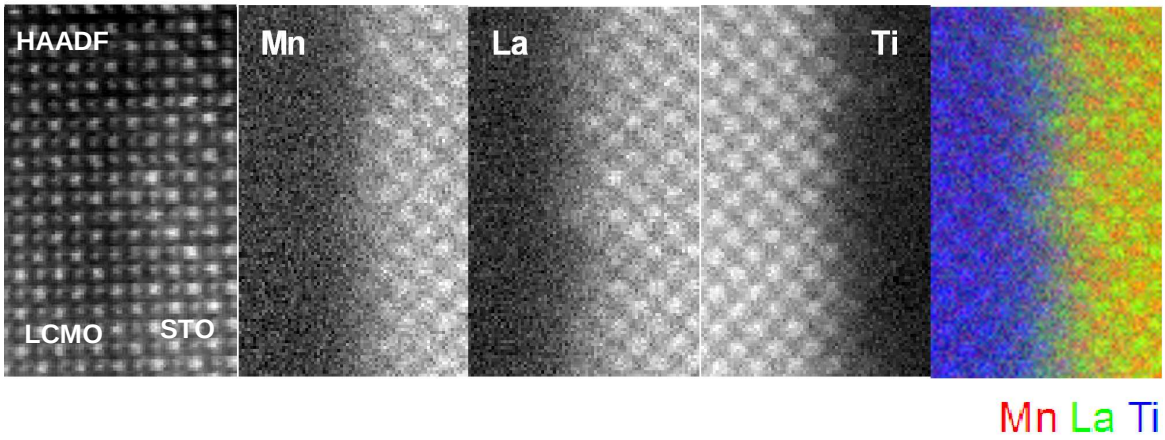

Figure 5.5.9: *HRSTEM image of the (110) 5 nm STO/LCMO/STO system lower interface, and Mn, La and Ti maps at this interface.*

To further understand the behaviour of the bilayers, EEL spectra were also obtained along the LCMO layers. No deviations from nominal stoichiometry were found, as expected from the EELS data obtained from the bare electrodes (figure 5.5.10). Yet, significant differences appear concerning the Mn oxidation state. The Mn L_3 edge onset and the Mn L_3 /Mn L_2 edge intensity ratio data corresponding to the LCMO layer in the (001)STO/LCMO/STO system are given in figure 5.5.11 (a) and (b).

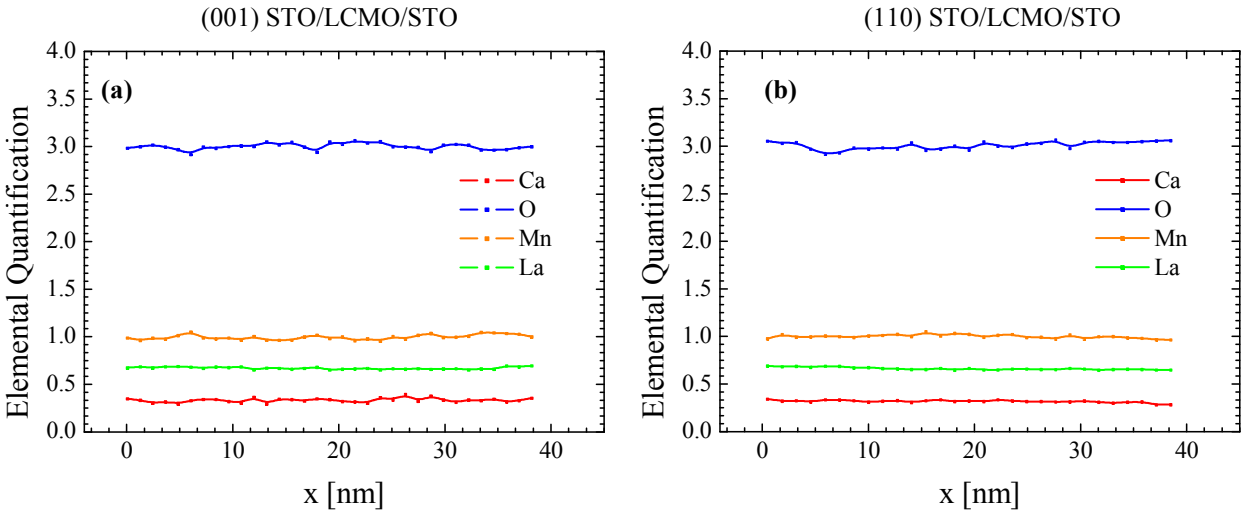

Figure 5.5.10: *EELS elemental quantification along the (001) (a) and (110) (b) LCMO layers in the 5nm STO/LCMO/STO system.*

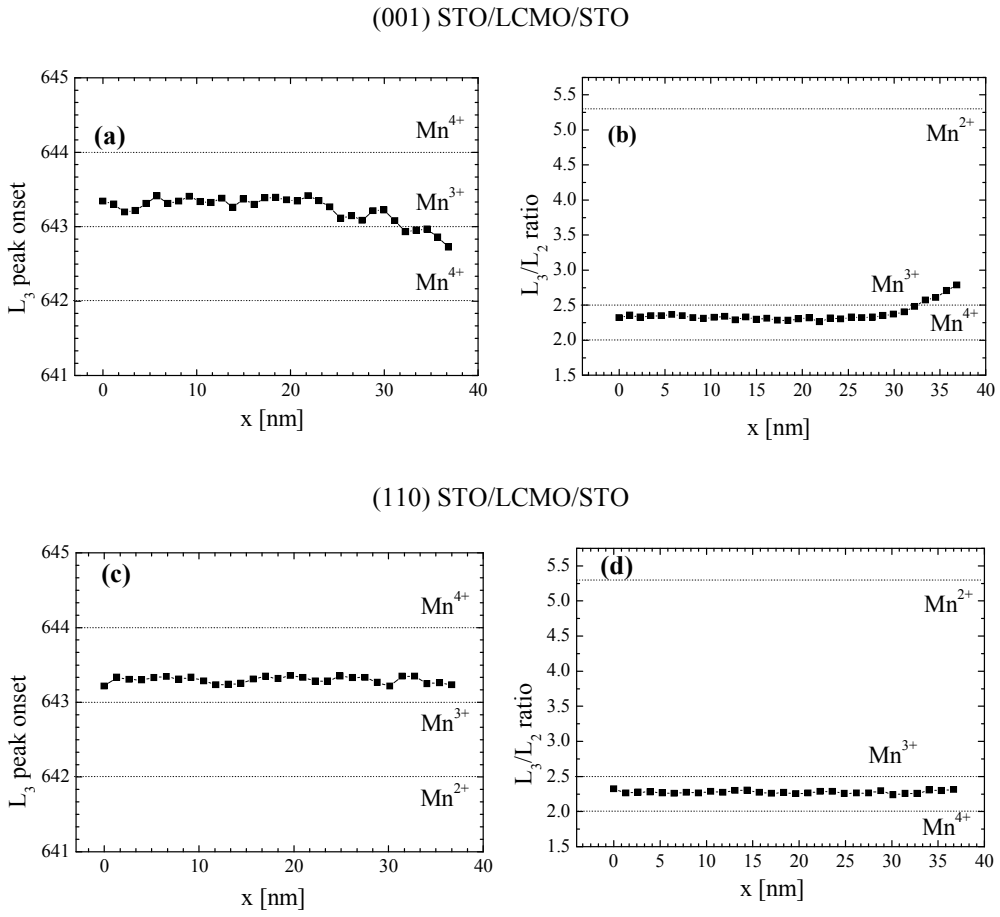

Figure 5.5.11: *(a), (c) Mn L_3 peak onset and (b), (d) Mn L_3/ Mn L_2 relative intensity along the LCMO layer of the (001) and (110) 5 nm STO/LCMO/STO systems, respectively.*

It is clear that a shift of the L_3 edge position towards lower energies and a rising of the Mn L_3 /Mn L_2 edge intensity ratio take place near the interface with the STO capping, indicating a reduction of the Mn near that interface. This reduction was not found in the single layer, and must thus be correlated with an interface effect. The Mn L_3 edge onset and the Mn L_3 /Mn L_2 edge intensity ratio data corresponding to the LCMO layer in the (110) STO/LCMO/STO system are given in figure 5.5.11 (c) and (d). In this case, it is clear that the Mn oxidation state remains constant.

When growing an STO capping on a (001) LCMO electrode, its magnetic properties are greatly compromised. The microscopic reason for this macroscopic behaviour has been identified: upon growth of the STO capping on the LCMO layer, a Mn reduction appears near the capping/electrode interface. Conversely, in the case of (110) LCMO, the Mn oxidation state remains unchanged after growing the STO capping layer, and the magnetic properties of the (110) STO/LCMO/STO system

are much more promising than those of their (001) counterparts. As no anomalous cation distribution along the (001) layer is found, and no cation interdiffusion through this interface is detected, it is proposed that electrons are injected into the (001) LCMO from the STO capping layer, and that this injection does not take place in the case of the (110) system, because of the different terminating layers found in each case. This is in good agreement with literature[51-53], as it has been reported that the MnO_2 planes are electron doped in the case of a TiO_2 type interface: other authors have studied the (001) STO/$La_{2/3}Sr_{1/3}MnO_3$ (LSMO) interfaces and found that a distinction has to be made between the TiO_2/ $La_{2/3}Sr_{1/3}O/MnO_2$ (TiO2) and the SrO/ MnO_2 (SrO) stacking at the interface. In particular they observed that the MnO_2 planes are electron doped in the case of a TiO_2 type interface[51-53] -evidence of electron doping in this case has been given by the study of Mn white lines fine structure in EELS experiments. In the case of a (110) interface, possible terminating layers are SrTiO or O_2, instead of SrO or TiO_2.

On the other hand, less subtle effects, such as interdiffusions at the interface may also need to be taken into account. In particular, oxide layers growing on a different oxide compound have been reported to incorporate O from the underlying layer: Herranz and coworkers[78] demonstrared that, when $LaAlO_3$ (LAO) layers are grown on STO, the growing layer takes some of the O from the STO substrate, thus effectively creating O vacancies extending from the interface into the STO substrate. The fact that the growing STO capping layer may take oxygens from the LCMO films in the (001) STO/LCMO/STO system cannot be ruled out, especially as the Mn reduction near the upper interface is important and extends a few nanometers deep into the LCMO electrode. Nevertheless, the concentration of oxygen vacancies seems to lay under the EELS detection limits, and thus, would not fully account for the Mn oxidation state variation. What is clear is that (110) STO/LCMO is a chemically (in addition to electronically) robust interface, as in this case no O incorporation from the LCMO electrode into the growing STO layer is suggested by the Mn local oxidation state data.

Nevertheless, not everything is ideal concerning the growth of STO on (110) LCMO. The Mn oxide grains often interrupt the STO layer, making it impossible to have a continuous STO capping, as they make the LCMO layer irregular, in a tower battlement-like shape (see figure 5.5.12 (a) – (e)). On the other hand, as evidenced in figure 5.5.12 (f), Ti diffusion takes place into the grain boundaries, and Ti ends up decorating the surface of the MnO_2 grains.

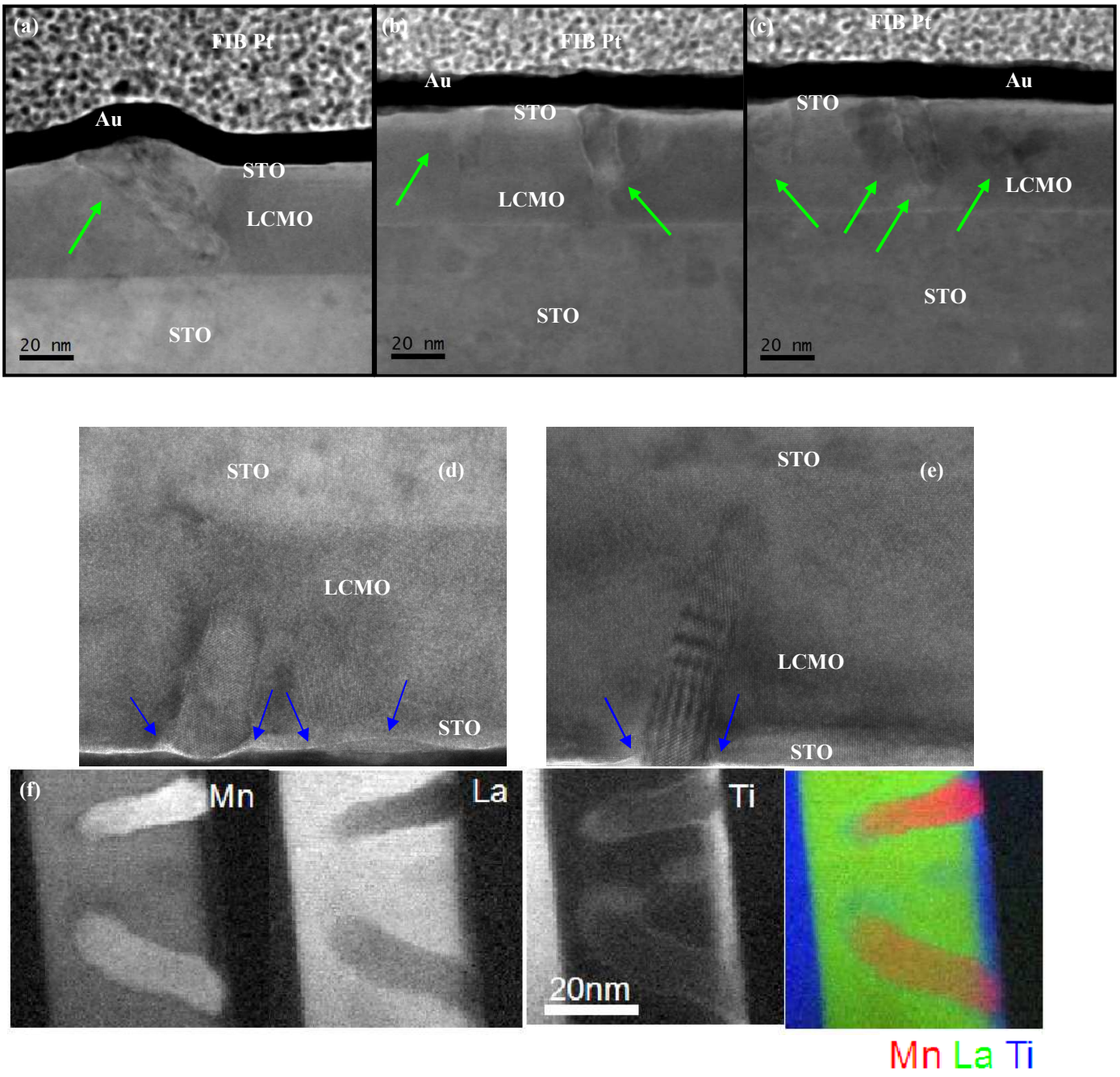

Figure 5.5.12: *(a-c) BF-STEM general images of three different regions of the layer. Mn oxide grains are indicated by arrows. (d-e) (110) 5 nm STO/LCMO interface HRTEM images. Arrows indicate the points where STO layer gets interrupted. (d) Low magnification Mn, La and Ti maps in the (110) 5 nm STO/LCMO/STO system.*

5.5.6 Conclusions

EELS analyses have shown that the microstructure, local chemistry and Mn oxidation state of ~ 40 nm thick LCMO films grown at ~0.11 nm/min is radically different from that of LCMO films of the same thickness grown at ~0.40 nm/min. (001) LCMO electrodes are chemically and electronically homogeneous, and defect-free. Conversely, (110) LCMO layers grown at ~0.11 nm/min present some anomalous grains (identified as MnO_2) inside the layer. Whereas (001) LCMO is fully strained, (110) LCMO is partially relaxed. Magnetic performance is found to be better for relaxed (110) LCMO than for fully strained (001) LCMO in spite of the MnO_2 grains.

EELS data also show that, when growing a STO capping layer on top of the (001) and (110) LCMO layers, a Mn reduction is produced at the capping/electrode interface in the (001) system but not in the (110), which explains the better magnetic properties of (110) interfaces. This would be so because an electron injection would take place from the STO capping layer into the (001) LCMO electrode, and not into the (110) LCMO because of the nature of the STO terminating planes in the (110) growth direction.

5.6 References

5.6. References

1. Infante, I.C., Thesis, Universitat Autònoma de Barcelona (2008)
2. Abad, L., Thesis, Universitat Autònoma de Barcelona (2007)
3. Tokura, Y., Reports on Progress in Physics 69, 797–851 (2006)
4. Dagotto, E., Yunoki, S., Cengiz, S., Alvarez, G., Moreo, A., Journal of Physics: Condensed Matter 20, 434224 (2008)
5. Israel, C., Calderon, M.J., Mathur, N.D., Materials Today 10,10 (2007)
6. Sugano, S., Tanabe, Y., Kamimura, H., Multiplets of Transition-Metal Ions in Crystals, Academic Press, New York (1970)
7. Kanamori, J., Journal of Applied Physics 31, 14S (1960)
8. Fontcuberta, J., Martinez, B., Seffar, A., Piñol, S., Garcia-Muñoz, J.L., Obradors, X., Physical Review Letters, 76, 7 (1996)
9. Sun, J.Z., Gallagher, J.Z., Ducombe, P.R., Krusin-Elbaum, L., Altman, R.A., Gupta, A., Lu, Y., Gong, G.Q., Xiao, G., Applied Physics Letters 69, 3266 (1996)
10. Jo, M.H., Mathur, N. D., Todd, N.K., Blamire, M.G., Physical Review B 61, 14905 (2000)
11. Bowen, M., Barthélémy, A., Bibes, M., Jacquet, E., Contour, J.P., Fert, A., Ciccacci, F., Duò, L., Bertacco, R., Physical Reviwe Letters 95, 137203 (2005)
12. Lu, Y., Li, X.W., Gong, G.Q., Xiao, G., Gupta, A., Lecoeur, P., Sun, J.Z., Wang, Y., Dravid, V.D., Physical Review B 54, R 8357 (1997)
13. Viret, M., Drouet, M., Nassar, J., Contour, J.P., Fermon, C., Fert, A., Europhysics Letters 39, 545 (1997)
14. Bibes, M., Bouzeouane, K., Besse, M., Barthélémy, A., Fusil, S., Bowen, M., Seneor, P., Contour, J.P., Fert, A., Applied Physics Letters 83 2629 (2003)
15. Garcia, V., Bibes, M., Barthélémy, A., Bowen, M., Jacquet, E., Contour, J.P., Fert, A., Physical Review B 69, 052403 (2004)
16. Garcia, V., Bibes, M., Maurice, J.L., Jacquet, E., Contour, J.P., Barthélémy, A., Applied Physics Letters 87, 212501 (2005)
17. Ishii, Y., Yamada, H., Sato, H., Akoh, H., Kawasaki, M., Tokura, Y., Applied Physics Letters 87, 22509 (2005)
18. Singh, M.P., Carvello, B., Ranno, L., Applied Physics Letters 89, 022504 (2006)
19. Ruotolo, A., Oropallo, A., Granozio, F.M., Pepe, G.P., Perna, P., Di Uccio, P.S.,

Applied Physics Letters 88, 252504 (2006)

20. Xiong, Z. H., Wu, D., Vardeny, Z.V., Shi, J., Nature 427, 821 (2004)
21. Hueso, L. E., Pruneda, J.M, Ferrari, V., Burnell, G., Valdés-Herrera, J.P., Simons, B.D., Littlewood, P.B., Artacho, E., Fert, A., Mathur, N.D., Nature 445, 410 (2007)
22. Sun, J.Z., Abraham, D.W., Rao, R.A., Eom, C.B., Applied Physics Letters 74, 3017 (1999)
23. Bibes, M., Valencia, S., Balcells, L., Martnez, B., Fontcuberta, J., Wojcik, M., Nadolski, S., Jedryka, E., Physical Review B 66, 134416 (2002)
24. Izumi, M., Konishi, Y., Nishihara, T., Hayashi, S., Shinohara, M., Kawasaki, M., Tokura, Y., Applied Physics Letters 73, 2497 (1998)
25. Ziese, M., Semmelhack, H.C., Kan, K.H., Physical Review B 68, 134444 (2003)
26. Dvorak, J., Idzerda, Y.U., Ogale, S.B., Shinde, S., Wu, T., Venkatesan, T., Godfrey, R., Ramesh, R., Journal of Applied Physics 97, 10C102 (2005)
27. Izumi, M., Ogimoto, Y., Okimoto, Y., Manako, T., Ahmet, P., Nakajima, K., Chikyow, T., Kawasaki, M., Tokura, Y., Physical Review B 64, 64429 (2001)
28. Dörr, K., Walter, T., Sahana, M., Muller, K.H., Nenekov, K., Brand, K., Schultz, L., Journal of Applied Physics 89, 6973 (2001)
29. Bibes, M., Balcells, L., Valencia, S., Fontcuberta, J., Wojcik, M., Jedryka, E., Nadolski, S., Physical Review Letters 87, 67210 (2001)
30. Sidorenko, A.A., Allodi, G., de Renzi, R., Balestrino, G., Angeloni, M., Physical Review B 73, 54406 (2006)
31. Takamura, Y., Chopdekar, R.V., Arenholz, E., Suzuki, Y., Applied Physics Letters 92, 162504 (2008)
32. Minohara, M., Furukawa, Y., Yasuhara, R., Kumigashira, H., Oshima, M., Applied Physics Letters 94, 242106 (2009)
33. Pradhan, A.K., Hunter, D., Williams, T., Lasley-Hunter, B., Bah, R., Mustafa, H., Rakhimov, R., Zhang, J., Sellmyer, D.J., Carpenter, E.E., Sahu, D.R., Huang, J.L., Journal of Applied Physics 103, 023914 (2008)
34. Egilmez, M., Saber, M.M., Fan, I., Chow, K.H., Jung, J., Physical Review B 78, 172405 (2008)
35. Zhang, H.D., An, Y.K., Mai, Z.H., Lub, H.B., Zhao, K., Pan, G.Q., Li, R.P., Fan, R., Physica B 403, 2014 (2008)
36. Lee, Y.P., Park, S.Y., Hyun, Y.H., Kim, J.B., Prokhorov, V.G., Komashko, V.A., Svetchnikov, V.L., Physical Review B 73, 224413 (2006)

37. Sukhorukov, Y.P., Nosov, A.P., Loshkareva, N.N., Mostovshchikova, E.V., Telegin, A.V., Favre-Nicolin, E., Ranno, L., Journal of Applied Physics 97, 103710 (2005)
38. Sun, Y.H., Zhao, Y.G., Zhang, X.L., Gao, S.N., Lang, P.L., Zhang, X.P., Zhu, M.H., Journal of Magnetism and Magnetic Materials 311 644 (2007)
39. Kang, Y.M., Ulyanov, A.N., Shin, G.M., Lee, S.Y., Yoo, D.G., Yoo, S.I., Journal of Applied Physics 105, 07D711 (2009)
40. Steren, L.B., Sirena, M., Guimpel, J., Physical Review B, 65, 094431 (2002)
41. Jin, S.W., Gao, G.Y., Huang, Z., Yin, Z.Z., Zheng, X., Wu, W., Applied Physics Letters 92, 261901 (2008)
42. Zheng, R.K. Wang, Y., Chan, H.L.W., Choy, C.L., Luo, H.S., Applied Physics Letters 92, 082908 (2008)
43. Adamo, C., Ke, X,., Wang, H.Q., Xin, H.L., Heeg, T., Hawley, M.E., Zander, W., Schubert, J., Schiffer, P., Muller, D.A., Maritato, L., Schlom, D.G. Applied Physics Letters 95, 112504 (2009)
44. Sarkar, T., Ghosh, B., Raychaudhuri, A.K., Chatterji, T., Physical Review B 77, 235112 (2008)
45. Nakajima, T., Tsuchiya, T., Daoudi, K., Uedab, Y., Kumagai, Y., Materials Science and Engineering B 144 104 (2007)
46. Moshnyaga, V., Damaschke, B., Shapoval, O., Belenchuk, A., Faupel, J., Lebedev, O.I., Verbeeck, J., van Tendeloo, G., Mücksch, M., Tsurkan, V., Tidecks, R., Samwer, K., Nature Materials 2, 247 (2003)
47. Moshnyaga, V., Sudheendra, L., Lebedev, O.I., Koster, S.A., Gehrke, K., Shapova, O., Belenchuk, A., Damaschke, B., van Tendeloo, G., Samwer, K., Physical Review Letters 97, 107205 (2006)
48. Yang, H., Chi, Z.H., Yao, L.D., Zhang, W., Li, F.Y., Jin, C.Q., Yua, R.C., Journal of Applied Physics 100, 044105 (2006)
49. Haberkorn, N., Lovey, F., Condó, A.M., Guimpel, J., Journal of Applied Physics 97, 053511 (2005)
50. Varela, M., Oxley, M. P., Luo, W., Tao, J., Watanabe, M., Lupini, A. R., Pantelides, A. R., Pennycook, S. J., Physical Review B, 79, 085117 (2009)
51. Bowen, M., Maurice, J.L., Barthélémy, A., Bibes, M., Imhoff, D., Bellini, V., Bertacco, R., Wortmann, D., Seneor, P., Jacquet, E., Vaurès, A., Humbert, J., Contour, J.P., Colliex, C., Blügel, S., Dederichs, P.H., Journal of Physics : Condensed Matter 19, 315208 (2007)

52. Maurice, J.L., Imhoff, D., Contour, J.P., Colliex, C., Philosophical Magazine 86, 2127 (2006)
53. Samet, L., Imhoff, D., Maurice, J.L., Contour, J.P., Gloter, A., Manoubi, T., Fert, A., Colliex, C., The European Physical Journal B 34, 179 (2003).
54. Simon, J., Walther, T., Mader, W., Klein, J., Reisinger, D., Alff, L., Gross, R., Applied Physics Letters 84, 3882 (2004)
55. Egerton, R. F., "Electron Energy Loss in the Electron Microscope" (2nd ed.), Plenum Press, 1996.
56. Kurata, H., Colliex, C., Physical Review B, 48, 2102 (1993)
57. Garvie, L. A .J., Craven, A. J., Ultramicroscopy 54, 83 (1994)
58. Schmid, H. K., Mader, W., Micron 37, 426 (2006)
59. Marchetti, V., Ghanbaja, J., Gérardin, P., Loubinoux, B., Holzforschung 54, 553 (2000)
60. Valencia, S., Balcells, L., Fontcuberta, J., Martínez, B., Applied Physics Letters 82, 4531 (2003)
61. Valencia, S., Balcells, L., Martinez, B., Fontcuberta, J., Journal of Applied Physics 93, 8059 (2003)
62. Biswas, A., Rajeswari, M., Srivastava, R.C., Li, Y.H., Venkatesan, T., Greene, R.L. Millis, A.J., Physical Review B 61, 9665 (2000)
63. Biswas, A., Rajeswari, M., Srivastava, R.C., Venkatesan, T., Greene, R.L., Lu, Q., de Lozane, A.L. Millis, A.J., Physical Review B 63, 184424 (2001)
64. Chen, X.J., Habermeier, H.U., Zhang, H., Gu, G., Varela, M., Santamaria, J., Almasan, C.C., Physical Review B 72, 104403 (2005)
65. Potin, V., Hahn, E., Rosenauer, A., Gerthsen, D., Kuhn, B., Scholz, F., Dussaignec, A., Damilano, B., Grandjean, N., Journal of Crystal Growth 262, 145 (2004)
66. Peiró, F., Ferrer, J.C., Cornet, A., Morante, J.R., The Journal of Vacuum Science and Technology B 15, 1715 (1997)
67. Abad, L., Martinez, B., Balcells, L., Applied Physics Letters 87, 212502 (2005)
68. Gommert, E., Cerva, H., Wecker, J., Samwer, K., Journal of Applied Physics 85, 5417 (1999)
69. Daoudi, K., Tsuchiya, T., Yamaguchi, I., Manabe, T., Mizuta, S., Kumagai, T., Journal of Applied Physics 98, 013507 (2005)
70. Maurice, J.L., Pailloux, F., Barthélémy, A., Durand, O., Imhoff, D., Lyonnet, R., Rocher, A., Contour, J.P., Philosophical Magazine 83, 3201 (2003)

71. Fontcuberta, J., Infante, I.C., Laukhin, V., Sánchez, F., Wojcik, M., Jedryka, E., Journal of Applied Physics 99, 08A701 (2006)
72. Wu, X.W., Rzchowski, M.S., Wang, H.S., Li, Q., Physical Review B 61,501 (2000)
73. Campillo, G., Berger, A., Osorio, J., Pearson, J.E., Bader, S.D., Baca, E., Prieto, P., Journal of Magnetism and Magnetic Material 237, 61 (2001)
74. Paranjape, M., Raychaudhuri, A.K., Mathur, N.D., Blamire, M.G., Physical Review B 67, 214415 (2003)
75. Qin, Y.L., Zandbergen, H.W., Yang, Z.Q., Aarts, J., Philosophical Magazine 85, 4465 (2005)
76. Personal communication from Dr. M. Varela.
77. Tse, Y.Y., Chakalov, R.I., Jones, I.P., Muirhead, C.M., Huhtinen, H., Palai, R., Joural of Physics: Conference Series 126, 012051 (2008)
78. Herranz, G., Basletic, M., Bibes, M., Carretero, C., Tafra, E., Jacquet, E., Bouzehouane, K., Deranlot, C., Hamzic, A., Broto, J.M., Barthelemy, A., Fert, A., Physical Review Letters, 98, 216803 (2007)

6. Conclusions

6. Conclusions

6. Conclusions

6.1 General conclusions

The capabilities of EELS as a unique tool for the characterisation of solid state samples at the nanoscale have been demonstrated and applied to a number of materials science problems.

1) Quantitative low-loss EELS analyses have been used to assess the local composition in semiconducting materials via plasmon energy location, and to assess the local optoelectronic properties of semiconducting nanostructures.

- Local plasmon position determination has been applied to investigating the formation of lateral superlattices induced by phase separation in III-V semiconducting layers.
    - Previous two-beam BFTEM observation of InGaAs/InAlAs buffer (tensile)/InP structures using excitation g = 022 had shown quasiperiodic strong contrast modulation fringes perpendicular to the (002) direction, which seemed to indicate the presence of In-rich and Al-rich regions. HAADF observation has yielded the same quasiperiodic contrast, thus confirming the hypothesis of compositional-related contrast.
    - EELS spectra analysis has assessed a plasmon position variation, according to contrast variation as observed in HAADF. The use of a Matlab script to determine the local plasmon energy from a low-loss spectrum image, in an automated and reliable way, has been demonstrated.

- EELS has been applied to characterize the effects caused by doping GaN nanowires with Mg in order to obtain p-type nanostructures.
    - As observed by (S)TEM, the presence of Mg results in the formation of triple-twin (3T) defects, which increase with increasing Mg concentration. High concentration of misplaced atoms cause local changes in crystal structure equivalent to three non-relaxed atomic cells of zinc-blende (ZB), which define quantum wells (QW) along the wurtzite (WZ) nanowire growth axis.
    - Local EEL spectra obtained on the ZB-like and wurtzite planes show modifications in the local density of states, in which the band to band electronic transition energies change from 3.4 eV (for the wurtzite band gap) to 3.2 eV in the ZB-like lattice regions, the latter being in good agreement

with the band gap measured in GaN ZB structures by EELS. The results are confirmed by specific ab initio atomistic simulations of these two situations. EELS characterization of the optoelectronic properties of the given nanostructures at a subnanometric scale has been successfully demonstrated.

2) Elemental identification through core-loss EELS has been applied to assess interdiffusions at different kinds of interfaces.

- The composition of FePd films sputter deposited on monocrystalline V (001) buffer layers grown on MgO (001) substrates as a function of deposition temperature has been assessed through EELS and correlated with the magnetic properties.
  - A phase displaying perpendicular magnetic anisotropy (PMA) is found in films grown at temperatures above 400 °C in spite of the absence of long range chemical ordering.
  - It has been found that above 400 °C a strong V interdiffusion into the FePd layer takes place, and a FeV alloy is formed. The formation of the FeV alloy is accompanied by a two-dimensional to three dimensional growth mode transition and an increase of the mosaic spread at these temperatures. The observed PMA is thus attributed to the V interdiffusion into the FePd layer and the formation of a FeV alloy.

- $NiFe_2O_4$ (NFO) thin films of various thicknesses grown (001) $SrTiO_3$ (STO) substrates have been evaluated by EELS.
  - It is observed that NFO first grows as islands that eventually reach coalescence to form a continuous layer. A thin continuous layer, probably some kind of Fe oxide, is observed to appear at the interface between the STO and the NFO, thus making it possible for the NFO film to grow on (001) STO without APBs appearing in the layer.
  - Ti diffusion into the (001) NFO layer grown on STO has been found, probably due to the poor quality of the STO substrate.

3) Quantitative core-loss EELS has been applied to determining the stoichiometry of metal oxide nanostructures.

- Iron oxide single crystal nanowires grown by molecule-based CVD were characterized by EELS.
    - The results of the EELS analysis of the iron oxide (and of its HRTEM characterization) were consistent with magnetite, as intended in the synthesis process -moreover, no chemical variations were found within the nanostructures. In particular, the Fe/O ratio yielded a value of 0.78 ± 0.05. This figure remained consistently invariant for various wires from different batches. Catalytic (Au) diffusion into the surface of the nanowires was observed through EELS and HAADF. A higher fraction of gold was found in the thin parts of NWs, which suggests a surface diffusion process for the catalyst.
    - Core shell SnO_2/Fe_3O_4 nanowires were also considered. No interdiffusion was observed between the SnO_2 shell and the magnetite core. Spectrum image mapping of cross-sectional samples of the core shell structure suggested a complete wrapping of the SnO_2 interior by the iron oxide phase.

- The capability of EELS to determine the composition of MnOx/MnOy, FeOx/FeOy and FeOx/MnOy nanoparticles obtained by chemical methods has been demonstrated. These systems are a specially striking example of a characterization that clearly requires EELS because of the reduced sizes involved in the problems at hand.
    - MnOx/MnOy and FeOx/FeOy core-shell particles have been found to correspond to MnO/Mn_2O_3, with and additional MnO thin outer layer, and FeO/Fe_3O_4 systems.
    - Nominal FeOx/MnOy onion-like structures have been found out, in fact, to be tri-magnetic hetero-onion nanoparticles composed by core-Fe_3O_4 /shell1-$MnFe_2O_4$/shell2-Mn_2O_3.

4) The careful EELS characterization of LCMO thin films as a function of substrate/layer strain, layer orientation, layer thickness and growth rate has been carried out. In addition, STO/LCMO bilayers have also been characterized.

- In the context of the LCMO characterization by EELS, local Mn oxidation state determination is of the outmost importance. In this sense, a Matlab-based software package, MANGANITAS, has been developed to calculate the Mn L_3 peak onset and the Mn L_3/L_2 intensity ratio (both of which are measures of the Mn oxidation state) from a given series of EEL spectra.

- EELS analysis of (001) LCMO grown on $LaAlO_3$ (LAO), and thus under compressive, moderate strain (~-1.8 %), has revealed the existence of a cationic segregation process of the La atoms of the layers towards free surface. This segregation has been found together with a concomitant Mn oxidation state variation through the layer thickness, which, in turn, would result in phase separation and depleted magnetic properties. It is proposed that strain should be at the origin of this cationic migration since a way to accommodate structural strain in thin films could be by means of the segregation of ions with larger or smaller size.

- EELS analysis has also been carried out in moderately thin LCMO films grown on STO (001) and (110) substrates. In this case, LCMO grows under tensile, smaller strain (~+1.2 %). It is found that in partially relaxed (110) films cationic composition and valence state of $Mn^{3+/4+}$ ions are preserved across the film thickness -for (110) orientation, strain relaxation is apparent to be achieved via defect creation. In contrast, in fully strained (001) films, the Ca/La ratio gradually changes across the film, being La rich at film/substrate interface and La depleted at free surface; Mn valence state changes accordingly. These observations suggest that a strongly orientation-dependent adaptative composition mechanism dominates stress accommodation in manganite films.
    - Comparison between the two encountered stress accommodation mechanisms, namely defect formation for (110) orientation and cation migration for (001) orientation, in two systems with the same layer/substrate mismatch and grown in the same conditions, strongly suggest that strain accommodation via cation

migration is more detrimental to the magnetic performance than accommodation via defect creation, both because it is less effective (i.e: layers remain in higher strain conditions) and because it modifies the optimal hole doping (~1/3) in extensive regions of (001) films.

- For thicknesses below ~20 nm, a different behavior emerges, as La migration towards free surface occurs in absence of plastic relaxation irrespective of LCMO orientation. It is thus clear that the properties of moderately thin LCMO films (t>20nm) cannot be extrapolated to the thinnest ones (t<20nm). For very thin samples, growth kinetic effects rather than equilibrium balances related to stored elastic energy seem to be determinant for the chemical inhomogeneities found across the layers. It thus follows that growth rate and growth mechanism should play a critical role in the properties of LCMO layers.

- In this sense, when new LCMO layers are grown on (001) and (110) STO at a much slower growth rate the microstructure, local chemistry and Mn oxidation are radically altered. Low growth rate (001) LCMO films are chemically and electronically homogeneous, and defect-free, and (110) films present some anomalous grains (identified as MnO_2) inside the layer. Whereas (001) LCMO is fully strained, (110) LCMO is partially relaxed. Magnetic performance is found to be better for relaxed (110) LCMO than for fully strained (001) LCMO in spite of the MnO_2 grains.

- Finally, EELS data also show that, when growing a STO capping layer on top of the (001) and (110) LCMO layers, a Mn reduction is produced at the capping/electrode interface in the (001) system but not in the (110), which explains the better magnetic properties of (110) interfaces. This would be so because an electron injection would take place from the STO capping layer into the (001) LCMO electrode, and not into the (110) LCMO because of the nature of the STO terminating planes in the (110) growth direction.

- In summary, cation migration as strain relieving mechanism has been identified and demonstrated in LCMO films; concomitant Mn oxidation sate variation has been found to lead to phase separation and, thus, to depleted magnetic properties. This strain relieving mechanism has been found to be highly dependent on layer/substrate

strain magnitude and sign, on growth rate and on substrate orientation, and to take place only from a critical layer thickness onwards.

6.2 Closing remarks

It is worth remembering, as the fact that EELS is of great help for solving materials science problems becomes more evident, and more of a widespread opinion, that it still remains a playground for physicists.

Maybe what makes EELS so attractive is that it puts the experimentalist in contact with many different and challenging investigations, which require different approaches and know-hows, instead of being a routine technique. Yet, the beauty of EELS seems to lie, in fact, in the number of branches of physics that converge in it (atomic physics, solid state physics, optics, electromagnetism, etc.) and in the physics that is learned by working in it.

Appendixes

Appendix A: Sample preparation

Appendix A: Sample preparation

A.1. Introduction

As for any work devoted to a TEM-related technique, sample preparation is a most critical issue, and, sometimes, a source of endless frustration. The chosen sample preparation method depends, of course, on the morphology of the given sample (whether it is a powder sample, nanowires, a thin layer on a substrate) and, in the case of thin layers, of the nature of the substrate.

In this sense, the more favourable case would be that of layers grown on Si substrates, where the thickness of the mechanically polished sample can even be controlled by direct observation of its optical properties[2]. Multilayer samples[3] and brittle ceramic[4] or III-V semiconducting substrates[5] require a more careful approach.

A.2. Conventional preparation

For a thin layer grown on a substrate, the sample must be somehow thinned down to below a 50 nm thickness. This thinning can be done in two different geometries. If we want to observe the sample along the growth direction (i.e.: the direction of the fast incident electrons is the same as the growth direction of the sample), then we will produce a planar view (PV). If, on the contrary, we want to observe it in one direction perpendicular to the growth direction, then we will produce a cross section (XT).

If a XT is to be prepared, the sample is cut in slices of about 2.5x0.75 mm. Then two of these slices are glued together so that the active (the layer) faces of the two slices are facing each other, separated by the glue (figure A.1(a)). The obtained result will look like a kind of sandwich. This sandwich needs to be mechanically flat polished by both sides, down to a thickness of about 60 μm, as to obtain a thin foil with the glue line in the middle (figure A.1(b)).

In the case of a PV, a piece of about 2.5x2.5 mm is cut from the sample. This piece gets mechanically flat polished -by the face opposite to the active one, of course- down to a thickness of about 60 μm.

This flat mechanical polishing is usually carried out by attaching the sample to a micrometer to enable control of the sample thickness at any given time, and grinding it with silicon carbide or diamond paper under a constant water flow. In the case of certain substrates, such as MgO, the use of water in the mechanical polishing process needs to be avoided. As an alternative to the micrometer, a tripod can be used.

Disc grinding is then usually carried out: the sample is attached to a rotating stage and, by means of a spinning disc coated in diamond paste (diluted in a commercial lubricant), a semispherical indentation is made in the centre of the sample. Thinnest point is usually about 25 μm thick (figure A.1(c)). It is quite clear that disc grinding must be carried out on the face opposite to the active one in the case of PV geometry.

The roughness of the grinding is given by the grain size of the diamond paste. In the case of $SrTiO_3$ (STO) or $LaAlO_3$ (LAO) substrates, the use of diamond paste with grain size above 0.1 μm is liable to destroy the sample.

Of course, the final thickness that can be achieved after flat polishing depends, again, on the nature of the substrate. For STO, it is advisable not to get any thinner that 60 nm. For LAO one can take the risk to go down to 50 μm, as LAO is less likely to be destroyed during sample preparation (but more likely to be destroyed when manipulating the finished sample). As for Si, one can safely achieve a 20 μm thickness and skip disc grinding.

After mechanical polishing, the sample is glued to a Cu grid and then ion milling is performed.

In ion milling, the sample is attacked with argon ions until a hole is produced (figure A.1(d)). The beach around the hole will be electrotransparent and is usually referred to as the observable zone. The conditions of the argon attack greatly influence the quality of the final TEM sample[6]. In the doing of this thesis, all the conventionally prepared samples underwent an Ar+ bombardment at an anode / cathode potential bias of 5 kV and an attack angle of 7° using a PIPS-Gatan instrument.

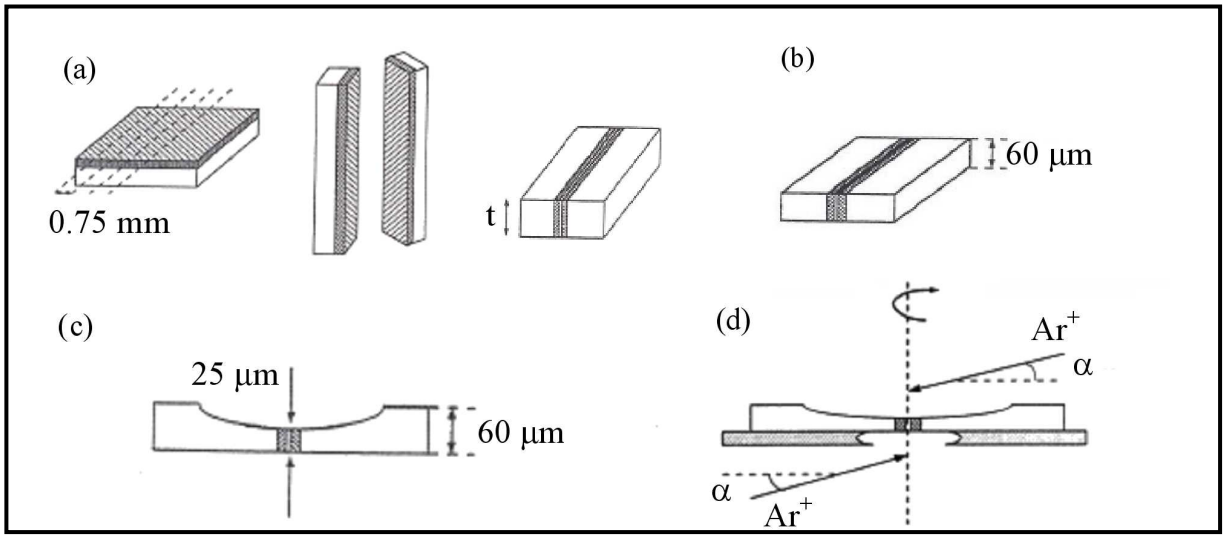

Figure A.1: *schematic representation of the different steps needed for the conventional preparation of a XT sample[5,7].*

A.3. FIB preparation

Although it may be faster to produce a XT by FIB than by conventional methods, the main reason for using FIB is that the amount of material lost from the bulk sample is much more controlled. The benefits of this are twofold: on one hand, if there is a feature of interest in the bulk sample, FIB preparation can assure that that feature will appear in the final TEM sample[8,9,10]; on the other hand, if a bulk sample is relatively small, then FIB preparation allows for a great number of TEM samples to be made.

In the doing of this thesis, most $La_{2/3}Ca_{1/3}MnO_3$ (LCMO) / STO XT samples were prepared by FIB, due to the reduced amount of available bulk sample.

To produce a FIB-prepared sample, first step is to cut a 2.5 x 2.5 mm piece from the bulk sample, put it in a SEM stab and, in case the substrate is not a good electrical conductor, deposit a sufficient layer of Au on it (figure A.2 (a)). Then, the stab is entered into the FIB, together with a suitable Cu grid. This grid is usually semicircular, with three arms, labelled A, B and C, where TEM samples will be attached to at the end of the process. The Cu grid is kept upright (at 90º from the stab surface) by an ex-professo support (figure A.2 (b)). Pt is deposited on the interest region (which can be any region if the sample is homogeneous) first electron -assisted (to minimize sample damage) and then ion-assisted. The interest region has a rectangular shape. An ion attack is used to carve two trenches at either side of the interest region. The resulting parallelepiped is cut from the substrate, and attached to a micromanipulator by Pt deposition (figure A.2 (c) and (d)). The micromanipulator is withheld and the stab is moved so that the cupper grid is now at the centre, instead of the bulk sample. The micromanipulator is then used to carry the sample to one of the arms in the Cu grid, attached to the grid by Pt deposition and cut from the micromanipulator by an ion attack. Once the sample is on the grid, ion polishing with diminishing ion intensity is used to achieve electrotransparency in the sample (figure A.2 (e) and (f)).

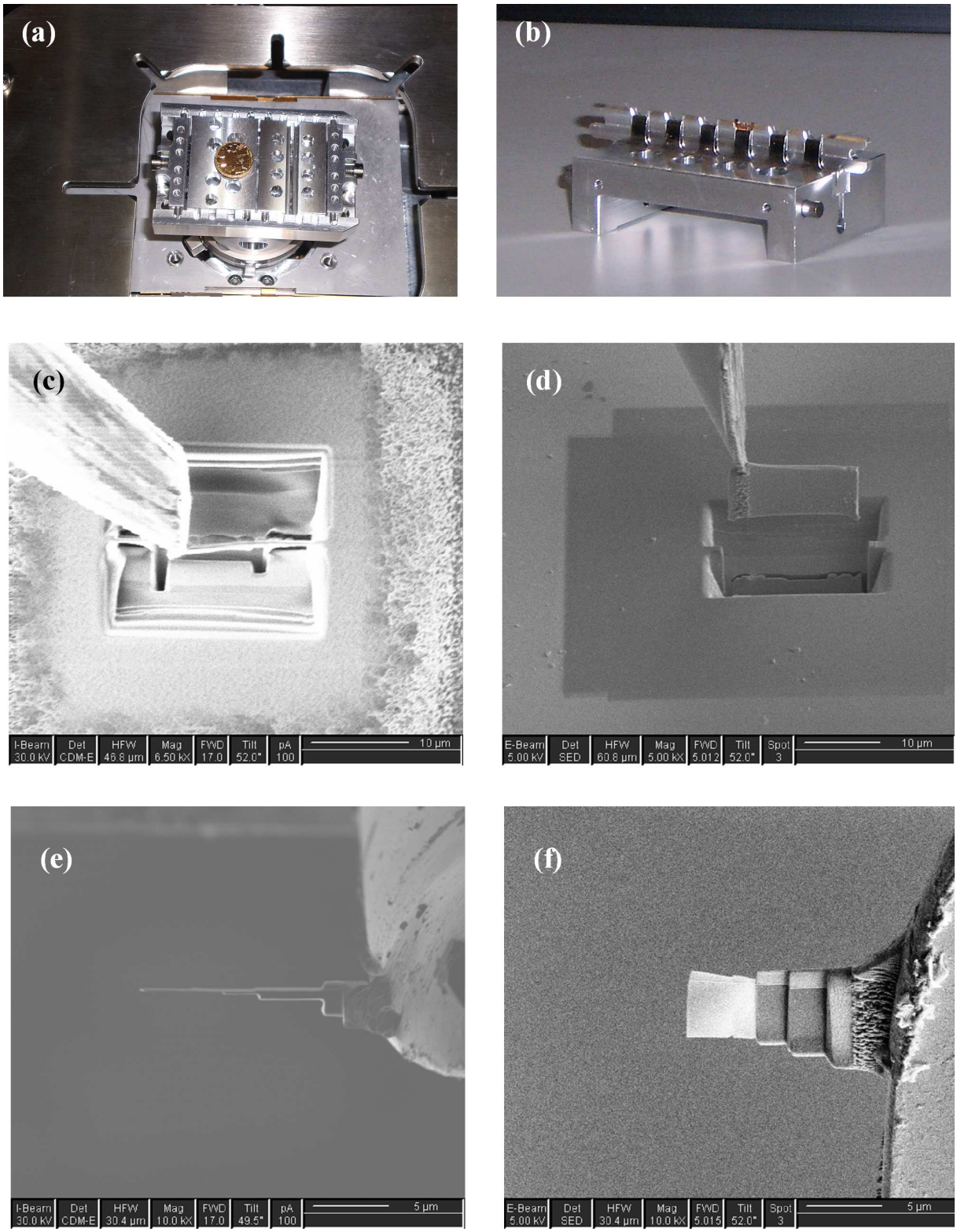

Figure A.2: *(a) SEM stab containing several samples for FIB preparation, where Au has been deposited. (b) Cupper grid kept upright. (c) Ion and (d) electron beam images of the sample attached to the micromanipulator. (e) Ion and (f) electron beam images of the thinned sample, attached to the cupper grid.*

We are grateful for the training and help in ex-situ lift-out FIB preparation to our colleagues at MIND-IN2UB, Dept. Electrònica (UB) R. Jiménez, Dr. F. Hernández and Dr. A. Romano, and in in-situ lift-out FIB preparation to R. Córdoba at Instituto de Nanociencia de Aragón.

From October 2008 on, samples have been prepared in a FEI Strata Dual Beam FIB with an Omniprobe arm.

A.4. Powder samples. Nanowires

Powder samples are easiest to prepare, as the particles involved are already electrotransparent in nature. It is just a matter of getting them dispersed and of putting them on an appropriate support for the TEM.

The usual procedure[11] is as follows

1. mix the powder with some kind of solvent (usually ethanol)
2. disperse the obtained mixture with ultrasounds
3. let one drop of the dispersed mixture fall on an appropriate grid, using a pipette
4. wait until the solvent evaporates

The appropriate grid for these samples is a Cu grid containing a holey carbon film. The particles will usually fall on the carbon; yet, some of them will end up suspended at the shore of the holes, and these ones will be optimal for analysis.

As for nanowires (NWs), they are usually mechanically removed from the substrate and made to fall on a holey carbon grid. Sometimes, the substrate / NW interface is of great importance. In this case, a XT of the whole system is prepared. A different problem arises when it is critical to observe the NW along its growth direction (as in the case of core-shell NWs). Then, a XT of the NWs (not of the whole system) must be obtained.

A.5. References

1. Williams, D. B. and Carter, C.B., "Transmission Electron Microscopy: A Textbook for Materials Science Basics", Plenum Press (1996)
2. McCaffrey, J.P., Hulse, J., Micron 29, 139 (1998)
3. Weaver, L., Microscopy Research and Related Technique, 36, 368 (1997)
4. Strecker, A., Salzberger, U., Mayer, J., Praktische Metallographie. 30, 482 (1993)
5. Peiró, F., Thesis, Universitat de Barcelona (1993)
6. Strecker, A., J. Mayer, J., Baretzky, B., Eigenthaler, W., Gemming, T., Schweinfest R., Rühle, M., Journal of Electron Microscopy 48, 235 (1999)
7. Romano, A., Vanhellemont, J., Bender, H., Morante, J.R., Ultramicroscopy, 31, 183 (1989)
8. Gianuzzi, L.A., Drown, J.L., Brown, S.R., Irwin, R.B., Stevie, F.A., Microscopy Research and Related Technique, 41, 285 (1998)
9. Lee, M.R., Bland, P.A., Graham, G., 67, 581 (2003)
10. Gasser, P., Klotz, U.E., Khalid, F.A., Beffort, O., Microscopy and Microanalysis, 10, 311 (2004)
11. Arbiol, J., Thesis, Universitat de Barcelona (2001)

Appendix B: Resum en català

Resum en català

En el microscopi electrònic de transmissió (TEM), un electró incident sofreix tant xocs elàstics com inelàstics en travessar la mostra prima d'estat sòlid que s'està caracteritzant. En cas de xoc inelàstic, l'electró incident cedeix part de la seva energia als electrons de la mostra. La quantitat d'energia perduda es pot mesurar amb un filtre magnètic situat al final de la columna, i un gràfic que indiqui quants electrons han perdut quina quantitat d'energia ens donarà un espectre de pèrdua d'energia dels electrons, o espectre EELS. Així, en un espectre EELS l'ordenada correspon al número d'electrons, o comptes, i l'abscissa, a la pèrdua d'energia.

Cal notar que la majoria d'electrons no patiran cap xoc inelàstic en absolut. En conseqüència, la contribució més important a un espectre EELS vindrà donada per electrons que no han perdut energia, donant lloc al que es coneix com a pic de zero pèrdues, en anglès zero loss peak (ZLP).

Pel que fa als electrons incidents que han perdut una certa quantitat d'energia, la poden perdre ionitzant electrons de la mostra, en transicions entre estats atòmics profunds ocupats i estats atòmics profunds lliures o estats de la banda de conducció, en transicions interbanda o excitant vibracions col·lectives dels electrons de la banda de conducció.

Els electrons incidents porten un cert moment, i és important recordar que en un scattering inelàstic no només s'intercanviarà energia, sinó que també es pot transferir moment. De fet, aquest és el motiu pel qual és no trivial comparar els resultats d'EELS amb els obtinguts per mitjà d'una espectroscòpia òptica, com ara l'espectroscòpia d'absorció de raigs X (XAS).

Avui en dia l'EELS s'ha convertit en un instrument crucial a la ciència de materials, per causa de la progressiva reducció de l'escala característica implicada en el desenvolupament d'aquesta disciplina, i també gràcies a la millora instrumental que ha tingut lloc en els darrers anys tant en la microscòpia electrònica en general com en l'EELS en particular.

Com que els experiments d'EELS es duen a terme en el TEM, l'EELS es beneficia de la gran resolució espacial que s'hi pot assolir -els electrons es poden enfocar fins a formar un feix

subnanomètric. En particular, si es fa servir un canó d'emissió de camp, es pot obtenir un feix d'1nm amb corrent suficient. En un instrument corregit d'aberracions, la mida del feix pot baixar fins a 0.1 nm. A més, els resultats d'EELS es poden combinar fàcilment amb la caracterització estructural obtinguda a través dels modes d'imatge i de difracció del TEM.

Hi ha un límit fonamental en la resolució espacial que es pot obtenir per EELS més enllà de les limitacions dels sistemes òptics del TEM. Aquest límit ve donat per la deslocalització que es produeix en els xocs inelàstics i que depèn de l'energia intercanviada (com més petita l'energia, més gran la deslocalització). Tot i així, afortunadament, aquest límit no impedeix obtenir informació espectroscòpica de columnes atòmiques individuals.

En aquesta tesi, s'han explorat les capacitats de l'EELS com a eina de caracterització de mostres d'estat sòlid a la nanoescala, i s'han aplicat a diversos problemes de ciència de materials.

En primer lloc, s'ha considerat l'anàlisi quantitativa de la regió de baixes pèrdues de l'espectre:

- La determinació local de l'energia del plasmó s'ha aplicat a la investigació de fenòmens de segregació lateral en semiconductors III-V. En aquest sentit, s'ha desenvolupat un programa en entorn Matlab per trobar l'energia del plasmó de manera fiable i repetitiva. Observacions anteriors en camp clar en condicions de dos feixos havien revelat un contrast en capes d'InAlAs que semblava correspondre a regions més riques en In o en Al. Les imatges en HAADF d'aquestes capes mostren el mateix contrast quasiperiòdic. La variació del plasmó té la mateixa periodicitat (d'uns 130 nm) i efectivament sembla correspondre's amb una variació composicional.

- L'EELS de baixes pèrdues també s'ha aplicat a la caracterització de nanofils de GaN dopats amb Mg per obtenir nanoestructures de tipus p. Les observacions de (S)TEM indiquen la formació de defectes en els nanofils, més com més dopada està l'estructura. Els defectes són equivalents a tenir tres plans de GaN de tipus zinc-blenda (ZB) en un nanofil de GaN de tipus wutzita (W). Els espectres EELS obtinguts en les regions ZB i W demostren que les seves propietats optoelectròniques són diferents, i en particular que el gap passa de ser de 3.4 eV (per la wurtzita) a 3.2 eV en les zones

de ZB, número que està en bon acord amb el gap obtinguts per EELS en GaN ZB. Els resultats s'han contrastat amb simulacions ab initio dels espectres EELS obtinguts. L'EELS ha permès, doncs, caracteritzar les propietats optoelectròniques dels nanofils a una escala subnanomètrica.

La identificació elemental per EELS de pèrdues profundes s'ha aplicat a l'estudi d'interdifusions en diferents tipus d'interfícies:

- La composició de capes de FePd crescudes per polvorització catòdica sobre una capa tampó monocristal·lina de (001) V, sobre un substrat de (001) MgO, en funció de la temperatura de creixement, s'ha estudiat per EELS i s'ha correlacionat amb les seves propietats magnètiques. S'ha trobat una fase amb anisotropia magnètica perpendicular (PMA) a partir de 400ºC, malgrat l'absència d'ordre químic de llarg abast. També a partir dels 400ºC, s'ha trobat una forta difusió del V cap a la capa de FePd. La PMA observada s'ha atribuït a la formació d'un aliatge FeV.

- Capes primes de $NiFe_2O_4$ (NFO) de diferents gruixos i crescudes sobre (001) $SrTiO_3$ (STO) han estat estudiades per EELS. El NFO creix en els primers estadis com a illes que coalesceixen per formar una capa contínua. Entre capa i substrat sempre s'observa una capa contínua, molt prima, d'òxid de Fe. Probablement aquesta capa intermèdia permet que la capa de NFO creixi sense defectes sobre el STO. A més, s'ha trobat difusió del Ti del susbstrat cap a la capa, probablement deguda a la baixa qualitat cristal·lina del substrat.

L'EELS quantitatiu de pèrdues profundes s'ha aplicat a determinar l'estequiometria de nanoestructures d'òxids metàl·lics:

- S'ha caracteritzat per EELS nanofils d'òxid de ferro crescuts per dipòsit químic en fase vapor (CVD). Els resultats d'aquesta caracterització, així com els de la caracterització per TEM, apunten que l'òxid obtingut és magnetita, tal i com era l'objectiu de la síntesi. A més, no s'han trobat variacions químiques ni dins d'un mateix nanofil ni entre nanofils diferents, crescuts alhora o no. S'ha trobat interdifusió del catalític, en aquest cas or, cap a la superfície dels nanofils. De fet, s'ha trobat una fracció d'or més important en les zones més primes del fil, suggerint un procés de

difusió superficial del catalític. També s'han caracteritzat nanofils core-shell de SnO_2/Fe_3O_4. En aquest cas no s'ha trobat interdifusió entre les dues parts de l'estructura.

- S'ha trobat per EELS la composició de nanopartícules de MnOx/MnOy, FeOx/FeOy i FeOx/MnOy obtingudes per mètodes químics. S'ha trobat que les partícules core-shell MnOx/MnOy i FeOx/FeOy corresponen als sistemes MnO/Mn_2O_3, amb una capa addicional externa de MnO, i FeO/Fe_3O_4, respectivament. S'ha trobat també que les partícules a què nominalment s'atribuïa una composició FeOx/MnOy corresponen a un sistema triple de nucli-Fe_3O_4 /capa1-$MnFe_2O_4$/capa2-Mn_2O_3.

S'ha dut a terme la caracterització detallada de capes primes de $La_{2/3}Ca_{1/3}MnO_3$ (LCMO) en funció de la desadaptació entre capa i substrat, l'orientació de la capa, el seu gruix i el seu ritme de creixement. A més, s'ha caracteritzat el sistema STO/LCMO/STO:

- En el context de la caracterització per EELS de les capes de LCMO, la determinació local de l'estat d'oxidació del Mn té una gran importància. En aquest sentit, s'ha desenvolupat un software en entorn Matlab, el MANGANITAS, que calcula la posició del pic L_3 del Mn i la relació d'intensitats entre els pics L_3 i L_2 del Mn (que són mesures de l'estat d'oxidació del Mn) a partir d'una sèrie donada d'espectres EELS.

- L'anàlisi per EELS de capes de (001) LCMO crescudes sobre $LaAlO_3$ (LAO), i, per tant, sota tensions de tipus compressiu, ha mostrat l'existència d'un procés de segregació catiònica dels àtoms de La de les capes cap a la superfície lliure. S'ha trobat també una variació concomitant en l'estat d'oxidació del Mn al llarg de la capa, i, per tant, una segregació de fases que afecta negativament les propietats magnètiques. Es proposa que les tensions són a l'origen de la migració catiònica, ja que una manera d'acomodar aquestes tensions seria la segregació dels ions amb radis iònics més grans (o més petits, si les tensions fossin de tipus expansiu).

- L'anàlisi per EELS també s'ha dut a terme per capes moderadament gruixudes de LCMO crescudes sobre STO (001) i (110). En aquest cas les capes creixen sota tensions expansives, i menys importants que en el cas del MAO. Es troba que per les capes (110), on les tensions relaxen mitjançant la creació de defectes, la composició

nominal i l'estat de valència $Mn^{3+/4+}$ es mantenen al llarg de la capa. En canvi, per les capes (001), tensionades, hi ha una migració de Ca cap a la superfície lliure, i l'estat d'oxidació del Mn canvia d'acord amb la variació en composició. Es proposa, per tant, que un mecanisme de canvi de composició, fortament depenent de l'orientació, governa la química de les capes de LCMO de gruix moderat. Les mesures magnètiques indiquen que la migració catiònica és més negativa per a les propietats de les capes que la formació de defectes.

- Per gruixos de les capes per sota d'uns 20 nm, on l'energia elàstica acumulada és menor, emergeix un nou patró de comportament: es troba migració de La cap a la superfície lliure per les dues orientacions, i per cap de les dues orientacions s'observen defectes. Es proposa que els factors cinètics de creixement són els que determinen el comportament de les capes més primes. D'això se segueix que el ritme i els mecanismes de creixement juguen un paper crucial en les propietats del LCMO.

- En aquest sentit, quan les capes de (001) i LCMO (110) es creixen a un ritme molt més baix, la microestructura, la composició local i l'estat d'oxidació del Mn canvien radicalment. Les capes de (001) LCMO crescudes a ritme baix són homogènies tant química com electrònicament, i sense defectes, i les capes (110) presenten grans anòmals (identificats com a MnO_2) dins de la capa. Les capes (001) estan totalment tensionades i les (110) parcialment relaxades. Les propietats magnètiques són millors per les capes (110), relaxades, que per les (001), tensionades, malgrat els grans de MnO_2.

- Finalment, les dades d'EELS també mostren que quan es creix una capa de STO sobre LCMO (001) i (110), es produeix una reducció del Mn en la interfície superior en el sistema (001) però no en el (110), cosa que explica les millors propietats magnètiques de les interfícies (110). Això seria així perquè es produeix una injecció d'electrons des del STO cap al LCMO en les capes (001), però no en les (110) a causa del tipus de plans de STO en contacte amb el LCMO en aquest cas.

- En resum, s'ha identificat la migració catiònica com a mecanisme d'acomodació de les tensions en capes de LCMO; també s'ha trobat una variació concomitant de l'estat d'oxidació del Mn, que porta a una separació de fases i, en conseqüència, a un

empitjorament de les propietats magnètiques. S'ha trobat que aquest mecanisme és fortament depenent del mòdul i el signe de la desadaptació entre capa i substrat, del ritme de creixement de les capes i de l'orientació del substrat. A més, s'ha identificat un gruix crític des del què es produeix.

Appendix C: Scientific Curriculum

Date and place of birth:
Barcelona, 13-02-1982
Education and scientific degree:
Graduate in Physics, University of Barcelona 2005
Master in Nanotechnology, University of Barcelona 2007

Journal Publications

1. Clavero, C.; García-Martín, J. M.; Armelles, G.; Cebollada, A.; Huttel, Y.; Estradé, S.; Arbiol, J.; Peiró, F.; Balcells, Ll., Perpendicular magnetic anisotropy in chemically disordered FePd-FeV(100) alloy thin films, Journal of Applied Physics, 99, 073903 (2006).
2. Martí,X.; Sánchez, F.;Hrabovsky, D.; Fontcuberta, J.; Laukhin, V.; Skumryev,V.; García-Cuenca,M.V.; Ferrater, C.; Varela, M.; Estradé, S.; Arbiol, J.; Peiró, F., Epitaxial growth of biferroic YMnO3(0001) on platinum electrodes, Journal of Crystal Growth, 299, 288 (2006).
3. Infante, I.C.; Sánchez, F.; Fontcuberta, J.; Fusil, S.; Bouzehouane, K.; Herranz, G.; Barthélémy, A.; Estradé, S.; Arbiol, J.; Peiró, F.; Mossanek, R.J.O.; Abbate, M.; Wojcik, M., Structural and functional characterization of (110)-oriented epitaxial La2/3Ca1/3MnO3 electrodes and SrTiO3 tunnel barriers., Journal of Applied Physics, 101, 093902 (2007).
4. Rigato, F.; Estradé, S.; Arbiol, J.; Peiró, F.; Lüders, U.; Martí, X.; Sánchez, F.; Fontcuberta, J., Strain-induced stabilization of new magnetic spinel structures in epitaxial oxide heterostructures., Materials Science and Engineering B, 144, 43 (2007).
5. Infante, I.C.; Sánchez, F.; Fontcuberta, J.; Wojcik, M.; Jedryka, E.; Estrade, S.; Peiro, F.; Arbiol, J.; Laukhin, V.; Espinós, J.P., Elastic and orbital effects on thickness-dependent properties of manganite thin films., Physical Review B, 76, 224415 (2007).
6. Estradé, S.; Arbiol, J.; Peiró, F.; Abad, Ll.; Laukhin, V.; Balcells, Ll.; Martínez, B., Cationic Diffusion in La2/3Ca1/3MnO3 Thin Films Grown on LaAlO3 (001) Substrates, Applied Physics Letters, 91, 252503 (2007).
7. Tarancón, A.; Morata, A.; Dezanneau, G.; Skinner, S.J.; Kilner, J.A.; Estradé, S.; Hernández, F.; Peiró, F.; Morante, J.R., GdBaCo2O5+x layered perovskite as an intermediate temperature solid oxide fuel cell cathode, Journal of Power Sources, 174, 2957 (2007).
8. Rossinyol, E.; Pellicer, E.; Prim, A.; Estradé, S.; Arbiol, J.; Peiró, F.; Cornet, A.; Ramon Morante, J., Gadolinium doped Ceria nanocrystals synthesized from mesoporous silica., Journal Of Nanoparticle Research, 369, 2957 (2008).
9. Infante, I.C.; Sánchez, F.; Fontcuberta, J.; Estradé, S.; Peiró, F.; Arbiol, J.; Wojcik, M.; Jedryka, E., Effects of SrTiO3 capping in La2/3Ca1/3MnO3 electrodes of different orientations, Journal of Applied Physics, 103, 07E302 (2008).
10. Balcells, Ll.; Abad, Ll.; Rojas, H.; Perez del Pino, A.; Estrade, S.; J. Arbiol, J.; Peiro, F.; Martinez, B., Transport properties across the La2/3Ca1/3MnO3 /SrTiO3 heterointerface, Journal of Applied Physics, 103, 07E303 (2008).
11. Morata, A.; Chesnaud, A.; Tarancón, A.; Estradé, S.; Peiró, F.; Morante, J.R.; Dezanneau, G., A Versatile and Low-Toxicity Route for the Production of Electroceramic Oxide Nanopowders, European Journal of Solid State and Inorganic Chemistry, 2008, 954 (2008).
12. Balcells, Ll; Abad, Ll; Rojas, H; Perez del Pino, A; Estrade, S; Arbiol, J; Peiro, F; Martínez, B., Electronic Effects in Manganite/Insulator Interfaces: Interfacial Enhancement of the Insulating Tunneling Barriers, Small, 3, 365 (2008).
13. Furtmayr, F.; Vielemeyer, M.; Stutzmann, M.; Arbiol, J.; Estradé, S.; Peiró, F.; Morante, J. R.; Eickhoff, M.., Nucleation and growth of GaN nanorods on Si (111) surfaces by plasma-assisted molecular beam epitaxy-The influence of Si- and Mg-doping., Journal of Applied Physics, 104, 034309 (2008).

14. Estradé, S.; Arbiol, J.; Peiró, F.; Infante, I. C.; Sánchez, F.; Fontcuberta, J.; de la Peña, F.; Walls, M.; Colliex, C., Cationic and charge segregation in La2/3Ca1/3MnO3 thin films grown on (001) and (110) SrTiO3, Applied Physics Letters, 93, 112505 (2008).

15. Arbiol, J.; Morral, A. F. I.; Estradé, S.; Peiró, F.; Kalache, B.; Cabarrocas, P. R. I.; Morante, J. R., Influence of the (111) twinning on the formation of diamond cubic/diamond hexagonal heterostructures in Cu-catalyzed Si nanowires, Journal of Applied Physics, 104, 064312 (2008).

16. Barth, S.; Estrade, S.; Hernandez-Ramirez, F.; Peiro, F.; Arbiol, J.; Romano-Rodriguez, A.; Morante, J. R.; Mathur, S.; Studies on Surface Facets and Chemical Composition of Vapor Grown One-Dimensional Magnetite Nanostructures, Crystal Growth and Design, 9, 1077 (2009).

17. Cebollada, A.; García Martín, J. M.; Clavero, C.; Balcells, Ll.; Estradé, S.; Arbiol, J.; Peiró, F.; Smith, C.; Clarke, R.; Martínez, L.; Huttel, Y.; Román, E.; Telling, N.D.; van der Laan, G. Growth and magnetic characterization of Co nanoparticles obtained by femtosecond pulsed laser deposition, Physical Review B, 79, 014414 (2009).

18. Arbiol, J.; Estradé, S.; Prades, J. D.; Furtmayr, F.; Stark, C.; Lauferd, A.; Stutzmann, M.; Eickhoff, M.; Gass, M. H.; Bleloch, A. L.; Peiró, F.; Morante, J. R., Double-Twin Domains in Mg doped GaN Wurtzite Nanowires: Structural and Electronic Properties of This Zinc-Blende-like Stacking, Nanotechnology, 20, 145704 (2009).

19. Zardo, I.; Wei, L.; Conesa-Boj, S.; Estradé, S.; Alet, P. J.; Frimmer, M.; Simon, J.; Roca i Cabarrocas, P.; Peiró, F.; Arbiol, J.; Morante, J. R.; Fontcuberta i Morral, A., Gallium assisted Plasma Enhanced Chemical Vapor Deposition of silicon nanowires., Nanotechnology, 20, 155602 (2009).

20. Xiang, Y.; Cao, L.; Conesa-Boj, S.; Estrade, S.; Arbiol, J.; Peiro, F.; Heiss, M.; Zardo, I.; Morante, J. R.; Brongersma, M. L.; Morral, A. F. I., Gallium assisted plasma enhanced chemical vapor deposition of silicon nanowires Single crystalline and core-shell indium-catalyzed germanium nanowires-a systematic thermal CVD growth study, Nanotechnology, 20, 245608 (2009).

21. Estradé, S.; Rebled, J. M.; Arbiol, J.; Peiró, F.; Infante, I. C.; Herranz, G.; Sánchez, F.; Fontcuberta, J.; Córdoba, R.; Mendis, B. G.; Bleloch, A. L., Effects of Thickness on the Cation Segregation in Epitaxial (001) and (110) La2/3Ca1/3MnO3 thin films, Applied Physics Letters, 95, 072507 (2009).

Book Publications

1. Estrade, S.; Arbiol, J.; Peiro, F., EELS and STEM assessment of composition modulation in InAlAs tensile buffer layers of InGaAs/InAlAs/(100)InP structures. *Springer Proceedings in Physics -Microscopy of Semiconducting Materials 2007*. Springer Netherlands (2007).

2. Hernandez-Ramírez, F.; Prades, J.D.; Barth, S.; Romano-Rodriguez, A.; Mathur, S.; Tarancón, A.; Casals, O.; Jimenez-Diaz, R; Rodriguez, J; Pellicer, E.; Juli, M.A.; Andreu, T.; Estrade, S.; Rossinyol, E.; Morante, J.R., Morante, Fabrication of Nanodevices Based on Individual SnO2 Nanowires and Their Electrical Characterisation. *Metal Oxide Nanostructures and Their Applications* (Ed. A. Umar). American Scientific Publishers (ASP) (2009).

Referee for the following journals

1. Sensors & Actuators: B. Chemical.
2. Central European Journal of Chemistry.
3. Crystal Research and Technology.
4. Journal of Sensors.

Research stages abroad

1. Stage at Laboratoire de Physique des Solides - Groupe STEM (Orsay, France), 3 months (2007).
2. Stage at SuperSTEM UK (Daresbury, UK), 3 months (2008).

Attendance to Transmission Electron Microscopy Schools

1. Title: EMAT Winter School on Transmission Electron Microscopy 2005. Antwerp (Belgium), 10 january - 4 february 2005. University of Antwerp.
2. Electron Crystallography School 2005- ELCRYST 2005: New frontiers in Electron Crystallography. Bruxels(Belgium), 2-8 september 2005. Satellite conference of the XX IUCr congress.
3. Nanotem School. Cadiz, 8-9 june 2006. European Network of Excellence SANDiE and Cadiz University.
4. IMC16 (16th international microscopy congress) One-day pre-Congress School. Sapporo (Japan), 3 september 2006. International Microscopy Society.
5. Winter HAADF and EELS Workshop (WHEW). Orsay (France), 10-12 december 2007. Laboratoire de Physique des Solides. French Microscopical Society.
6. SuperSTEM Summer School. Warrington (UK), 27-29 June 2008. SuperSTEM UK.

Conferences

1. Authors: Cebollada, A; Clavero, C.; Costa-Krämer, J.L.; García J.M.; Armelles, G.; Huttel, Y.; Balcells, LL.; Lukaszev, R.A.; Estradé, S.; Arbiol, J.; Peiró, F. Title: Structure-Magnetism correlations in continuous and self-organized, high anisotropy epitaxial FePd Alloys. Kind of participation: Presentation of communication. Conference: XIV Congreso Internacional de Investigación en Materiales. Cancún, México (2005).
2. Authors: Estradé, S.; Arbiol, J.; Peiró, F.; Cornet, A.; Clavero, C.; Huttel, Y.; Cebollada, A.; Armelles, G. Title: Dependencia con la temperatura de la difusión del V de la capa tampón en capas magnéticas de FePd. Kind of participation: Presentation of communication. Conference: XXII Reunión Bienal de la Sociedad de Microscopía de España (SME XXII). Granada, Spain (2005).
3. Authors: Infante, I.C.; Lauhkin, V.; Sanchez, F.; Estradé, S.; Peiró, F.; Wojcik, M.; Jedryka, E.; Fontcuberta, J.Title: Reduced electronic phase separation in La2/3Ca1/3MnO3/SrTiO3(110) interfaces. Kind of participation: Presentation of communication. Conference: 3rd THIOX workshop: Workshop on Oxides at the Nanoscale. Zaragoza, Spain (2005).
4. Authors: Infante, I.C.;Laukhin, V.;Sánchez, F.;Estradé, S.;Arbiol, J.;Peiró, F.;Wojcik, M.;Jedryka, E.;Espinós, J.P.;Fontcuberta, J. Title: Dissimilar epitaxy of La2/3Ca1/3MnO3 on (001) and (110)SrTiO3 and impact on transport and magnetic properties. Kind of participation: Presentation of communication. Conference: III Joint European Magnetic Symposia, San Sebastián, Spain (2006).
5. Authors: Estradé, S.; Arbiol, J.; Peiró, F.; Abad, Ll.; Laukhin, V.; Balcells, Ll.; Martinez, B. Title: Effects of the annealing Treatment on La2/3Ca1/3MnO3 Layers Grown on (001) LaAlO3 Substrates. Kind of participation: Presentation of communication. Conference: IMC16 (The 16th International Microscopy Congress). Sapporo, Japan (2006).
6. Authors: Estradé, S.; Arbiol, J.; Peiró, F.; Infante, I.C.; Laukhin, V.; Sánchez, F.; Wojcik, M.; Jedryka, E.; Fontcuberta, J. Title: Comparative EELS Analysis of La2/3Ca1/3MnO3 Layers Depending on (001) or (110) SrTiO3 Substrate Orinetation. Kind of participation: Poster. Conference: IMC16 (The 16th International Microscopy Congress). Sapporo, Japan (2006).

7. Authors: García-Martin, J.M.; Cebollada, A.; Clavero, C.; González, J.B.; Asenjo, R.; García-Martín, A.; Armelles, G.; Smith, C.; Kumah, D.; Clarke R.; Balcells, Ll.; Estradé, S. and Peiró, F. Title: Magnetic nanoparticles obtained by advandec physical methods for magneto-plasmonic devices. Kind of participation: Presentation of communication. Conference: XV International Material Research Congress. Cancún, México (2006).
8. Authors: Infante, I.C.; Laukhin, V.; Sánchez, F.; Estradé, S.; Arbiol, J.; Peiró, F.; Wojcik, M.; Jedryka, E.; Espinós, J.P.; Fontcuberta, J. Title: Dissimilar epitaxy of La2/3Ca1/3MnO3 on (001) and (110)SrTiO3 and impact on transport and magnetic properties. Kind of participation: Presentation of communication. Conference: IV Reunión Nacional de Física del Estado Sólido (GEFES IV). Alacant, Spain (2006).
9. Authors: Abad, Ll.; Laukhin, V.; Balcells, Ll.; Estrade, S.; Arbiol, J.; Peiró F.; and Martínez, B. Title: Structural, magnetic and transport properties of La2/3Ca1/3MnO3/ LaAlO3 (001) epitaxial thin films. Kind of participation: Presentation of communication. Conference: IV Reunión Nacional de Física del Estado Sólido (GEFES IV). Alacant, Spain (2006).
10. Authors: Estradé, S.; Arbiol, J.; Peiró, F.; Infante, I. C.; Laukhin, V.; Sánchez, F.; Wojcik, M.; Jedryka, E.; Fontcuberta, J.; Title: Microscopía Electrónica de Transmisión de Capas de La1/3Ca2/3MnO3 Sobre Substratos de SrTiO3 (001) y (110) para Aplicaciones en Uniones Túnel Magnéticas. Kind of participation: Presentation of communication. Conference: IX Congreso Nacional de Materiales. Vigo, Spain (2006).
11. Authors: Estradé, S.; Arbiol, J.; Peiró, F.; Martí, X.; Sánchez, F.; Hrabovsky, D.; Fontcuberta, J. Title: TEM Characterization of biferroic YMnO3(0001) on platinum electrodes. Kind of participation: Presentation of communication. Conference: XXII Trobades científiques de la mediterrània. Maó, Spain (2006).
12. Authors: Fontcuberta, J.; Martí, X.; Sánchez , F.; Hrabovsky, D.; Laukhin, V.; Skumryev, V.; García-Cuenca, M.V.; Ferrater, C.; Varela, M.; Estradé, S.; Arbiol, J.; Peiró, F.; Lüders, U.; Bobo, J.F. Title: Tunable exchange bias with biferroic YMnO3 epitaxial films. Kind of participation: Presentation of communication Conference: XIII International Workshop on Oxide Electronics. Ischia, Italy (2006).
13. Authors: Infante, I.C.; Sánchez, F.; Bouzehouane, K.; Fusil, S.; Laukhin, V.; Pérez del Pino, A.; Estradé, S.; Arbiol, J.; Peiró, F.; Wojcik, M.; Jedryka, E.; Fontcuberta, J. Title: Fabrication and characterization of SrTiO3(110) nanometric barriers for magnetic tunnel junctions. Kind of participation: Poster. Conference: XIII International Workshop on Oxide Electronics. Ischia, Italy (2006).
14. Authors: Estrade, S.; Arbiol, J.; Peiro, F. Title: EELS and STEM assessment of composition modulation in InAlAs tensile buffer layers of InGaAs /InAlAs /(100)InP structures. Kind of participation: Poster. Conference: Microscopy of Semiconducting Materials. Cambridge, England (2007).
15. Authors: Arbiol, J.; Estrade, S.; Peiro, F.; Fontcuberta i Morral, A.; Morante, J. Title: Analysis of phase boundary defects on high-temperature Si NWs grown on silica amorphous substrates: HRTEM vs EELS low loss spectra. Kind of participation: Presentation of communication. Conference: Microscopy of Semiconducting Materials. Cambridge, England (2007).
16. Authors: Estrade, S.; Arbiol, J.; Peiro, F.; Rigato, F.; Sanchez, F.; Fontcuberta, J.Title: Comparative HRTEM and EELS study of epitaxial growth of NiFe2O4 spinel on MgAl2O4 and SrTiO3 substrates. Kind of participation: Presentation of communication. Conference: E-MRS Spring Meeting. Starsbourg, France (2007).
17. Authors: F. Rigato , S. Estrade , J.Arbiol , F. Peiro , X. Marti , F. Sanchez , J. Fontcuberta. Title: Strain-induced stabilization of new magnetic spinel structures in epitaxial oxide heterostructures. Kind of participation: Presentation of communication. Conference: E-MRS Spring Meeting. Starsbourg, France (2007).
18. Authors: Moreno, C.; Abellán, P.; Ruyter, A.; Hassini, A.; Estrade, S.; Pérez del Pino, A.; Sandiumenge, F.; Puig, T.; Obradors, X. Title: Epitaxial La2O3 islands on La1-xSrxMnO3 : toward nanoscale control of the magnetic anisotropy Kind of participation: Poster. Conference: E-MRS Spring Meeting. Starsbourg, France (2007).

19. Authors: Arbiol, J.; Estradé, S.; Peiró, F.; Fontcuberta i Morral, A.; Morante, J. R. Title: Wurtzite Phase on Si NWs. Kind of participation: Presentation of communication. Conference: E-MRS Spring Meeting. Starsbourg, France (2007).

20. Authors: Estradé, S.; Arbiol, J.; Peiró, F. Title: Variación de la Energía del Plasmón en Capas Tampón de InAlAs en Estructuras InGaAs/InAlAs/(100)InP. Kind of participation: Presentation of communication Conference: XXIII Reunión Bienal de la Sociedad de Microscopía de España (SME XXIII). Bilbao, Spain (2007).

21. Authors: Arbiol, J.; Estradé, S.; Spirkoska, D.; Fontcuberta i Morral, A.; Peiró, F.; Abstreiter, G.; Morante, J. R. Title: Estudio por HRTEM y EELS de Nanohilos de (Al)GaAs con y sin Heterostructura a partir de Semillas Cataliticas de Ga. Kind of participation: Presentation of communication. Conference: XXIII Reunión Bienal de la Sociedad de Microscopía de España (SME XXIII). Bilbao, Spain (2007).

22. Authors: Arbiol, J.; Fontcuberta i Morral, A.; Estradé, S.; Peiró, F.; Kalache, B.; Roca i Cabarrocas, P.; Abstreiter, G.; Morante, J. R. Title: Propiedades Estructurales y Discusión del Modelo de Crecimiento en Nanohilos de Si con Heterostructura Cúbica/Hexagonal (Si I/Si IV). Kind of participation: Presentation of communication. Conference: XXIII Reunión Bienal de la Sociedad de Microscopía de España (SME XXIII). Bilbao, Spain (2007).

23. Authors: Estradé, S.; Arbiol, J.; Peiró, F.; Infante, I. C.; Laukhin, V.; Sánckez, F.; Wojcik, M.; Jedryka, E.; Fontcuberta, J. Title: Migración de La en Capas de La2/3Ca1/3MnO3 crecidas sobre Sustratos de SrTiO3 con Orientaciones (001) y (110). Kind of participation: **Invited conference**. Conference: XXIII Reunión Bienal de la Sociedad de Microscopía de España (SME XXIII). Bilbao, Spain (2007).

24. Authors: Estradé, S.; Infante, I.C.; Laukhin, V.; Sanchez, F.; Wojcik, M.; Jedryka, E.; Fontcuberta, J.; Arbiol, J.; Peiró, F. Title: Cation migration in thin La2/3Ca1/3MnO3 layers depending on substrate orientation. Kind of participation: Poster. Conference: MRS. Boston, USA (2007).

25. Authors: Arbiol, J.; Estradé, S.; Peiró, F.; Morante, J.R.; Fontcuberta, A.; Morral, I. Title: Si Nanowires with Diamond Cubic / Diamond Hexagonal Heterostructures Using Cu as Catalyst. Kind of participation: Poster. Conference: MRS. Boston, USA (2007).

26. Authors: Furtmayr, F.; Vielemeyer, M.; Stutzmann, M.; Arbiol, J.; Estrade, S.; Peiro, F.; Morante, J.R.; Eickhoff, M. Title: Influence of Si- and Mg-impurities on the Growth Mechanism of GaN Nanorods on Si (111). Kind of participation: Presentation of communication. Conference: MRS. San Francisco, USA (2008).

27. Authors: Arbiol, J.; Estrade, S.; Peiro, F.; Furtmayr, F.; Vielemeyer, M.; Stutzmann, M.; Eickhoff, M.; Morante, J.R. Title: On the Epitaxial Growth of Gallium Nitride Nanorods on Si (111) Surfaces after Controlled Nitridation Procedure by Plasma Assisted Molecular Beam Epitaxy. Kind of participation: Poster. Conference: MRS. San Francisco, USA (2008).

28. Authors: Estradé, S.; Infante, I.C.; Sanchez, F.; Fontcuberta, J.; de la Peña, F.; Walls, M.; Colliex, C.; Arbiol, J.; Peiró, F. Title: Étude par EELS de la migration cationique dans des couches minces de La2/3Ca1/3MnO3 en fonction de son orientation. Kind of participation: Presentation of communication. Conference: JEELS. Poitiers, France (2008).

29. Authors: Infante, I.C.; Sánchez, F.; Fontcuberta, J.; Wojcik, M.; Jedryka, E.; Estradé, S.; Peiró, F.; Arbiol, J.; Laukhin, V.; Espinós, J.P. Title: (110)-textured La2/3Ca1/3MnO3 thin films. Optimal electrodes in manganite tunnel junctions. Kind of participation: Presentation of communication. Conference: IEEE International Magnetics Conference. Madrid, Spain (2008).

30. Authors: Arbiol, J.; Estradé, S.; Peiró, F.; Morante, J.R.; Colombo, Morral, A. Title: GaAs NWs and Related Quantum Heterostructures Grown by and Analytical Characterization. Kind of participation: Poster. Conference: 14th European Microscopy Congress, EMC 2008. Aachen, Germany (2008).

31. Authors: Estrade, S.; Infante, I.C.; Sanchez, F.; Fontcuberta, J.; de la Peña, F.; Walls, M.; Colliex, C.; Arbiol, J.; Peiró, F. Title: Dissimilar cation migration in (001) and (110) La2/3Ca1/3MnO3 thin films Kind of participation: Poster. Conference: 14th European Microscopy Congress, EMC 2008. Aachen, Germany (2008).

32. Authors: Estrade, S.; Infante, I.C.; Sanchez, F.; Fontcuberta, J.; Arbiol1, J.; Peiró, F. Title: Anisotropic strain relaxation in (110) La2/3Ca1/3MnO3 thin films. Kind of participation: Poster Conference: 14th European Microscopy Congress, EMC 2008. Aachen, Germany (2008).

33. Authors: Infante, I.C.; Hravobsky, D.; Laukhin, V.; Sánchez, F.; Herranz, G.; Wojcik, M.; Jedryka, E.; Estradé, S.; Peiró, F.; Arbiol, J.; Fontcuberta, J. Title: Crystal Orientation and Interface Effects in Nanometric Manganite Thin Films. Kind of participation: Presentation of communication Conference: THIOX -Thin Films For Novel Oxide Devices Final Meeting. Sestri Levante, Italy (2008).

34. Authors: Arbiol, J.; Estrade, S.; Daniel Prades, J.; Cirera, A.; Peiro, F.; Furtmayr, F.; Eickhoff, M.; H Gass, M.; Bleloch, A.L.; Ramon Morante, J. Title: HREELS and HRTEM Analysis of the Mg Doped GaN Nanowires: Consequences on the Electronic and Optoelectronic Properties. Kind of participation: Presentation of communication. Conference: MRS. Boston, USA (2008).

35. Authors: Barth, S.; Mathur, S.; Hernandez-Ramirez, F.; Estrade, S.; Romano-Rodriguez, A. Title: Molecule-based Chemical Vapor Deposition of One-dimensional Oxide Nanostructures: Growth, Characterization and Devices. Kind of participation: Presentation of communication. Conference: MRS. Boston, USA (2008).

36. Authors: Arbiol, J.; Estradé, S.; Prades, J. D.; Furtmayr, F.; Stark, C.; Lauferd, A.; Stutzmann, M.; Eickhoff, M.; Gass, M. H.; Bleloch, A. L.; Peiró, F.; Morante, J. R. Title: Triple twin domains in Mg doped GaN Wurtzite Nanowires: Structure and electronic properties of this Zinc-Blende-like stacking. Kind of participation: Presentation of communication. Conference: Microscopy of Semiconducting Materials, Oxford, UK (2009).

37. Authors: Estradé, S.; Arbiol, J.; Peiró, F.; Infante, I. C.; Sánchez, F.; Fontcuberta, J.; de la Peña, F.; Walls, M.; Colliex, C.. Title: Assessment of local Mn oxidation state at the nanometric scale through quantitative EELS. Kind of participation: Poster. Conference: Nanotech Insight, Barcelona, Spain (2009).

38. Authors: Conesa-Boj, S.; Estradé, S.; Zardo, I.; Morgan, C.; Fontcuberta i Morral, A.; Peiró, F.; Arbiol, J.; Morante, J.R. Title: Appearance of Hexagonal and Twinned-cubic Phase Domains in Silicon Nanowires Induced by Different Types of Catalytic Seeds. Kind of participation: Presentation of communication. Conference: MRS Spring Meeting 2009, San Francisco, USA (2009).

39. Authors: Alarcon-Llado, E.; Cusco, R.; Ibanez, J.; Artus, L.; Estrade, S.; Prades J.; Cirera, A.; Arbiol, J.; Peiro, F.; Morante, J. Title: Resonant Raman Scattering Characterization in ZnO Nanowires: Temperature and Quasimode Effects. Kind of participation: Poster. Conference: MRS Spring Meeting 2009, San Francisco, USA (2009).

40. Authors: Walls, M. G.; Estrade, S.; Arbiol, J.; Peiró, F.; Infante, I. C.; Sánchez, F.; Fontcuberta, J. Title: Atomic-scale mapping studies on STO- LCMO layers and their interfaces as a function of substrate orientation. Kind of participation: Poster. Conference: EDGE 2009, Calgary, Canada (2009).

41. Authors: Arbiol, J.; Conesa-Boj, S.; Rebled, J. M.; Estradé, S.; Spirkoska, D.; Heigoldt, M.; Heiss, M.; Gass, M. H.; Bleloch, A. L.; Abstreiter, G.; Fontcuberta i Morral, A.; Peiró, F.; Morante, J. R. Title: Bandgap Engineering of Semiconductor Nanowires: From Axial and Coaxial Quantum Wells to Local Stacking Transformations in Structure. Kind of participation: **Invited conference**. Conference: Joint Congress of the Spanish and Portuguese Microscopy Societies, Segovia, Spain (2009).

42. Authors: Estradé, S; Infante, I. C.; Sánchez, F. ; Fontcuberta, J. ; de la Peña, F. ; Walls, M. ; Colliex, C.; Arbiol, J.; Peiró, F. Title: Cationic Diffusion and Plastic Relaxation as Competing Mechanisms for Strain Accomodation in (001) and (110) LCMO layers. Kind of participation: Presentation of communication. Conference: Joint Congress of the Spanish and Portuguese Microscopy Societies, Segovia, Spain (2009).

43. Authors: Conesa-Boj, S.; Estradé, S.; Furtmayr, F.; Stark, C.; Stutzmann, M.; Eickhoff, M.; Arbiol, J.; Peiró, F.; Morante, J. R. Title: HRTEM and EELS analysis of Axial Quantum Wells in GaN/AlN Heterostructured Nanowires. Kind of participation: Poster (Award to the Best Materials Science Poster). Conference: Joint Congress of the Spanish and Portuguese Microscopy Societies, Segovia, Spain (2009).

44. Authors: Estradé, S.; Barth, S.; Hernandez-Ramirez, F.; Romano-Rodriguez, A.; Mathur, S.; Arbiol, J.; Peiró, F. Title: TEM-EELS Characterization of SnO2/Fe3O4 core-shell 1-dimensional nanostructures. Kind of participation: Poster. Conference: Joint Congress of the Spanish and Portuguese Microscopy Societies, Segovia, Spain (2009).

Teaching

1. Academic year 2006-2007.
- 1.1 Applied Electronics. Physics Degree. University of Barcelona.
- 1.2 Microscopy Techniques. Master in Nanoscience and Nanotechnology. University of Barcelona.

2. Academic year 2007-2008.
- 2.1 Applied Electronics. Physics Degree. University of Barcelona.
- 2.2 Microscopy Techniques. Master in Nanoscience and Nanotechnology. University of Barcelona.

3. Academic year 2008-2009.
- 3.1 Applied Electronics. Physics Degree. University of Barcelona.
- 3.2 Microscopy Techniques. Master in Nanoscience and Nanotechnology. University of Barcelona.

Languages spoken

Mother tongues: Catalan, Spanish.
Other languages:

1. English -*Certificate of Proficiency in English (grade A), Cambridge ESOL.*
2. French. - *DELF 1-6, ministère français de l'Éducation nationale.*
3. German. - *Mittelstufe, Goethe Institut.*